Exploration of Carbon Nanotube Composites and Piezoelectric Materials for Implantable Devices

Janelle Edusei

Supervised by Professor Wenhui Song

A dissertation submitted in partial fulfilment of the requirements for the degree of
Doctor of Philosophy

Division of Surgery and Interventional Science

University College London June 2021

Declaration

I, Janelle Aloma Davina Edusei confirm that the work presented in this thesis is my own. Where information has been derived from other sources, I confirm that this has been declared appropriately in the thesis.

Date: 03 June 2021

Acknowledgments

I would like to begin by thanking my supervisor Prof. Wenhui Song for her guidance and support throughout this project. Without her, this work would not have been possible. I would also like to thank my fellow PhD students Alexandru Chivu, for guiding me in the application of many techniques essential to my work, and Jinke Chang, for taking the time to read my thesis and offer invaluable feedback. I am truly grateful for their help and friendship.

The comradeship of my fellow PhD students in the Division of Surgery has been a great source of joy, strength and comfort. A special shout out goes to my friends in the 'Vegas!' PhD office – Kathleen Traver, Shiv Patel, Jerome Hunckler, Wai Ho, Medina Guliyeva and Jun Hon Pang. They have seen and shared the highs and lows and have always been ready and willing to listen and offer advice, opinion or a helping hand. I'll miss our philosophical chats and cosy movie nights.

Many thanks go to Bala Ramesh and Arnold Derbyshire, who were always happy to pause their own work to have a chat about my project and offer direction and suggestions. Thanks also to our Lab Manager Heike Lee-Muller for being understanding and accommodating, particularly when I needed supplies outside of Quartzy times! Thanks also to Dr. Gavin Jell for encouraging me to get involved with teaching activities outside of my project. Lecturing and lab demonstrating were certainly things which enhanced my PhD experience.

I'm also grateful to my close friend outside the lab, Krisztina Gyüre. She checked up on me regularly and helped me retain my sanity whilst also offering motivational messages and encouragement when I was struggling to maintain momentum.

My mentor, Dr. Peter Harris, has been supportive throughout this process, offering guidance and feedback on my experimental and written work. He provided the leads that gave rise to the account of the discovery of carbon nanotubes discussed in Sections 1.3.2 and 1.3.3 that have not been published elsewhere and are set out here to correct the record.

Finally, I'm grateful to my family, especially my parents, for listening to me rambling on about carbon nanotubes and electron micrographs; also for coming to drive me home from the lab in the wee hours of the morning more times than I can bring myself to admit. Without their continuous support, encouragement and love, I may have never reached this stage.

Abstract

This thesis describes an exploration of carbon nanotube (CNT) nanocomposites for application in implantable medical devices. The focus here is on materials and structures of interest as components of devices incorporating electrodes.

Electrodes for implantable devices are commonly required to interface between an electrical system, where the charge carriers are electrons presented through a metal, and human tissue, where the charge carriers are ions as well as electrons not in a metal. These interfaces are found to be prone to issues such as fibrosis and rejection. The properties of carbon nanomaterials, piezoelectric peptides/polymers and their composites suggest them as promising candidate materials that could resolve these issues. The superior conductivity, mechanical properties and chemical stability of carbon nanotubes have been explored in recent years for potential application in biomedical sensors and devices.

This work has explored piezoelectric materials, carbon nanotubes, polymers and nanocomposites of these as potential components of implantable devices. Diphenylalanine is a chiral, amphiphilic dipeptide molecule which has the ability to self-assemble into piezoelectric microtubules. The self-assembly process of diphenylalanine microtubules has been explored and its properties have been compared to the properties of poly[vinylidenefluoride-co-trifluoroethylene] (P[VDF-TrFE]) electrospun nanofibres. Later parts of this work considered the deposition of electrodes by printing. The development of CNT-polymer nanocomposites as printable inks for the fabrication of electrodes was explored.

The structure and properties of the piezoelectric nano/ micro-materials, CNT-peptide complex and conductive CNT-polymer printable inks were characterised by a range of microscopic and spectroscopic techniques. The viability of neural cells on the developed functional materials and electrodes were tested by metabolic activity measurements and immunochemical staining microscopy.

A CNT-polymer ink demonstrated good conductivity and dimensional stability when printed by 3D printer. Good biocompatibility of all the functional materials developed have been demonstrated in vitro, showing promise for further development of soft electrodes and applications in nanostructure piezoelectric sensors and implantable devices.

Impact Statement

Average human life expectancy (at birth) in the UK has increased since World War Two from 64.2 years to 81.1 years for someone born in 2015. This is a triumph of medicine, brought about through advances in biochemistry, prevention of diseases and treatment of diseases and disorders. These are however, only part of this achievement because they only extend the period of time over which a person avoids early death. There is another broader dimension which is quality of life, defined by the maintenance of the senses, mobility, mental agility, and the amenability of the body to repair. Like for like organ and tissue replacement (heart, kidneys, cornea etc.) is now more or less routine. The use of prosthetics to replace lost hair, teeth, eyes, noses and limbs has a long history. Lost limbs are increasingly being replaced by bionic prosthetics.

An aging UK population has led to a rise in the need for implantable medical devices, including heart pacemakers, bionic limbs and cochlear implants, among others. There are currently 11 million people with sensorineural hearing loss in the UK. Of these, approximately 0.1% use cochlear implants; this small percentage is in part due to the limited hearing quality achievable with current devices. The small size of the cochlea and the range of sound frequencies a viable implant needs to respond to would be expected to be among the fields to which nanotechnology can be applied. It would seem also to offer an area of application for piezoelectric materials that provide the natural interface between the electrical and mechanical regime of the human perception of sound.

The materials currently used for components in implantable medical devices are generally not able to fully integrate with human tissue; that is, all materials seem to present at least one issue with regard to tissue compatibility. This issue leads to deterioration of the implanted device and an unsatisfactory experience for the patients. This has prompted researchers to seek new materials with greater capability and compatibility than those currently employed.

This research has explored possibilities from a materials perspective, with a focus on materials that form the interface between the device and human tissue. Carbon nanotubes were selected as a starting material and were combined with a polymer to produce an ink that could be deposited with a defined geometry onto a glass substrate. This work was part of a larger project to create a self-powered piezoelectric cochlear implant. The research contributes to the process of continuous improvement of hearing aids over the years.

The work described here was disseminated to engineers specialising in a complementary subject area during an industry placement at Hayward Tyler Ltd. in Luton, 2017, and also presented as a poster to specialist academics at the British Society of Nanomedicine conference in London, 2018. The work draws on experiences with techniques developed and results collected during a 3-month period as a visiting researcher at the Indian Institute of Science, Bangalore, India.

Table of Contents

List of Figures

13

17

List of Tables

22

Abbreviations

AAO		Anodised aluminium oxide
ATR-FTIR		Attenuated total reflectance Fourier transform infrared spectroscopy
AFM		Atomic force microscopy
BMIMCl		1-Butyl-3-methylimidazolium chloride
BSA		Bovine serum albumin
BSC		Biosafety cabinet
CD		Circular dichroism
CNT		Carbon nanotube
CPC		Conductive polymer composite
CVD		Chemical vapour deposition
DAPI		4′,6-Diamidino-2-phenylindole
DBS		Deep brain stimulation
DFF		D-diphenylalanine
DMEM		Dulbecco's Modified Eagle Media
DMF		Dimethylformamide
DMSO		Dimethylsulfoxide
DNA		Deoxyribose nucleic acid
FD		Force-deformation (graph)
FmocFF		Fmoc-diphenylalanine
FTIR		Fourier transform infrared spectroscopy
FWHM		Full width (at) half maximum
HBTU		Hexafluorophosphate benzotriazole tetramethyl uronium (2-(1H-benzotriazol-1-yl)-1,1,3,3-tetramethyluronium hexafluorophosphate)
HDF		Human dermal fibroblasts
HFIP		Hexafluoroisopropanol
HOBt		Hydroxybenzotriazole
HRSEM		High resolution scanning electron microscopy
HSC		Human Schwann cells
IMS		Industrial methylated spirit
IPA		Isopropanol
LFF		L-diphenylalanine
MWCNT-COOH		Carboxylic acid functionalised multiwall carbon nanotubes
MWCNT-NH_2		Amine functionalised multiwall carbon nanotubes
MWDFF		Multiwall carbon nanotube-D-diphenylalanine complex
MWFmocFF		Multiwall carbon nanotube-Fmoc-diphenylalanine complex
MWLFF		Multiwall carbon nanotube-L-diphenylalanine complex
NFES		Near field electrospinning
NMM		N-methylmorpholine
NMP		N-methyl-2-pyrrolidone
PAN		Polyacrylonitrile

PDMS		Polydimethylsiloxane
PEDOT		Poly(3,4-thylenedioxythiophene)
PEDOT:PSS		Poly(3,4-thylenedioxythiophene):poly(4-styrene sulfonate)
PEGDA		Polyethylene glycol diacrylate
PLL		Poly-L-lysine
PSS		Poly(4-styrene sulfonate)
PSSS		Poly(sodium-4-styrene sulfonate)
PVDF		Polyvinylidene fluoride
PVDF-TrFE		Poly[vinylidenefluoride-co-trifluoroethylene]
PVP		Polyvinylpyrrolidone
PZT		Lead zirconium titanate
RI		Refractive index
SEM		Scanning electron microscopy
TEM		Transmission electron microscopy
XRD		X-ray diffraction

Chapter 1   **Introduction**

1.1.   **Implantable Medical Devices**

There are seven domains of medicine, developed in the last eighty-five years, that are responsible for a dramatic improvement in longevity and quality of life in longevity. These are antibiotics, drugs, cancer, transplant organs, artificial organs, genetics and bionics.

Implantable medical devices such as pacemakers, artificial organs, bionic limbs and cochlear implants have been developed as solutions to health issues and injuries [1]. A natural consequence of longevity is an increase in the occurrence of ailments associated with old age, such as Type 2 diabetes and hearing loss.

Complications arising from diabetes include ulcers that can lead to amputation. Amputations in the UK that are related to diabetes account for 80% [2] of amputations annually. The proportion of the UK population with diabetes is predicted to increase from 8.6% to 9.7% [2] over the next 15 years and amputations will likely increase proportionally.

Sensorineural hearing loss is a disability which currently affects 11 million people [3] in the UK. This number is also expected to increase to 15.7 million people over next 15 years; the condition is currently costing the NHS an average of £450 million [3] a year.

While there have been significant improvements in the technology used in implantable medical devices, full integration with the human body remains difficult to achieve and a significant factor in this is fibrosis formation at the point of connection and in the surrounding tissue. Build-up of scar tissue often causes the device to fail as electrical signals are unable to pass between body tissue and the device. Device failure is not only costly and resource-consuming but is frustrating for the patient, with many people eventually forgoing the prosthetic or bionic principally due to the disappointment and inconvenience of device failure.

This dissertation considers specifically cochlear implants.

1.1.1.   **Sensorineural Hearing Loss and Cochlear Implants**

It is accepted that the loss of a limb alone can lead to the need for a prosthetic or bionic replacement, but there are several nerve injuries that can require neurons to be

repaired or stimulated to regain function. An example is sensorineural hearing loss, in which hearing loss is caused by the death of hair cells in the cochlea.

The cochlea is a spiral-shaped cavity located in the inner part of the ear. The adult human cochlea is approximately 9 mm in diameter, with an uncoiled length of around 30 mm (**Figure 1.1**). It is lined with epithelial cells that carry hairs from the base to apex of the cochlea. These hair cells sense the vibrations transferred to the cochlea from the eardrum from different frequencies of sound depending on their position. The vibrations are then mechano-transduced into electrical signals which are received by the spiral ganglion neurons and carried to the auditory nerve.

1 cm

Figure 1.1 Illustrative diagram of the spiral coil of a human cochlea, showing the surgical incision and application of a cochlear implant electrode array (white and grey coil)

Hearing loss can result from any of several different causes, including natural aging, genetic factors, congenital defects and chronic exposure to loud sounds. As the hair cells die, the spiral ganglion neurons, which are the path between acoustic sounds and the auditory nerve, start to degenerate and recede. An associated consequence of hair cell death is that the hearing frequency range of the patient is reduced.

Sensorineural hearing loss is often treated with external devices such as hearing aids or with surgically implanted devices such as cochlear implants. A cochlear implant aims to overcome hearing loss caused by hair cell death by replacing the function of the hair cells, although hair cells and spiral ganglion neurons are inextricably linked. Cochlear implants can be considered as having two parts – one external and one internal (**Figure 1.2**). The external part consists of a microphone, a speech processor (which converts sounds to electrical signals), a transmitter and a battery. The internal part comprises a receiver and electrodes which transmit the electrical signal to the auditory nerve [4].

27

Sending a signal to the spiral ganglion neurons from a cochlear implant does not halt the degeneration; rather, the spiral ganglion neurons continue to recede as a result of the missing hair cells. The continued recession of the spiral ganglion neurons reduces the efficacy of a cochlear implant, as signals from the device electrodes are no longer able to reach the spiral ganglion neurons. A short-term solution is to increase the voltage to boost the signal, but increasing the voltage then becomes part of a vicious cycle of reduced function and increased voltage until the device fails entirely.
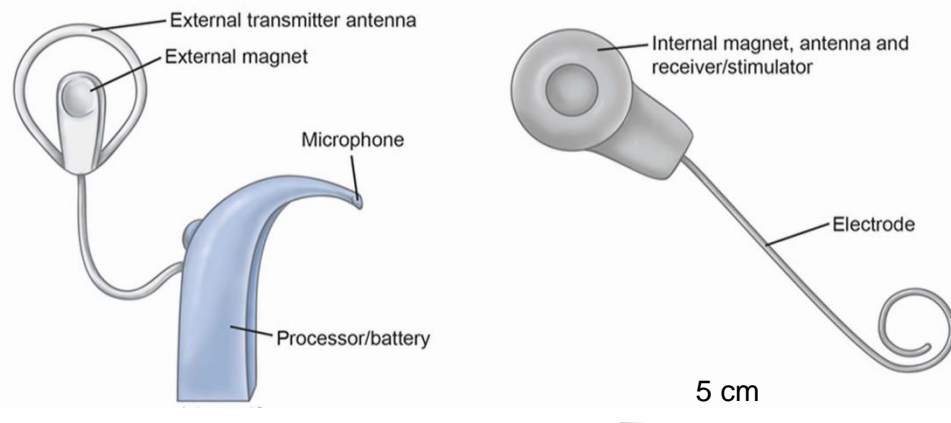
Figure 1.2 *Diagram of external and internal components of a cochlear implant. Figure prepared by J. Gregory, 2008*

Cochlear implants are also subject to engineering limitations. The maximum number of electrodes in a cochlear implant is currently 24 [5], compared to 30,000 [6] hair cells in a natural cochlea. This results in a cochlear implant having a vastly lower fidelity than a natural cochlea, particularly with regard to sounds in the low frequency range. There are on the internet various postings that simulate the sound of speech as perceived by a cochlear implant user [7]; it compares with recordings of the sound of a steam locomotive departing from a railway station. It is understandable that cochlear implant users do not enjoy music beyond the rhythm. Also, cochlear implants have high power consumption and require batteries which need to be replaced or recharged regularly. Significant improvement on that would be a worthy pursuit.

An ideal system would have good sound fidelity, integrate with the body seamlessly, be self-powering and encourage nerve cell growth to prevent spiral ganglion neuron recession. Improving sound fidelity might equate with an increased number of electrodes or sensory channels – we may not know what form this might take; we will only know when someone offers it up for evaluation. In the meantime, the use of nanotechnology might have something to offer.

1.1.2. **Challenges of Implantable Electrodes**

According to the Oxford Dictionary of Physics, an electrode is "A conductor that emits or collects electrons in a cell, thermionic valve, semiconductor device" [8]. In the context of medical devices, an electrode can be a device which delivers, receives, or delivers and receives, an electromotive force (emf) or current [9].

In currently available bionics and implantable devices, the electrodes are usually made of platinum, platinum alloys or gold. These materials are, however, grossly mismatched with the human body, being both smooth and hard compared to nerve tissue that on the scale of tens of microns are granular and soft. This causes inflammation at the implantation site and the electrodes are eventually encapsulated by scar tissue as the body rejects the foreign material. Pure copper and pure silver both have higher conductivity than the majority of materials currently used but they are also highly toxic to the human body, causing necrosis and haemorrhage within three weeks of implantation [10]. As such, silver and copper are not used as implantable device electrodes. Researchers are seeking novel materials that can better integrate with human tissue while maintaining or enhancing the conductivity achieved with currently available electrodes [1].

1.1.3. **Piezoelectric Cochlear Implants**

Piezoelectricity is a phenomenon exhibited by non-centrosymmetric crystals in which a crystal can convert a mechanical stress into an electrical potential. The converse is also possible and both effects will be examined here in greater detail in a later section. The current generation of cochlear implants use a battery-powered processor to convert an acoustic signal to an electrical one. A cochlear implant based on piezoelectric materials might remove the need for an external battery since the acoustic sounds would be converted to electrical signals by means of mechanotransduction via the direct piezoelectric effect. One of the main advantages of such a device is that it would require only one surgical procedure, implantation, and would be self-powering afterward. There have been a number of reports in which piezoelectric materials have been applied in cochlear implants. In these, thin films of (lead zirconate titanate) PZT [11] or polyvinylidene fluoride (PVDF) [12] are often discussed, although a recent paper described the use of aluminium nitride (AlN) [13] as a piezoelectric material of choice. Researchers have investigated the feasibility of piezoelectric cochlear implants *in vivo* and obtained promising results [12, 13].

It has been argued that a cochlear implant could not feasibly be powered by piezoelectric response alone [4], but that statement was made in response to a previous paper that had explored the optimisation of energy harvesters activated by walking. The energy harvester functions in much the same way as self-winding watches which are powered by the motion of the wearer. With the self-winding watch in mind, all hope should not be lost because a minimally supported system could be employed in which the piezoelectric material is used to drive the implant where possible and a battery used the remaining time. A similar approach was used by the watchmakers A-L Breguet and Fils, who developed self-winding watches that were equipped with a power reserve to power the watch at times when movement was unable to produce enough power.

Aside from concerns regarding the potential limitations of a piezoelectric material-powered implant, researchers must also contend with the materials design and fabrication challenges that arise when developing such new types of implants. The materials used must have high efficacy to generate enough charge to stimulate the spiral ganglion neurons with minimal or no external amplification. Any device fabricated from the material must also be small and flexible enough to fit inside and bend with the turns of the cochlea without causing damage to the surrounding tissue. Ceramic materials are not inherently flexible, although the development of piezoelectric composites may offer a possible solution. The development of new piezoelectric materials and composites, and new morphologies of existing piezoelectric materials, are methods through which researchers hope to develop piezoelectric materials with improved properties and thus improve the prospect of fabricating fully implantable, self-powered cochlear implants.

1.2.   **Piezoelectric Materials**

1.2.1.   **The Piezoelectric Effect**

The pyroelectric effect is when a potential difference across a material is produced by heating it. The piezoelectric effect is the ability of non-centrosymmetric crystals to transduce mechanical stress into an electrical potential and *vice versa*. The production of an electrical potential from a mechanical stress is called the direct piezoelectric effect. Piezoelectricity was first observed in ceramics by Pierre and Jacques Curie in 1880 [14]. They found that pyroelectric materials; materials that generate an electric charge when they are heated or cooled, also produce electricity when the crystal is deformed. This effect, coined as "piezoelectricity", was found to be present in all

30

pyroelectric materials, although the reverse is not true (**Figure 1.3**). This led to a search for piezoelectric materials which had not previously been identified. In 1921, W. Guyton Cady developed the first quartz crystal oscillator – a circuit that uses the resonance of a vibrating piezoelectric crystal, to create an electrical signal with constant frequency. The oscillator was applied as a frequency standard and in 1923, was used as part of the first international direct comparison of frequency standards. Piezoelectric materials are a subset of dielectric materials; that is, they are electrical insulators which can become polarised in an electric field. The indirect or converse piezoelectric effect is transduction of an electrical potential into a mechanical movement. The phenomenon is observed for single crystals of piezoelectric materials, in which there is only one crystal domain, or in polycrystalline piezoelectric materials that have undergone a process called 'poling'. This process involves applying a strong electric field across the piezoelectric material, often at elevated temperatures, to force the crystal domains to align in a particular direction. The aligned domains give the crystal an overall dipole and cause it to become sensitive to minute changes in the physical or electrical environment [14].
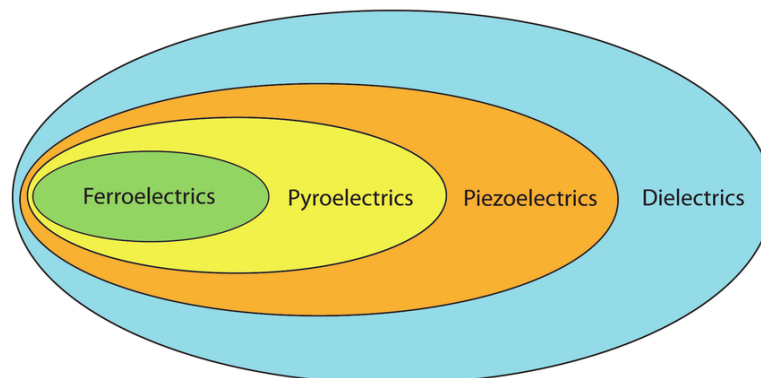
Figure 1.3 *Representation of the relationship between dielectric, piezoelectric, pyroelectric and ferroelectric materials. Reprinted from [15]*

The piezoelectric coefficient, expressed in picometres per volt, pmV^{-1}, or the equivalent picocoulombs per Newton, pcN^{-1}, is a measure of the volume change of a crystal when it is subjected to an electric potential. The magnitude of the piezoelectric coefficient measured can be affected by environmental conditions, e.g. temperature, and sample properties, or extent of the poling of the material.

The piezoelectric response of different materials varies with the direction of the applied mechanical stress compared to the symmetry of the crystal. The piezoelectric coefficient is represented by d_{ij} where i indicates the direction of the applied electric

field relative to the polarisation of the crystal and j indicates the direction of movement. There are two common methods to determine a piezoelectric coefficient. For small samples, piezoresponse force microscopy (PFM) is used. The sample is located in an atomic force microscopy chamber on a conductive substrate. An electric field is generated by applying an electric potential between the substrate and cantilever or between two separate sections of the substrate (as demonstrated in **Figure 1.4**). The strength of the electric field is varied by changing the magnitude of the applied voltage. The application of an electric potential induces the inverse piezoelectric effect, causing the crystal to move.
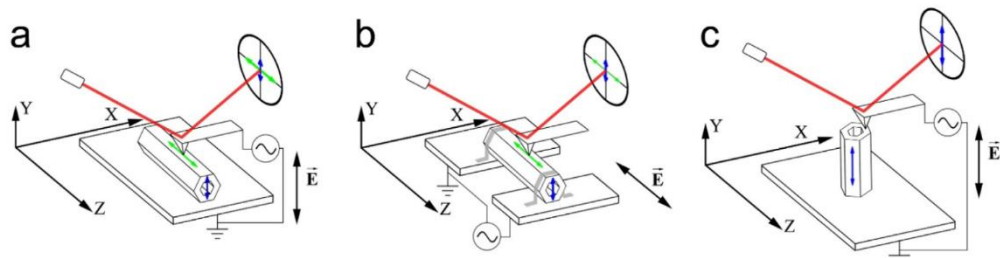
Figure 1.4 *Schematics of different configurations for the measurements of piezoelectric coefficients by piezoresponse force microscopy here illustrated with a diphenylalanine crystal of hexagonal cross section. a) Measurement of d_{15} (displacements shown by horizontal arrow) and d_{14} (vertical arrow), b) Measurement of $(d_{33})_{clamp}$ (horizontal arrow) and d_{31} (vertical arrow), c) Measurement of d_{33} (vertical arrow). Red line shows laser beam reflecting from the cantilever. Figure and caption adapted from* [16]*.*

The magnitude of lateral or vertical movement of the crystal is measured by the cantilever and is proportional to the applied voltage. A linear graph of displacement against voltage yields the piezoelectric coefficient (d) as the gradient. This can also be considered as the rate of change of displacement (s) with respect to the applied voltage (E), under constant tension (T), Equation 1.1.

$$d = \left(\frac{\partial s}{\partial E} \right)_T \qquad (\ 1.1\ )$$

For large samples, as crystals or layers on a substrate, the Berlincourt method [17] is usually employed. The sample to be tested is located between two metal contacts and a cyclical stress, usually between 10 Hz and 1 kHz, is applied. A capacitor connected in parallel collects the charge produced by the direct piezoelectric effect. The measured charge and resonance response of the sample are compared with a crystal of known characteristics. The piezoelectric coefficient is then determined by calculating the rate of change of charge collected by the capacitor (Q) with respect to the applied stress (σ), where electric flux density (D) is held constant, Equation 1.2.

$$d = \left(\frac{\partial Q}{\partial \sigma} \right)_{D}$$

(1.2)

Materials may show a very high piezoelectric response in one direction but significantly lower response in other directions. An example of this is diphenylalanine, a material of interest in this work, for which four piezoelectric coefficients were measured by Vasilev *et al.* [16]. They reported the coefficients as $d_{15} = 80$ pmV^{-1}, $d_{31} = 4$ pmV^{-1} and $d_{33} = 18$ pmV^{-1}. It is clear that the lateral piezoelectric response is much stronger than the vertical. In comparison, different piezoelectric coefficients for PVDF have been reported as $d_{15} = 27$ pm/V, $d_{31} = 20$ pmV^{-1}, $d_{33} = 32$ pmV^{-1} [20]. Though the d_{33} is the largest value, the d_{15} and d_{31} values are similar in magnitude. The piezoelectric coefficients for some commonly studied piezoelectric materials are shown in **Table 1.1** below.

Table 1.1 Piezoelectric coefficients of commonly studied piezoelectric materials. ZnO, BaTiO$_3$ and quartz are bulk ceramic piezoelectric materials, PVDF and PVDF-TrFE are piezoelectric polymers and diphenylalanine and collagen are naturally occurring piezoelectric materials

Material	Piezoelectric Coefficient/ pmV^{-1}	Measurement Method	Reference
ZnO	$d_{33} = 13$	Berlincourt	[18]
BaTiO$_3$	$d_{33} = 190$	Berlincourt	[18]
Quartz	$d_{11} = 6$	Berlincourt	[18]
PZT	$d_{33} = 233$	PFM	[19]
PVDF	$d_{33} = 32$	PFM	[20]
PVDF-TrFE	$d_{33} = 25.2$	PFM	[14]
Diphenylalanine	$d_{15} = 80$	PFM	[16]
Collagen	$d_{15} = 2$	PFM	[14]

Many different types of material display piezoelectric properties, including inorganic crystals, polymers, and naturally occurring peptides and proteins.

1.2.2. **Inorganic Piezoelectric Materials**

Crystalline inorganic materials consist of a regular array of atoms, ions or molecules, with a repeat unit called a unit cell. The piezoelectric effect in inorganic materials arises from structural asymmetry inside the unit cell. When the material is not subject to an external force, the asymmetry is localised and the crystal is in electrical equilibrium. However, deformation of the crystal causes this equilibrium to be disrupted and a net

dipole to be induced in the material. Electrons in each unit cell move in response to the dipole, causing a potential difference to be generated through the crystal. This is the origin of the association between mechanical deformation and the output of electricity.

Quartz is an example of a widely used inorganic piezoelectric material. It is chiral and exists in two forms – *α* quartz, which is the stable form at room temperature, and *β*-quartz, which is formed when *α*-quartz undergoes an inversion transition at 573 °C. The room temperature variant of quartz is piezoelectric but the high temperature form is not [21]. Other inorganic piezoelectric materials include ceramics such as zinc oxide (ZnO), barium titanate ($BaTiO_3$), lead zirconate titanate (PZT) [22] and lead-free piezoelectric ceramics such as bismuth sodium titanate (BNT).

While ZnO is also pyroelectric, $BaTiO_3$, PZT and BNT belong to a sub-class of piezoelectric and pyroelectric materials, known as ferroelectric materials. Like many inorganic materials, ferroelectric materials have a multi-domain crystalline structure with clear boundaries between domains. In each domain, the electric dipole moments are uniformly polarised. This spontaneous, localised polarisation can be spread across the whole crystal by the application of an electric field. As a result of these electrical properties, ferroelectric materials are used extensively in the electronics industry, where they have been applied as capacitors with tuneable capacitance and researched for applications as actuators.

The toxicity that arises from the use of lead compounds, such as PZT, as well as the rigidity and brittleness that is common for inorganic piezoelectric materials, reduce the opportunities for applying the established and well characterised piezoelectric materials to newer technologies such as bioelectronics. Application of piezoelectric materials in biomedicine requires piezoelectric materials with different qualities to widely used ceramics.

1.2.3. Piezoelectric Synthetic Polymers

Piezoelectric polymers, also called bulk piezoelectric polymers, have lower piezoelectric coefficients than inorganic piezoelectric materials but offer more flexibility in fabrication and applications. The term 'piezoelectric polymer' is used in reference to polymers and their derivatives that are inherently piezoelectric [23]. The piezoelectric effect in bulk piezoelectric polymers arises from a net dipole in the macromolecular chain. When the polar monomers within a polymer are forced to align in an electric field or under tension or compression, this results in piezoelectricity.

Polymer materials when first prepared frequently do not have the molecular orientation to achieve a large dipole. In these cases the dipole can be enhanced by poling. Poling may take place after deposition, or as part of a multistage preparative procedure. Highly crystalline polyureas, for example, require poling at a high (in the context of its melting behaviour) temperature to allow dipole rotation and, therefore, poling at lower temperatures leads to lower piezoelectric strength [24].

Polyamides (nylons) are a group of bulk piezoelectric polymers **(Figure 1.5a)**. In 1980, Newman *et al.* [25] discovered that nylon 11 displayed piezoelectric properties. This began a chain of investigations into the piezoelectric response of polyamides with an odd number of amide units. Amide units in nylons pack to maximise hydrogen bonding between units. For nylons with even numbers of amide units, the packing arrangement is antiparallel, resulting in a cancellation of dipoles. Conversely, nylons with odd numbers of amide units pack in a parallel arrangement, aligning all the dipoles in the same direction and causing an overall dipole within the polymer [26].

Polyureas are another example of bulk piezoelectric polymers. Similarly to polyamides, polyureas consist of a carbon backbone and a functional group, N-C=O-N in this case **(Figure 1.5b)**, which contributes to the formation of dipoles within the molecule. Their thermal stability and piezoelectric strength depend greatly on their degree of crystallinity and the extent of dipole rotation possible.

a   **b**
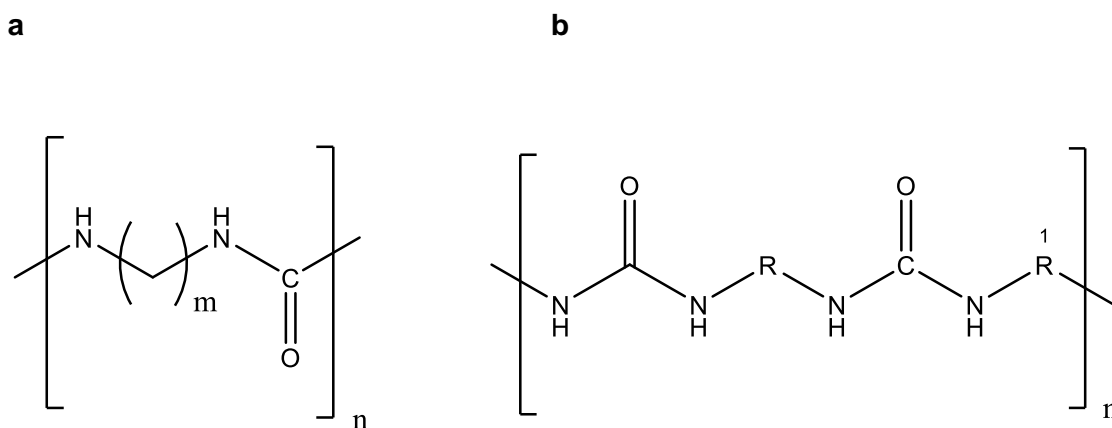
Figure 1.5 *Example skeletal formulae of a repeating unit of a a) polyamide structure, b) polyurea structure*

Polyvinylidene fluoride (PVDF) is the most studied bulk piezoelectric polymer, which becomes piezoelectric after being poled. Above a characteristic temperature, known as the Curie temperature, piezoelectric materials become paraelectric and lose their

piezoelectric properties. The poling temperature of PVDF must be below its Curie temperature to prevent PVDF from transforming into a different non-piezoelectric form.

PVDF exists in alpha (α), beta (β) and gamma (γ) phases (**Figure 1.6**) with the β phase showing the highest piezoelectric response.
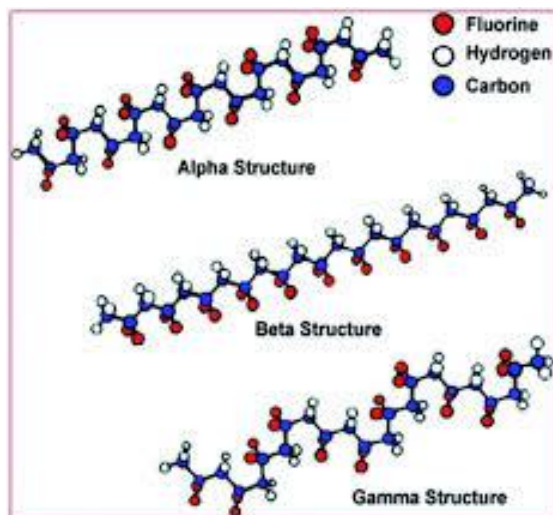
Figure 1.6 Ball and stick representations of the different conformations of polyvinylidene fluoride. Reprinted with permission from [27] Copyright 2009 American Chemical Society

The polymer is non-centrosymmetric but the arrangement of the molecules in the alpha and gamma phases mean that their net dipole is weak and they therefore do not display strong piezoelectric properties. However, once PVDF is poled in a strong electric field, around 50 MVm^{-1} [26], and the macromolecular chains are aligned and packed into the beta phase, a large net dipole is induced and a large piezoelectric response can be observed. PVDF is available in various physical forms, most notably powder, film and fibre forms and it has been reported that mechanical stretching of PVDF films during poling can enhance the alignment of molecules in the β phase. PVDF films and fibres have been applied as scaffolds or substrates for cell culture [28] and as components in piezoelectric devices [23]. The powder form is usually a starting material for manufacturing one of the other forms. The piezoelectric properties of PVDF have been applied in cell culture environments, investigating both the effect of the direct and converse piezoelectric effect on the proliferation, morphology, metabolic activity and differentiation of cells. It was suggested that application of the piezoelectric effect within a cell culture environment, led to increased cell differentiation and proliferation in many cases [29]. This will be discussed in detail in a later section.

In addition to its piezoelectric properties, PVDF is also of interest due to its mechanical properties. Laiarinandrasana *et al.* [30] report the Young's modulus of PVDF as being approximately 2 GPa, which is of a similar magnitude to nylon-6. However, PVDF films have also been shown to be flexible and have good thermal stability.

A way of further improving the properties of PVDF is to design and synthesise a copolymer. A widely studied copolymer of PVDF is the block copolymer poly[vinylidene fluoride–co-trifluoroethylene] (PVDF-TrFE) [20]. The TrFE molecule contributes three fluorine atoms to the polymer. However, since two of the fluorine atoms are on opposite sides of the carbon bond, their dipoles cancel out and only one fluorine atom contributes to the overall dipole (**Figure 1.7**).
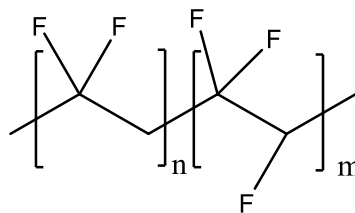
Figure 1.7 *Skeletal formula of PVDF-TrFE showing monomers of PVDF (left bracket) and TrFE (right bracket)*

PVDF-TrFE crystallises in an all-trans conformation, increasing the probability of obtaining the β phase but the flexibility of the carbon-carbon single bond allows the fluorine molecules to rotate and reduces the alignment of the dipoles. It is necessary to pole PVDF-TrFE to maximise the β phase present. PVDF remains piezoelectric until it melts at a temperature of 177 °C. This contrasts to PVDF-TrFE which undergoes a piezoelectric-paraelectric transition at its Curie temperature (110 °C) before melting at 150 °C. The lower Curie temperature is beneficial as it allows the piezoelectric-paraelectric transition to be studied. Another copolymer of PVDF, polyvinylidene fluoride-chlorotrifluoroethylene (PVDF-CTFE), has been shown to increase the ease with which the carbon-carbon bond can rotate, allowing a greater proportion of β phase to be obtained during poling compared to the PVDF homopolymer and other copolymers. This could be steric hinderance due to the larger covalent radius of the chlorine atom, which causes greater repulsion from other halogen atoms in the vicinity [20].

1.2.4. **Piezoelectric Natural Polymers**

Piezoelectricity in naturally occurring and living materials was first suggested by A.J.P. Martin in 1941 [31] when he researched the cause of the observation that a strand of

human hair becomes charged when it is rubbed against another strand of hair. He found that the effect arose because the cuticle cells, made primarily of keratin, are piezoelectric and become charged upon the application of a shear stress. Following this suggestion, researchers began to investigate the presence of piezoelectricity in other biomolecules and discovered that bone, DNA and other naturally occurring peptides and proteins also display piezoelectric properties [26]. The piezoelectric effect in bone is caused by the presence of collagen and hydroxyapatite. Collagen has a triple helix form, while hydroxyapatite crystallises with a hexagonal habit. It was previously believed that hydroxyapatite could not exhibit piezoelectricity because it belongs to a centrosymmetric hexagonal space group ($P6_3$), however computational models have since shown that hydroxyapatite lacks an inversion centre and can therefore exhibit piezoelectricity [14]. The discovery of piezoelectricity in helical collagen fibres led researchers to question whether helical DNA could also exhibit piezoelectricity. A study of aligned DNA films revealed that DNA can, although the effect is less prevalent than in collagen [32]. Some examples of naturally occurring piezoelectric polymers and their properties are shown in **Figure 1.8**.

1.2.5. **Organic Piezoelectric Materials**

Piezoelectricity has been observed in organic crystals and is quite common in some classes of compound, such as peptides and proteins. Natural biomaterials tend to exhibit a weak piezoelectric response. The piezoelectric coefficients of most proteins tend to be small; well-formed organic non-centrosymmetric crystals are higher. A recent study by Yuan *et al.* [33] reported a coefficient of β glycine as d_{16}= 178 pmV^{-1}, which is at the high end of the range. Numerous peptides including *cyclo*-glycine-tryptophan, cyclo-phenylalanine-tryptophan, bis-cyclic-β-peptides and diphenylalanine have also been identified as displaying piezoelectric properties.

Diphenylalanine

Of the aforementioned materials, with a piezoelectric coefficient of 80 pmV^{-1}, diphenylalanine stands out as an organic crystal with a piezoelectric coefficient comparable to well-known inorganic piezoelectric materials such as those listed in **Table 1.1**.

Diphenylalanine is a dipeptide molecule that occurs naturally; it is found in amyloid β, a key component of the plaques characteristic of Alzheimer's disease [34]. When diphenylalanine is dissolved in hexafluoroisopropanol (HFIP), it has the ability to self-assemble into a range of morphologies, depending on the concentration of the solution.

Self-assembly is the ability of some molecules to spontaneously organise into different nanoscale structures without external influence. The process is driven by non-covalent interactions and the nature of the structure formed is dependent on the concentration of the solution. At high concentration, diphenylalanine self-assembles into microtubes with a hexagonal external cross section, which display piezoelectric properties.
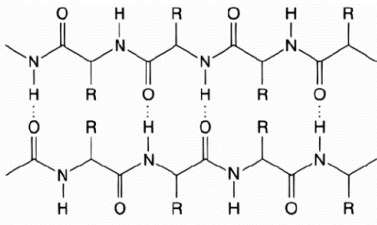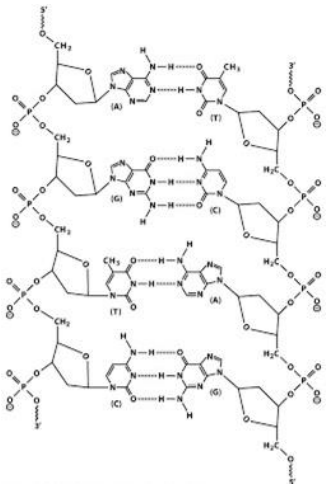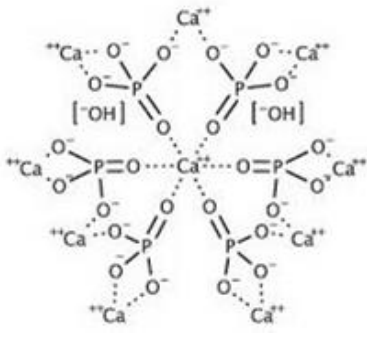
Natural Polymer	Skeletal Structure	Young's modulus	Piezoelectric Coefficient
Keratin		2 GPa [35]	d_{33} = 0.1-0.2 pmV^{-1} [36]
DNA		0.3-1 GPa [37]	d_{14} = 0.003 pmV^{-1} [38]
Hydroxyapatite		7-13 GPa [39]	d_{33} = 0.04 pmV^{-1} [40]

Figure 1.8 *Structure, mechanical properties and piezoelectric properties of natural piezoelectric polymers*

Similarly to hydroxyapatite, discussed above, diphenylalanine has a hexagonal crystal habit. However, while hydroxyapatite belongs to a centrosymmetric space group, P6$_3$/m, diphenylalanine is chiral and has two enantiomers which belong to two

enantiomorphic space groups within the hexagonal crystal system, $P6_1$ and $P6_5$. Both L and D enantiomers of diphenylalanine self-assemble into hexagonal microtubes and their properties are much the same but with a few notable differences discussed later in Chapter 3.

The morphology of self-assembled diphenylalanine is usually determined by the concentration of the original solution. It has been found that the morphology can be adjusted by the use of a mixed solvent [41]. A study by Safaryan *et al.* [42] produced modified self-assembled structures by adding ethylene glycol to the initial solution of diphenylalanine in HFIP. The modified diphenylalanine crystals had a microribbon morphology and an orthorhombic crystal structure. The researchers showed that these microribbons were also piezoelectric and had a piezoelectric response slightly smaller than their hexagonal habit relatives.

Another study by Huang *et al.* [41] showed that self-assembling diphenylalanine in different ratios of a water-acetonitrile (ACN) (methylcyanide) mixed solvent led to a structural transition from hollow peptide microtubes to solid peptide nanofibres as the ACN percentage increased. A follow-up study by Huang *et al.* [43] probed the effect of temperature on diphenylalanine structures self-assembled in a water-ACN mixed solvent. These researchers revealed that heating the diphenylalanine structure led to a reversible structural transition from nanorod to solution.

The results in the aforementioned studies and other reports in the literature show clear links between the properties of the solvent and the self-assembled structure obtained. It is important to note that the self-assembly of diphenylalanine relies on both hydrogen bonding and aromatic interactions. As such, the precipitating solvents can facilitate or disrupt the hydrogen bonding capability of diphenylalanine based on their polarity and proticity. The polarity and proticity of solvents will be discussed further in Chapter 3.

In contrast to PVDF, which is polarised perpendicular to the long axis of the fibre, diphenylalanine is polarised parallel to the long axis, giving rise to a strong lateral piezoelectric signal; the perpendicular signal is close to zero. Studies have shown that diphenylalanine self-assembled structures can be grown in vertically aligned forests attached to a siliconised glass substrate [44].

The self-assembly of diphenylalanine and its piezoelectric properties have generated much interest with researchers investigating possible applications of diphenylalanine as piezoelectric transducers [42] and as carriers for drug delivery systems [45]. Nguyen *et al.* [46] expanded on the idea of growing vertically aligned peptide microrods, seeking to produce a peptide-based power generator. The researchers formed a seed layer from

a concentrated solution of diphenylalanine and grew diphenylalanine microrods on top in the presence of an electric field. The microrods obtained had a hexagonal habit, with diameter (~ 15 μm) similar to that of L-diphenylalanine microtubes but were smaller in length (~ 60 μm). The microrod array was assembled between two gold electrodes to form a power generator and the generator was compressed to elicit a piezoelectric response.

In a similar way that templates can be used to arrange diphenylalanine into peptide microtube arrays, diphenylalanine has itself been used as a template for producing metal and polymer nanotubes. Multiple studies [47, 48] have reported the use of the hollow channel of diphenylalanine microtubes as a structure within which to chemically deposit a platinum, gold or silver nanowire. The subsequent dissolution of the peptide microtube using a proteinase enzyme has been described by Reches and Gazit [48].

1.2.6. **Piezoelectric Composites**

Inorganic piezoelectric materials that have low toughness can be combined with polymers that have high elasticity and easy processability to form piezoelectric composites. Piezoelectric properties may be conferred on the composite material through the addition of ceramic piezoelectric micro or nanosized particles. This concept was described by Petrossian *et al.* [49], who reported the formation of a PZT-polyurethane composite which maintained the piezoelectric properties of PZT microparticles while exhibiting high structural flexibility. Another study published in 2019 by Stuber *et al.*, [50] reported the formation of lead-free piezoelectric composites for energy harvesting. They fabricated a composite material containing 1-8% potassium sodium lithium niobate (KNLN) mixed in a polydimethylsiloxane (PDMS) polymer matrix using wet spinning and sintering techniques. The composite had a d_{33} of 35 pmV^{-1}, comparable to that of PVDF.

1.2.7. **Manufacturing Techniques of Piezoelectric Materials**

Owing to the size of the piezoelectric effect and the uses to which it is put, macroscopic piezoelectric devices in general are quite small. In American parlance, devices use sub-inch (2.5 cm or less) slices, discs, spheres or layers on a substrate material.

The ability of piezoelectric materials to be conveniently applied as part of a layered structure makes them good candidates for use in microelectronic devices. Researchers have investigated different methods for depositing piezoelectric materials onto

substrates from solutions. The most common methods are electrospinning, spin coating and solvent evaporation [20]. Each deposition method produces piezoelectric films or fibres with slightly different physical properties, thus allowing the deposition method to be used to tailor the form and properties of the piezoelectric material towards the requirements of the desired application.

Sol-gel and Sintering

Sol-gel is a method that involves deposition of an inorganic colloidal solution or suspension onto a substrate, followed by solvent removal through centrifugation and thermal treatments to obtain a film or crystal. In a study by Sharma *et al.* [17], PZT pellets were prepared using a combination of sol-gel and sintering techniques. PZT sol-gel precurser materials – lead acetate trihydrate, zirconium n-propoxide, titanium isopropoxide, and butanol – were mixed, hydrolysed using distilled water and then condensed in a ventilated oven to produce a viscous gel. The gel was then dried and crushed to obtain PZT powder, and subsequently calcined at 750 °C to remove impurities and any remaining solvent. The PZT powder was used to create a pellet and the pellet was sintered at 1200 °C.

Sintering is the process of heating particles in close proximity to the point of coalescence but without reaching the melting point of the material. It is often used as a stand-alone technique but can also be applied as a final stage in the sol-gel process. Sintering is regarded as a beneficial method in materials processing since it facilitates densification of the material, reduction of porosity and, depending on sintering temperature, can lead to improved mechanical properties. In the case of piezoelectric materials, sintering can also lead to improved dielectric and piezoelectric properties [51].

Electrospinning

Electrospinning is used for the deposition of piezoelectric polymers. Electrospinning involves the creation of an electric field between a needle and a plate or drum collector. A solution of polymer is then extruded inside the field from a syringe external to the field. For PVDF, the solvent is commonly dimethylformamide (DMF), with acetone added to increase the evaporation rate and facilitate the electrospinning. The electric field draws the polymer out into fine, poled fibres, the diameter, porosity and uniformity of which are controlled by the concentration of the solution, humidity of the environment and the spinning parameters (voltage, flow rate, distance between syringe and collector). The electrospun fibres can be collected as a randomly orientated fibre mat on a metal plate or as aligned fibres either on a rotating drum or between two metal rods.

3D Printing

3D printing is a development from computer inkjet printer technology. It builds 3-dimensional structures by overprinting layers. A number of variations on 3D printing techniques for piezoelectric materials have been reported. These include methods in which poling is performed during (near-field direct writing method) or after (photocurable resin method) [52] the printing process. In a recent study, Cui *et al.* [53] described the 3D printing of PZT nanoparticles suspended in a photocurable resin. They were able to print high resolution 3D structures with a minimum feature size of 20 μm, each layer being cured before the addition of subsequent layers. After deposition, the structure was poled under an applied voltage of 32 kV using the corona poling method; that is, the printed structure was placed on a conductive plate connected to a high voltage supply. A conductive needle, at a distance of 2cm above the sample surface, was connected to the same high voltage supply and created an inhomogeneous electric field within which the PZT structure was poled.

Spin-coating

Spin coating has been reported for the deposition of inorganic, polymer and organic piezoelectric materials [17, 23]. Spin coating is the deposition of a solution or suspension onto a substrate being spun at a predetermined rate inside a chamber. The chamber temperature can be controlled and the spin rate, temperature and humidity determine the roughness, thickness and porosity of the obtained film. Spin coating is usually employed when a uniform layer thickness is required since spin coating avoids the 'coffee ring' phenomenon seen when solvents evaporate slowly under ambient conditions [54]. Many studies have shown that altering the spin coating temperature and humidity can also affect the dominant phase obtained when depositing PVDF solutions. A study by He *et al.* [55] reported that PVDF crystallised mainly in its γ phase at room temperature, while mainly α phase films were obtained at 100 °C . This is similar to the results obtained by Li *et al.* [54] who obtained α phase PVDF films by spin coating at temperatures between room temperature and 120 °C. The results presented by He *et al.* [55] also included an experiment in which $Mg(NO_3)_2.6 H_2O$ was added to the PVDF solution before spin coating. The resultant film was mainly β phase and this was attributed to the presence of the hydrate salt. It was suggested that the hydrated inorganic salt crystallises first and acts as a nucleation site for PVDF crystallisation and that this encourages hydrogen bonding between the hydroxyl groups of the inorganic salt and the electronegative fluorine atoms on the polymer.

Thin films can be obtained by deposition of a polymer solution onto a substrate and subsequent heating. The piezoelectric films are heated to a temperature below their

43

Curie temperature and any residual solvent is removed by pressing the film at high pressure [20].

1.2.8. **Interaction Between Piezoelectric Materials and Cells**

Living tissue is generally not tolerant of exotic (that is, not of its own kind) materials. It is particularly intolerant of inorganic materials that are even slightly soluble. This is of particular importance with regard to inorganic heavier elements such as barium in $BaTiO_3$, lead in PZT, organic materials containing extended conjugated π-bonded chains, and finely divided silicates, which have a tendency to be carcinogenic. Such materials would therefore need to be isolated in some way to avoid a toxic response.

Piezoelectric natural macromolecules such as chitosan have been incorporated into scaffolds for tissue regeneration or combined with other molecules or polymers to create composite materials. An example of this is a strontium substituted hydroxyapatite-chitosan composite developed by Turnbull *et al.* [56] for use as a bone regeneration scaffold. The researchers produced a scaffold by freeze-drying a mixture of strontium substituted hydroxyapatite and chitosan. Human bone marrow mesenchymal cells were then seeded on top of the scaffold and their proliferation and morphology recorded.

The effect of piezoelectric materials on living cells and tissues has been widely investigated. Several sources have reported that the introduction of a piezoelectric material increased and accelerated cell growth, particularly in the cases of bone formation and wound healing [26, 57]. In 2001, Wiesmann *et al.* [58] applied a pulsed voltage to osteoblast cells to explore their mineral distribution.. They reported a marked increase in mineral deposits found on the stimulated cells compared to control samples in which the osteoblasts were not electrically stimulated. The formation of mineral globules is a typical stage of osteogenesis, suggesting that the stimulated cells started forming bone faster than non-stimulated cells. This can be related to Wolff's law [14], which states that the bones in a healthy person or animal will adapt to a change in the applied stress. It was postulated that if stress applied to bone results in a deformation, it is transduced into an electric field which stimulates osteoblast proliferation and mineral deposition. The proliferation and deposition are localised to areas of lower bone density since higher density regions require greater stress to induce a deformation.

This presence of piezoelectricity in such a wide range of inorganic, organic and living tissue suggested that it would be worthwhile to search for other piezoelectric materials as candidates in the development of human tissue compatible nanocomposites.

Researchers have sought to harness the tuneable properties of piezoelectric materials and evident biological response to piezoelectric activity by incorporating piezoelectric materials into medical devices and scaffolds. The influence of piezoelectric activity on bone regeneration and wound healing has already been discussed above [58], however, piezoelectric materials have also been applied in a nerve environment, in which electrical signals are abundant.

Studies into the behaviour of Schwann cells and PC12 cells in the presence of stimulated piezoelectric materials have focused mainly on the direct piezoelectric effect, mechanically stimulating a piezoelectric material to induce a current [29]. However, other studies related to the electrical stimulation of nerve environment cells have shown that direct application of an AC or DC current through cell culture medium can have a noticeable effect on cell growth. One such study [59] reported that applying a DC electric field through Schwann cell growth medium resulted in an alignment of the Schwann cells perpendicular to the field, whereas application of an AC field caused a change in the cell morphology, with the Schwann cells appearing flatter on the glass substrate and with more cell extensions.

Another study [60] investigated the effect of co-culturing Schwann cells with dorsal root ganglion (DRG) explants on PVDF-TrFE aligned fibres. The Schwann cells were suspended in Matrigel and injected into electrospun PVDF-TrFE fibres. The DRG explants were then plated onto the fibres and Schwann cells. Both the Schwann cells and DRG neurites extended along the length of the fibres and the Schwann cells formed myelin sheaths around the neurites. This is consistent with results from an earlier investigation [61] studying DRG explants grown on aligned PVDF-TrFE fibres, which also showed the DRG neurites aligned along the fibre length. The paper questioned how the fibres were effecting alignment in the cells without being subjected to any external mechanical deformation. It was suggested that the fibre stiffness was low enough that the action of the cell attachment onto the fibre could cause enough deformation to induce a current. This effect is not observed for cells grown on β PVDF membranes however, as reported in a study by Hoop *et al.* [29].

Hoop *et al.* [29] described the differentiation of PC12 cells grown on a β PVDF membrane stimulated with ultrasound. They recorded that PC12 cells grown on a stimulated β PVDF membrane differentiated and produced bipolar neurite extensions aligned in the direction of the electric field. This contrasted to the multipolar neurite extensions

observed when PC12 cells were differentiated on PLL coated substrates using nerve growth factor [29]. PC12 cells grown on an unstimulated β PVDF membrane showed only small extensions from the central body and did not differentiate. This could suggest one of two things; either the substrate was too stiff for the cells to deform, or that the physical geometry of the substrate did not encourage differentiation and neurite extension. The Young's modulus of PVDF is in the GPa range and neurite differentiation in response to substrate deformation is usually studied within the range (10 Pa – 750 kPa) [29]. In the cases of neural type cells grown on piezoelectric fibres, it is more likely that the cells are aligning with the morphology of the substrate, than that a piezoelectric effect is being induced by cell attachment.

Researchers are taking advantage of materials which are able to enhance and direct cell growth, and devices using piezoelectric materials to stimulate cell growth are beginning to permeate the literature [28, 62]. Applications using piezoelectric materials for nerve regeneration are being investigated as well as applications using piezoelectric materials as transducers to connect nerves to external devices. An example of this is the use of piezoelectric materials to convert acoustic sounds to electrical signals in cochlear implants [18].

1.3.   **Carbon Allotropes**

One of the materials explored in this work was carbon nanotubes, an allotrope of carbon that is of interest due to its linear morphology on a nanometre scale, high physical strength and high electrical conductivity [63].

Allotropy is the ability of chemical elements to exist in different structural forms in the same physical state due to the arrangement of atoms [64]. Allotropy is distinguishable from the simple classification of states of matter as solid, liquid and gas because allotropes can exist in the same state. Allotropy is very common; of the 92 stable elements, at least 38 have chemical (that is, not isotopic) allotropes at one atmosphere pressure.

Carbon has the highest number of allotropes of any element. On a scale of centimetres, carbon as cubes, spheres, rods and sheets would not count as allotropes but at the nanoscale, there is a range of structures, mostly discovered since 1950. These are distinguishable structures which are treated as allotropes and are the subject of intense research interest because of their structure and properties as nanomaterials.

Before nanosized allotropes of carbon were identified, three allotropes of carbon were formally recognised – diamond, graphite and amorphous carbon (**Figure 1.9**).

Diamond is cubic, comprised of sp^3 hybridised σ-bonded carbon atoms in a symmetrical giant lattice structure, with each atom connected to another with a bond angle of 109.5° (tetrahedral). The crystal structure of diamond falls into the Fd3m space group, with the atoms separated by 0.317 nm, the width of the cubic unit cell. Cubic diamond is stable below 650 K. It has high thermal conductivity but is an electrical insulator. Cubic diamond is found in nature but can also be synthesised by both high temperature, high pressure synthesis or by low pressure chemical vapour deposition (CVD) from a hydrocarbon/hydrogen mixture onto a cubic diamond seed [65].
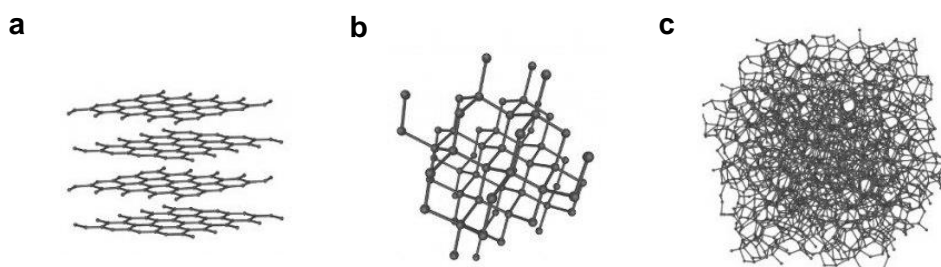
Figure 1.9 *Structural diagrams of carbon allotropes. a) graphite, b) diamond and c) amorphous carbon*

Graphite is the stable form of elemental carbon under standard conditions (20 °C, 1 atm). It has a layer structure [64] consisting of stacked sheets of covalently bonded carbon atoms with weaker van der Waals interactions between the layers (basal planes). Each carbon atom in a basal plane is σ-bonded to three others through sp^2 hybridised orbitals. The remaining p orbital on each carbon atom overlaps with the p orbitals on adjacent atoms to produce an extended conjugated π-system extending over the whole basal plane. This conjugated structure confers on graphite a high thermal and electrical conductivity. If the layers are flat, the overall structure is hexagonal, space group P6₃/mmc, with an interlayer spacing of 0.3355 nm [64]. Carbons frequently exhibit a turbostratic structure, meaning that the interlayer spacing in graphite is maintained but the layers are in rotational misalignment.

Apart from the basal plane surface, which accounts for the greater part of the surface area of graphite, there are two other important faces, usually referred to as the "zig-

zag" and "armchair" faces [65] (**Figure 1.10**). These become important when considering carbon nanotube structures and functionalised materials containing graphite because they influence the axial alignment of atoms in nanotubes, provide locations for the functional groups and in vegetable-originated charcoals are the active sites for chemisorption.

Historically, soot was assumed to be an amorphous deposit from a smoky flame and was accepted as elemental carbon in a form distinguishable from diamond and graphite. The commercial product, called carbon black, has subtypes named according to the process or precursor by which they are made - acetylene black, channel black, furnace black, thermal black, etc.
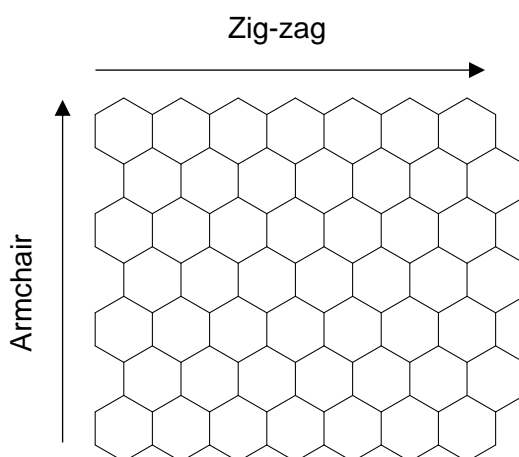
Figure 1.10 *Diagram of a single layer of graphite, showing the zig-zag and armchair edges, which, in the 3D structure of graphite, would form the zig-zag and armchair faces.*

Elemental carbon that does not occur naturally is produced by thermal decomposition of carbon containing materials, either during combustion of gases and liquids with a limited supply of oxygen or through pyrolysis of solids, including vegetable matter. From the structures of carbons resulting from the decomposition process, two categories arise – materials that on high temperature treatment transform toward graphite, called "graphitising", and otherwise "non-graphitising". Graphitising carbons are found to be those that pass through a melting stage in the range 400-500 °C before carbonisation. Typical graphitising carbons include petroleum, carbon blacks and pyrolysed polyvinyl chloride. Typical non-graphitising carbons include cellulose chars (that is, charcoals) and resin chars.

Charcoal is known as a "pyrolitic" carbon because it involves heating to decompose a precursor, cellulose. Charcoal has a macroscopic structure reflective of its source – wood charcoal has a grain and ring structure like that of the wood it was made from – because carbon does not melt or anneal after carbonisation below 2000 K.

Around the 1960s researchers realised that carbon could be the basis for the development of extremely strong materials based on the strength of the carbon-carbon bond. The strengths of non-terminal intra-molecular bonds as average bond energies [66] are shown in **Table** *1.2*.

Table 1.2 Table of some intramolecular bond strengths represented as average bond energies [66]

Bond	kJ/mol		Bond	kJ/mol
C≡C	837		C-C	348
C=N	613		C-N	305
C=C	612		S-S	264
C=C benzene	518		Si-Si	176
N=N	409		P-P	172
Si-O	374		N-N	163
C-O	360		O-O	146

Early approaches to the development of strong macromolecular structures based on carbon focused on the pyrolysis of organic polymers spun into fibres [67]. Early attempts used rayon, a natural wool cellulose dissolved in carbon disulphide and spun into fibre, which was successful in producing a polymer fibre for textiles but not as a viable precursor to carbon fibre. Much greater success was achieved with polyacrylonitrile (PAN) which when spun into a molecularly aligned filament and heated to 1500-2000 °C produces a 5-10 μm diameter carbonised fibre that comprises a string of pyridine rings [68]. On further heating beyond 2500 °C this graphitises with the elimination of nitrogen. These fibres have a high Young's modulus, in excess of 500 GPa, and moderate electrical conductivity.

1.3.1. **Nanotechnology**

Nanoscience can be defined as the study of chemistry, physics and materials science at the nanoscale. A material can be considered nanoscale if it has at least one dimension between 1-100 nm [69]. Nanotechnology is the combination of nanoscience, technology and engineering to create nanoscale objects which possess different properties to their bulk counterparts. As an upcoming field, there are different

definitions of nanoscience and nanotechnology, as well as ongoing debate regarding what can be classed as a nanomaterial [69, 70]. Throughout this dissertation, any references to nanoscience or nanotechnology will be based on the definitions above.

In a macroscopic object, for example, on the scale of centimetres, the properties of the material are dominated by the forces and interactions between the atoms or molecules that are surrounded by atoms or molecules of similar kind. The surface properties are different because of the absence of surrounding molecules external to the bulk. As an object becomes smaller, the ratio of surface moieties to bulk moieties increases, and the properties of the object tend toward those of the surface. That said, the surfaces of small particles are not flat in the way they are for macroscopic objects and this is also influential in determining the properties of small particles. The unprecedented properties conferred on nanomaterials by virtue of particle size can include electrical, optical, mechanical and antibacterial properties, among others. This allows the nanomaterials to be used for different applications from their macroscopic counterparts.

Since the rise of modern nanotechnology with the invention of the scanning tunnelling electron microscope in 1981 [71], nanotechnology and nanomaterials have spread out into diverse applications. From the application of graphene in modern electronics to the development of gold nanoshell and carbon nanotube therapies for cancer treatment, nanotechnology has a part to play in many areas of life. Several researchers are combining nanomaterials with bulk materials to incorporate the favourable properties of both.

1.3.2. **Carbon Nanomaterials**

In the 1960s, organic chemists were exploring the limits of bond angle strain among hydrocarbons by seeking to synthesise carbon-based molecules with three-dimensional structures. An example of this is cubane (C_8H_8), which is an octane with the carbons joined in the shape of a cube.

In 1970, R. W. Henson, in the Graphite and Carbon Studies group at the Atomic Energy Research Establishment (AERE), Harwell, who was studying radiation damage in the graphite moderator of nuclear reactors, suggested a structure for a C_{60} molecule and made a model of it. Unfortunately there was only weak evidence for the molecule and the structure was not published. The structure is later mentioned in an editorial in the journal *Carbon* by Thrower [72] who had been working with Henson at the time. The first mention of the C_{60} molecule in the literature was in an article by E. Osawa in 1970,

who predicted that a C_{60} molecule would be stable. He expanded on this in more detail in a book on aromatic molecules the following year [73].

In the early 1970s, Kroto and Walton at Sussex University studied the chemistry of unsaturated hydrocarbons. Then in the 1980s, Smalley and Curl at Rice University developed a technique expected to produce C_{60} molecules using laser vapourisation. Kroto and Smalley used the same technique using a graphite target and condensing the vapour in helium gas [74]. They produced a molecule identified by mass spectrometry as having an atomic mass number of 720, corresponding to C_{60}, among a number of other C_n molecules where n is even and greater than 20. They established that C_{60} is the shape of a regular truncated icosahedron and named it buckminsterfullerene after the architect Buckminsterfuller. They were awarded the 1996 Nobel Prize in Chemistry for the discovery.

A single plane of carbon atoms σ-bonded in a hexagonal arrangement is known as graphene. Graphene as a component of the graphite structure was identified immediately the structure of graphite was elucidated by X-ray powder diffraction, very soon after the development of X-ray crystallography.

Preparation of isolated graphene was reported by Geim and Novoselov [75] by exfoliation of crystalline graphite using adhesive (Scotch type) tape, producing crystals larger than 1 mm. It is very unlikely that Geim and Novoselov were the first to prepare it; it is known that other researchers [76, 77] prepared large numbers of ultra-thin samples of graphite by similar exfoliation of graphite fixed to glass with polyvinyl pyrrolidone using adhesive tape in a method developed by Hennig [76]. Their aim was to produce thin crystals to study the defect structure of graphite basal planes on the graphite- oxygen reaction [77]. If Geim and Novoselov found the process as easy as they say, it is very likely these others would have also achieved it. What Geim and Novoselov did differently to share a Nobel Prize was focus on the physics rather than the chemistry and make and publish physical measurements of their material.

Recent studies [78] have explored the application of graphene as sensors for biochemicals and organic molecules. When applied in this way, graphene is often modified to introduce oxygen containing groups and defects into the structure. These variations can change the properties of the material, increasing sensitivity to specific molecules and allowing further modification of the graphene structure with polymers and nanoparticles [78].

Carbon nanofibres have been employed for similar applications with Vamvakaki *et al.* reporting the development of a glucose sensor made from carbon nanofibres [79].

Carbon nanofibres are cylindrical nanostructures comprising graphene sheets arranged as vertically stacked cones, cups or plates. Carbon nanofibres have similar electrical properties to carbon nanotubes, which will be discussed in the following section, but are usually larger and contain more surface defects. The increased number of defects allows carbon nanofibres to be more easily modified but also lowers their mechanical strength and the uniformity of synthesised materials.

While graphene is considered to be a 2D material, since it can extend into the mm range in two directions, fibrous nanostructures such as carbon nanofibres and carbon nanotubes, are considered to be 1D since only their length is outside the nanoscale.

1.3.3. **Carbon Nanotubes**

A carbon nanotube is a graphene sheet in the form of a tube. There exist a number of different types, but all are cylindrical, made of carbon and have tubular, graphitic structures. The high profile of the carbon nanotube in research is indicated by the 50,000+ published papers and almost 6000 patent applications filed between 2000 and 2010 [80]. With a Nobel Prize having gone to the discoverers of the fullerenes and graphene, there has therefore been considerable interest in who to credit with the discovery of the carbon nanotube.

In a guest editorial in the journal *Carbon*, Monthioux and Kuznetsov [81] remarked that many of the papers on carbon nanotubes submitted to the journal *Carbon* started with reference to "the discovery of carbon nanotubes by Iijima in 1991 …", and they considered it "time to provide a clear picture of who should really be given the credit for the discovery of carbon nanotubes".

In 1991, Iijima and Ichihashi of NEC published a paper [82] in the journal *Nature* claiming to have found nanotubes in the carbon sooty deposit on graphite electrodes in the carbon arc systems used to make fullerenes. What Iijima described were tubes and scrolls of a form that previously would have been described as "whiskers" or filamentous carbon (ca 1970), following observation of similar hair-like growths on metals standing in strong electric fields [83]. Iijima's nanotubes were cylindrical tubes of a few layers of rolled up graphene and exhibit the expected high electrical conductivity and physical strength that was being sought in carbon fibre. Iijima's main claim was that he provided a detailed account of the structure of these materials. However, filamentous carbon had already been extensively researched over the previous decade and a half, and its structure had been described, particularly by Baker and Harris [84] at Harwell. They identified that the carbon filaments had an amorphous carbon interior,

graphitic tube exterior and a central hollow axial centre. Baker and Harris [85] later published a review in which they acknowledge a number of earlier observations of carbon nanotube-like structures.

Prior to the work of Baker and Harris, the first appearance of hollow carbon filaments can be traced back to Radushkevich and Lukyanovich at the Institute of Physical chemistry and Electrochemistry of Russian Academy of Sciences [86]. In their editorial, Monthioux and Kuznetsov determine that this was indeed the first report of a carbon allotrope with the same structure as that described for the carbon nanotube and that Radushkevich and Lukyanovich should be credited for the discovery.

In 1993, Iijima and Ichihashi [87], in a follow-up to their 1991 study, and Bethune and co-workers [88] at the IBM Laboratories at Almaden, published papers in the same issue of *Nature* claiming to have found single walled carbon nanotubes, again using the carbon arc synthesis method. Both teams used catalysts to produce the nanotubes with Iijima and Ichihashi using an iron catalyst while Bethune and colleagues employed a cobalt catalyst. Monthioux and Kuznetsov [81] concluded that it was probably fair to credit discovery of single walled carbon nanotubes (SWCNT) to both teams. They also commented, however, that an image in a paper on "filamentous carbon" produced in the decomposition of benzene [89] might include earlier evidence of a single layer carbon nanotube but the case is not convincing without diffraction evidence.

Aside from the number of walls a carbon nanotube has, its dimensions, chiral angle and functionalisation can greatly affect its properties. Multiwall carbon nanotubes, the first type to be reported, have five or more walls and tend to have diameters between 4 – 30 nm and lengths in the region of 1 μm. There are two models that describe the internal structure of multiwall carbon nanotubes. The first is the parchment model, which describes multiwall carbon nanotubes as a single roll of graphene that has been rolled continuously into a tube. In this model all the walls are connected. The second model, the Russian doll model, presents multiwall carbon nanotubes as a series of concentric cylinders of increasing diameter, fitted inside each other. This second model suggests that there could be some separation between each wall of the carbon nanotube although this is unlikely since restrictions on the carbon nanotube diameter mean that at least one of the layers will be in contact with another layer. The Russian doll model is more commonly described in the literature [90] and will be used to describe the structure of multiwall carbon nanotubes in this work.

Single wall carbon nanotubes have some distinctly different properties from multiwall carbon nanotubes [88]. They are smaller than multiwall carbon nanotubes, with diameters of approximately 1 nm and lengths from 100 nm – 30 μm [91] and exist in three

configurations [92]. The different configurations, labelled zigzag, armchair and chiral, are defined by the chiral angle; that is, the angle between the edge of the graphene sheet and the rolling direction (**Figure 1.11**).
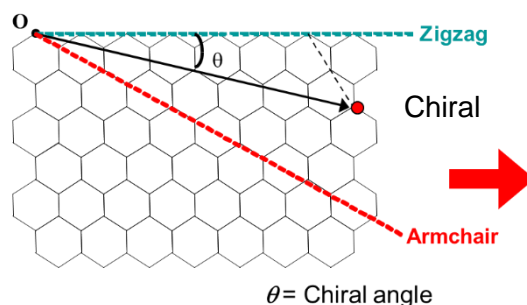
Figure 1.11 *Graphene sheet showing the chiral angles and rolling direction for the zigzag, chiral and armchair configurations of carbon nanotubes. Adapted from Prof. Kinloch, University of Manchester*

The configuration of a single wall carbon nanotube determines its conductive properties. Single wall carbon nanotubes in the armchair configuration are always metallic whereas chiral and zigzag nanotubes are metallic only in special cases and semi-conducting otherwise [88].

In the Russian doll model, multiwall carbon nanotubes, can also be considered as concentric single wall carbon nanotubes. This would suggest that the conductive properties of the multiwall carbon nanotube would depend on the configuration of each single wall carbon nanotube contributing to the structure; thus, if all the walls are semi-conducting, the multiwall carbon nanotube would be semiconducting. If at least one wall in the structure has metallic type conduction, however, the whole structure would be metallic, even if other layers are semi-conducting.

Double walled carbon nanotubes (DWNTs), are differentiated from multiwall carbon nanotubes because they can be metallic or semiconducting, depending on the structure of the inner tube. In this way they are similar to single wall carbon nanotubes, however they but can be more easily functionalised because of the presence of the outer wall [93].

A qualitative representation of the graphitic character of carbon nanotubes and the extent of defects in the structure can be obtained by Raman spectroscopy. A typical Raman spectrum for a single wall carbon nanotube shows four peaks – a radial breathing mode at 170 cm^{-1} (RBM), a defect band at 1350 cm^{-1} (D band), a graphite

band at 1650 cm^{-1} (G band) and a harmonic of the defect band at 2700 cm^{-1} (2D band). The spectrum for a multiwall carbon nanotube is almost identical with the radial breathing mode peak excluded. The radial movements of the walls in a multiwall carbon nanotube are not synchronised. Thus the scattering is cancelled out and a radial breathing mode is not observed.

The Young's modulus of individual carbon nanotubes has been measured by AFM. Values as high as 1 TPa [94] for multiwall carbon nanotubes and 1.5 TPa [94] for single wall carbon nanotubes have been reported. This is more than five times greater than the Young's modulus of steel (the density of steel being approximately 6x higher than that of carbon nanotubes). The exceptional mechanical properties observed along the length of carbon nanotubes arise from the strong covalent bonds formed between sp^2 hybridised carbon atoms. The network of planar bonds bears and distributes force effectively along the tubular graphitic structure.

Likewise, the conductivity of a single nanotube is reported as 10^6-10^7 Sm^{-1} [95], compared to 5.8 x10^7 Sm^{-1} [63] for copper. It must be noted, however, that carbon nanotubes have a much lower density (1.3 gcm^{-3}) than copper (8.9 gcm^{-3}). When corrected for this difference in density, carbon nanotubes have a higher specific conductivity (~7700 Sm^{2}kg^{-1}) than copper (~6500 Sm^{2}kg^{-1}). Electrons which contribute to the high conductivity of carbon nanotubes travel through the extended π-system which exists across the basal plane. Each carbon atom in the carbon nanotube structure has four valence electrons. Since only three electrons are involved in covalent bonding to other carbon atoms, the fourth electron is free to travel through the extended π-system. In metallic carbon nanotubes, the non-bonding electron from each carbon atom contributes to the sea of delocalised electrons which confers on carbon nanotubes the high electrical conductivities reported.

Carbon nanotubes are prone to agglomeration, caused by van der Waals forces between individual nanotubes. The randomly arranged aggregates fail to translate the outstanding anisotropic mechanical and electrical properties from nanoscale to macroscale.

Different manufacturing methods result in different structures and properties for carbon nanotube bulk arrangements such as films, fibres and foams. The aspect ratio, alignment and packing density, as well as synthesis method and post processing, influence the properties of bulk arrangements of carbon nanotubes. This has led to a wide range of values being reported in the literature for the Young's modulus and electrical conductivity of carbon nanotube bulk arrangements, particularly thin films [95]. In general, longer CNTs create thin films and fibres with higher electrical conductivity

and mechanical strength since there are fewer inter-tube junctions. **Table *1.3*** shows the highest reported values for mechanical strength and electrical conductivity for individual and bulk arrangements of carbon nanotubes.

Table 1.3 Highest reported mechanical and electrical properties of individual SWCNT, MWCNT, thin films of single wall carbon nanotubes and CNT fibres. The SWCNT films were produced by spin coating [96] or filtration [97], the DWCNT fibres were produced by wet spinning.

Sample	Young's modulus GPa	Conductivity Sm^{-1}
Individual SWCNT	1500 [94]	1.00×10^7 [95]
Individual MWCNT	1000 [94]	1.00×10^7 [98]
SWCNT film	193 [96]	6.60×10^5 [97]
DWCNT fibres	250 [63]	7.70×10^6 [63]

Though the intramolecular bonds formed within a carbon nanotube are of a strong, covalent type, the intermolecular bonds between individual carbon nanotubes are of a much weaker type, consisting predominantly of van der Waals forces. The van der Waals forces are weaker for end-end interactions than side wall-wall interactions due to the much lower surface area of the ends. When carbon nanotubes are deposited in bulk arrangements, the mechanical and electrical properties of the film or fibre are limited by the properties observed at junctions between the ends of carbon nanotubes. This is evident from the significantly lower values of Young's modulus reported for carbon nanotube films and fibres.

The highest reported value for the Young's modulus of a carbon nanotube film is approximately 193 GPa [96], almost an order of magnitude lower than that of a single wall carbon nanotube. This results from the many junctions between carbon nanotubes, and end-end interactions, which are much weaker than the side-wall-wall interaction due to much lower surface areas of the tube ends. Junctions between carbon nanotubes effectively act as defects in bulk systems, creating weak points which lead to the much lower recorded Young's modulus.

A similar case is seen for the conductivity of carbon nanotube films, which is in the region of 6.6×10^5 Sm^{-1} [97], an order of magnitude lower than the conductivity of individual single wall and multiwall carbon nanotubes The difference in conductivity

arises because a single carbon nanotube creates a direct electron path from end to end whereas in a thin film, inter-tube junctions introduce barriers to electron transport.

Similar mechanical strength is reported for carbon nanotube films and fibres although significantly higher conductivities can be achieved for carbon nanotube fibres. The conductivity reported here for a carbon nanotube fibre is within 30% of the highest value reported for an individual carbon nanotube. Pasquali, Tsentalovich *et al.* at Rice University [63] selected high aspect ratio carbon nanotubes which were initially purified and then dissolved at high concentration into chlorosulfonic acid. The obtained solution contained carbon nanotubes in a lyotropic liquid crystal state; that is, a liquid crystal state obtained by the influence of a solvent.

The carbon nanotubes were subsequently spun directly from the acid solution. This method induced carbon nanotube alignment along the length of the spun fibre, contributing to the high conductivity.

Alignment of carbon nanotubes minimises end-end tube aggregates and can lead to thin films with higher conductivities [99]. Despite this improvement, aligned carbon nanotube films are yet to achieve conductivities of the same heights as a single carbon nanotube.

Different approaches have been taken towards obtaining aligned carbon nanotube films, including solution shearing lower concentrations of carbon nanotubes from superacids, [100] and electric field alignment [101]. These methods are still exploratory and it is admitted either that they have yet to achieve outcomes that match the researcher's aspirations or achieve an acceptable result but using materials that would be undesirable in a biomedical application such as a residue of chlorosulfonic acid. Tune *et al.* [102] recently reported the formation of aligned carbon nanotube films by the application of a lateral shear force, which offered an ostensibly simple method for the alignment of carbon nanotube thin films. The efficacy of the shear alignment process proved to be greatest for films made from smaller diameter nanotubes, with single wall nanotubes showing the best alignment, double wall nanotube films showing some alignment and multiwall nanotube films showing the least alignment by the process. However, the technique is an unlikely candidate for commercial scale up.

Horizontal and vertical chemical vapour deposition growth of carbon nanotubes are often employed on a commercial scale to provide well-aligned carbon nanotube thin films [103].

1.4. Non-covalent and Covalent Functionalisation of Carbon Nanotubes

Functionalisation of carbon nanotubes involves modification of the outermost carbon nanotube side wall, often with the intention of separating large agglomerates of carbon nanotubes. The dispersed carbon nanotubes can then go on to form physical complexes; those that are held together by π-π interactions, and covalent complexes; those that are held together by covalent bonds between chemical moieties. Since the carbon atoms in the hexagonal lattice of carbon nanotubes are sp^2 hybridised, the delocalised electrons are π electrons which can participate in π-π interactions, also called π stacking, with the π electrons in nearby molecules. Pristine carbon nanotubes are chemically inert and are most likely to form physical complexes. On the other hand, functionalised carbon nanotubes have reactive chemical groups that are able to form covalent bonds with functional groups on other molecules, usually by amide linkages or ester bonds.

The functionalisation of multiwall carbon nanotube side walls is more easily achieved than functionalisation of single wall carbon nanotubes due to the greater number of defects in their graphitic structure. Functionalisation of the side wall of single wall carbon nanotubes introduces defects which affect the conductive and mechanical properties of the nanotube. In contrast, functionalisation of double wall carbon nanotubes affects only the outer tube, allowing the conductive properties of the tube to remain unchanged.

1.4.1. Non-covalent Functionalisation of Carbon Nanotubes

Solubility and Dispersity of Carbon Nanotubes

In suspension, carbon nanotubes form agglomerates, due to van der Waals forces between their surface atoms. Carbon nanotubes do not readily disperse in any solvent medium and are prone to aggregation and sedimentation regardless of their number of walls or their structure [104]. With this in mind, it must be noted that single wall carbon nanotubes are prone to aggregation even in dry form and are particularly difficult to maintain as dispersions in solvents [105]. Different solvents with various properties have been employed to encourage carbon nanotube dispersion and suspension. It is widely accepted that carbon nanotubes do not disperse well in high polarity, high proticity solvents such as water and alcohols. Typically, organic solvents such as dimethylformamide (DMF), N-methylpyrrolidone (NMP) and dichloromethane (DCM) are used to disperse carbon nanotubes and, in a study comparing the efficacy of

58

different dispersive solvents, Ausman *et al.* [104] suggested that basic, low polarity, low proticity solvents may be a good starting point for selecting a carbon nanotube dispersing medium. In addition to choosing an appropriate solvent, mechanical dispersion, generally by ultrasonic agitation (also called "sonication"), is also applied to improved carbon nanotube dispersion.

The power of the ultrasonic agitation and the length of time for which it is applied can change the properties of the final suspension. While many researchers report applying ultrasonic agitation for time-periods between 15 mins and 1 hour, a study by Arrigo *et al.* [106] found that exposing carbon nanotubes to ultrasonic agitation for extended periods of time (1 – 2 hours) led to the introduction of defects in the side walls and, in some cases, nanotube breakage. This is surprising given the high strength of nanotubes and the high energy required to produce a defect (breaking 3 bonds requires 1500 kJ mol^{-1} (**Table *1.2***). Another problem encountered with carbon nanotube dispersions is that they are often short-lived, remaining dispersed for between 30 mins – 24 hours before agglomerating, forming a sediment. The addition of a surfactant or the formation of a composite is often required to prevent aggregation and allow a uniform, dispersed, suspension to be maintained over a long time-period.

Another method for dispersing carbon nanotubes is to completely dissolve them in a superacid, where dissolution is considered to be a state in which each nanotube is completely separated from other nanotubes and surrounded by ions from the solvent medium. Superacids, such as chlorosulfonic acid (CSA), are acids more acidic than 100% sulphuric acid. They have been found to dissolve carbon nanotubes completely by protonating the carbon nanotube side walls [107], inducing repulsive forces between carbon nanotubes which are able to overcome the van der Waals forces that would otherwise cause agglomeration. Highly crystalline carbon nanotubes with minimal defects are more easily protonated than defective carbon nanotubes and dissolve more readily in CSA, resulting in a solution of highly crystalline carbon nanotubes from which defective carbon nanotubes can be filtered. Above a certain concentration threshold, the carbon nanotube solution enters a liquid crystalline phase, with properties between that of a liquid and a solid, crystalline material. In this state, the nanotubes become aligned in the solvent. Tune *et al.* [102] dissolved carbon nanotubes in CSA at low concentrations to obtain a solution which was later aligned by dry shearing, whereas Tsentalovich *et al.* [63] dissolved carbon nanotubes in CSA at higher concentrations, above the liquid crystalline transition concentration and the carbon nanotubes were aligned in mesophase during spinning. Both studies reported that the dissolution of carbon nanotubes in CSA did not introduce additional defects in the side walls of the nanotubes or permanently modify the nanotubes in any other way. Single wall, double

wall and multiwall nanotubes were spun into fibres and the highest performing fibre, produced from double wall carbon nanotubes, had a conductivity of 8.5 MSm^{-1} and Young's modulus of 250 GPa. This is significantly higher than a previously reported value of 80 GPa for the Young's modulus of carbon nanotube fibres [108].

Physically Linked Carbon Nanotube Complexes

The association of carbon nanotubes with a surfactant is an example of a physically linked carbon nanotube complex. A widely used surfactant is sodium dodecylbenzene sulfonate (SDBS), which has been presented in numerous studies as an effective surfactant for the dispersion of carbon nanotubes [109]. SDBS enables carbon nanotube dispersion by modifying the side walls of carbon nanotubes with sulphate groups. A study by Ausman *et al.* [104] compared the dispersion of single wall and multiwall carbon nanotubes dispersed by sonication and a combined surfactant and sonication methods. The nanotubes were suspended in water or a solution of SDBS in water and exposed to ultrasonic agitation for two hours. Following sonication, the researchers reported that multiwall carbon nanotubes had become better dispersed than single wall carbon nanotubes. This is consistent with other reports in the literature that show that single wall carbon nanotubes have a tendency to form bundles. The study also reported that nanotubes without surfactant were damaged and shortened by the ultrasonic agitation whereas surfactant treated nanotubes showed no side wall damage. The surfactant appears to reinforce the nanotube side walls, preventing damage; however, it could be argued that the untreated nanotubes would not have sustained damage had the ultrasonic agitation been applied for a shorter period of time. The surfactant has the desired effect of breaking up large carbon nanotube agglomerates and preventing damage from ultrasonic agitation but the side wall modification can have unwanted side-effects on the conductive properties of the nanotubes, as well as influence the interactions between nanotubes and other materials, making them unsuitable for the desired application [104].

There exist in the literature descriptions of chemical compounds, which can form both physical and covalent complexes with carbon nanotubes. An example of this is phthalocyanine, a planar, macrocyclic, organic compound consisting of four indole units joined together by nitrogen atoms (**Figure 1.12**).
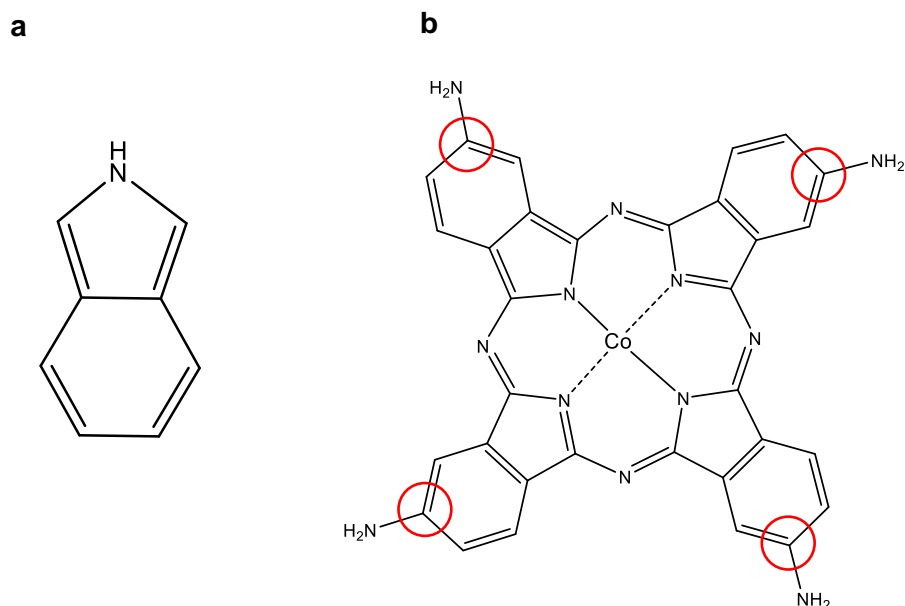
Figure 1.12 *Skeletal formulae of a) Indole, b) Tetraamino phthalocyanine coordinated to a central cobalt atom. Red circles indicate the meta position on the benzene rings*

The compound can accommodate a metal in its centre (metallophthalocyanines) and has an 18-π-electron aromatic system which affords it the ability to form π-stacking interactions with other aromatic molecules. Physically linked super macromolecular complexes of phthalocyanine and carbon nanotubes use the π-stacking interactions between the materials to exfoliate the carbon nanotubes without introducing defects into the carbon nanotube sidewalls. This maintains the sp^2 hybridised structure, thus preserving the electrical properties of the carbon nanotubes.

The formation of a carbon nanotube/ phthalocyanine physical adduct is described by Wang *et al.* [110], who prepared a suspension of pristine carbon nanotubes in a solution of tertiary butyl (tBu) substituted phthalocyanine. The mixture was allowed to stand for 72 hours until the intense green colour, usually observed for phthalocyanine solutions, had diminished. Wang attributed the disappearance of the solution colouring to the formation of a physical association between the carbon nanotube and phthalocyanine materials.

Internal Doping of Carbon Nanotubes

The original aim of Bethune's experiments [88] that led to his formation of single wall carbon nanotubes was to encapsulate metal nanoparticles within the hollow interior of

61

multiwall carbon nanotubes. The formation of single wall carbon nanotubes when using copper as a dopant was an unexpected outcome of the experiments. Since this time, many groups have continued to study the internal doping of carbon nanotubes with nanoparticles.

It has been claimed that gold nanoparticles can be encapsulated within multiwall carbon nanotubes. The process is said to take place by the initial physisorption of gold nanoparticles onto the side walls of the MWCNTs followed by transfer into the internal cavity (through a supercritical CO_2 solvent) [111]. The nanoparticles inside the carbon nanotubes had a diameter of 7.3 nm, 84% of the internal diameter of the carbon nanotube. The van der Waals forces between nanoparticles and the internal cavity of carbon nanotubes is stronger than that between nanoparticles and the side walls of carbon nanotubes meaning that once encapsulated, there is an energy barrier for the nanoparticles to leave the internal cavity of the nanotube. There have also been claims that copper oxide (CuO) and zinc oxide (ZnO) nanoparticles have also been successfully encapsulated within multiwall carbon nanotubes [112]. The nanoparticles inside the carbon nanotubes had a diameter of 1-3 nm, which was approximately 30% of the internal diameter of the carbon nanotube.

In both the aforementioned examples of internal doping of carbon nanotubes, the carbon nanotubes were shortened before encapsulation of nanoparticles was attempted. The shortened nanotubes had a length of between 324 nm and 2 μm. The purpose of shortening the nanotubes was to avoid a resistance to motion which could prevent individual nanoparticles from becoming encapsulated inside long nanotubes (10-50 um). A key difference between the studies was the behaviour of nanoparticles once inside the internal cavity of the carbon nanotube. The gold nanoparticles were formed externally, transported into the internal cavity and then ripened inside the nanotubes until the nanoparticle diameter approximately matched the diameter of the carbon nanotube. This, it was claimed, created an additional barrier for the removal of nanoparticles from the internal cavity since the nanoparticles were held tightly within the nanotubes by strong van der Waals forces, which are distance dependent. The metal oxide nanoparticles were also formed externally and transported into the internal cavity of the carbon nanotube. The size of the nanoparticles was not altered at any stage in the preparation. The mixture was instead washed with concentrated nitric acid to remove metal oxide nanoparticles adsorbed on the nanotube side walls. The washing step had the unwanted side-effect of also washing away some nanoparticles inside the nanotube. This, it was claimed, occurred because the van der Waals forces between the nanoparticles and the nanotubes were weak due to the nanoparticles being significantly smaller than the nanotube diameter.

1.4.2. **Covalent Functionalisation of Carbon Nanotubes**

Wet Chemical Functionalisation

Deliberate modification of carbon nanotube side walls to form carboxylic acid or amine groups has been cited as a method for improving the dispersibility of carbon nanotubes. Modification can be achieved by numerous methods, the most common of which are acid treatment and plasma functionalisation.

Acid treatment of carbon nanotubes involves stirring pristine carbon nanotubes in a concentrated solution of 1:3 nitric acid:sulphuric acid for 12 h [113]. In a sheet of graphene, the hexagonal lattice, or basal plane, is chemically inert; however, the edge of the sheet, or edge plane, is more reactive and susceptible to attack from acid groups. Due to this, acid treatment usually leads to the addition of functional groups to the ends of carbon nanotubes, which have greater edge plane character and show greater chemical reactivity than the side walls, which have more basal plane character [114]. Although far fewer functional groups attach to side walls than to the nanotube ends, defects are often introduced into the side walls, decreasing their graphitic character and in the case of single wall carbon nanotubes, altering their properties. Treatment with nitric and sulphuric acid attaches carboxyl (COOH) groups to the carbon nanotubes. The COOH groups can be converted into OH or NH_2 groups through further treatment. Other functional groups, such as N and F, can be obtained by plasma functionalisation.

Potassium permanganate ($KMnO_4$) oxidative treatment of carbon nanotubes also leads to the addition of functional groups to the ends of carbon nanotubes. Potassium permanganate is dissolved in aqueous sulphuric acid ($H_2SO_{4(aq)}$) and added to a suspension of pristine carbon nanotubes in the same solvent [115]. The reaction mixture must be refluxed at a temperature of 120 °C to facilitate effective functionalisation; this is due to low contact between hydrophobic carbon nanotubes and water soluble $KMnO_4$. Higher temperature increases the oxidising potency of $KMnO_4$, which is already a strong oxidising agent at room temperature. This can contribute to the generation of defects in the nanotubes side walls and disruption of the carbon nanotube graphitic structure.

Ozone treatment leads to the formation of carboxyl groups on the ends and side walls of carbon nanotubes. Ozone can be bubbled through an aqueous solution at basic pH to yield highly reactive hydroxyl radicals (OH•) [116]. The OH• can then react with the ends and defects of carbon nanotubes in suspension. Ozone can also be used as a dry

functionalisation method to directly functionalise carbon nanotubes without conversion of ozone to OH$^{\bullet}$. This will be discussed in the next section.

Dry Chemical Functionalisation

The **plasma functionalisation** process involves exposing the carbon nanotubes to a glow discharge plasma formed by heating a mixture of argon and either oxygen, ammonia (NH_3) or tetrafluoromethane (CF_4), depending on the desired functionalisation. Oxygen plasma creates OH and COOH functional groups, ammonia creates NH_2 and CONH groups and tetrafluoromethane creates F groups [117]. In many cases, plasma functionalisation is preferred to acid functionalisation due to its ability to graft a greater range of functional groups onto the carbon nanotube without breaking the carbon nanotubes into smaller segments. The process also exfoliates the carbon nanotube bundles and creates active sites on the basal plane of the nanotubes, allowing functional groups to be added to the side walls as well as the nanotube ends [118]. This leads to a greater degree of carbon nanotube functionalisation which is useful for the dispersion of carbon nanotubes in solvents and also for covalent complex formation. Covalently attaching functional groups to carbon nanotube side walls tends to induce the formation of defects. Though the level of damage to the graphitic structure can be somewhat controlled by the parameters under which the plasma is applied, disruption of the sp^2 hybridised structure will cause the electrical conductivity and mechanical strength of plasma functionalised carbon nanotubes to be lower than that of an individual nanotube.

Ozone can also be applied as a dry carbon nanotube functionalisation technique, as mentioned above. The treatment involves flowing an oxygen/ozone mixture through a reactor containing pristine carbon nanotubes [116]. In a comparison of the wet and dry methods of ozone functionalisation [116], the dry method was claimed to be more effective at oxidising the carbon nanotube surface. It was suggested that this is due to the wet reaction being kinetically restricted by OH$^-$ ions being adsorbed from the basic suspension onto the surface of carbon nanotubes, thus blocking the reaction site from attack by an OH$^{\bullet}$ and preventing functionalisation.

Carbon nanotubes with different functional groups can be applied in a range of settings and have been discussed in the literature for applications in sensing and electronics. A study by Hsieh *et al.* [119] discussed the use of functionalised carbon nanotubes as a component in the electrodes of a capacitor. The researchers reported that amide functionalised carbon nanotubes show more capacitive behaviour than pristine (unfunctionalised) nanotubes because of the presence of oxygen and nitrogen

containing groups. It was suggested that the polar surface groups adsorbed water, increasing ohmic resistance and contributing to the charge build-up on the electrodes.

Covalently Linked Carbon Nanotube Complexes

The formation of physically linked phthalocyanine-carbon nanotube complexes is discussed above in Section 1.4.1. The benzene rings in phthalocyanine can also be substituted with a functional group at the meta position (**Figure 1.12**), which can be used to facilitate the formation of covalent complexes.

This is demonstrated in a study by Ballesteros *et al.* [120], in which the researchers formed a covalent linkage between carboxyl functionalised single wall carbon nanotubes and zinc tetraamino phthalocyanine. Their research claims the formation of an amide linkage between the carboxyl group on the carbon nanotubes and the amine groups on the phthalocyanine. Covalent functionalisation was confirmed by thermogravimetric analysis, which showed a faster mass loss with increasing temperature (up to 800 °C) for the covalent complex compared to the mass loss recorded for nanotubes or phthalocyanine alone.

In another study, Dinesh *et al.* [121] combined amine functionalised multiwall carbon nanotubes with diphenylalanine derivatives to create a chemically and physically bonded complex. The initial complex was synthesised by the formation of an amide linkage between the carbon nanotube and diphenylalanine moieties. This was followed by self-assembly and the formation of hydrogen bonds between the amine terminus of the carbon nanotube and the carboxyl terminus of diphenylalanine. The researchers observed a dendritic network outstretching from a central carbon nanotube covalent composite seed. When hydrogen bonding was disrupted, the seed remained intact while the dendritic network was damaged. This supports the claim that the dendrites were formed by a physical association between the materials and not a covalent bond.

The formation of an amide linkage between two moieties is a widely exercised method for the preparation of covalently bonded complexes. The complexes are often synthesised with the intention of applying them in a tissue engineering or bio-interface setting. Matsumoto *et al.* at Toyo University [122] illustrated this concept by preparing a covalently bonded complex comprising amine functionalised multiwall carbon nanotubes and nerve growth factor, which bears acid groups. The researchers cultured primary neurons on the covalently bonded complex and observed that cells grown on the composite showed similar neurite outgrowth to cells grown in the presence of nerve growth factor alone. The difference between these two cases is found when *in vivo* applications are considered. Free nerve growth factor would provide a temporary

differentiation cue for promoting neurite outgrowth before degrading and being removed by the body. On the other hand, nerve growth factor immobilised on carbon nanotubes could potentially act as a permanent differentiation cue since carbon nanotubes are not readily degraded.

1.5. Conductive Carbon Nanotube Composite Inks and Electrodes

Carbon nanotube composite materials may be formulated to incorporate the favourable properties of each of the materials involved. For example, many hydrogels can encapsulate cells and support cell growth but typically have weak mechanical properties, such as low strength and poor stability. Incorporating carbon nanotubes into a hydrogel can improve the mechanical properties while maintaining cell adhesion and proliferation [123].

A good example of this is the use of carbon nanotube composites in electronics and sensing applications in the form of conductive polymer composites. Researchers [124] have introduced carbon nanotube/ graphene or conductive polymers such as polyaniline (PANi) into insulating polymer substrates to increase the conductivity of the material and in some cases to induce interesting properties such as pyroresistivity. The positive temperature coefficient effect, in which an increase in temperature leads to an increase in resistance, can be useful for applications in temperature sensors and resettable fuses [125].

The manipulation of carbon nanomaterials into a form which can be deposited onto a solid surface has been widely explored in recent years, with many researchers seeking to make use of the nanomaterials' conductive properties for nano and micro-sized circuitry and bio-scaffolds. The first concern for developing a nanomaterial-based ink is creating a homogeneous suspension in a solvent. As discussed in Section 1.4.1, carbon nanomaterials are prone to agglomeration when suspended in solvents and may require the introduction of a surfactant to achieve an acceptable result. But, arguably, if a nanomaterial is stable in suspension, it might follow that the lower interaction between particles would lead to lower mechanical stability in the deposited material. In the case of carbon nanotubes, the random orientation of individual carbon nanotubes also has a detrimental effect on the mechanical properties of a bulk arrangement. It has also proven difficult to process the nanomaterials into specified shapes at the desired resolution with researchers often reporting particle agglomeration prior to 3D printing or uneven particle distribution after printing [126, 127, 128]. To address

these issues, a polymer matrix or binder may be added to the nanomaterial to disperse and stabilise the nano-ink formulation. The addition of a binder can also improve the ink processability, making it easier to deposit in a desired shape with required resolution, while maintaining the continuity, physical shape and desired mechanical properties of the nanomaterial after deposition. The binder can be applied to the ink via covalent or non-covalent linkage to carbon nanotubes, depending on the binder material and type of carbon nanotubes used.

1.5.1. **Percolation Theory**

Percolation theory was developed in 1941 by later chemistry Nobel laureate (1974), Paul Flory, at the Standard Oil Development Company. It was elaborated on in 1944 by Walter Stockmayer at MIT.

The role of the carbon nanotube in a conducting carbon nanotube composite is to provide a conductive path through which electrons can flow. The carbon nanotubes can be thought of as a network of resistors, offering a multitude of pathways for electricity to flow, via the touching points of the non-aligned labyrinthine threads. Of interest is how the resistance and impedance of such a structure might depend on the thread density and mean thread length. An appropriate theoretical approach is percolation theory, whose origins are found in the statistical analysis of connected points in a random graph.

Percolation theory is applied in materials science to model the phase transition that occurs in a composite when one of the constituents is present at or above a threshold amount. At this value, called the percolation threshold [129], a giant lattice exists in the structure, imbuing the material with properties not observed below the threshold value. In the case of conducting polymer composites (CPCs), the percolation threshold refers to the minimum amount of a conductive filler that must be added to an insulating material for a large increase in the conductivity of the composite material to be observed. The filler particle size and shape as well as the size and geometry of the cluster will determine the ability of a filler to form a conductive network. Fillers with high conductivity and high aspect ratio are likely to have a low percolation threshold.

Consider a system consisting of random clusters of carbon nanotubes deposited between two gold conductors; each nanotube is likely to be in contact with other nanotubes but these connections may not lead to a continuous connection from one gold conductor to the other. Connected nanotubes that do form such a pathway between gold electrodes can be referred to as the 'backbone'. The backbone

67

contributes to the conductivity of the system while other connected nanotubes which do not link the gold connectors, called dead ends or dangling bonds, do not contribute to the system conductivity.

The high conductivity and high aspect ratio of carbon nanotubes predispose them to a low percolation threshold when incorporated into conductive polymer composites. Percolation thresholds of between 0.002% and 4% [130, 131] have been reported for carbon nanotubes embedded in polymer composites. The processing techniques used to produce CPCs have also been found to affect the percolation threshold, with lower percolation thresholds being observed for composites in which the filler was dispersed by ultrasonic agitation compared to those in which the filler was dispersed by the application of shear stress [130]. Many CPCs are formulated to contain the minimum amount of CNTs required to reach the percolation threshold due to the processability issues [130] which may arise upon the addition of greater quantities of CNTs. The carbon nanotube composites explored in this work contained CNT quantities well above the percolation threshold to maximise conductivity. Composites containing lower amounts of carbon nanotube were only explored briefly during optimisation but would warrant a more extensive study.

The process of heating a material and cooling it slowly is known as annealing and has been shown to modify the mechanical properties of materials by removing internal stresses and defects. A study by Deng *et al.* [132] showed that annealing a carbon nanotube composite at temperatures between 130 °C and 165 °C also modified the conductive properties of the material and led to a decrease in the percolation threshold. A later study by Zhang *et al.* [133] reported that annealing CPCs containing pristine multiwall carbon nanotubes and the thermoplastic polymer, polypropylene, at temperatures between 100 °C and 200 °C caused changes to their percolation time – the length of time taken for the material to exhibit a large increase in conductivity once heat is applied. As well as observing a decrease in percolation threshold for annealed CPCs, the researchers found that CPCs annealed at higher temperatures had shorter percolation times than CPCs annealed at lower temperatures. Dynamic percolation induced by annealing was found to reduce the percolation threshold of conductive polymer composites by allowing oriented polymer chains and conductive filler particles to relax within the composite and become mobile, forming a network [133].

1.5.2. **Carbon Nanotube/ Thermoplastic Composites/ Inks**

A thermoplastic polymer is a polymer that softens and becomes mouldable when heated [134]. They are often used as binders or dispersants for insoluble molecules. When the solvent is removed by heating, the thermoplastic polymer becomes soft and pliable and when cooled, the material sets into a shape. Since no new chemical bonds are formed during heating or cooling, the process is reversible. This allows the material to be reheated and remodelled multiple times.

Carbon Nanotube/ Conjugated Polymer Composites

Conjugated polymers are organic molecules in which the carbon atoms in the carbon chain backbone are linked by alternating single and double bonds [135]. They are inherently conductive or semiconducting due to the overlapping π orbitals from the double bonds. Their favourable conductive properties are often overshadowed by their brittleness and poor chemical stability, limiting the applications of conjugated polymers in isolation. The addition of carbon nanotubes into a conjugated polymer system aims mainly to enhance the conductivity and mechanical properties of the polymer. The conductivity of a carbon nanotube/ conjugated polymer composite is mainly dependent on the conductivity of the polymer.

An example of a carbon nanotube/ conjugated polymer composite is described in a study by Alshammari *et al.* [126], who printed conductive patterns using a MWCNT/ poly(3,4-ethylenedioxythiophene) polystyrene sulfonate (PEDOT:PSS) ink. The ink consisted of 0.03% MWCNT in an aqueous dispersion of PEDOT:PSS. The researchers deposited the ink onto a glass substrate using an inkjet printing technique and applied an electric field of strength 50- 1500 V m^{-1} during the printing process to encourage alignment of the carbon nanotubes. Printed patterns in which the carbon nanotubes were aligned displayed a conductivity of 6700 Sm^{-1} compared to 4400 Sm^{-1} for printed patterns in which the carbon nanotubes were randomly orientated. Inks containing higher percentages of carbon nanotubes were also prepared although attempted printing of these inks resulted in agglomerated nanotubes and low quality patterns.

Carbon Nanotube/ Thermoplastic Polymer Composites in Aqueous Solvents

Carbon nanotube inks for biological applications are often water-based [136] or, alternatively, the carbon nanotube complex may be incorporated into a hydrogel network. Hydrogen bonding in water can make it difficult to maintain a physically stable carbon nanotube dispersion due to the hydrophobic character of carbon nanotubes.

Complexes consisting of carbon nanotubes and water-soluble polymers, however, can help to overcome this. This was demonstrated by Kim *et al.* [137] in their study of aqueous carbon nanotube inks. The researchers formed a composite ink comprised of carboxyl functionalised nanotubes and polyvinylpyrrolidone (PVP), and suspended the mixture in water. The water soluble PVP was able to maintain the suspension of carbon nanotubes while also facilitating nanotube dispersion. The ink was deposited into different structures by 3D printing and maintained as self-supporting 3D shapes by the fast evaporation of water from the ink upon deposition. Subsequent thermal treatment of the printed shapes at 450 °C removed PVP from the structures by decomposition (the melting point of PVP is 150 °C). The final material was mainly composed of carbon nanotubes; the remaining 25% was composed of amorphous carbon from pyrolysed PVP. The conductivity of printed ink depositions was measured as 2540 Sm^{-1}, significantly higher than the MWCNT/PEDOT:PSS composite discussed above due to the much higher carbon nanotube content in the CNT aqueous ink discussed here.

Carbon Nanotube/ Thermoplastic Polymer Composites in Organic Solvents

While polymers with a high number of atoms with electronegativity greater than carbon or hydrogen (O,N), such as polyethylene glycol and polyvinyl pyrrolidone, are soluble in protic, hydrogen bonding solvents, polymers with long aliphatic or aromatic carbon chains and few electronegative atoms are more likely to dissolve in aprotic solvents such as DMF or N-methyl-2-pyrrolidone (NMP). This was the case for the dissolution of long carbon chain thermoplastic polymers to facilitate the formation of carbon nanotube/ polymer composite materials, as discussed in a recent study by Gbordzoe *et al.* [138].

The researchers investigated three different polymers – thermoplastic polyurethane (TPU), polyetherimide (Ultem), poly(methyl methacrylate) (PMMA), and probed the characteristics of composites formed by combining these polymers with carbon nanotubes. Composite fabrication followed a two-step procedure; first, the formation of separate polymer solutions in NMP, and the formation of a carbon nanotube film by CVD. Next, the polymer solution was drop-coated onto the carbon nanotube film and the composite film was stretched to align the nanotubes and increase electrical conductivity. The material was then heated and pressed under vacuum to remove the NMP solvent before cooling to obtain the final composite film [138]. The films contained between 50-70% carbon nanotube and had conductivities ranging between 1×10^4 and 1.8×10^4 Sm^{-1}.

The measured conductivities are an order of magnitude greater than the conductivity measured for the CNT/PVP ink developed by Kim *et al.*, even though the CNT/PVP ink

contains a greater proportion of carbon nanotubes. The difference likely arises from the alignment of the carbon nanotubes in the Gbordzoe study [138]. The alignment of carbon nanotubes appears to have a greater effect than the addition of a larger amount of randomly arranged carbon nanotubes.

1.5.3. Carbon Nanotube/ Thermosetting Polymer Composites/ Inks

Thermosetting polymers are formed by the formation of crosslinks between low molecular weight monomers, often described as resins, to form a network of long carbon chain polymers that set into a permanent shape when cured. The curing process can comprise the application of heat, or radiation, often ultraviolet. A hardener is often mixed with the resin prior to curing to act as a crosslinking agent or photocatalyst.

Carbon Nanotube/ Resin Composites

Other studies have described the use of thermosetting polymers as stabilising agents, to help maintain the continuity of the ink during deposition and after drying. An example is to be found in a recent study by Luo *et al.* [127], which describes the combination of pristine multiwall carbon nanotubes with polydimethylsiloxane (PDMS) to create an ink. Isopropanol (IPA) was used as a solvent to create an ink from the nanotube and polymer physical complex and the ink was deposited using a direct writing technique facilitated by a modified 3D printer. The researchers reported that the ink was able to be deposited as a range of complex printed patterns and analysis by scanning electron microscopy revealed that the carbon nanotubes were well distributed within the polymer matrix. The ink properties were carefully considered during ink preparation – particularly the ink conductivity and viscosity. The researchers varied the carbon nanotube content to control the ink viscosity and measured the ink conductivity at each nanotube concentration. As would be expected, the conductivity and shear viscosity increased as the carbon nanotube content increased. The inks also exhibited a shear thinning effect, becoming less viscous as the shear rate increased. The optimised ink, which maintained the structure of complex patterns when printed, contained 7% carbon nanotubes and had a conductivity of ~ 75 Sm^{-1}. The highest conductivity, 174 Sm^{-1}, was measured for the ink containing 10% carbon nanotubes, the highest CNT concentration explored in this study.

Carbon Nanotube/ Aqueous Resin Composites

While multiple studies report the use of organic solvents in the formation of carbon nanotube/ thermosetting polymer composites [127, 139] the use of aqueous solvents has

71

also been described. A study by Botelho *et al.* [140] described the dispersion of carbon nanotubes in water by sonication with a poly(sodium 4-styrene sulfonate) (PSSS) surfactant and subsequent mixing with a phenolic resin. The moisture content of the composite was then adjusted back to the original moisture content of the phenolic resin by heating under vacuum. The composite material was poured into a mould of the desired shape prior to curing and the carbon nanotube/ phenolic resin composites were cured in an autoclave under a heating cycle (30-200 °C), at elevated pressure (7 atm, 709 kPa) for ~ 7h.

The composite materials obtained contained between 0.05-2% carbon nanotubes. The conductivity of these composites was not reported in the study but the researchers report a sharp increase in mechanical strength at 0.1% carbon nanotube content, attributed to the percolation threshold being reached and a giant interconnected lattice being formed within the composite structure. It is therefore likely that composites at and above 0.1% carbon nanotube content would also display conductive properties; it can be predicted that their conductivities are likely to be significantly lower than any of the composites discussed here above due to the low carbon nanotube filler content and non-conductivity of the phenolic resin polymer matrix. A comparison of the conductive properties of the carbon nanotube composites discussed above are presented in **Table 1.4**. As expected, composites with a higher content of carbon nanotubes have higher conductivities (**Figure 1.13**). The exception to this is the CNT/PVP composite which has the highest carbon nanotube content but does not have the highest conductivity. This is undoubtedly due to the lack of carbon nanotube alignment in the composite.

1.5.4. Manufacturing Techniques for the Production of Carbon Nanotube and Carbon Nanotube Composite Electrodes

The method used to deposit a carbon nanomaterial depends heavily on the carbon nanotube or composite formulation and desired application. There have been demonstrations of many different methods, including photolithography, electrodeposition, soft lithographic patterning and various printing techniques, some of which are able to support the deposition of multiple layers.

Lithographic Techniques

Photolithography is a microfabrication process used to transfer a pre-defined pattern on a photomask to a photoresist [141]. The process is commonly used in the production of electronic integrated circuits and can be used for the deposition of single or multiple pattern layers.

Table 1.4 Comparison of the conductive properties of carbon nanotube/ polymer composites. The carbon nanotube content, solvent system and any alignment processes are also shown. Where the carbon nanotube and polymer content do not reach a total of 100%, the remaining amount consists of solvent and any surfactants present in the mixture.

Carbon Nanotube Composite	Carbon Nanotube Content/ %	Polymer Content/ %	Solvent	Alignment Process	Conductivity/ S m^{-1}
CNT/PDMS *	7	93	IPA	None	75 [127]
CNT/PVP *	75	17 (pre-pyrolysis)	Water	None	2540 [137]
CNT/ PEDOT:PSS +	0.03	0.9	Water	Electric field	6700 [126]
CNT/PMMA *	55	1	NMP	Mechanical Stretching	12900 [138]
CNT/Ultem °	54	1	NMP	Mechanical Stretching	13900 [138]
CNT/TPU *	57	1	NMP	Mechanical Stretching	15000 [138]
CNT/phenolic resin +	0.05-2	66	Water	None	Not reported [140]
For those indicated by *, the reference is to a single recent source and the data are typical of many sources. For those indicated by +, there are fewer sources but the reference is representative of several. For the source indicated by °, this is from a single institution studying a proprietary product.					
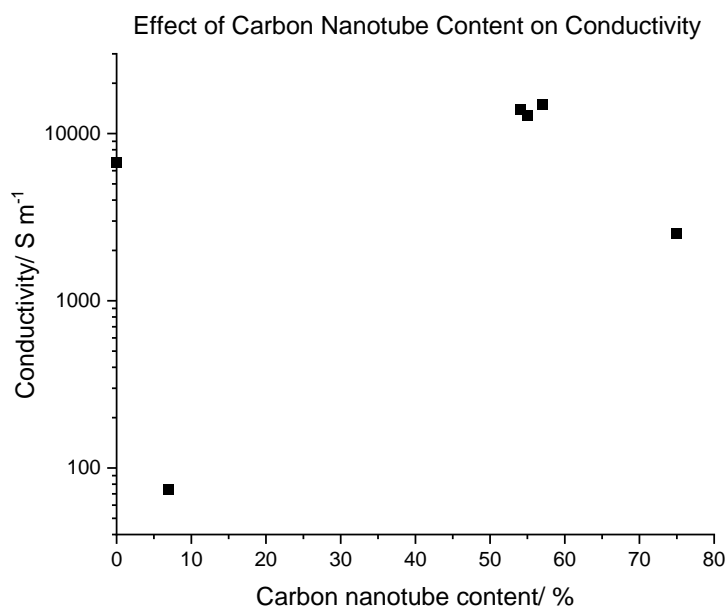
Figure 1.13 Comparison of the electrical conductivity of carbon nanotube/ polymer composites in relation to their carbon nanotube content

The photoresist is a light sensitive organic material which is applied to a substrate, normally by spin coating. There are two different kinds of photoresist – positive and negative. Positive photoresists become more soluble in developing medium after exposure to UV light while negative photoresists become insoluble after exposure to UV light. After application, the photoresist is soft-baked; that is, it is heated to remove any solvent. The photomask, a translucent fused silica blank with the desired pattern defined on the surface by a metal film, is then placed on top of the photoresist. After the application of the photoresist and photomask, the system is exposed to UV light. Any non-metal coated areas of the photomask allow the UV light to pass through, modifying the photoresist underneath. The photoresist is then developed and the modified area is either removed or becomes a new layer on top of the substrate, for positive and negative photoresists respectively. The final step in photolithography is hard-baking, which hardens the photoresist and improves its adhesion to the substrate underneath.

The resolution of patterns formed by photolithography is limited particularly by the diameter of the laser or electron beam used to create the photomask and is typically 100 nm [142]. Photolithography is often used as a method to deposit a catalyst material in a defined pattern prior to carbon nanotube growth by chemical vapour deposition (CVD).

Soft lithographic patterning uses a patterned elastomeric stamp, typically made of polydimethylsiloxane (PDMS), to transfer micro and nanosized patterns to a substrate. First, a master stamp mould incorporating the desired pattern is created, usually by photolithography or electron beam lithography. The elastomer is then poured into the mould and cured to create a soft stamp. The stamp can then be used to directly pattern a material onto a substrate. Although the fabrication of the initial master mould is expensive, it has the advantage that it can be used multiple times to create identical stamps.

Electrodeposition

Electrodeposition is a technique that can be used for the formation of thin film electrodes. It can be split into two groups – electroplating, for the deposition of metals, or electrophoretic deposition, for the deposition of colloidal particles in suspension [143]. The deposition of carbon nanotubes falls into the second group. For the deposition process, an electrochemical cell is arranged, consisting of a cathode and anode immersed in an electrolyte. The electrolyte contains a charged species of the material to be deposited. A potential difference is created between the two electrodes, causing the charged species in the electrolyte to move towards one electrode, either the

cathode or anode, depending on the charge of the electrolyte species. Positively charged electrolyte materials will coat the cathode, whereas negatively charged species will coat the anode. Carbon nanotubes have been reported to have a net negative charge in suspension, therefore it is expected that they would form a coating on the anode.

Self-assembly

Self-assembly is the spontaneous organisation of nano- and mesoscopic particles into stable, ordered structures. Self-assembly processes are generally driven by non-covalent interactions such as van der Waals forces, π-π and hydrogen bonds.

Self-assembly of carbon nanotube-based electrodes is usually by chemical vapour deposition (CVD) [134]. A carbon source and catalyst impregnated substrate are placed into a reactor and heated in an inert gas atmosphere. Thermal decomposition of the carbon source causes the formation of carbon nanotubes. In this way, aligned forests of carbon nanotubes can be grown on the substrate surface and if a catalyst pattern is pre-defined, carbon nanotube microelectrode arrays can be directly self-assembled.

Printing

Some printing techniques that are commonly applied to electrode deposition include inkjet printing [128], screen printing [144], direct writing [127] and 3D printing [137]. These methods are often used to produce patterns with multiple layers.

Inkjet printers eject droplets of ink on a substrate according to user-defined specifications. The process requires an ink with low viscosity and low surface tension. Low viscosity is required to enable the ink to pass through the nozzle without clogging while the low surface tension ensures that the ink droplet will deposit onto the substrate when ejected rather than attached to the nozzle head. A review article by Tortorich *et al.* [145] discusses the inkjet printing of carbon nanotube inks and notes that maintaining a dispersed suspension is also critical to producing a suitable ink. Different methods of dispersing carbon nanotubes for use in inks are described, many of which methods have also been discussed in Section 1.4.1. Once a carbon nanotube dispersion with appropriate surface tension and viscosity has been obtained, the ink can be transferred to an inkjet printing cartridge, ready for deposition. The resolution of the printed patterns is dependent on but not better than the diameter of the nozzle.

Screen printing is the process of applying ink to a substrate on which is laid a stencil. Inks for screen printing tend to have high viscosity and high surface tension since they are generally used to deposit larger patterns than inkjet printing [146]. A study by Metters *et al.* [144] demonstrated the screen printing of successive layers to produce a single wall

carbon nanotube electrode consisting of four layers in total. A base layer of carbon-graphite ink was first applied to a flexible, polyester film. A silver/ silver chloride reference electrode layer was then applied, followed by a dielectric layer to maintain the separation between electrodes. The single wall carbon nanotube layer was the final layer to be applied.

Direct writing is just what its name implies- the deposition of a 2D ink pattern onto a substrate either by a hand-held syringe or using an automated syringe printing system. In the latter case, the substrate may be positioned on an X-Y stage. Direct writing can print inks with a wide range of viscosities (1-1000 Pa s) and surface tensions, since the printing parameters can be finely tuned to obtain an acceptable result. Two key parameters which are often linked to the quality of the printed pattern are the printing speed and printing pressure. A 2018 study by Luo *et al.* [127] explored the effect of different printing parameters on structures printed using carbon nanotube-PDMS inks. The researchers developed five inks containing 5%, 6%, 7%, 9% or 10% pristine multiwall carbon nanotubes with viscosities of ~ 1000 Pa s. The inks were printed at different printing pressures ranging from 100- 700 kPa and printing speeds between 10 mm s^{-1} to 30 mm s^{-1}. Below a printing pressure threshold of 150 kPa, the printing system was unable to extrude any ink but at pressures above the threshold, could print simple structures with 5% and 7% carbon nanotube-PDMS inks and complex structures with 9% carbon nanotube-PDMS ink. Printing at a speed of 10 mm s^{-1} caused the printed shapes to collapse whereas shapes printed at 30 mm s^{-1} were weak and brittle. Structures printed at a speed of 20 mm s^{-1} were able to retain their extruded shapes and had improved mechanical properties compared to those printed at 30 mm s^{-1}. Although direct writing has been described here as a technique for the deposition of 2D features, the term is occasionally used interchangeably with 3D printing. This is the case for some of the printed patterns described in the Luo *et al.* study. In addition to the 2D patterns, ink was also deposited as 3D cylinders or 3D square meshes.

3D printing

When considering the printing of carbon nanotube inks, 3D printing can be thought of as an extension of direct writing in which a Z direction is added to the stage, allowing 3-dimensional structures to be printed. Architectures printed using this method can either be deposited layer by layer and dried/ cured as a complete structure (higher viscosity inks) or dried/ cured after the addition of each layer or a series of layers. Kim *et al.* [137] demonstrated the first method in their formulation of carbon nanotube-PVP inks.

Carbon nanotube inks are susceptible to nozzle clogging during printing. This is often caused by suboptimal ink properties or pauses in printing. Luo *et al.* [127] found that the

viscosity of high concentration (> 9% carbon nanotube) CNT/PDMS ink was too high to allow the ink to pass through a nozzle of diameter 290 μm. Similarly, Vuorinen *et al.* [128] reported that continuous printing produced stable, reproducible patterns while pauses in printing led to nozzle clogging.

Near field electrospinning (NFES) is an extension of the electrospinning technique discussed in 1.2.7. It differs from plain electrospinning in that the voltage required is significantly lower than for traditional electrospinning and the needle–connector distance is 5 mm or less, allowing the material deposition process to be more carefully controlled. NFES can be used to directly deposit fibres with micro or nanoscale resolution as straight lines and arcs or combined with an X-Y stage to print more complex structures such as grids [147]. The deposition of a multiwall carbon nanotube/PVDF composite nanofibre was investigated by Liu *et al.* [148]. The obtained fibres contained 0.03% MWCNT and displayed better mechanical and piezoelectric properties compared to PVDF electrospun fibres. The increase in piezoelectricity was attributed to the alignment of the PVDF molecules and individual carbon nanotubes along the length of the fibre, contributing to increased formation of β phase PVDF in the fibres.

Assembly of Carbon Nanotube Composite Electrodes

Electrodes containing carbon nanotubes have the capacity to be flexible, physically stable and tailorable to user requirements. It is also possible to manufacture transparent electrodes using SWNT-based inks deposited as thin films [149]. The range of deposition techniques available further increase the diversity of possible applications, making carbon nanotubes a feasible alternative electrode material to those more commonly used.

Electrodes formed from carbon nanotube-based inks can be deposited by a range of techniques, some of which have been discussed above. The properties of the final electrode can vary greatly depending on the deposition method chosen. Electrode formation may be a one-step process, or it may involve multiple steps and a combination of techniques. This can be favourable for producing complex structures, as demonstrated by Vuorinen *et al.* [128]. The researchers produced a bi-layer electrode on an adhesive plaster, (for attachment to the skin) using screen printing to deposit a silver element and inkjet printing to deposit a graphene/ PEDOT:PSS pattern.

Another study by Gabay *et al.* [150] describes the assembly of a carbon nanotube-based multi-electrode array using lithography and CVD techniques. The substrate and the

electrode array were prepared and defined by photolithography and a carbon nanotube layer was subsequently grown in pre-determined areas on the substrate by CVD.

A range of carbon nanotube-based electrodes have been developed to date, for applications from short term non-invasive motion sensing [103] to longer term direct nerve recording and stimulation [151, 152]. The electrodes have been fabricated with a number of different structures, including standalone electrodes, microelectrode arrays and thin films. The fabrication method often depends on the electrode structure, with filtration regularly being used for the production of transparent and translucent thin films [99, 149]. Another method which is commonly employed is CVD, which has been used for the production of microelectrode arrays [153], as shown in **Figure 1.14**. Vertically aligned carbon nanotubes were grown on SiO_2 in a microelectrode array pattern. The carbon nanotubes had poor adhesion to the silica surface and were subsequently transferred to a PDMS substrate.
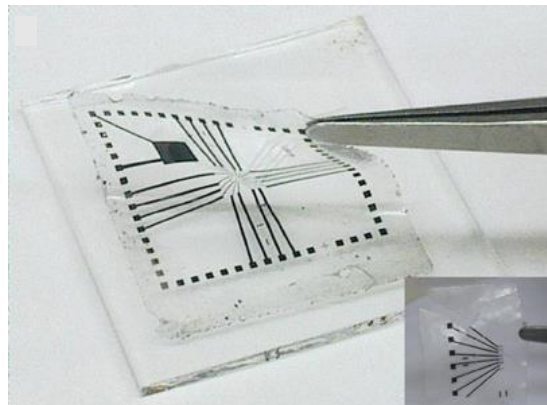
Figure 1.14 *A flexible CNT-based microelectrode array deposited by CVD. Inset: flexible CNT-based microelectrode array designed for in vivo applications. Reprinted from [153].*

1.6. Biomedical Applications of Carbon Nanotube Composites

1.6.1. Carbon Nanotube-Based Sensing Electrodes

Electrodes are often used in the detection of different chemicals inside and outside the body. This can include a wide range of applications, from the detection of neurotransmitters such as acetylcholine, for monitoring the progression of Alzheimer's Disease [154], to the detection of nitrous oxides for testing air quality [155].

The screen printed single wall carbon nanotube electrodes described by Metters *et al.* [144] were tested for their sensitivity to capsaicin, one of the main chemicals responsible for the hot flavour of peppers. The researchers recorded that the carbon nanotube electrodes were sensitive to capsaicin and could detect presence of the chemical down to micromolar levels. The electrochemical response of the electrodes was measured by cyclic voltammetry, using a three-probe method in a pH 1 buffer. The carbon nanotube electrodes produced augmented oxidation and reduction peaks compared to screen printed electrodes without a carbon nanotube layer. The researchers deduced that the enhanced sensitivity of the carbon nanotube electrode was due to the ability of carbon nanotubes to adsorb and desorb capsaicin on their basal planar walls.

1.6.2. **Carbon Nanotube- Based Nerve Stimulation Electrodes**

Nerve stimulating electrodes can be implanted into the body to deliver a current, with the intention of inducing a cell or tissue response. For this application, the electrode-cell interface is particularly important. While nerve cells are soft and rough, implanted electrodes tend to be rigid and smooth. This mismatch in physical properties reduces the interaction between nerve cells and electrodes, and can lead to an elevated immune response. The development of novel electrodes with similar properties to nerve cells is expected to improve the electrode-cell interface and have a direct impact on the long-term outcomes of implanted electrodes [152].

A notable example of implanted nerve stimulation electrodes is deep brain stimulation (DBS), which was approved in 2002 for the treatment of Parkinson's Disease [152]. The treatment involves implanting an electrode into the brain and applying a pulsed current to a target area for an extended period of time. Deep brain stimulation electrodes are conventionally made of a platinum-iridium alloy; however, a study by Vitale *et al.* [152] describes the use of a carbon nanotube fibre electrode for DBS. The researchers implanted carbon nanotube fibre electrodes into the brains of rats with dopaminergic neuron loss and applied a pulsed current with a pulse duration of 60 µs. Platinum-iridium electrodes were implanted into rats in a parallel control experiment and the efficacy of stimulation and inflammatory response were compared for both electrode types. The carbon nanotube fibre electrode stimulated the neurons with similar efficacy to the platinum-iridium electrodes despite having an active surface area more than 10x smaller than the platinum-iridium electrodes. The cell response tests yielded mixed results. Activated macrophages were confined to a distance of approximately 50 µm from the carbon nanotube fibre electrode, compared to 150 µm for platinum-iridium electrodes. However, neuron damage around the carbon nanotube fibre electrode

extended to twice the distance of the platinum-iridium electrode. This was attributed to damage caused during the implantation procedure.

Charge injection capacity is an important factor in electrodes for cell stimulation. Charge injection capacity is the amount of charge that an electrode can reversibly transfer to the surrounding tissue without causing an irreversible chemical reaction. While large electrodes may have large charge injection limits, they also cause more damage to the tissue upon implantation than smaller electrodes, which have smaller charge injection limits. There seems, therefore, to be a trade-off between minimising the damage during implantation and maximising the charge injection capacity. A material which can be fabricated into a small electrode while maintaining a large surface area could satisfy both the size and charge injection capacity criteria. In their 2013 review, Bareket-Keren et al. [153] discussed carbon nanotubes as a material which could potentially fulfil these criteria.

 One feature of carbon nanotubes discussed by Bareket-Keren et al. is the high surface area of carbon nanotubes, which was linked to increased charge injection capacity and decreased interfacial impedance. This suggestion has been supported by multiple studies, in which the charge injection capacity of carbon nanotube fibre electrodes [152] and carbon fibre electrodes [151] have been recorded. Researchers reported an order of magnitude increase in the charge injection capacity of carbon nanotube fibre electrodes compared to carbon fibre electrodes. Some studies describe the coating of carbon fibre electrodes with electroactive materials such as poly (3,4-thylenedioxythiphene) (PEDOT). Although the charge injection capacity of PEDOT-coated electrodes is higher than that of carbon nanotube fibre electrodes [156], PEDOT electrode coatings have been found to degrade after multiple cycles. A study by X. Luo et al. [157] sought to address this problem by developing a carbon nanotube-PEDOT composite material for coating platinum electrodes. The composite material was deposited on platinum electrodes as a film that maintained the conductivity of carbon nanotubes and PEDOT, while providing improved stability compared to PEDOT-only films. The coated electrodes were used to stimulate cells with a biphasic pulsed current for a duration of two weeks.

Table 1.5 Charge injection capacities of materials commonly used for neural stimulation and recording

Material	Charge Injection Limit/ mC cm^{-2}	Reference
Carbon fibre	0.1	[151]
Carbon nanotube fibre	6.52	[156]
PEDOT	15	[156]
CNT-PEDOT	2.5	[157]
Platinum	0.05-0.26	[156]
With the exception of CNT-PEDOT, these are values reported in 2017 and were regarded by the authors as in line with previously reported data. The paper from 2011 was the only paper of several studied that reported the charge injection limit for a CNT-PEDOT composite.		

A further property of carbon nanotubes discussed by Bareket-Keren *et al.* [153] is the ability of carbon nanotubes to support neuron adhesion due to the roughness of their surface. In an early study, Gabay *et al.* [150] developed a carbon nanotube microelectrode array. They reported that the roughness of the carbon nanotubes enhanced cell adhesion, encouraging cells cultured *in vitro* to spontaneously migrate towards carbon nanotube coated areas. Increased roughness also increases the surface area of the electrode, decreases the impedance and increases the charge injection capacity.

A number of studies have described the application of carbon nanotubes and carbon nanotube composites as standalone electrodes or multielectrode arrays (**Figure 1.15** and **Figure 1.16**) for sensing, cell stimulation, recording nerve signals or as substrates for cell growth [128, 150]. A study by Vitale *et al.* [152] demonstrated that a standalone carbon nanotube fibre electrode was capable of neural stimulation and recording. The researchers implanted electrodes into the primary motor cortex of rats and supplied a biphasic pulsed current to the tissue through the electrodes. The results described the efficacy of the carbon nanotube fibre electrodes for nerve stimulation compared to metal electrodes, noting that the carbon nanotube fibre electrodes were able to form a stable interface with nerves without showing signs of degradation over time. The potential for long-term stability makes carbon nanotube fibre electrodes particularly attractive, especially when compared to metal electrodes coated with organic materials, in which the organic materials have been shown to degrade over multiple stimulation cycles [152].

The study also included a demonstration of the ability of the carbon nanotube fibre electrode to register nerve signals. Recordings of the local field potential were taken over a two-week period following a two-week post-operative rehabilitation period. The local field potential is the mass potential difference between a large group of nerves and their surrounding area after the excitatory and inhibitory signals have been summed and filtered through a low-pass frequency filter.
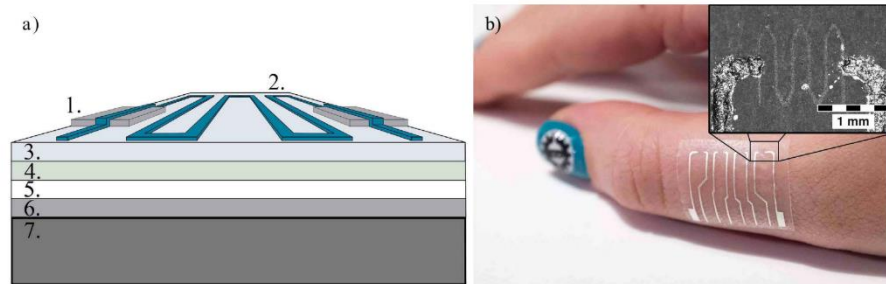
Figure 1.15 *Temperature sensor developed by Vuorinen et al. a) Schematic diagram of the temperature sensor showing the multi-layered structure of printed functionalities and different bandage layers. The different components are 1. Screen printed silver conductors, 2. Wave patterned graphene/ PEDOT:PSS temperature sensor, 3. PU surface layer, 4. Adhesive layer, 5. Protective paper, 6. PET film and 7. Cooling/ heating element. b) Photograph of the sample, with sensor array of four sensors, being attached to the skin. Reprinted from [128].*
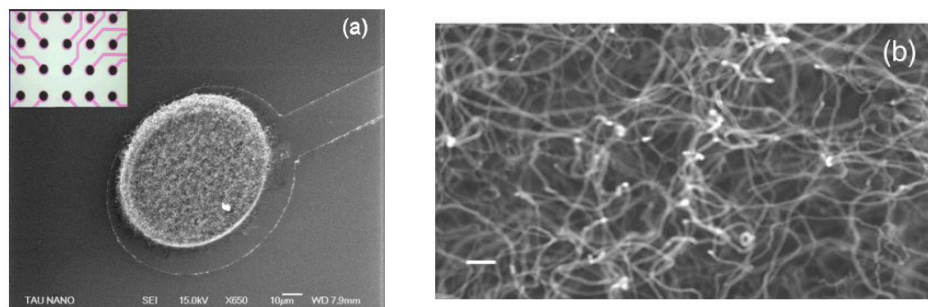
Figure 1.16 *Microfabricated carbon nanotube microelectrode array (MEA) for potential application in the recording of extracellular signals. a) Tilted HRSEM image of an 80 μm CNT island centred on a 100 μm conductive titanium nitride pad, patterned on a silicon dioxide substrate (bar is 10 μm). Inset: optical microscope image of a regular array of 20 CNT islands out of the total 60 comprising the entire MEA (bar is 100 μm). b) HRSEM image of the CNT island surface (bar is 100 nm). Reprinted from [150].*

The study showed that the carbon nanotube fibre electrode was able to measure signals in the local field potential range. After initial fluctuations immediately after implantation, the signal:noise ratio stabilised and no degradation in signal quality was recorded over the four-week experimental period. Also, the low impedance carbon

nanotube electrode-tissue interface had a higher signal:noise ratio compared to a high impedance metal electrode-tissue interface, allowing a higher quality signal to be picked up by the carbon nanotube fibre electrode.

An example of immobilised carbon nanotubes being used as scaffolds for nerve growth can be found in a study by Se-Jun *et al.*, [136] which describes the formation of a conductive carbon nanotube-polyethylene glycol diacrylate (PEGDA) 3D scaffold onto which neural stem cells were seeded. Results showed that the cells were able to adhere to the scaffold and proliferate over the seven-day growth period. The presence of carbon nanotubes in the scaffold was found to enhance differentiation of the neural stem cells. Cells grown on scaffolds containing larger proportions of carbon nanotubes were found to have increased dendrite lengths compared to control samples in which carbon nanotubes were not present.

Another factor which affected neural stem cell differentiation was the application of a potential difference across the scaffold. A biphasic pulsed current was delivered to the scaffold to stimulate the cells and this resulted in enhanced differentiation into mature neurons. Cells exposed to electrical stimulation showed higher expression of common neuromarkers in comparison to PEGDA scaffolds not exposed to stimulation. The researchers reported that electrical stimulation via carbon nanotubes significantly enhanced the cell viability of cells grown on carbon nanotube- PEGDA scaffolds.

1.6.3. Concerns Regarding Carbon Nanotube Toxicity

Investigations into the biocompatibility of carbon nanotubes have yielded conflicting results, with some studies claiming that carbon nanotubes support and even enhance cell growth [150], while others suggest that carbon nanotubes are highly toxic [158]. The discrepancies between the two groups could arise from differences in experimental methods, carbon nanotube type, functionalisation and concentration. The length of carbon nanotubes has been found to have a profound effect on their toxicity. A study by Boyles *et al.* [159] discussed the inflammatory response of cells to long and short carbon nanotubes and found that long carbon nanotubes, of length > 15 µm, induced frustrated phagocytosis; the phagocytes, which have diameters of ~ 10 µm, are unable to fully engulf the carbon nanotubes and instead leak proteinase, inducing an inflammatory response. The researchers also reported that carbon nanotubes of length < 15 µm did not cause cytotoxicity, regardless of the presence or absence of metal catalyst particles and independent of the carbon nanotube configuration (zigzag, armchair, chiral).

1.7. **Background, Aim, Hypotheses and Objectives**

This is a project which was run alongside a larger EPSRC funded project (EP/M026884/1 Piezoelectric Nano-Fibre Based Acoustic Sensors for Artificial Cochlea) [160] which closed on 31st May 2019.

This PhD project was not a formal part of that project and was supported on a basis of access to facilities and consumables only.

1.7.1. **Background and Aim**

This project aimed to explore techniques, materials, concepts and options likely to be of interest to the main project, that did not necessarily fall within the specified scope of work but would fall within the sphere of interest of the development of an implantable cochlear device.

The main project was using copper as an interim candidate material for the construction of acoustic devices comprising fibrous membranes, in the knowledge that the bio-incompatibility of copper would require them at some stage to seek an alternative. A part of this project was then to explore alternative small scale fabrication techniques with non-metallic electrically conducting materials. Carbon nanotubes were explored for this purpose and the laboratory was already making extensive use of 3D printing for the fabrication of porous cellular structures for biomedical implants.

This project arose from a suggestion by a member of the project team that there might exist a peptide with piezoelectric properties that might be suitable for incorporation in a composite to provide the electrical acoustic link for a cochlear device. A search of the literature turned up diphenylalanine which was usually described as a peptide capable of self-assembly from solution and in a defined crystalline habit. There then followed the question of how to fabricate a composite material containing diphenylalanine into a macrostructure, manufacturable as an electrode.

1.7.2. **Hypotheses**

Diphenylalanine could be a candidate material for development toward an acoustic implantable device.

Carbon nanotube nanocomposite materials of interest could be fabricated by 3D printing and it would be appropriate to explore the feasibility and practical criteria for this to be achieved successfully.

1.7.3. **Objectives**

- To explore the self-assembly of diphenylalanine crystals to understand their molecular assembly under different conditions and on different substrates (Chapter 3)
- To compare the physical properties of an organic piezoelectric material with those of a piezoelectric polymer to gain insight into their respective suitability for use as the piezoelectric component in an implantable device (Chapter 3)
- To synthesise a carbon nanotube complex with enhanced conductive properties (Chapter 4)
- To test the capability of the synthesised carbon nanotube-diphenylalanine complex to facilitate the growth of aligned diphenylalanine microtubes with enhanced piezoelectric properties (Chapter 4)
- To develop a printable conductive ink based on the carbon nanotube-diphenylalanine complex for the deposition of custom electrodes for implantable devices (Chapter 5)

Chapter 2   **Materials and Methods**

2.1.   **Materials**

Details of the materials (reagents and consumables) used throughout this work are listed alphabetically in **Table 2.1** below.

Table 2.1 Table of reagents and consumables used for experimental work

Material	Supplier	Product number	Grade/ Details
Reagents			
1-butyl -3-methyl-imidazolium chloride (BMIMCl)	Sigma-Aldrich	94128-5G	-
Amine functionalised multiwall carbon nanotubes (MWCNT-NH2)	Haydale	HDPlas® MWCNT-NH2	≥99% Length ~ 1500 nm, Ø ~ 9.5 nm
Carboxyl functionalised multiwall carbon nanotubes (MWCNT-COOH)	Haydale	HDPlas® MWCNT-COOH	≥99% Length ~ 1500 nm, Ø ~ 9.5 nm
D,D diphenylalanine	Bachem	4008206.1	-
Dimethylformamide (DMF)	Sigma-Aldrich	1029372500	>99.9%
Dimethylsulfoxide (DMSO)	Sigma-Aldrich	5439001000	≥99.7%
Dopamine hydrochloride	Sigma-Aldrich	H8502-10G	-
Fmoc-L-diphenylalanine	Bachem	4015688	-
Hexafluoroisopropanol (HFIP)	Sigma-Aldrich	8451570100	≥99%
Hexafluorophosphate Benzotriazole Tetramethyl Uronium (HBTU)	Sigma-Aldrich	12804-25G-F	>98%
Hydrochloric acid (HCl)	Sigma-Aldrich	320331-500ML	37%
Industrial Methylated Spirit (IMS)	Fisher Scientific	11482874	99%
Isopropanol	Sigma-Aldrich	1096342511	ACS reagent, analysis grade
L,L diphenylalanine	Sigma-Aldrich	P4126-1G	-
Medical grade silicone adhesive	Polymer Systems Technology	Med1-4013	-

			5% w/w in water and 1-propanol, ≥1.00 meq/g exchange capacity
Nafion ® D-520 dispersion	Alfa Aesar	42118.AE	
N-methylmorpholine (NMM)	Sigma-Aldrich	8058941000	>98%
Potassium chloride (KCl)	Sigma-Aldrich	1049380050	≥99.99%
Potassium ferrocyanide (K4[Fe(CN)6]. 3H2O)	Sigma-Aldrich	455989-100G	≥ 99.95%
PVDF-TrFE copolymer powder	Piezotech	FC25	-
Sodium hydroxide (NaOH)	Sigma-Aldrich	221465-500G	>97%
Consumables			
24 x 50 mm rectangular coverslip	Agar Scientific	AGL462450-15	#1.5 thickness
0.5mm diameter platinum wire	CH Instruments	CHI115	-
12 mm diameter coverslip	Fisher Scientific	11708701	#1 thickness
15 ml centrifuge tubes	Alpha Laboratories	BC030	-
3 mm diameter glassy carbon electrode	CH Instruments	CHI104	-
50 ml centrifuge tube	Alpha Laboratories	CT1120	-
Agate pestle and mortar	Sigma-Aldrich	Z112526-1SET	-
Anodised aluminium oxide (AAO) templates	Whatman	WHA68097023	pore size 200 nm, depth 60 um
Carbon tape	Agar Scientific	AGG3347N	-
Glass microscope slides	VWR	631-0108	-
Holey carbon coated copper TEM grids	Agar Scientific	AGS147	200 mesh
Microcentrifuge tubes	Alpha Laboratories	LW3335	-
Porcelain pestle and mortar	Sigma-Aldrich	Z247472, Z247510	-
SEM stubs	Agar Scientific	AGG301A	-
silver/ silver chloride reference electrode	CH Instruments	CHI111	-
Tempfix	Agar Scientific	AGG3305	-
Universal indicator paper	Johnson Test Papers	140.4	-

2.2. **Characterisation Techniques**

A range of instrumental techniques were used to characterise the materials and composites prepared in this study.

2.2.1. **Fourier Transform Infrared Spectroscopy**

Fourier transform infrared spectroscopy provides information about the different chemical groups in a molecule because different molecular bonds absorb different frequencies of infrared radiation depending on their bond strength and polarity, and to some extent chemical environment. Transmission FTIR instruments produce a spectrum by measuring the amount of infrared radiation transmitted through a sample compared to a blank which is either run separately or in parallel by beam splitting.

Attenuated total reflection (ATR-FTIR) is a type of FTIR in which it is the infrared radiation reflected from a sample which is measured, rather than the infrared radiation transmitted [161]. The radiation originates from an infrared source beneath the sample stage and is directed upwards toward a crystal with a high refractive index (RI) (usually zinc selenide- RI= 2.43, germanium- RI= 4.01, or diamond- RI= 2.40). The infrared beam is internally reflected at the interface between the crystal and the sample, forming an evanescent wave which can extend up to 3 µm into the sample (***Figure 2.1***). As the evanescent wave interacts with the sample, some of its energy may be absorbed at specific wavelengths, resulting in an attenuated total reflection of the beam. After one or multiple internal reflections, the beam is directed towards the detector.

The instrument used in this work was an attenuated-total-reflection FTIR (ATR-FTIR) instrument (Jasco FTIR 4200), equipped with a diamond crystal. The samples were placed onto the sample stage of the instrument and scanned between 600 – 4000 cm^{-1} at a resolution of 2 cm^{-1}. A total of 64 scans per run were performed and each sample was examined three times. FTIR spectra below are displayed in terms of % transmittance and are representative of the obtained data.
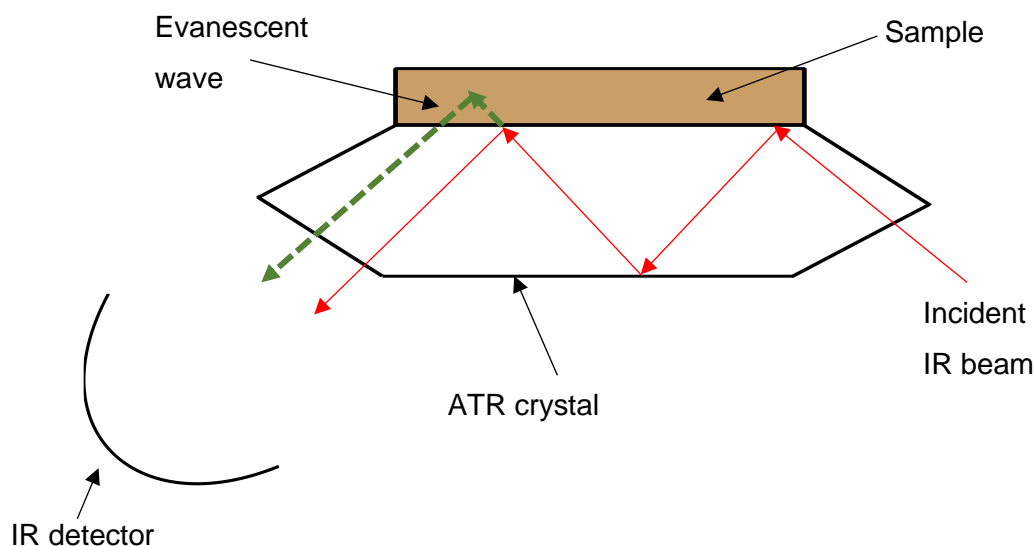
Figure 2.1 *Schematic diagram of IR beam internally reflected between ATR crystal and sample before approaching the detector. The green dashed line represents the evanescent wave that enters the sample and is diminished as some of the energy is absorbed.*

2.2.2.   **Raman Spectroscopy**

Raman spectroscopy was employed in this work to provide information about the graphitic structures within commercially purchased carbon nanotubes, and carbon nanotube complexes and composites synthesised in the laboratory. Raman spectroscopy is complementary to infrared spectroscopy through a 'rule of mutual exclusion' which means that some vibrations that are revealed by absorption in the infrared do not scatter in Raman spectra and *vice versa*.

The Raman spectrum of a pristine multiwall carbon nanotube typically shows three or four peaks – a band arising from vibrations within the graphitic lattice (G band), a band caused by damage or the introduction of defects into the graphitic structure during synthesis (D band) and bands arising from possible resonances of the G and D bands (2D, 2G and D+G). Comparison of the G band and D band peaks, caused by graphitic lattice and defect vibrations, can provide useful information about the graphitic quality of a carbon nanotube and the degree of side wall and nanotube functionalisation [107]. The ratio of D band intensity:G band intensity for a carbon nanotube gives a numerical representation of graphitic quality, with D:G band ratios <1 being indicative of high quality carbon nanotubes while D:G band ratios >1

indicate that there are a large number of defects present in the carbon nanotube structure.
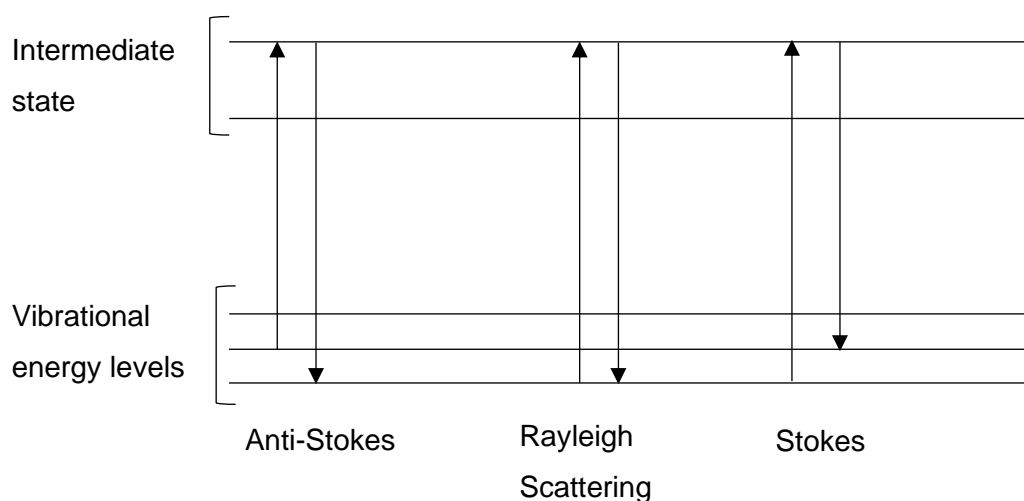
Figure 2.2 *Diagram showing the excitation and relaxation of an electron for Anti-Stokes, Stokes and Rayleigh scattering*

When molecules interact with light, their electron clouds can become deformed. This electron cloud deformation results in a change in polarisability. Raman spectroscopy provides information about the vibrational modes in a molecule based on changes in the polarisability of its molecular bonds [162]. When a photon is absorbed by a molecule, one of its electrons may jump to a higher energy intermediate state. The electron then relaxes back to a lower vibrational energy level, releasing a photon in the process. The new vibrational energy level may be higher energy, lower energy or the same energy as the original electron state. Thus the released photon may have, respectively, lower energy (Stokes), higher energy (anti-Stokes) or the same energy (Rayleigh scattering) as the incident photon (**Figure 2.2**). Any difference between the energy of the incident and released photons is measured as the Raman shift, which has units cm^{-1}. In practice, it is the Stokes lines that are mainly used for analysis.

Raman spectroscopy is often used to provide information complementary to infrared spectroscopy, which looks at changes in the dipole moments of polar molecules/ functional groups. Homoatomic bonds do not possess a spontaneous dipole and therefore do not give rise to peaks in infrared spectra. Such bonds can however be polarised by incident light, making Raman spectroscopy a useful tool for studying the vibrational transitions in non-polar molecules.

The instrument used in this work was a Renishaw inVia Raman microscope. A beam of monochromatic radiation in the form of a laser beam, is used to illuminate the sample. Using the instrument in the microscope mode, the laser is focused onto a small area of interest in the sample. Then in its spectroscopic mode, photons are scattered by the molecule at wavelengths corresponding to transitions between different energy levels in the molecule and cause a shift in wavenumber from the incident light. The scattered photons are then collected by a detector and a spectrum is produced of the shift in wavenumber with peaks at the most abundantly scattered wavenumbers.

Powder samples were placed on a glass microscope slide, flattened using a second microscope slide and imaged. The sample surface was brought into focus using the eyepiece on the microscope and extended scans were performed between 400 – 3000 cm^{-1}. Scans were made using a x20 objective lens with three accumulations. The samples were irradiated with a cobalt Samba 532 nm laser at 50% power with an exposure time of 10 s. Each sample was scanned three times and spectra displayed in this work are representative of the obtained data.

2.2.3. X-Ray Diffraction

X-ray diffraction (XRD) can be used to determine the unit cell dimensions of crystals and indicate the purity of chemicals by revealing the presence of compounds with a different crystal structure. X-ray diffraction provides a method by which the crystal structure of diphenylalanine and carbon nanotubes can be confirmed, and any similarities between these structures and that of a carbon nanotube-diphenylalanine complex can be identified.

Powder X-ray diffraction directs a beam of X-ray radiation towards a powder sample that is rotated and thereby receives X-rays from all angles with respect to the crystal. The regular spacing of atoms in a lattice cause reflected X-rays to interfere and produce fringes at discrete angles described by Bragg's Law, Equation 2.1:

$$n\lambda = 2d \sin\theta \qquad\qquad (\ 2.1\ )$$

where:

λ = the wavelength of the X-ray

d = the interplanar spacing in the crystal

θ = the diffracted angle and

91

$n = 1$ (for small angles).

The atoms in crystalline samples have long range order and produce X-ray diffraction patterns with well-defined Bragg peaks. The diffraction pattern will show peaks of intensity of diffracted X-rays at discrete angles corresponding to each plane of the crystal (**Figure 2.3**). The pattern of peaks can be used to confirm or deny the presence of particular crystal phases [163]. The atoms in amorphous samples do not possess long range order and their diffraction patterns therefore do not show sharp Bragg peaks. Instead, XRD spectra of an amorphous sample consists of a broad (halo) peak. The peak intensity is indicative of the shape and size of a crystal since the intensity is dependent on the type of atoms present and their position within the crystal. Peak width in powder samples offers additional information on crystallite size, with larger crystallites of a material having greater line broadening at half the maximum peak intensity, the full width at half maximum (FWHM), than smaller crystallites of the same material.
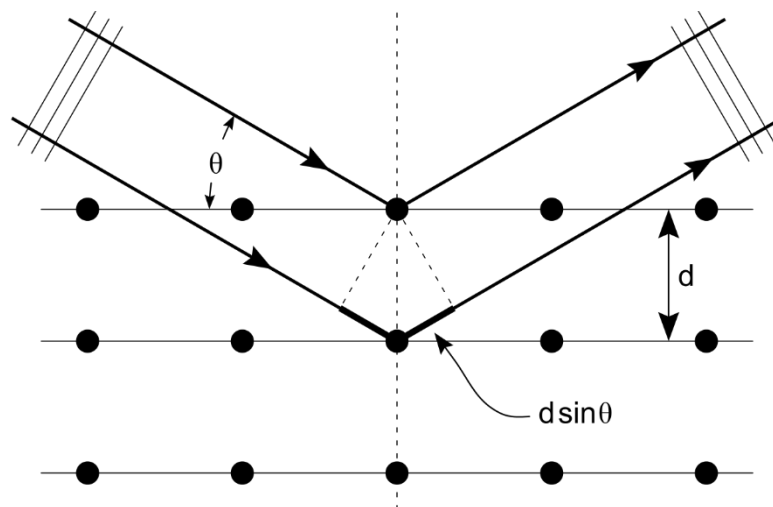
Figure 2.3 *Diagram of the atoms in a crystal lattice, where the first plane is n=1. The diagram shows the angle, θ, of the incident and reflected X-rays of wavelength λ, and the distance between crystal planes, d. Reproduced under the Creative Commons Attribution-Share Alike 3.0 Unported license.*

The reflection planes within a crystal are defined by a group of numbers known as Miller indices. For a cubic system, the Miller index of a crystal plane consists of three numbers, denoted (h, k, l), which define its position in space (**Figure 2.4a**).
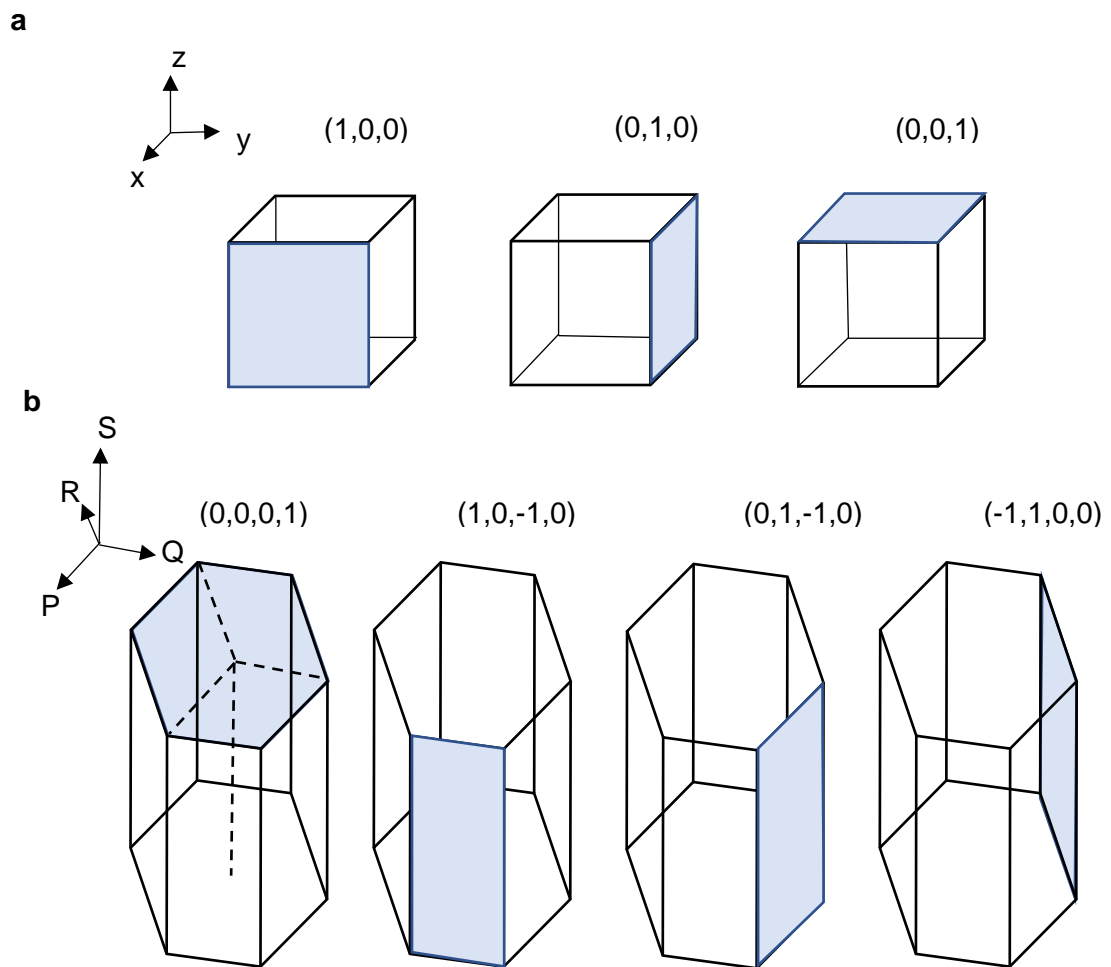
Figure 2.4 *a) Miller planes located on the faces of a cubic crystal. b) Miller planes located on the faces of a hexagonal crystal. The dashed lines indicate the axes directions which are coincident with the 3-fold axis of symmetry for a hexagonal crystal. The corresponding Miller indices are labelled above each diagram.*

For hexagonal systems, an additional fourth index, i, is added to create a Miller-Bravais index (**Figure 2.4b**). The 'i' index serves to differentiate between permutations of crystallographically equivalent planes. The index is often referred to as a 'redundant' index since it adds no information about the position of the plane in space and is instead always equal to the negative sum of the 'h' and 'k' values (h + k + i = 0).

Powder samples were placed into a fused silica glass XRD sample holder and flattened with a glass microscope slide. The samples were placed into a Rigaku Miniflex X-ray diffractometer equipped with a Cu Kα X-ray source (X-ray wavelength = 0.154 nm). The samples were scanned with a step size of 0.02 degrees at a scan rate of 2

degrees per min. Each sample was scanned once for 45 mins and the small step size ensured a high signal:noise ratio.

2.2.4. **Circular Dichroism Spectroscopy**

Measuring the circular dichroism spectra of diphenylalanine materials provides a means by which the secondary structure of the L- and D-diphenylalanine enantiomers can be probed. The chirality of self-assembled microtubes prepared from a mixture of the two enantiomers, can also be determined.

Circular dichroism spectroscopy is a technique that passes circularly polarised light through a sample. Chirality is revealed by rotation of the plane of polarisation. In the case of proteins, secondary structure can also be revealed [164]. In a CD measurement, equal intensities of right and left circularly polarised light are alternately beamed through a sample. If the sample is chiral, one of the two polarisations is absorbed more than the other (**Figure 2.5**) The wavelength-dependent difference in absorption represents the CD spectrum of the sample. Measurements are often taken in the far UV range (180 – 250 nm) and results are presented as an absorption spectrum. For the determination of the secondary structure of a protein, a sample concentration of ~0.1 mg ml^{-1} and a cuvette with a path length of 1 mm are commonly used. This produces a strong circular dichroism signal without causing the instrument to become saturated.

600 μl of each sample suspension was pipetted into a quartz cuvette with a path length of 1 mm. Samples were covered with a Teflon cap and scanned in CD spectrometer (Jasco, J-720). The samples were scanned between 190-250 nm with a resolution of 100 millidegrees and scan speed of 50 nm/min. Ten accumulations were averaged to obtain the final spectrum for each sample.

2.2.5. **Impedance and Resistance Measurements**

Impedance measurements provide information about the resistance of a material and capacitance of a structure at a range of frequencies. Through measuring the impedance of the carbon nanotube starting materials and composites, their ability to perform effectively as conductive electrode materials can be assessed. The materials can be classified as having behaviour corresponding to that of resistors, capacitors or inductors based on their impedance/ frequency relationship.
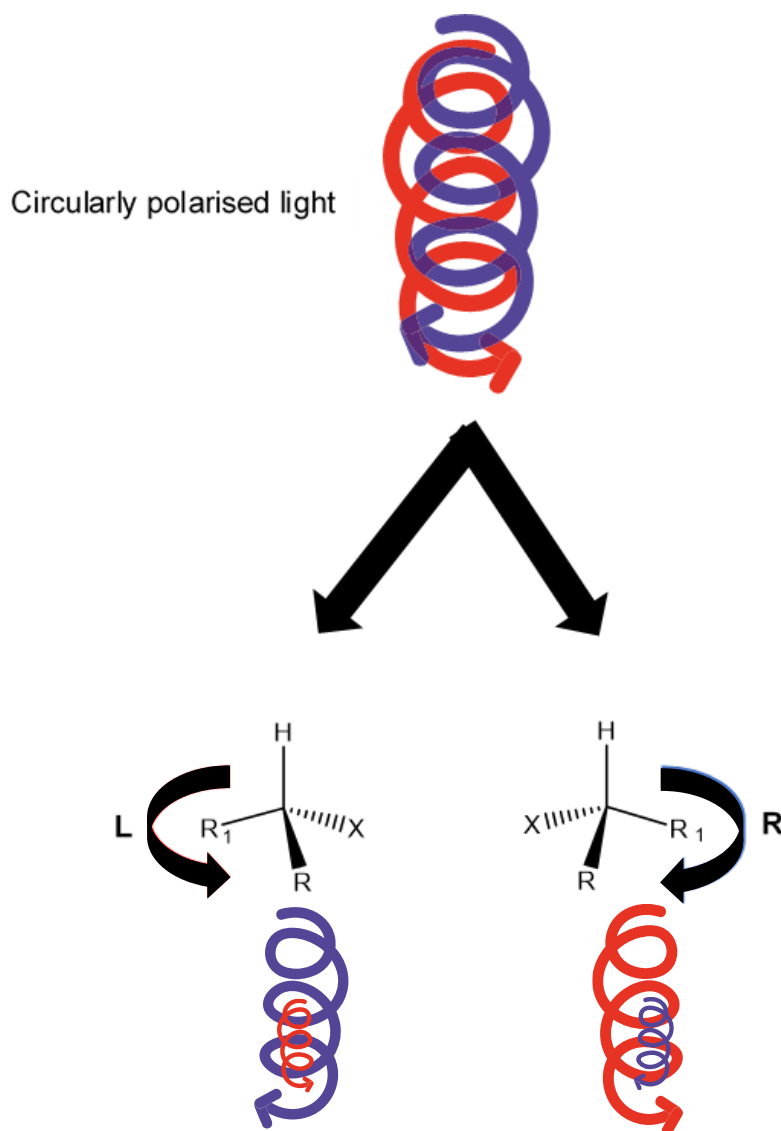
Figure 2.5 *Equal amounts of right and left circularly polarised light are passed through L and D enantiomers of a chiral molecule. Light polarised in one direction is absorbed to a greater extent by an enantiomer than light polarised in the opposite direction.*

Impedance describes the opposition to current in an AC circuit whereas resistance describes the opposition to current in a DC circuit. While resistance has no relationship with frequency, impedance is a combination of resistance (R) and another parameter, reactance (X), which is the resistance due to the inductance and capacitance of the material. Since inductance and capacitance vary with frequency, the change in the impedance of a material over a range in frequencies depends on the inductive and capacitive properties of the material. The impedance (Z) and resistance of a series circuit can be represented by Equation 2.2 and Equation 2.3:

$$Z = \sqrt{R^2 + X^2} \hspace{4cm} (\ 2.2\ )$$

$$R = \frac{V}{I} \qquad\qquad (2.3)$$

where:

v = voltage and

I = current

For impedance and resistance analysis, microscope slides were cut into strips ~ 1 cm width and ~3 cm length. The slides were washed in isopropanol (IPA) under ultrasonic agitation for 10 mins. The IPA was discarded and replaced with deionised water before the slides were exposed to a further 10 mins of ultrasonic agitation. The cleaned slides were then transferred to a watch-glass and dried in an oven at 45 °C for 30 mins. The central portion of the slides were masked with tape and gold was then sputter coated onto the slides using a (Quorum, Q150R S, 60 mA, 240 s) to create impedance analysis slides, as illustrated in **Figure 2.6**. For each experiment, slides were labelled and the dimensions of the central (non-gold coated) sections (l x w x h) were recorded using a digital caliper (HITEC, 101-45) before applying samples.
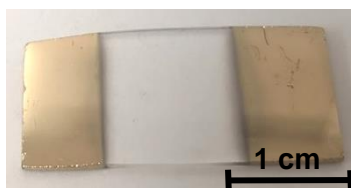
Figure 2.6 *Photograph of gold sputtered impedance analysis slide used for sample impedance measurements. Samples were applied to the central, clean glass section of the slide.*

The impedance of the samples was measured using an IM6 Electrochemical Workstation (Zahner) in Electrochemical Impedance Spectroscopy (EIS) mode with a two electrode setup. The measurements were made using a 1V AC wave with an amplitude of 100 mV and the results were displayed as a Bode plot. A Bode plot is a graphic representation of impedance and phase angle, each separately plotted against frequency as the X axis. The frequency is usually displayed on a logarithmic scale and the phase angle as a linear scale. The impedance may be presented as logarithmic or linear scale. Bode plots were displayed over a frequency range of 1- 1000,000 Hz.

The resistance of the materials was measured using a multimeter (UT60A, UNI-T).

Samples for impedance and resistance measurements were prepared in triplicate and the mean resistance for each sample was used to calculate the conductivity.

2.2.6. **Contact Angle**

In this work, contact angle measurements helped predict whether cells were likely to attach more favourably to carbon nanotube-based nanocomposites compared to other materials such as glass.

The angle formed between a solid surface and a droplet of liquid, is defined as the contact angle. It demonstrates the wettability of a surface and is useful when considering hydrophilic/hydrophobic interactions, for example, predicting the cell adhesion properties of a material. Materials are broadly classified as hydrophilic or hydrophobic depending on whether their contact angle with pure water is less than or greater than 90°.

Although there are a number of different ways to obtain the contact angle of a material, the sessile drop technique is commonly used [165]. A droplet of water is deposited onto a surface from a syringe as shown in **Figure 2.7a**. A 2D image of the droplet shape is then captured by a camera within the instrument and the contact angle between the droplet and surface is determined by Young's equation, Equation 2.4*:*

$$cos\theta = (\gamma_{SV} - \gamma_{SL}) - \gamma_{LV} \qquad\qquad (2.4)$$

where:

θ = contact angle

γ_{SV} = surface tension at the solid-air

γ_{LV} = surface tension at the liquid-air interface and

γ_{SL} = interfacial tension at the solid-liquid interface.
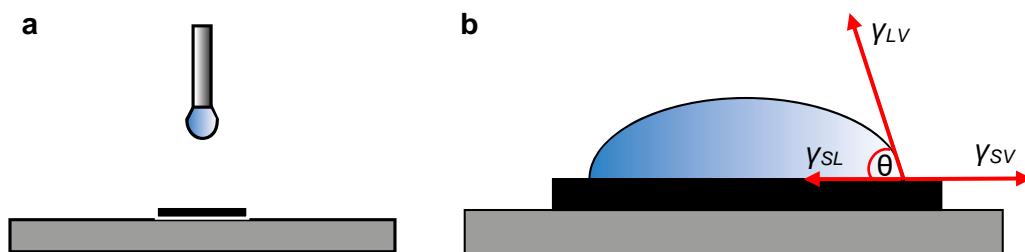
Figure 2.7 Schematic diagram of contact angle setup. a) Black solid sample on stage underneath approaching water droplet, b) water droplet on surface of a material with Young's equation parameters labelled: θ= contact angle, γ_{SV}= surface tension at solid-air interface, γ_{LV}= surface tension at liquid-air interface, and γ_{SL}= interfacial tension at the solid-liquid interface.

The contact angle of the nanocomposites was measured using a drop shape analysis instrument (Kruss DSA100). Water was deposited onto the samples in 10 µl droplets and the contact angle and image were captured by the associated software.

2.2.7. **Rheology**

Rheology is the study of the deformation or flow of a material under stress. It can be used to probe the viscous properties of a material and identify Newtonian or non-Newtonian flow behaviour [166]. In this work, the viscous properties of carbon nanotube-based inks were probed to compare different ink formulations to determine the effect of viscosity on ink printability.

Newtonian fluids, such as water, maintain a constant viscosity regardless of the shear stress applied. Non-Newtonian fluids, however, display an increase in viscosity (shear-thickening) or reduction in viscosity (shear-thinning) as shear stress is increased.

Rheological measurements are made using a rheometer, two key components of which, are the Peltier plate (a sample holder that is electrically cooled to remove heat generated) and a smooth 'measuring bob' connected to an arm which controls the distance between the parts (**Figure 2.8**). A rheometer can make measurements using one of two modes: rotational mode (commonly used for determination of viscosity) or oscillatory mode (for probing viscoelastic properties). In rotational mode, the measuring bob rotates in one direction around the axis of the arm whereas in oscillatory mode, the measuring bob oscillates around the axis of the arm. During measurements, the Peltier plate remains stationary while the measuring bob rotates or oscillates. The sample is in contact with both surfaces while the measurement is being carried out.

In both rotational and oscillatory measurement modes, either shear rate range or shear stress range is pre-defined within the software by the user and the other property is measured. The number of data points, and thus the sampling rate are also defined within the software. For measurements made in rotational mode, viscosity is calculated post-measurement within the software using Equation 2.5:

$$viscosity = shear\ stress / shear\ rate \qquad\qquad (\,2.5\,)$$

For materials which contain dispersed particulates, as is the case for carbon nanotube composites, the microstructural arrangement of the material may differ from sample to sample. The same is true for thixotropic materials; that is, materials with time and stress dependent rheological properties [167]. To overcome this, a pre-shear condition

can be applied to the material prior to measurement. This ensures that the sample is well mixed and that results obtained from different samples are comparable.

The viscosities of the carbon nanotube/ Nafion ® inks were determined using a Bohlin Instruments rheometer in viscometry (rotational) mode. 1.5 ml of ink was deposited onto the Peltier plate and the measuring bob was moved down towards the ink. The ink was pre-conditioned by shearing at 400 s^{-1} for 20 s prior to viscosity measurements. The shear rate was ramped from 0 – 200 s^{-1} for each measurement.
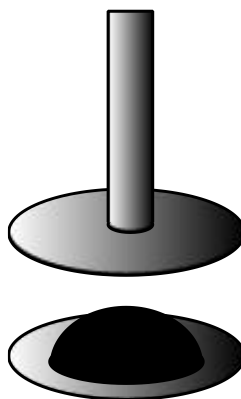
Figure 2.8 *Diagram of the measurement area of a rheometer. The upper plate (measurement bob) is lowered towards the bottom plate (Peltier plate) on which the sample is deposited. The measurement bob rotates or oscillates during measurement.*

2.2.8. **Tensile Testing**

Free-standing casts of carboxyl ink, amine ink and Nafion were prepared and subjected to tensile stress to provide an initial evaluation as to their suitability as electrode materials.

Tensile testing involves subjecting a sample of known dimensions to increasing force until failure [168]. Measurement of sample elongation while force is increased yields a force-displacement graph. The initial length of the sample (L_0) and the cross-sectional area (A) can then be combined with the force and displacement data to calculate stress and strain, using Equation 2.6 and Equation 2.7 below, which can then be used to plot a stress-strain graph. The ultimate tensile strength of the material can be calculated by measuring the maximum stress applied to the material before failure.

$$stress = \frac{F}{A}$$

$$(2.6)$$

$$strain = {\Delta L}/{L_0} \qquad\qquad (2.7)$$

where:

F = applied force and

ΔL = the difference between the initial and final lengths of the sample (elongation)

The ultimate tensile strengths of free-standing nanocomposite films were evaluated using an ElectroForce Biodynamic® Test Instrument 5160 (TA, USA) and associated WinTest software.

Nanocomposite samples for bulk and nanoscale measurements were prepared by first depositing ink onto a glass slide within 1 cm x 3 cm areas. 75 µl of ink was extruded from a 10 ml syringe. The ink was extruded for 30 s by a flow rate control pump, at a flow rate of 9 ml/hr. Ink was then spread onto glass slides using a spatula. The slides were dried on a hotplate in air at 60 °C for 15 mins and then dried further on a hotplate at 160 °C for 5 mins to remove any remaining DMF/NMM mixed solvent. The slides were then immersed in distilled water for 30 mins to release the casts from the glass surface. The casts were then cut into 1 cm x 0.5 cm strips. The depths of the carboxyl and amine inks were measured with a digital caliper and were found to be 30 µm and 60 µm respectively.

Nafion casts were prepared by depositing 100 µl Nafion D-520 dispersion onto glass slides cut into 1 cm x 3 cm areas. The glass slides were dried on a hotplate at 60 °C for 15 mins and the strips were then removed from the glass and cut into 1 cm x 0.2 cm strips. The depth of the Nafion casts were measured as 20 µm, using a digital caliper.

Extension measurements were made using the ElectroForce Biodynamic® Test Instrument. The load was ramped at 0.225 N/sec from 0 N towards 50 N until failure. The sample width and depth were used to calculate the cross-sectional area.

2.2.9. **Field Emission Scanning Electron Microscopy**

Scanning electron microscopy was used to characterise the structure and topography of carbon nanotubes, diphenylalanine materials, complexes and composites at high magnification. These revealed their morphology, crystal habit and extent of physical contact between constituents to explore the effects of different preparative routes.

In scanning electron microscopy a beam of electrons is emitted from the surface of a conductor under the influence of a strong electrostatic field and accelerated towards a sample while being focused by multiple condenser lenses (**Figure 2.9**). Upon contact with the sample surface, the incident electrons interact with the outer electrons in surface atoms of the sample. The electron beam is inelastically scattered and a variety of signals produced by electron-sample interactions are detected by different detectors. The instrument used in this work was a Zeiss Crossbeam 350, a high-resolution field emission scanning electron microscope (FE-SEM). The output of secondary electrons was recorded in the form of micrographs at a range of magnifications.
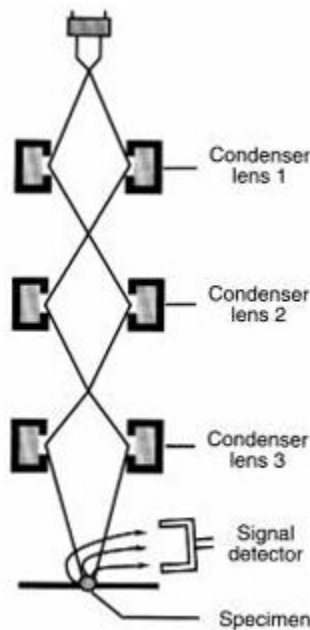
Figure 2.9 *Schematic diagram of the column of a scanning electron microscope. The condenser lenses, sample and secondary electron detector are labelled. Image reproduced from* [169].

For electronically conductive materials, the technique can be used directly while biological or insulating materials need to be coated with a conductive layer beforehand. Prior to coating, sensitive biological samples could become damaged upon contact with the high energy electron beam. The coating forms a protective layer on the sample, allowing it to be imaged without sustaining damage. In the case of uncoated insulating materials, accelerated electrons may collect on the surface of the sample (known as charging), causing some parts of the final image to appear 'bleached'. The conductive coating acts as a channel for the removal of charging electrons, allowing a high resolution image to be obtained. Gold is often used as a coating material due to its high conductivity and ability to facilitate high resolution imaging.

Sample preparation varied depending on the nature of the sample. Specific sample preparation methods will be detailed in the relevant chapters.

Following appropriate sample preparation, samples were mounted onto SEM specimen aluminium SEM stubs and imaged at a voltage of 3 kV, unless otherwise stated. Multiple (three or more) micrographs were captured for each sample. The displayed micrographs are representative of the samples imaged.

2.2.10. Transmission Electron Microscopy

Transmission electron microscopy provides a useful method for visualising the nanoscale arrangement of a carbon nanotube-diphenylalanine complex. The difference in the electron density of carbon nanotubes and diphenylalanine provides contrast to allow identification of the two materials within the complex. The technique also offers insight into the self-assembly of diphenylalanine and the structure of self-assembled diphenylalanine microtubes.

Transmission electron microscopy facilitates the visualisation of structures between 0.1- 200 nm in size. The instrument used in this work was a JEOL JEM-2100 200 kV transmission electron microscope. A beam of electrons is emitted from a lanthanum hexaboride (LaB_6) electron source, collimated by a condenser lens and accelerated towards a thin sample within a vacuum chamber. The incident electrons either pass through, or are deflected by, the sample. Those that pass through the sample are focused and magnified by a magnetic objective lens, before being further magnified by a projection lens and projected onto a fluorescent screen underneath to produce an image (**Figure 2.10**).

The sample is scanned by moving the stage containing the sample, which enables the macro sample to be scanned visually under high magnification. Areas of interest identified using the fluorescent screen would then be recorded electronically as a permanent record. Contrast in the image can arise from differences in sample thickness or density (mass-thickness contrast), atomic number of constituent atoms in the material (Z contrast), crystal structure or orientation (diffraction contrast) and other mechanisms [170]. Areas of high electron density within the sample will cause a higher proportion of the incident electron beam to be absorbed and, conversely, sample regions with low electron density will allow more of the electron beam to pass through. For pristine carbon nanotubes, dark and bright regions in the image correspond to regions of high and low electron density respectively. Dark regions near the end of

nanotubes may correspond to metal nanoparticles catalysts left over from the carbon nanotube growth process.
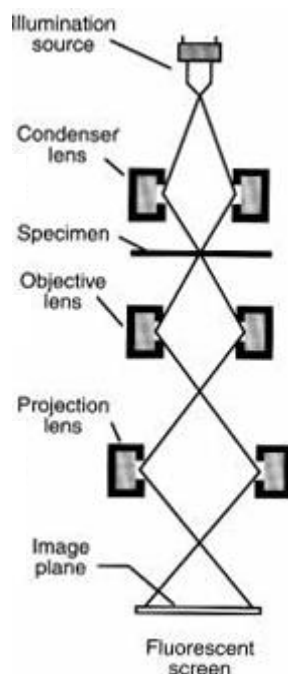
Figure 2.10 *Schematic diagram of the column of a transmission electron microscope. The sample fluorescent screen and various lenses are labelled. Image reproduced from [169].*

Sample preparation varied according to the nature of the sample. Specific sample preparation methods will be detailed in the relevant chapter.

Following appropriate sample preparation, samples were imaged at a voltage of 200 kV. Multiple (more than three) micrographs were captured for each sample. The displayed micrographs are representative of the samples imaged.

Diphenylalanine is a difficult material to image by transmission electron microscopy because of its low thermal conductivity, low melting point (235 °C) and its morphology; it would melt or burn very soon after contact with the electron beam. Electron beam damage could occur within five seconds so a region of representative interest in the sample had to be identified and a permanent image recorded within that time. Damage would occur only within the immediate region of the focused electron beam which at a magnification of 40 000x might correspond to an area of 30 µm^2.

2.2.11. **Atomic Force Microscopy**

Atomic force microscopy (AFM) is a type of scanning probe microscopy that allows for the imaging of non-conductive samples. Scanning probe microscopes operate on the principle of measuring a physical interaction between a sharp tip and a sample (**Figure 2.11**) to produce an image with atomic scale resolution [171].

Atomic force microscopy was used to measure the nanoscale piezoelectric properties of diphenylalanine and PVDF-TrFE, and to measure the nanoscale mechanical properties of diphenylalanine, PVDF-TrFE and carbon nanotube nanocomposites.

Early scanning probe microscopes, such as scanning tunnelling microscopes, have applications limited to electrically conductive and semi-conductive samples since a tunnelling current is required to flow through the vacuum gap between the tip and sample for an image to be produced. AFM produces images by measuring the deflection of a cantilever as a result of atomic forces between the tip and sample. This removes the need for a conductive sample and allows the application of scanning probe microscopy to be extended to biological and other non-conductive materials.
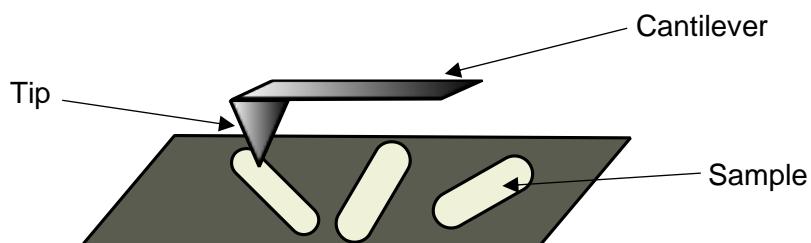
Figure 2.11 *Diagram of scanning probe microscopy components (not to scale)*

Two particular imaging modes of AFM are contact and tapping modes, during which the tip is either in constant contact with the sample or taps the sample at intervals defined by the resonant frequency of the cantilever. Other AFM functions use contact or tapping modes to extend the applications of AFM to the measurement of physical properties. In this work, the piezoelectric and mechanical properties of materials have been explored by AFM, using piezoresponse force microscopy, an extension of the AFM contact mode, and force-distance measurements, an extension of the AFM tapping mode.

To obtain an accurate AFM response, it is important for the sample to be secured to the substrate during measurement, particularly for contact mode techniques. Samples were secured either by mechanical clamping or partial embedding in a thermoplastic resin such as Tempfix. Sample-specific securing techniques will be discussed in the relevant sections.

Piezoresponse force microscopy (PFM) measurements were made by probing individual electrospun nanofibres on a gold-coated glass slide. The slide was electrically grounded to an Asylum MFP-3D AFM stage and a conductive AFM cantilever (AC, 240R2, Olympus) was used for PFM measurement. An image of the nanofibre was first obtained in tapping mode before changing to Single Frequency Piezo Force Measurement mode (Single Freq PFM). The contact resonance frequency of the cantilever was acquired while the cantilever was in contact with the nanofibre and measurements were then made at a frequency close to the resonant frequency of the cantilever, to avoid amplification artifacts. The measurements yielded graphs of amplitude (A) against voltage (V), from which the d_{33} was calculated using Equation 2.8 [172] below

$$d_{33} = \frac{A}{VQ} \qquad\qquad (2.8)$$

where Q is the quality factor of the cantilever. For low frequency applications, including Single Freq PFM, Q = 1. [172]

The surface modulus of a material can be regarded as the nanoscale equivalent of the Young's modulus. It is determined by applying increasing force to the sample, through the cantilever, to provide a force-deformation (FD) graph. The maximum applied force is decided on the need not to damage the cantilever, and in the case of rare or precious samples, to preserve the sample. Elastic moduli of the sample can then be determined through quantitative analysis of the linear region of the FD graph.

Surface moduli of diphenylalanine microtubes were calculated from data obtained using a Bruker Dimension 3100 AFM, equipped with a silicon (Bruker RTESPA525A) cantilever (spring constant 200 Nm^{-1}). The surface moduli of individual PVDF-TrFE nanofibres were determined from data obtained using an Asylum MFP-3D AFM in force spectroscopy mode. The surface moduli of the nanocomposite films were probed using the same by AFM mechanical measurements on an Asylum MFP-3D AFM in AMFM mode. Samples were scanned using a new cantilever, with a tip diameter of 20 nm. The diameter was estimated within the software, using the Hertz punch model, which

predicts the interaction between tip and sample based on the interaction between the spherical surface of an elastic body and a patterned substrate.

2.3.   **Cell Culture Materials**

Reagents and consumables used for cell culture are detailed in **Table 2.2**.

Table 2.2 Table of reagents and consumables used for cell culture

Materials	Supplier	Product number	Grade
Cells			
Human Dermal Fibroblasts	Culture Collections	HDF (106-05a) UK	-
Human Schwann Cells	Caltag Medsystems	SC-1700	-
Cell Culture Reagents			
10x phosphate buffer saline	Sigma-Aldrich	D1283-500ML	-
Bovine serum albumin (BSA)	Sigma-Aldrich	A7030-100G	-
DAPI	Thermo Fisher	D1306	-
Distilled water	Life Technologies	10977049	-
Dulbecco's Modified Eagle Medium (DMEM) (low glucose)	Life Technologies	31885049	-
Fetal bovine serum (FBS) (for HDF)	Gibco ™	10270106	-
Fetal bovine serum (FBS) (for HSC)	Caltag Medsystems	SC-0025	-
Hoescht dye (DNA Quantification Kit)	Sigma-Aldrich	MDQ1-96RXN	-
Human Schwann cell (HSC) basal medium	Caltag Medsystems	SC-1701-b	-
Mounting Medium (Fluoroshield ™)	Sigma-Aldrich	F6182-20ML	-
Paraformaldehyde (PFA)	Sigma-Aldrich	158127-100G	95%
Penicillin streptomycin (for HDF)	Sigma-Aldrich	P0781	-
Penicillin Streptomycin (for HSC)	Caltag Medsystems	SC-1752	-
Phalloidin (AlexaFluor ™ 488)	Thermo Fisher	A12379	-
Phosphate buffer saline (PBS)	Gibco ™	20012068	pH 7.2

	Caltag		
poly-L-lysine (PLL)	Medsystems	SC-0413	-
Presto Blue assay	Thermo Fisher	A13261	-
Schwann cell growth supplement (SCGS)	Caltag Medsystems	SC-0413	-
Triton-X 100	Sigma-Aldrich	93443-100ML	-
Trypan Blue assay	Sigma-Aldrich	T8154	-
trypsin-EDTA solution	Sigma-Aldrich	T4049	-
Consumables			
CoolCell	Corning ®	CLS432001	-
Poly-D-lysine coated T75 flask	Corning ® Biocoat	734-0192	-
T75 flasks	Corning ®	734-2705	-

2.4. **General Human Dermal Fibroblast Cell Culture**

A T75 flask containing Human Dermal Fibroblasts (HDF) (P5) were obtained from a colleague in the same laboratory. The flask was transferred to a class II microbiological safety cabinet (BSC) and the medium changed. The medium used for HDF culture was DMEM supplemented with 10% FBS and 1% penicillin/ streptomycin (p/s). The medium was warmed to 37°C in a water bath prior to each use and was changed every 2-3 days until cells were 90% confluent.

For the subculture of HDFs, phosphate buffer saline (PBS), 0.25% trypsin-EDTA solution and complete medium were warmed to 37°C in a water bath prior to use. The cells were first washed with PBS. 2 ml trypsin-EDTA was then added to the flask and incubated for 5 mins. The flask was tapped gently to dislodge cells and 5 ml medium was added to neutralise the trypsin-EDTA. The cell suspension was aspirated into a 15 ml centrifuge tube and centrifuged at 1200 rpm for 5 mins. The supernatant was aspirated and the cell pellet resuspended in 10 ml medium. 60 µl cell suspension was transferred to a microcentrifuge tube for cell counting. The cell suspension and Trypan Blue assay were added to a clean microcentrifuge tube in equal volumes and the live cells were counted using a haemocytometer. The remaining cell suspension was subcultured in T75 or T150 flasks at a density of 2000 cells/ cm^2.

2.5. **General Human Schwann Cell Culture**

Human Schwann cells (P0) were purchased from Caltag Medsystems (SC-1700). Prior to thawing, the cells were moved from liquid nitrogen to a -80°C storage freezer for 2 hours to reduce cell shock during thawing. The cells were then thawed quickly in a water bath at 37°C, transferred to a class II microbiological safety cabinet (BSC) and pipetted into a poly-D-lysine coated T75 flask (Corning ® Biocoat, 734-0192) containing 10 ml HSC complete medium. The complete medium was comprised of HSC basal medium supplemented with 5% foetal bovine serum (FBS), 1% Schwann cell growth supplement (SCGS) and 1% penicillin streptomycin (p/s). The medium was warmed to 37°C in a water bath prior to each use. The flask was then incubated at 37°, 5% CO_2. Medium was discarded one month after reconstitution due to degradation of the SCGS component. The medium was changed every 2-3 days until cells were 90% confluent.

For the subculture of HSCs, PBS, 0.25% trypsin-EDTA solution and complete HSC medium were warmed to 37°C in a water bath prior to use. The cells were washed with 8 ml PBS. 8 ml fresh PBS was then added to the flask followed by 2 ml trypsin-EDTA. The flask was incubated for 2 mins and the liquid was then aspirated into a 50 ml centrifuge tube. The flask was incubated for a further minute before adding 10 ml complete medium to neutralise the trypsin-EDTA. The flask was tapped gently to release any remaining cells from the flask surface and the cell suspension was aspirated and added to the 50 ml centrifuge tube containing 5 ml FBS. The walls of the flask were washed with 5ml complete medium and the washings were added to the 50 ml centrifuge tube. The centrifuge tube containing the cell suspension was centrifuged in a MSE centrifuge (Minstrel 1000) at 1000 rpm for 5 mins. The supernatant was aspirated and the cell pellet was resuspended in 10 ml complete medium. 60 μl cell suspension was transferred to a microcentrifuge tube for cell counting. Cell suspension and Trypan Blue assay were added to a clean microcentrifuge tube in equal volumes and the live cells were counted using a haemocytometer. The remaining cell suspension was seeded into poly-D-lysine coated flasks at 5000 cells/ cm^2 according to the supplier's recommendation.

Cells which were not immediately required were frozen for later use. The 50 ml centrifuge tube containing HSC suspension was centrifuged at 1000 rpm for 5 mins and supernatant aspirated. The cell pellet was then resuspended in freezing medium comprised of 90% FBS and 10% dimethylsulfoxide (DMSO). 1 ml of cell suspension in freezing medium was added to cryogenic vials and placed in a CoolCell at room temperature. The CoolCell unit was then transferred to the -80°C freezer where the

cells were frozen at a rate of -1°C/ min to -80 °C. After 24 hrs the cells were transferred to liquid nitrogen (-196 °C) for long term storage.

2.6.   **Measurement of Cell Viability**

Cell viability can be assessed by measuring the metabolic activity of cells grown *in vitro*. A comparison of the metabolic activity of cells grown in a test environment to the metabolic activity of cells grown in a control environment provides an initial indication of the suitability of the test material for use in a biological context.

A commonly used reagent for measuring cell viability is Presto Blue, a solution based on the organic molecule resazurin (a weakly fluorescent, blue/ purple coloured, cell-permeable, non-cytotoxic stain). When Presto Blue enters a living cell, it is reduced to resorufin, which has a bright pink colour and is highly fluorescent. The change in fluorescence gives an indication of cell health since non-viable cells cannot reduce the reagent.

For assessment of HDF metabolic activity, the materials on coverslips were transferred to fresh 24-well plates. Presto Blue assay diluted to 10% v:v in supplemented DMEM medium was then added to each well and incubated for 2 hours (day 1), 1 hour 40 mins (day 3) or 1½ hours (day 7). Following incubation, Presto Blue from each well was transferred to a black 96-well plate and read in a fluorescence plate reader (Fluoroskan Ascent ™ FL, Thermo Labsystems) with excitation 530 nm and emission 620 nm.

For assessment of HSC metabolic activity, the materials on coverslips were transferred to fresh 24-well plates. Presto Blue assay diluted to 10% v:v in complete HSC medium was then added to each well and incubated for 2 ½ hours (day 1), 1 ½ hours (day 3) or 1 hour (day 5). Following incubation, Presto Blue from each well was transferred to a black 96-well plate and read in a fluorescence plate reader with excitation 530 nm and emission 620 nm.

2.7.   **Measurement of Cell Proliferation**

Cell proliferation can be measured quantitatively by a number of methods, one of which is measurement of the amount of DNA present in a sample.

A tool often used to facilitate this is the total DNA assay, in which cells are lysed to release DNA and the DNA then labelled with a bisbenzimide (Hoeschst) fluorescent

stain. Higher fluorescence is equated with higher DNA content and thus a greater number of cells.

The total DNA assay was used to assess the proliferation of HSCs. At each time point, the cells in 24-well plates were studied with the Presto Blue metabolic activity assay (Section 2.6). Following this, the cells were washed with PBS and 300 µl distilled water was added to each well. The plates were sealed with parafilm and frozen to -20 °C. The plates were thawed completely and the freeze-thaw process was repeated five more times to ensure complete cell lysis and full release of DNA into the solution. After the sixth time, 50 µl samples of each well were transferred to a black 96-well plate along with 50 µl Hoechst dye (obtained from the DNA quantification kit). The plate was read in a fluorescence plate reader with excitation 355 nm and emission 460 nm. The resulting fluorescence readings were compared to those from a standard DNA sample and were deemed to be above the noise threshold.

2.8.   **Cell Fixing, Staining and Mounting**

Human Schwann Cells were fixed and stained for fluorescence microscopy. Fluorescence microscopy facilitates visualisation of the structural and internal components of a cell since different dyes are able to selectively stain cellular organelles. In this work, visualisation of the cell cytoskeleton and cell nucleus were of interest; therefore, dyes were chosen to stain actin in the cell cytoskeleton and DNA inside the cell nucleus.

Cells were fixed with formaldehyde, permeablised with Triton-X 100 solution, blocked with bovine serum albumin (BSA) and stained with fluorescent dyes. The cells were imaged using a confocal microscope.

2.8.1. **Cell Fixing**

Formaldehyde solution was prepared by dissolving 4 g of paraformaldehyde (PFA) powder in 50 ml distilled water. A single sodium hydroxide (NaOH) pellet (prill) was added and the mixture was stirred at 60 °C overnight to fully dissolve the PFA. The solution was then made up to 100 ml with 10 ml 10x PBS and 40 ml distilled water to yield a 4% formaldehyde solution. Cells were fixed by adding 200 µl 4% of formaldehyde to each well. The cells were left to sit at 20 °C for 30 mins before removing the formaldehyde and replacing with 200 µl PBS.

110

2.8.2. **Cell Mounting**

Fixed, stained cells on coverslips were removed from PBS and dipped in distilled water to remove any PBS salts. Any excess water was removed and the samples were briefly allowed to dry in air while the mounting medium slide was prepared. A drop of mounting medium was placed onto a rectangular coverslip and the sample coverslip was inverted onto the drop, ensuring that no bubbles were present. The samples were left undisturbed, on a flat surface, for 18 h to allow the mounting medium to cure.

After the mounting medium was cured, the edges of the coverslip were sealed with clear cosmetic nail varnish to prevent oxidation of the fluorescent dyes. The mounted samples were stored in a microscope box until imaging.

2.8.3. **Human Schwann Cell Staining**

Bovine serum albumin with a concentration of 1% in PBS was prepared and used to dilute Triton-X and phalloidin. Cells were first permeabilised with 0.1% Triton-X 100 in 1% BSA and incubated for 30 mins at 20 °C. Triton-X was removed, replaced with 1% BSA and incubated for 30 mins. Phalloidin was prepared at a dilution of 1:300 in 1% BSA and DAPI was prepared at a dilution of 1:1000 in PBS. Following incubation with BSA, cells were incubated with phalloidin for 1 h at 20 °C to stain the cytoskeleton. Phalloidin was removed and wells were washed twice with 1% BSA. The wells were then washed with PBS before adding the nuclear stain, DAPI, and incubating for 2 mins before removing. Wells were washed with PBS and then stored in PBS until mounting.

2.9. **Fluorescence Microscopy**

Samples were imaged using a Nikon C2+ confocal microscope at X10 or X20 magnification. The samples were excited with laser wavelengths of 488 nm (phalloidin) and 405 nm (DAPI).

2.10. **Statistical Analysis**

Statistical analysis was carried out using Student's t-test in Origin ® graphing and analysis software.

Student's t-test was introduced in 1908 by W. S. Gosset [173] as a method for monitoring the quality of stout. The test is now commonly used to compare pairs of small, independent samples, with equal variance and normal distributions. The t-test was selected as the method for statistical analysis in this case simply because it is often used for comparing sets of data obtained from cell culture experiments and thus allows easy comparison with statistics of results elsewhere. Student's t-test assumes equal variance which was not the case for most data sets in this work. The Welch correction, which is a library routine in the Origin software, was therefore applied to correct the t-test for non-equal variance. Data sets were normalised against the negative control and comparison was made between experimental data sets and their respective positive control. The comparison yielded a value, known as the p-value, which represented the probability that the experimental data was significantly different from the control data. Lower p-values indicate a greater separation between the experimental and control data. A p-value of less than 5% ($p < 0.05$) was considered statistically significant. Significant results will be highlighted using an asterisk where relevant.

Chapter 3   **Controlled Assembly of Piezoelectric Materials**

3.1.   **Piezoelectric Nanostructures**

As explained in Section 1.2.1, the piezoelectric materials are materials that can transduce mechanical stress into an electrical potential, and *vice versa.* Macro piezoelectric materials have many mainstream applications such as microphones, weighing devices, time keeping and ultrasound scanning. Nanoscale piezoelectric materials are being exploited for applications as biofunctional materials; for example, to provide a stimulus for neural cell differentiation or as mechanotransducers in biomedical devices [28].

The small size of nanoscale piezoelectric materials confers on them different physical properties than those observed for their bulk counterparts. As with nanomaterials in general, these properties may manifest in numerous ways including surface effects from increased surface area:volume ratio, or increased performance arising from highly ordered polymer structures or organic or ceramic single crystals devoid of defects. In this way, nanoscale piezoelectric materials can display improved mechanical properties such as increased strength, high Young's modulus, compared to bulk piezoelectric materials [61].

When selecting materials for a cochlear implant, the effect of the material on body tissues both during implantation and over an extended time period must be considered. The device will have to be be small enough to be inserted into the cochlea (average diameter 9 mm) and flexible enough to curve with the cochlear turns. Flexible nanomaterials have been found to produce more desirable research outcomes since they can be fabricated to a smaller size than macro materials and apply less pressure to intra-cochlear blood vessels [5], reducing long-term detrimental effects on neural elements (hair cells, spiral ganglion neurons) in the vicinity.

Nanoscale piezoelectric materials offer significant increases in mechanical and piezoelectric properties compared to bulk piezoelectric materials but the processability of nano and micro-sized ceramic particles poses a significant challenge for their widespread application. The high surface energy and large surface area of nanosized particles make them susceptible to agglomeration and reduce the ease with which they can be arranged into highly organised structures [49].

The formation of highly ordered piezoelectric structures can be facilitated by the use of micro or nanoscale processing methods. These are often applied to piezoelectric polymers and organic piezoelectric materials. An example of this is found in PVDF nanofibres obtained by an electrospinning process [60]. The nanofibre properties and physical arrangement on the substrate can be controlled by modifying the electrospinning conditions. Studies in the literature have indicated that electrospun polymeric fibres provide a favourable environment for cell attachment and proliferation due to their flexibility and ability to better match the mechanical properties of cells in culture. The self-assembly of diphenylalanine into microtubes [48] offers another example of a highly ordered piezoelectric structure. A range of nanostructures can be obtained from diphenylalanine solutions with different concentrations [174], although these structures do not all exhibit a piezoelectric response.

3.2.   **Aims**

The work in this chapter on the controlled assembly of piezoelectric materials involves the exploration of the formation and properties of two piezoelectric materials — micro-structured diphenylalanine microtubes and nanostructured poly[vinylidene fluoride-co-trifluoroethylene] (PVDF-TrFE) nanofibres. Characterisation of the materials provides an understanding of the relationship between their structure and properties and offers guidance as to their suitability as the piezoelectric component of an implantable device. Diphenylalanine was prepared and characterised by myself, while the preparation and characterisation of PVDF-TrFE was carried out by Dr. Giuseppe Viola (post-doctroal researcher, UCL), Jinke Chang (PhD student, UCL) and Dr. Mohamed Jomaa (post-doctoral researcher, UCL) as part of the larger EPSRC funded project. The culture of Human Schwann cells on both materials was carried out by myself.

The objectives of this work were to:

- Investigate diphenylalanine as a potential source of piezoelectric function for an implantable device
    - form diphenylalanine microtubes from different chiral forms of diphenylalanine;
    - characterise the diphenylalanine microtubes;
    - investigate the effect of changing the physical and chemical conditions of the microtube self-assembly;
    - evaluate the effect of piezoelectric materials on Human Schwann Cell proliferation and growth;

- Investigate PVDF-TrFE as a potential source of piezoelectric function for an implantable device (work carried out by Dr. Giuseppe Viola, Jinke Chang and Dr. Mohamed Jomaa)
    - electrospin random and aligned PVDF-TrFE nanofibres;
    - characterise the electrospun nanofibres;

3.3. Piezoelectric Peptide: Diphenylalanine

3.3.1. Chiral Forms and Derivatives of Diphenylalanine

Diphenylalanine is an amphiphilic dipeptide comprising two phenylalanine molecules joined by an amide linkage. The dipeptide is non-centrosymmetric, allowing for piezoelectric properties, and contains two chiral carbon centres, giving rise to multiple chiral forms. The L and D enantiomers of diphenylalanine (**Figure 3.1**) are non-superimposable, mirror images of each other.

The chiral property is seen in many natural systems, with many L form peptides being present in animal organs and tissue. Chiral molecules have also been used as drugs and it has been recognised that chiral opposites can have drastically different effects inside the body. If diphenylalanine is to be used as a component in an implantable device, it is prudent to investigate and identify any differences between the behaviour of the L and D enantiomers.

A study by Reches and Gazit [48] showed that L- and D-diphenylalanine enantiomers react differently when incubated with the enzyme proteinase K. The L form was fully digested after 1 h while the D form showed no visible reaction. This difference could indicate that the L and D forms of diphenylalanine may interact differently with enzymes inside the body.

Recently, researchers have shown an increased interest in diphenylalanine due to its presence in amyloid beta fibrils and its ability to self-assemble into a range of nanostructures [175]. Diphenylalanine can also be chemically modified, giving rise to an extended range of self-assembly possibilities and creating different routes for chemical synthesis. One such chemical modification is the protection of the diphenylalanine primary amine group by the addition of a sterically large chemical group such as fluorenyl-methyloxy-carbonyl (Fmoc) or tert-butyloxy-carbonyl (t-Boc). In this work, Fmoc-diphenylalanine (**Figure 3.1c**) has been studied to enable comparison of its structure and cell interactions with those of L- and D-diphenylalanine.

115
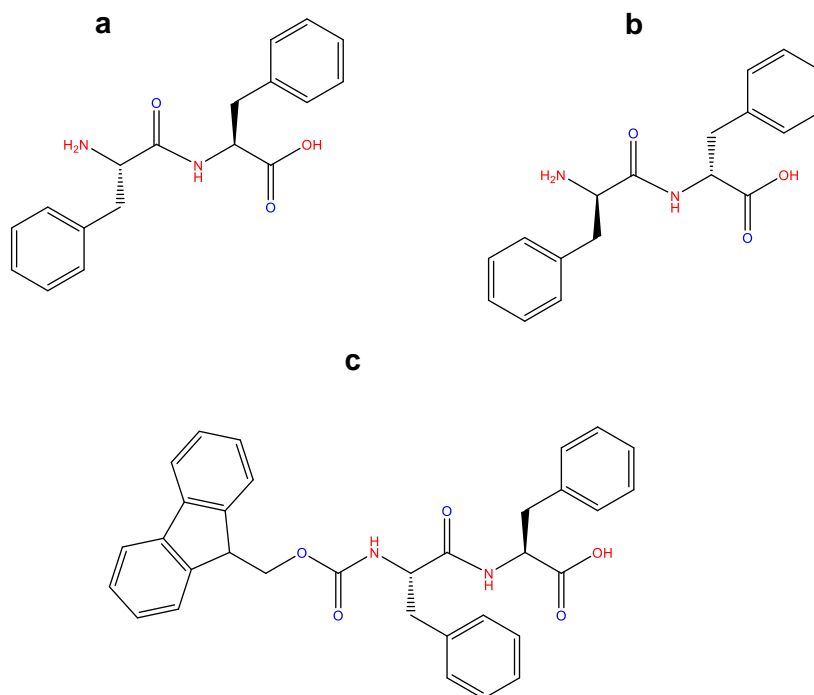
Figure 3.1 *Skeletal formulae of a) L-diphenylalanine, b) D-diphenylalanine and c) Fmoc-diphenylalanine molecules. Hydrogen bond donor/ acceptor sites are shown in red. Hydrogen bond acceptor only sites are shown in blue.*

3.3.2. Formation of Diphenylalanine Peptide Microtubes

The formation of diphenylalanine microtubes was adapted from the procedure developed by Reches and Gazit [48]. 100 mg L,L- or D,D- diphenylalanine powder were dissolved in 1 ml of hexafluoroisopropanol (HFIP) in a 10 ml round bottom flask at 20 °C, 1 atm pressure. Then 2 ml of deionised water added to the solution. After the dilution of the diphenylalanine (FF) solution with water, microtubes began to self-assemble in suspension, some of which were large enough to be visible by eye. The mechanism of microtube formation is discussed in detail in Section 3.6.2.

3.3.3. Formation of Fmoc-Diphenylalanine Hydrogels

As described above, L-diphenylalanine and D-diphenylalanine can self-assemble into peptide microtubes. The protective group on Fmoc-diphenylalanine prevents that

molecule from doing the same, instead it can self-assemble into a hydrogel. The method for preparing Fmoc-diphenylalanine hydrogels was:

100 mg Fmoc-diphenylalanine were dissolved in 1 ml dimethylsulfoxide (DMSO). Deionised water was added in 200 µl aliquots up to a total volume of 3 ml, resulting in the immediate formation of a hydrogel [176].

Fmoc-diphenylalanine was intended to provide a comparison for covalent functionalisation, rather than for use as piezoelectric component. Fmoc-diphenylalanine does not self-assemble into the same piezoelectric crystals as L- and D-diphenylalanine but while making measurements of the properties of the materials of direct interest here, it required little marginal effort to make similar measurements of Fmoc-diphenylalanine.

3.3.4. Physical and Chemical Properties of Diphenylalanine

Spectroscopic techniques were used to investigate the molecular-scale interactions and resulting crystalline structure of diphenylalanine. These interactions were the driving force for the self-assembly of diphenylalanine into hexagonal microtubes. The properties of self-assembled diphenylalanine microtubes were studied, exploring the differences between enantiomers and Fmoc protected diphenylalanine.

3.3.4.1. Morphology of Diphenylalanine Microtubes

The morphology of the diphenylalanine microtubes was observed by scanning electron microscopy. Suspensions of diphenylalanine microtubes were prepared as described in Section 3.3. 50 µl aliquots of each sample were pipetted directly onto SEM stubs and dried in restricted circulating air controlled at 20-25 °C in a protected envelope (inverted cylindrical evaporating basin with a lip) to avoid contamination by dust for 18 h overnight. After drying, the samples were sputtered with gold according to the local customary procedure (20 mA, 120 s) and stored until imaging. The imaging process was followed as detailed in Section 2.2.9. The samples were imaged with magnifications between 200x – 30,000x.

The SEM images in **Figure 3.2** show the hexagonal structure of diphenylalanine microtubes and the open-end hollow channel inside the microtubes. From the micrograph in **Figure 3.2f**, the D-diphenylalanine microtube wall thickness can be measured as ~0.5 µm while the channel diameter is ~3.43 µm. The outer diameters of

L-diphenylalanine and D-diphenylalanine microtubes were measured as ~2.1 μm and ~4.6 μm respectively. In the micrographs of L-diphenylalanine and D-diphenylalanine shown in **Figure 3.2c** and **Figure 3.2d** some hexagonal microtubes with closed ends can be seen, as well as shattered microtubes which were damaged during the process of applying the microtube suspension to the SEM stubs. The peptide lengths appears to vary more for L-diphenylalanine than D-diphenylalanine. There is no clear explanation for this, since the microtubes were precipitated in parallel, under identical conditions.
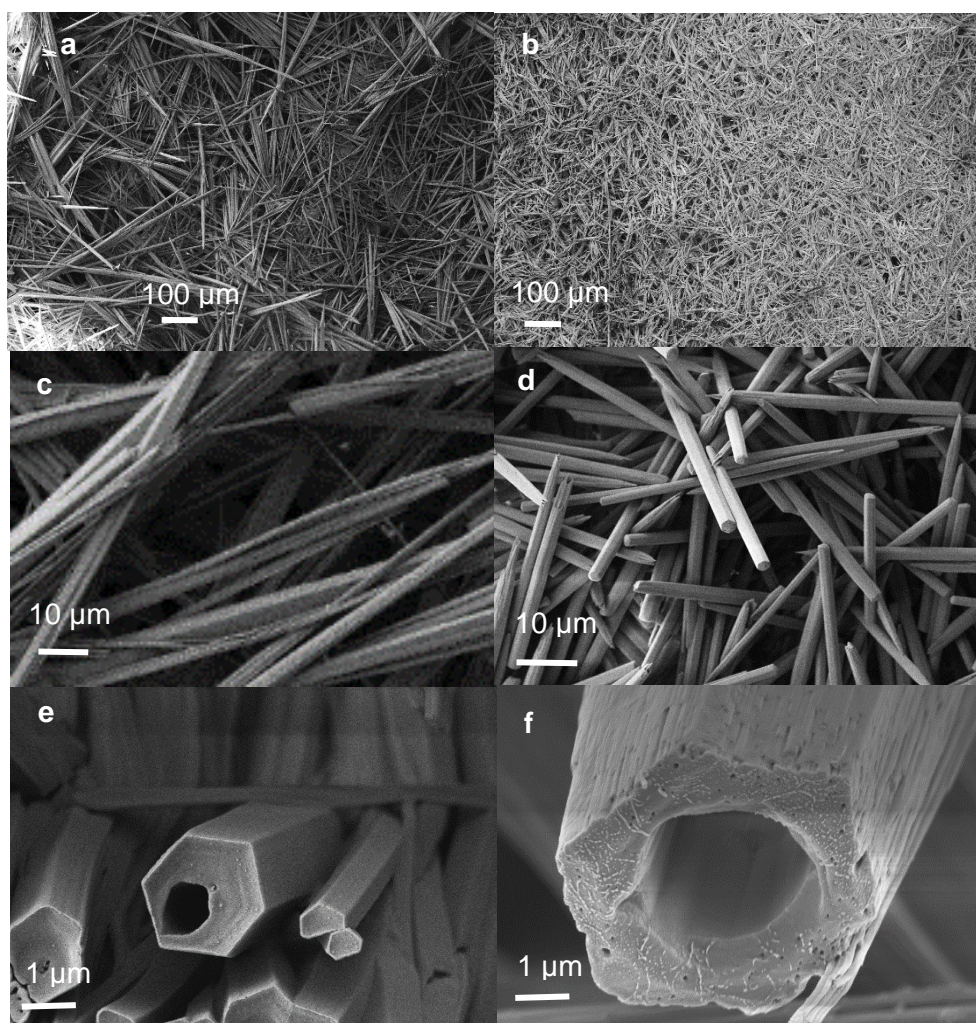
Figure 3.2 *Scanning electron micrographs of the structure of capped and uncapped L- and D-diphenylalanine microtubes at different magnifications. a, c, e) L-diphenylalanine, b,d,f) D-diphenylalanine*

3.3.4.2. **Diphenylalanine Crystal Structure**

The crystal structures of diphenylalanine materials were investigated using X-ray powder diffraction. Powder samples of LFF, DFF and FmocFF were characterised using the procedure described in Section 2.2.3.

Diphenylalanine microtubes were prepared using the method described in Section 3.3. The microtubes were dried in the glass preparation vial at 20 °C overnight. Dried microtube samples were then characterised using the procedure described in Section 2.2.3.

All the studied chiral forms and derivatives of diphenylalanine display a crystalline structure. Their crystal structures are observed for both powder and microtube or hydrogel forms of the peptides. The X-ray diffractograms shown in **Figure 3.3** indicate the crystal structures of L-, D- and Fmoc-diphenylalanine. In X-ray diffraction, the characteristic parameter is the diffraction angle (2θ), and the relative intensities of the diffracted rays can also offer insight into the crystal structure of the sample. Differences can be seen between the heights of particular peaks but the peak positions remain the same for powder and microtube samples of L- or D- diphenylalanine indicating the same crystal structure. Conversely, there are fewer diffraction peaks for Fmoc-diphenylalanine and the peaks appear in different positions to those for L- and D-diphenylalanine. This indicates that Fmoc-diphenylalanine has a different crystal structure to the chiral forms of diphenylalanine. The lattice structures of the peptides are studied in **Table 3.1**, **Table 3.2** and **Table 3.3**.

Most reflection planes recorded by XRD are the same for both L and D-diphenylalanine, with the exception of the (3,0,1) plane predicted and recorded only for L-diphenylalanine and the (4,-1,0) plane predicted and recorded only for D-diphenylalanine. A peak at 18.29° is predicted by the computer simulated diffractogram for L-diphenylalanine, based on the structure published by C. H. Görbitz [177]. Experimental results show that the peak is present for L-diphenylalanine powder but appears to be missing for the L-diphenylalanine microtubes. On closer inspection, the missing peak can be found as a shoulder of a more intense peak at 18.43°.

Table 3.1 Experimental XRD peak positions for L-diphenylalanine in powder and self-assembled forms. Peak positions are compared to peak positions calculated from published structure [178] and Miller indices are assigned to each peak. Peak positions for experimental data were measured manually using Origin

Sample XRD Peak Position (2θ)/ °			Miller Index	d-spacing (based on calculated values) /nm
LFF	LFFMT	Calculated	h,k,l	
7.36	7.38	7.32	2,-1,0	1.21
8.31	8.59	8.63	2,0,0	1.02
10.98	11.27	11.26	3,-1,0	0.79
12.71	12.80	12.77	3,0,0	0.69
16.64	16.75	16.81	1,0,1	0.53
17.81	17.78	17.80	2,-1,1	0.50
18.22	-	18.29	2,0,1	0.49
20.90	20.76	20.73	3,0,1	0.43
21.16	21.27	21.27	5,0,0	0.42

Table 3.2 Experimental XRD peak positions for D-diphenylalanine in powder and self-assembled forms.

Sample XRD Peak Position (2θ)/ °			Miller Index	d-spacing (based on calculated values) /nm
DFF	DFFMT	Calculated	h,k,l	
7.19	7.19	7.35	2,-1,0	1.20
8.35	8.63	8.56	2,0,0	1.03
11.07	11.26	11.36	3,-1,0	0.78
12.58	12.77	12.80	3,0,0	0.69
15.15	15.15	15.46	4,-1,0	0.57
16.84	16.80	16.82	1,0,1	0.53
17.85	17.73	17.88	2,-1,1	0.50
18.30	18.30	18.34	2,0,1	0.48
21.09	21.09	21.37	5,0,0	0.42

Table 3.3 Experimental XRD peak positions for Fmoc-diphenylalanine in powder and self-assembled forms.

Sample XRD Peak Position (2θ)/ °		Miller Index	d-spacing (based on calculated values) /nm
FmocFF	Calculated	h,k,l	
4.88	5.71	0,1,1	1.55
7.69	8.53	0,1,2	1.04
-	11.66	0,2,2	0.76
18.61	18.72	0,4,1	0.47
19.8	20.34	0,2,5	0.44
21.25	21.35	0,4,3	0.42
23.21	23.26	0,5,1	0.38

Comparison of the diffractograms recorded for microtube and powder forms of diphenylalanine shows that peak intensities in the range $2\theta < \sim30°$ are high and broadly similar, while in the range $2\theta > 30°$ intensities are lower, with the microtube intensities seemingly higher than those of the powders. This is undoubtedly associated with differences in morphology but the differences were not explored further in this work. It is also noticeable that for both L- and D- diphenylalanine samples, the peaks located at 2θ positions 7.36° and 8.31°, with Miller indices (2,-1,0) and (2,0,0) respectively, have lower intensity for the microtube samples than the powder samples.
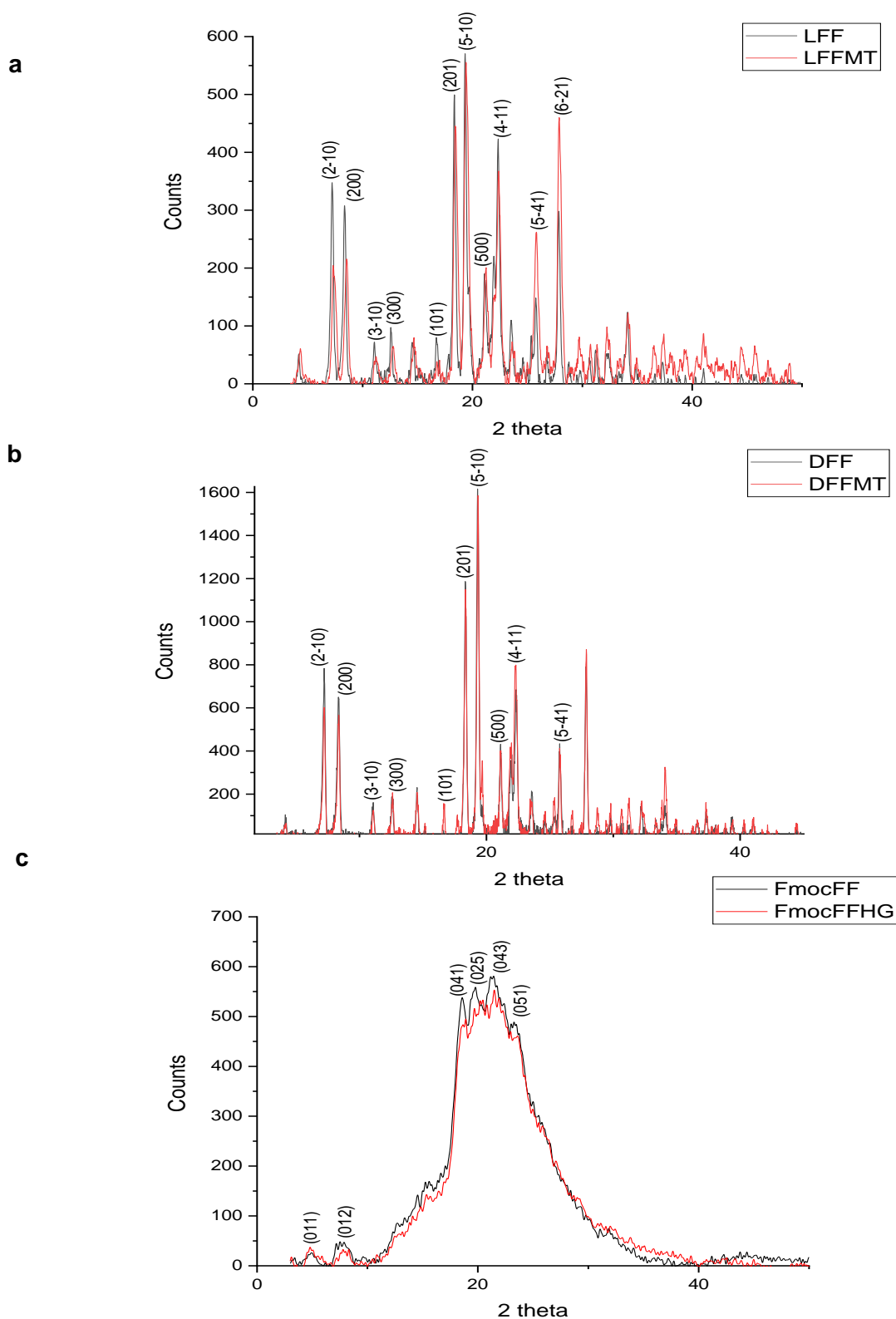
Figure 3.3 X-ray diffractograms of a) L-diphenylalanine in powder (black line) and microtube (red line) forms, b) D-diphenylalanine in powder and microtube forms, c) Fmoc-diphenylalanine in powder and hydrogel forms.

3.3.4.3. **Bond Structure of Diphenylalanine**

The bond structure of diphenylalanine materials were evaluated by attenuated total reflectance Fourier transform infrared spectroscopy (ATR-FTIR) and Raman spectroscopy. The application of ATR-FTIR yields spectra which display the characteristic absorption bands of bonds present in a molecule.

Powder samples of L-diphenylalanine, D-diphenylalanine and Fmoc-diphenylalanine powder were placed onto the stage of a Jasco FTIR 4200 instrument and imaged as described in Section 2.2.1.

The spectra of L-, D- and Fmoc-diphenylalanine are displayed in **Figure 3.4**. The L- and D-diphenylalanine spectra are essentially identical, even when studying the fingerprint region (400-600 cm^{-1}). This is expected considering the molecules are chemically identical and differ only in being enantiomers.

Strong absorption bands are observed for primary amine (N—H) and the (C=O) of amide I (C(=O)NH) functional groups while aromatic (C—C and C—H) bonds appear as absorption band groups (multiplets) in the spectra. A broad absorption band is also observed for the O—H functional group which is attributed to extensive hydrogen bonding between neighbouring diphenylalanine molecules. This band broadening masks the aliphatic C—H bond stretching band in the spectra for L- and D-diphenylalanine. Likewise, in the spectrum of Fmoc-diphenylalanine, the amide I peak visible in the spectra of L- and D-diphenylalanine, is indistinguishable due to broadening of the aromatic C—C peak group.

Since Fmoc-diphenylalanine has reduced hydrogen bonding capability, O—H broadening is not observed in the Fmoc-diphenylalanine FTIR spectrum. This allows the band arising from the C—H aliphatic bond (2970 cm^{-1}) to be clearly differentiated from the band arising from the C—H aromatic bond (3040 cm^{-1}). A full description of the vibrational modes and FTIR absorption band positions of L-, D- and Fmoc-diphenylalanine can be found in **Table 3.4**.
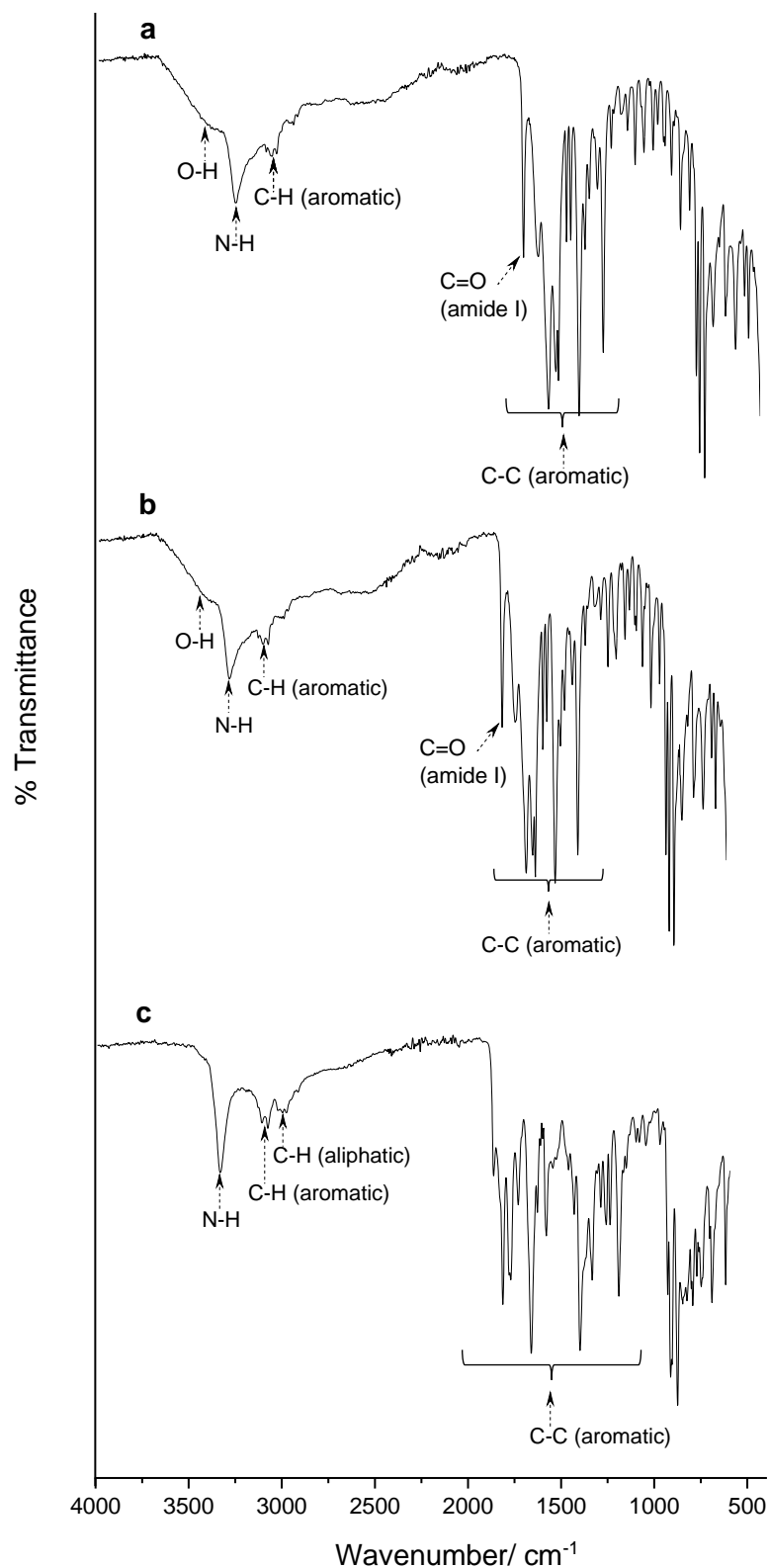
Figure 3.4 *Fourier transform infrared spectra for powder samples of a) L-diphenylalanine, b) D-diphenylalanine and c) Fmoc-diphenylalanine. Characteristic peaks of each molecule are labelled*

Table 3.4 Key vibrational modes and FTIR absorption band positions of L-, D- and Fmoc-diphenylalanine, as interpreted from the graph
* C—H aliphatic stretching band for L- and D-diphenylalanine is largely masked by the O—H stretching band.

	Wavenumber/ cm^{-1}		
Vibrational Mode	LFF	DFF	FmocFF
O-H stretching	3000-3500	3000-3500	-
N-H stretching	3250	3250	3300
C-H stretching (aliphatic)	2950*	2950*	2950
C-H stretching (aromatic)	3010-3080	3010-3080	3010-3080
C=O stretching (amide I)	1686	1686	-
C-C stretching (aromatic)	1300-1600	1300-1600	1000-1800

Raman spectroscopy provides data complementary to that obtained by FTIR, including information related to low polarity bonds and aromatic systems that are less infrared active.

Powder samples of the diphenylalanine materials (LFF, DFF and FmocFF) were configured for Raman spectroscopy by placing a small quantity of sample on a horizontal glass microscope slide, which was then levelled by applying a second microscope slide to create a sandwich, rotating the second slide around the vertical axis to create a circular region of approximately uniform thickness. The sample was then imaged in a Renishaw inVia Raman microscope. The settings of the Raman microscope are detailed in 2.2.2.

The Raman spectra for L-, D- and Fmoc-diphenylalanine are shown in **Figure 3.5** below. The majority of diphenylalanine Raman spectrum peaks occur due to scattering from the C—H and C—C bonds in the ring structures of the peptide molecules. This is confirmed by literature [179]. The key peak positions and their corresponding bonds can be found in **Table 3.5**.
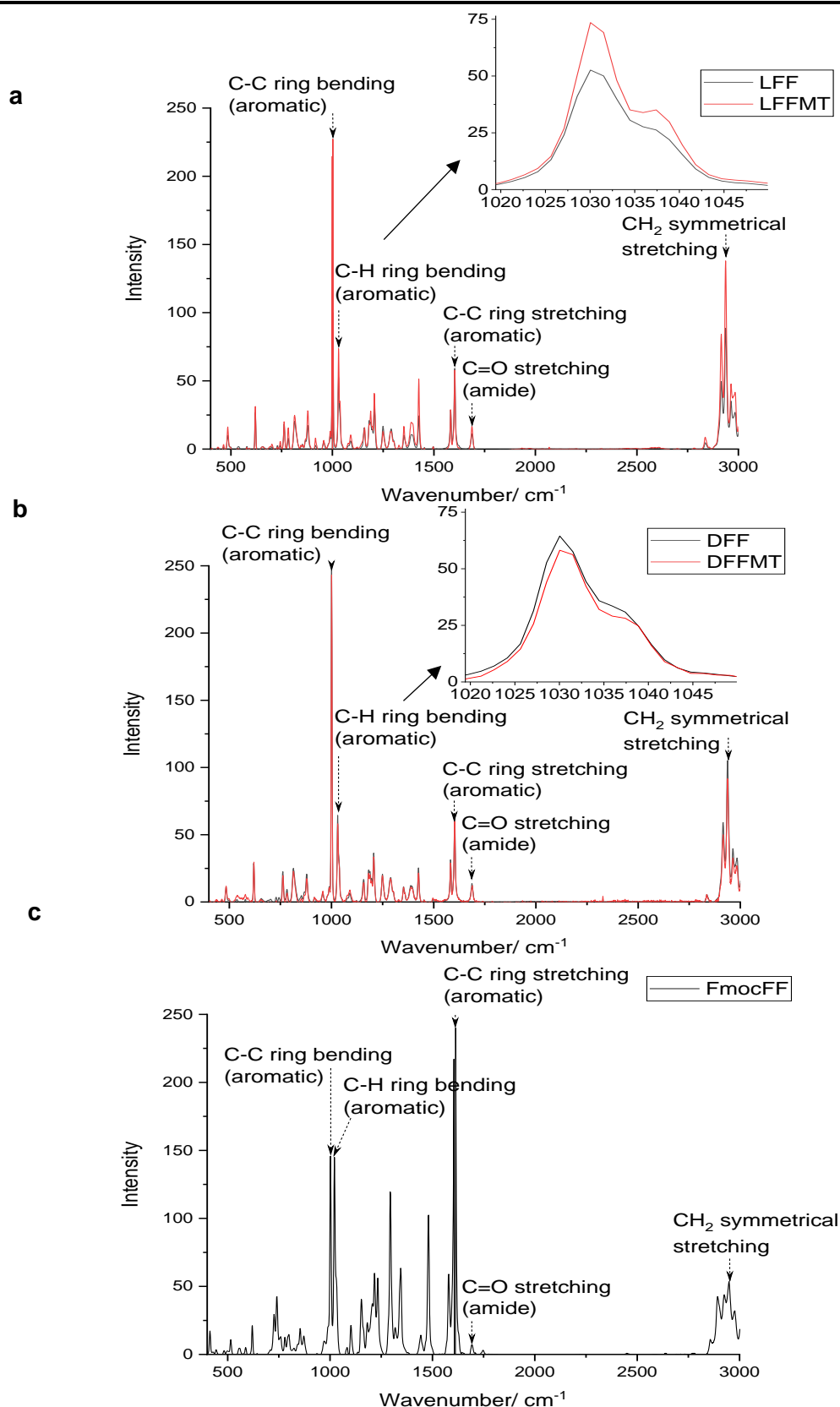
Figure 3.5 *Raman spectra of a) L-diphenylalanine and b) D-diphenylalanine in powder (black line) and microtube (red line) form and c) Fmoc-diphenylalanine in powder form. Inserts show an enlarged view of peak splitting which occurs at ~1032 cm^{-1}.*

For the spectrum of Fmoc-diphenylalanine, many of the peaks corresponding to the same bond vibrations are more intense than those seen for L- and D-diphenylalanine, particularly the ring stretching peak at ~1600 cm^{-1}.

The inserts shown in **Figure 3.5a** and **Figure 3.5b** allow closer inspection of the peak at 1032 cm^{-1}. This peak is a doublet, with more pronounced separation observed for LFFMT.

Table 3.5 Table showing key characteristic Raman spectrum peak positions of L-diphenylalanine, D-diphenylalanine and Fmoc-diphenylalanine

	Wavenumber/ cm^{-1}		
Vibrational Mode	LFF	DFF	FmocFF
C-H stretching (aliphatic)	2985	2982	2973
CH$_2$ symmetrical stretch	2937	2939	2949
O=C stretching (amide)	1689	1689	1695
C-C ring stretching (aromatic)	1603	1604	1608
C-H ring bending (aromatic)	1032	1031	1024
C-C ring bending (aromatic)	1002	1001	1002

3.3.4.4. **Comparison of Diphenylalanine Chiral Enantiomers**

Circularly polarised light was passed through samples of L- and D-diphenylalanine and a racemic mixture of the two enantiomers to evaluate their chirality. The secondary structure of the peptide was also determined and used to gain insight into the peptide folding process that occurs during self-assembly.

Diphenylalanine microtubes were assembled by the steps detailed in Section 3.3. A suspension of mixed chirality microtubes was also prepared from a 50:50 mixture of L- and D- diphenylalanine. The mixed chirality microtubes were prepared by dissolving 50 mg each of L-diphenylalanine and D-diphenylalanine in 1 ml HFIP. The solution was left to stand for 10 mins before adding 2 ml deionised water.

All the peptide microtube suspensions were diluted to 50 ml with deionised water to yield a diphenylalanine concentration of 2 mg ml^{-1}. The suspensions were diluted to a final concentration of 0.08 mg ml^{-1} shortly before measurement to avoid structural rearrangement of the diphenylalanine microtubes.

The samples were transferred to quartz cuvettes and scanned using a Jasco J-720 circular dichroism (CD) spectrometer as described in Section 0.

The CD spectrum for diphenylalanine shows three distinct peaks, similar to those reported for helical structures, such as β-turns [180]. Circular dichroism spectra showing the expected peaks for α-helix, β-turns and β-sheet structures are shown in **Figure 3.6a** and the CD spectra of L and D-diphenylalanine are shown in **Figure 3.6b**. A table of peaks for common secondary structures and experimentally obtained data is found in **Table 3.6**. A comparison of the figures and peak positions shows that the spectra for L- and D-diphenylalanine match the β-turn structure within a tolerance of 2 nm. The spectra for L- and D-diphenylalanine are almost perfect mirror images, reacting to the circularly polarised light in opposite ways, as is expected for optical isomers. The CD spectrum for a hybrid material produced from a racemic mixture of L and D diphenylalanine is also shown in **Figure 3.6b** and shows that the presence of both enantiomers cancels the chiral response observed for microtubes formed from single chirality solutions. The formation and morphology of this hybrid material will be discussed in a later section.

Table 3.6 Table of characteristic circular dichroism wavelengths of common secondary structures (from R. Eaton and K. Thalassinos) and L- and D- diphenylalanine microtubes. For the preparations in this work, the sign before the wavelength indicates whether the peak extends above or below the x-axis.

Secondary Structure	Sign (+/-) and Wavelength/ nm		
α-helix	+195	-208	-222
β-turn	-190	+200-205	+220-230
β-sheet		+195-200	-210-220
Random coil		-199	-225
L-diphenylalanine	-189	+198	+218
D-diphenylalanine	+189	-198	-218

a

b
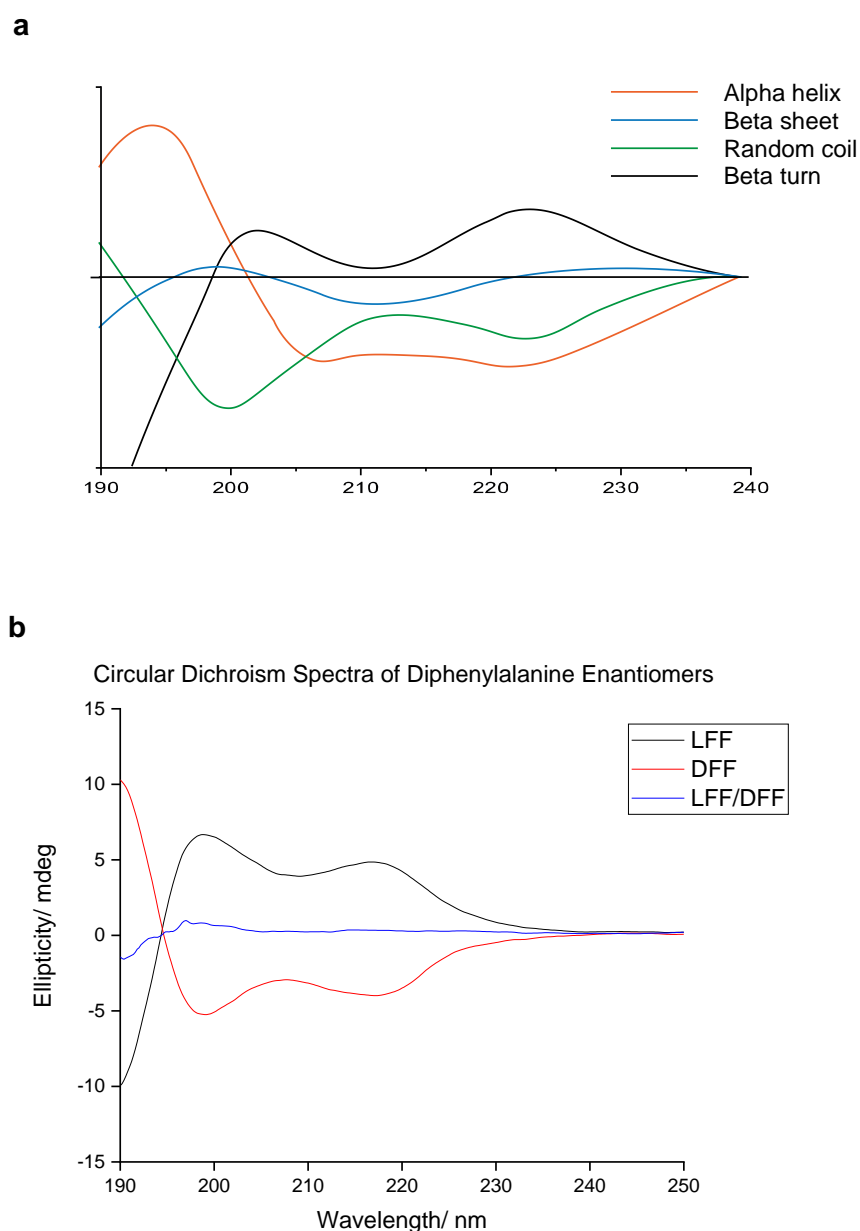
Figure 3.6 Circular dichroism spectra showing a) Characteristic CD spectra for different secondary structures of peptides and proteins, reprinted from R. Eaton and K. Thalassinos, b) L-diphenylalanine microtubes (black), D-diphenylalanine microtubes (red) and a racemic mixture of L and D-diphenylalanine microtubes (blue)

3.3.4.5.   **Diphenylalanine Nanoscale Mechanical Properties**

Atomic force microscopy was used to determine the nano-mechanical properties of the diphenylalanine microtubes. The microtubes were prepared using the method described in Section 3.3.2 and the suspension tipped into a petri dish. The solvent was then allowed to evaporate under ambient conditions. The samples were then mounted onto Tempfix according to the following procedure:

129

Slices of Tempfix (Agar Scientific, AG16219) were placed onto AFM discs and heated to 40 °C on a hotplate to melt the polymer. This provided a medium in which diphenylalanine microtubes could be immobilised for further characterisation. Dried diphenylalanine microtubes were then partially embedded in the Tempfix and cooled to set, leaving the upper portions of the microtubes exposed to the cantilever tip.

The surface moduli of samples were measured using methods described in Section 2.2.11. These measurements were made and the analysis performed by Dr. Richard Thorogate, Laboratory and Research Manager at the London Centre for Nanotechnology. The information returned was limited to numerical values of the surface moduli.

The measured surface moduli for L-, D- and LL,DD-diphenylalanine microtubes are detailed in **Table 3.7**.

Table 3.7 Surface modulus of L-diphenylalanine (n= 15) and D-diphenylalanine (n= 14) microtubes and LL,DD- diphenylalanine hybrid structures (n= 21) measured by AFM

Sample	Surface Modulus/ GPa	SD +/-
LFF	6.59	2.30
DFF	6.80	1.91
LL,DD-FF	8.17	1.60

3.3.5. **Seeded Epitaxy of Diphenylalanine Nanotubes**

In this chapter, the self-assembly of diphenylalanine into hexagonal microtubes has been discussed. However, microtubes formed in solution are randomly oriented and, as an aggregate, would be unlikely to show any directional piezoelectric effect. In an attempt to address this, diphenylalanine microtubes were grown under controlled conditions from a starting droplet of diphenylalanine solution deposited on a substrate. The expectation was that aligned microtubes would grow from the starting crystals on the substrate surface. This was based on what was – in hindsight – a false interpretation of the mechanism by which a method reported elsewhere worked. That method [44] used rapid evaporation of a droplet of HFIP from a solution containing diphenylalanine, where the surface tension of the droplet would assist in the orientation of the nanotubes as they were deposited from solution. This interpretation was used to design an experiment in which the self-assembly from solution would be effected partly by the propensity of HFIP to quickly evaporate from a droplet and from the addition of

water through vapour transport to the droplet from a water bath over which the droplet
was suspended. In the event this thinking was over-elaborate, the experiment
succeeded.

A seed layer of L-diphenylalanine was used as the starting point for epitaxial growth. A
volume of 60 µl diphenylalanine solution in HFIP (100 mg ml^{-1}) was drop coated directly
onto a scanning electron microscopy (SEM) stub mounted on the inside of a petri dish
lid **Figure 3.7**. The droplet was left to stand for 15 s to allow some of the solvent to
evaporate. The lid and SEM stub were then inverted and placed onto an empty petri
dish. The dish was sealed with parafilm to slow down evaporation and 4 ml deionised
water was added to the petri dish through a smaller, secondary hole in the lid, using a
22-gauge needle. The water level was ~ 3 mm away from the stub surface. The petri
dish was left to stand for 18 h to facilitate microstructure formation and the syringe was
kept in place to slow down evaporation further. After 18 h, the SEM stub was removed
from the petri dish and dried in air at 20 °C for 30 mins before being sputter coated with
a layer of gold (20 mA, 120 s). The sample was stored in an SEM box until imaging and
were examined under SEM as described in Section 2.2.9..
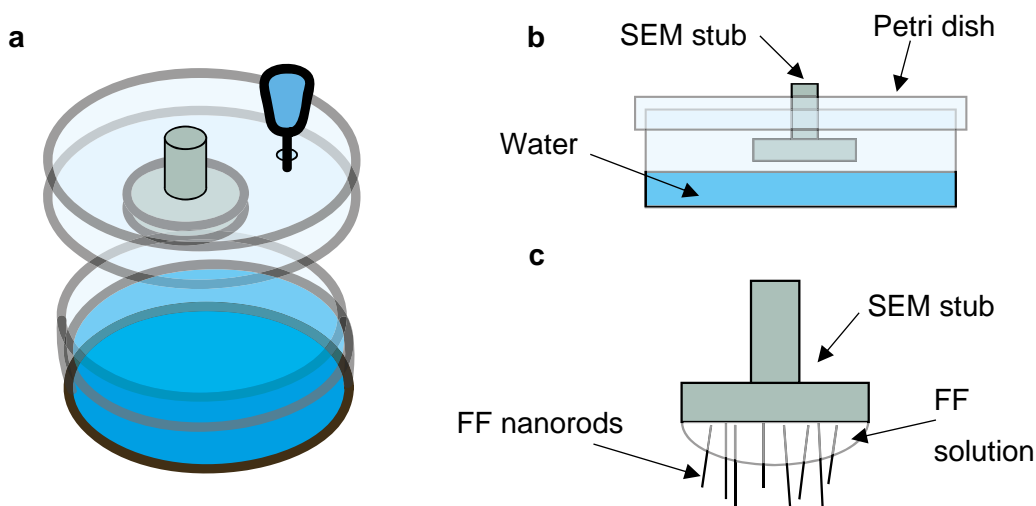
Figure 3.7 *Diagram of setup for epitaxial growth of aligned diphenylalanine (FF)
nanostructures. a) Representative diagram of epitaxial growth system, b) annotated
cross section of epitaxial growth system, c) Annotated diagram of diphenylalanine
nanorods growing from diphenylalanine seed layer and inverted diphenylalanine
solution.*

The SEM image in **Figure 3.8a** depicts the starting diphenylalanine seed layer and the aligned diphenylalanine nanorods by epitaxial growth are shown in **Figure 3.8b**. These solid, filled structures differ from the hollow microtubes that formed under the conditions described in Section 3.3.2.
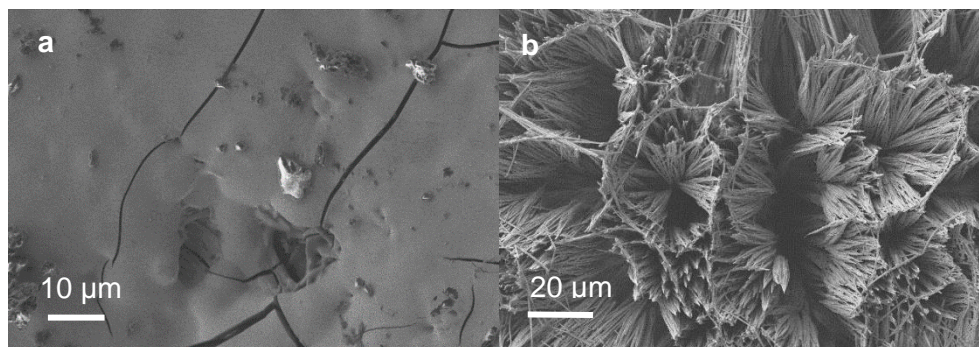
Figure 3.8 *Scanning electron micrographs of a) diphenylalanine deposited from solution as a seed layer for epitaxial growth b) diphenylalanine nanorods produced by epitaxial growth from a diphenylalanine seed layer on an SEM stub*

3.3.6. Templated Growth of Diphenylalanine Nanotubes

Anodised aluminium oxide (AAO) templates are porous honeycomb structures that can be used as templates for nanofabrication. Anodised aluminium oxide templates with a pore size of 200 nm were used to direct the growth of diphenylalanine nanostructures. A solution of L-diphenylalanine (100 mg ml^{-1}) was prepared and transferred to a small petri dish. Alongside this, an AAO template was sputter coated with gold (60 mA, 240 s). The gold-coated AAO template was placed briefly into deionised water, then placed onto the surface of the solution with the gold side down. The template floated briefly before sinking to the bottom of the solution. The petri dish was sealed with parafilm and left to stand for 18 h.

After 18 h, the template was removed from the petri dish and dried on filter paper for 30 mins before being coated with another layer of gold (20 mA, 120 s). The sample was stored in a clean lidded petri dish until imaging.

A growth mechanism dominated by aromatic interactions was originally suggested by Reches and Gazit [44] for the self-assembly of diphenylalanine nanotubes in the absence of water. The limited water in the system and geometric restrictions imposed by the

AAO template, was postulated to cause a reduction in hydrogen bonding. As a result, it is likely that the microtube formation was dominated by aromatic stacking in the direction of the growth axis (along the length of the AAO template pore).

The self-assembly of diphenylalanine based on the confines of an anodised aluminium oxide template (**Figure 3.9a**) produced vertically oriented diphenylalanine nanotubes, seen in **Figure 3.9b**. The SEM image shows that the nanotubes self-assembled into a range of sizes (Ø ~ 400 nm – 2 μm) and the hexagonal structure is somewhat disrupted. This could influence the piezoelectric properties of the array since the hexagonal forms of diphenylalanine have been shown to display the greatest piezoelectric response.
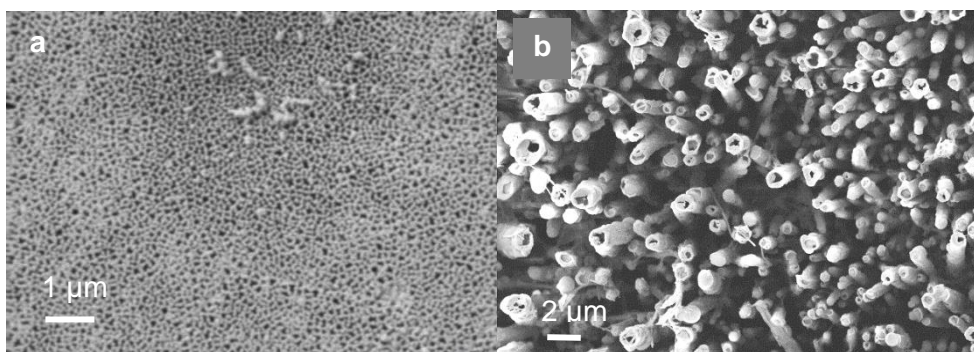
Figure 3.9 *Scanning electron micrographs of a) anodised aluminium oxide template of pore size 200 nm, b) diphenylalanine nanotubes self-assembled on an anodised aluminium oxide template*

3.3.7. **Controlled Growth of Diphenylalanine Microtubes**

In crystallography, it is well understood that many factors can affect the habit and size of crystals. In the case of diphenylalanine crystallisation, initial solution concentration, temperature and solvent choice can greatly affect whether diphenylalanine will form crystals and the characteristics of the crystals formed. The impact of preparative conditions on diphenylalanine crystallisation are discussed in the following sections. Diphenylalanine microtubes were grown at different temperatures, and under acidic and basic conditions [181].

Effect of Temperature on Diphenylalanine Microtube Self-assembly

Diphenylalanine self-assembly at different temperatures has previously been
demonstrated by Huang *et al.* [41, 43] and aspects of their method were adapted to
develop the procedure to follow.

Three samples of 100 mg L-diphenylalanine dissolved in 1 ml HFIP were prepared and
then heated or cooled to different temperatures (40 °C, 25 °C and 0 °C). The solutions
were maintained at their respective temperatures for 20 mins while aliquots of
deionised water were warmed or cooled to temperatures corresponding to the peptide
solutions. After 20 mins, water at the same temperature as the peptide solution was
added in 200 µl aliquots up to 2 ml and then made up to 4 ml. Upon the addition of
water, diphenylalanine microtubes crystallised from the solution. Microtube precipitation
was observed until approximately 5 mins after the initial addition of water. The samples
were left to stand at their respective temperatures for 10 mins after the addition of
water before being transferred to microscope slides and inspected under a light
microscope.

Microtubes were deposited onto microscope slides using a modified pipette with a wide
opening to minimise microtube damage. The microtubes were imaged using an Evos
XL Core inverted microscope with a x10 objective lens. The lengths of a sample of 50
microtubes were measured in FIJI image processing software.

The modal length of 50 microtubes formed at different temperatures followed the trend
40 °C > 25 °C > 0 °C. The histograms seen in **Figure 3.10** show that there is a skewed
distribution between the microtube lengths seen at each experimental temperature and
that there is some overlap in the microtube lengths observed at all three temperatures.
The maximum represents the position of the mode microtube length at each
temperature. The range of microtube diameters increases with increasing temperature,
as shown in **Figure 3.11**, although the majority of microtube diameters are measured
to be between 5 and 15 µm for all temperatures measured. A summary of the
microtube lengths and diameters is shown in **Table 3.8**.

Table 3.8 Maximum, minimum and modal lengths and diameters of L-
diphenylalanine microtubes grown at different temperatures

	Preparation temperature/ °C	0	20	40
Length/ µm	Min	73.5	132.8	165.5
	Max	352.5	1198.6	2025.7
	Mode	150.0	300.0	700.0
Diameter/ µm	Min	2.2	2.9	4.6
	Max	12.3	23.5	51.1
	Mode	5.5	8.8	10.0
Modal ratio l/d	-	27.3	34.1	70.0

a

Distribution of L-diphenylalanine microtube lengths at 0 degrees C

b

Distribution of L-diphenylalanine microtube lengths at 20 degrees C

c

Distribution of L-diphenylalanine microtube lengths at 40 degrees C
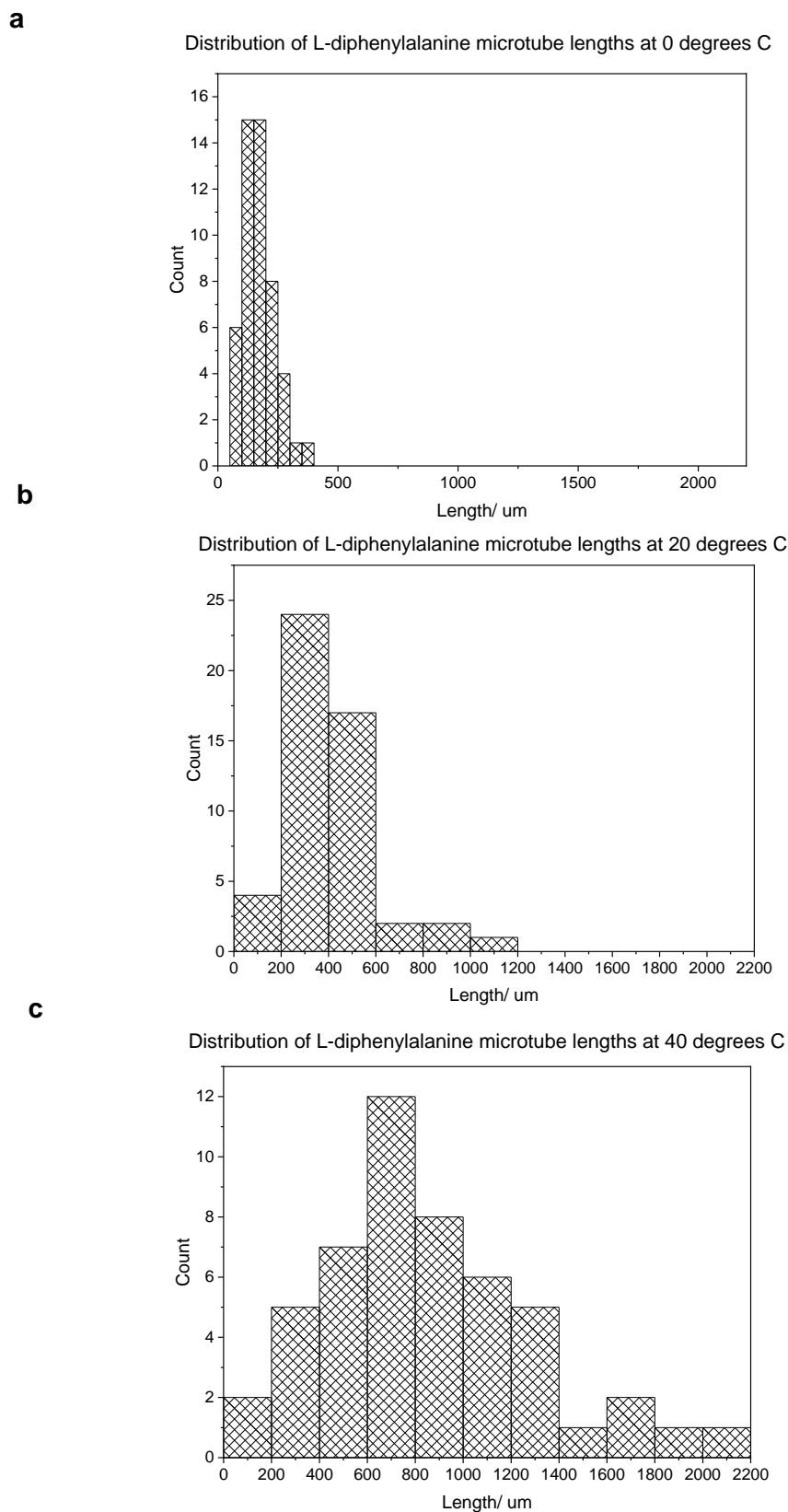
Figure 3.10 *Histograms showing the length distributions of L-diphenylalanine microtubes prepared at a) 0 °C, b) 20 °C, c) 40 °C.*

a

Distribution of L-diphenylalanine microtube diameters at 0 degrees C

b

Distribution of L-diphenylalanine microtube diameters at 20 degrees C

c

Distribution of L-diphenylalanine microtube diameters at 40 degrees C
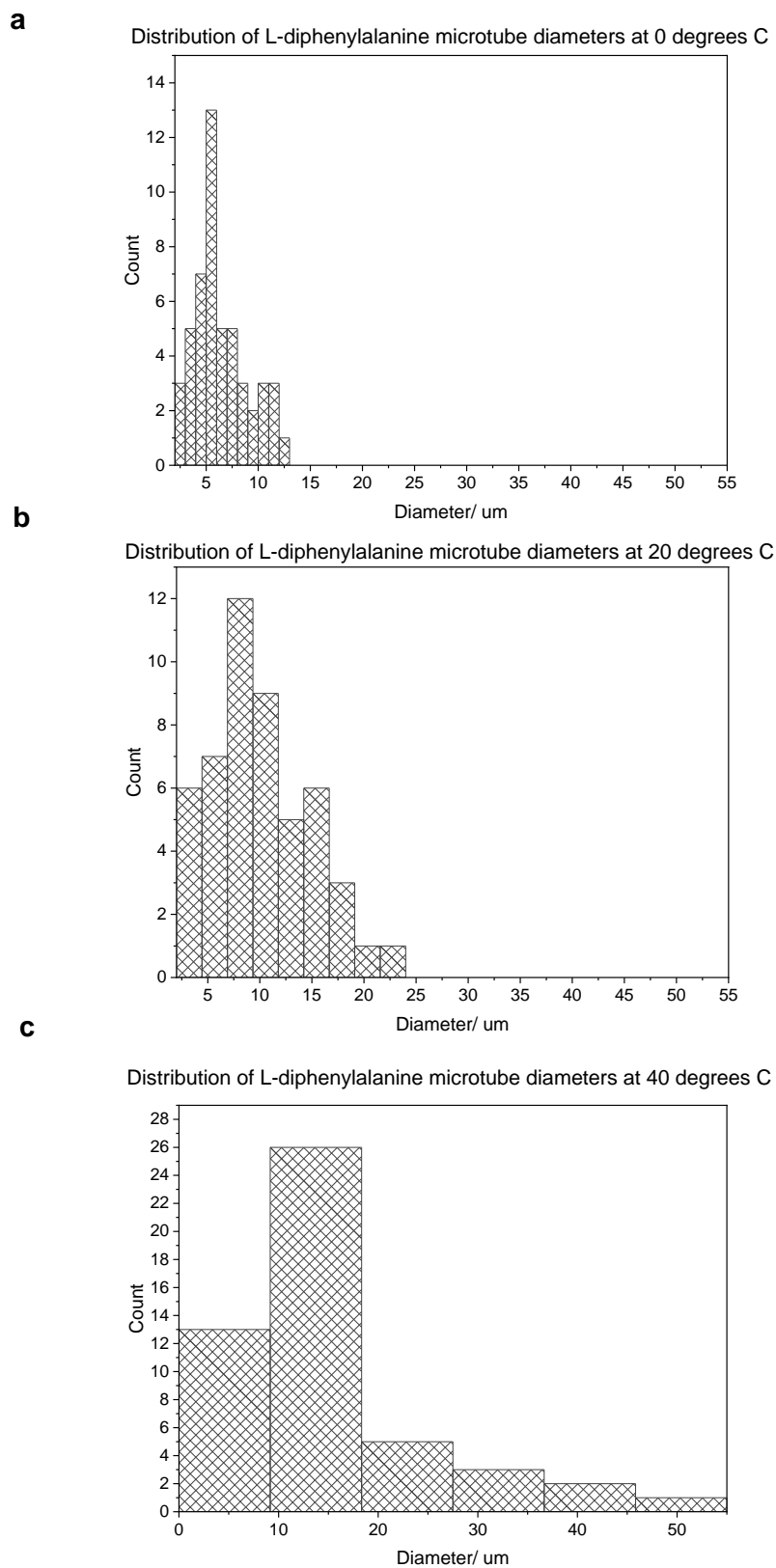
Figure 3.11 *Histograms showing the diameter distributions of L-diphenylalanine microtubes prepared at a) 0 °C, b) 20 °C, c) 40 °C.*

Effect of pH on Diphenylalaine Microtube Self-assembly

Disruption of hydrogen bonding in a diphenylalanine solution was expected to interrupt the self-assembly process due to the protonation or deprotonation of the amine or carboxyl terminus respectively. The pH of diphenylalanine solutions was changed to measure the effect on diphenylalanine self-assembly.

A solution of diphenylalanine was prepared with a concentration of 100 mg ml^{-1}. Three 200 µl aliquots of the diphenylalanine solution were placed in separate vials and a total of 400 µl of either aqueous hydrochloric acid ($HCl_{(aq)}$), aqueous sodium hydroxide ($NaOH_{(aq)}$) or deionised water was added to each vial [182]. The pH of each liquid or suspension (diphenylalanine solution, HCl, NaOH, H_2O and combinations of the above) was measured using universal indicator paper. The vials were then sealed for 18 h to facilitate microtube formation.

The experiment was conducted once under these conditions, following a preliminary experiment under similar conditions. The photographs in *Figure 3.12* show solutions/ suspensions of diphenylalanine after the addition of water, HCl or NaOH. It is observed that the only solution which was able to form microtubes was the solution at pH 7, after the addition of water. The solutions to which HCl or NaOH were added showed no microtube formation. Before the addition of any precipitating solvent, each original solution of diphenylalanine in hexafluoroisopropanol (HFIP) had a pH of 5. After the addition of the acid, the solution became more acidic, immediately changing to pH 2. Conversely, upon the addition of the first 200 µl of NaOH, the pH of the solution increased to 9 before reaching a pH of 10 on addition of the second 200 µl aliquot.
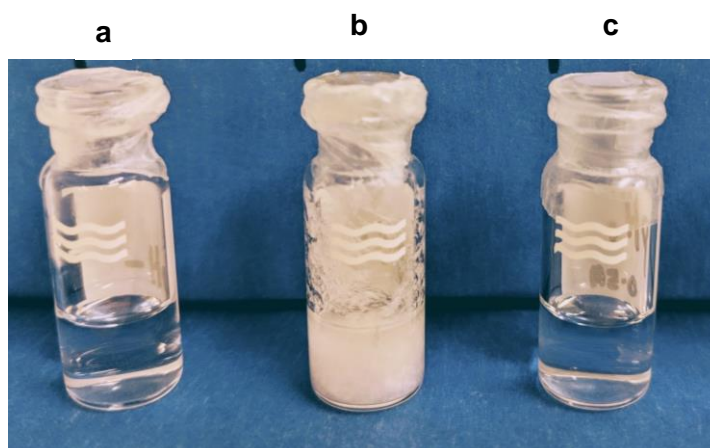
d	Solvent added	HCl (aq)	Deionised water	NaOH (aq)
	pH of diphenylalanine solution	5	5	5
	pH of solvent	1.5	6.8	13
	pH after solvent addition	2	7	10

Figure 3.12 Photographs of attempted diphenylalanine microtube formation by the addition of a) HCl, b) deionised water, c) NaOH. Precipitation was attempted from diphenylalanine dissolved in HFIP. d) Table showing the pH of the solvents added and their effect on the final pH of the diphenylalanine suspension/ solution

3.3.8. Self-Assembly of a Mixed Chirality Diphenylalanine Hybrid

As previously reported and described in Section 3.3.2, L- or D-diphenylalanine self-assembles into hexagonal habit microtubes when dissolved in HFIP and subsequently exposed to water. A search for the self-assembly behaviour of a racemic mixture of L- and D-diphenylalanine did not immediately yield any reports in the literature. In this work, L- and D-diphenylalanine were dissolved in HFIP to create a racemic mixture and precipitated in the same way as single chirality solutions. The morphology of the obtained crystals was studied by scanning electron microscopy.

It can be seen from the SEM images in **Figure 3.13** that a number of different structures can be formed with the same 1:1 ratio of L:D diphenylalanine in solution. It can also be seen that the hybrid microtubes appear to lose their rigid hexagonal

structure and become curved, a feature which is not seen for L or D assemblies. The formation of mixed microrods and microribbons was observed in addition to the formation of microtubes, although the experimental conditions were the same. The physio-chemical properties were not investigated.
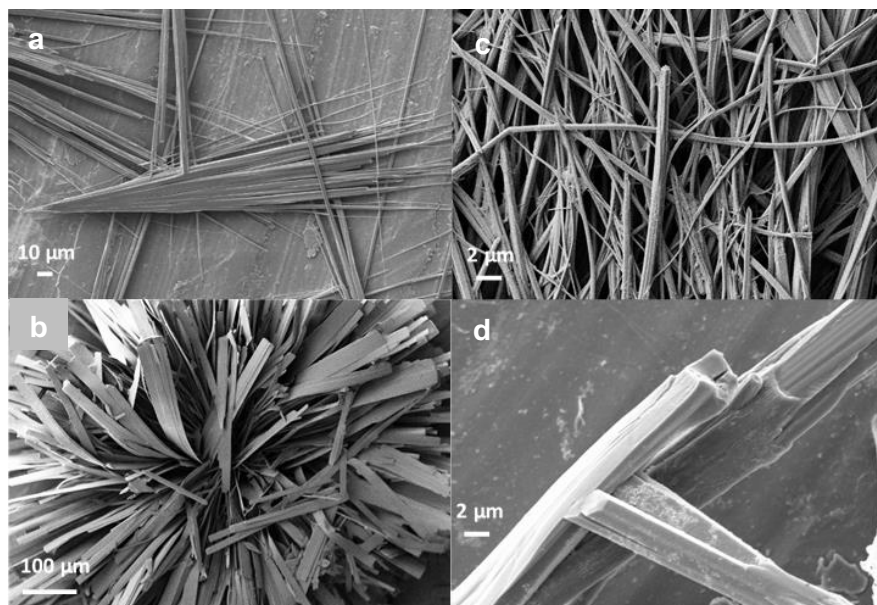
Figure 3.13 *Scanning electron micrographs of L- and D-diphenylalanine hybrid self-assembled structures. The structures were precipitated when water was added to a racemic mixture of L- and D-diphenylalanine dissolved in hexafluoroisopropanol. a) Diphenylalanine microneedles, b) Diphenylalanine microribbons, c, d) Curved diphenylalanine microstructures*

3.4. Piezoelectric Polymeric Nanofibres: Poly[Vinylidene Fluoride-co-Trifluoroethylene]

Poly[vinylidene fluoride-co-trifluoroethylene] is a block copolymer comprising repeating units of PVDF covalently linked to repeating units of TrFE. The polymer can be synthesised to contain different ratios of TrFE and the percentage of TrFE in the copolymer directly affects the Curie Temperature – the temperature above which a piezoelectric material becomes depolarised and loses its piezoelectric properties.

The Curie Temperature of PVDF-TrFE decreases as the TrFE percentage increases, causing copolymers with a high TrFE percentage to become depolarised at a lower temperatures. The PVDF-TrFE used in this work contains 25% TrFE, resulting in a Curie temperature of 110 °C.

3.4.1. **Electrospinning of Piezoelectric Poly[Vinylidene Fluoride-co-Trifluoroethylene] Nanofibres**

The preparation of randomly oriented and aligned PVDF-TrFE electrospun fibres was carried out by Viola, Chang and Jomaa at UCL. It is included here to provide a comparison to diphenylalanine as a potential piezoelectric component in an implantable device.

In the procedure used by Viola, Chang and Jomaa, PVDF-TrFE copolymer powder was dissolved in DMF to produce solutions with concentrations of 12%, 16%, 20% and 24% by weight. The polymer was dissolved in 3 ml DMF each time and stirred on a hotplate at 70 °C for 2 h to ensure homogeneity. The solution was then cooled to 20 °C and 2 ml acetone added to facilitate electrospinning. The electrospinning equipment used for the experiments in this project was comprised of a custom-built electrospinning box, flow rate control pump, high voltage power supply and 2 steel rods. These parts and their setup are depicted in **Figure 3.14**.

Random and Aligned Fibres

Randomly oriented and aligned fibres were separately spun using the setup shown in **Figure 3.14a** and **Figure 3.14b** respectively, which was custom built for the laboratory. For the aligned fibres, the steel rods were electrically earthed using copper wire to improve the electric field and the distance between the steel rods was kept constant, as shown in **Figure 3.14c**.

Fibres were spun for 30 min intervals inside an electrospinning unit from an 18-gauge needle at a distance of 18 cm from the metal plate below. The voltage between the needle and the plate was set to 20 kV.
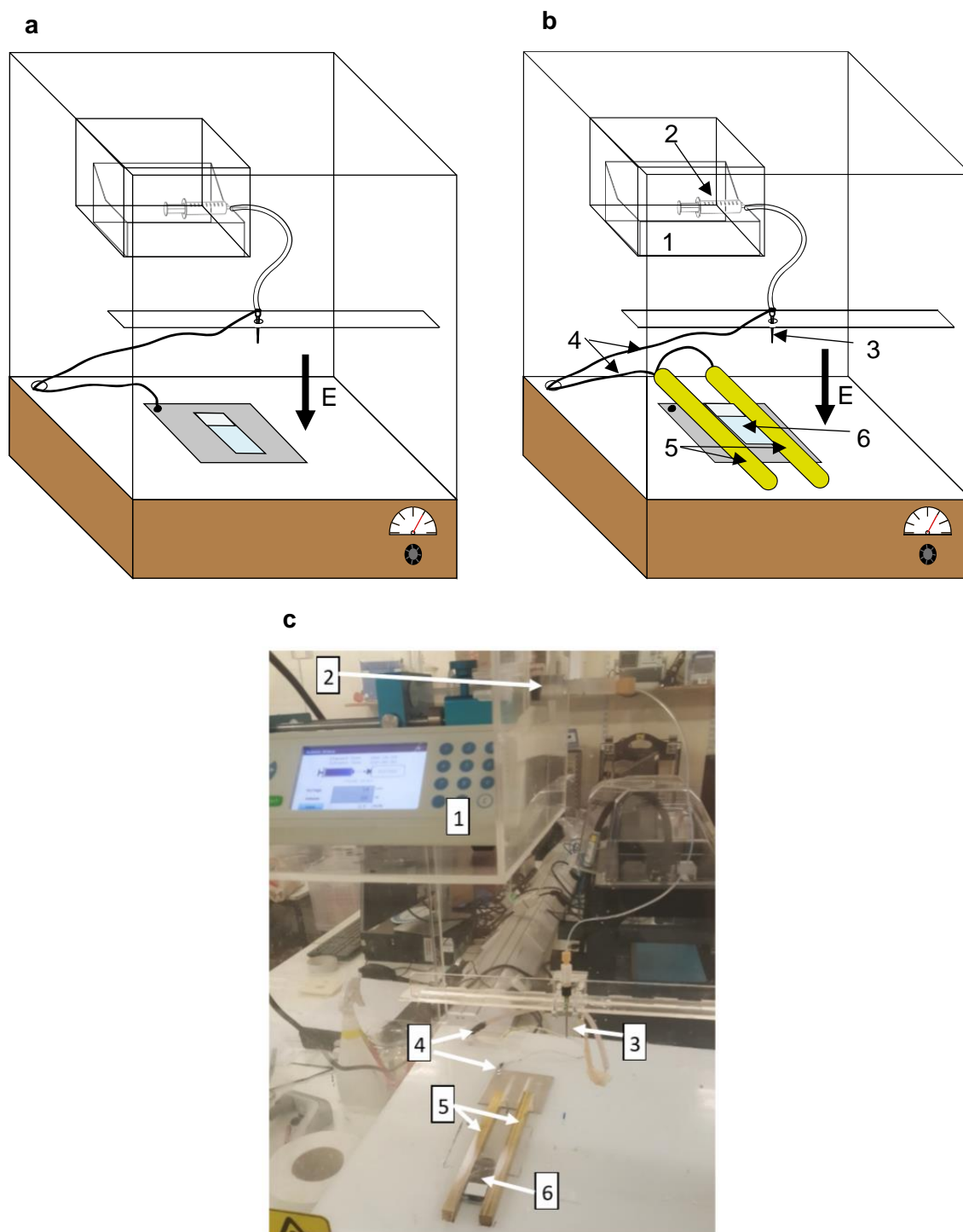
Figure 3.14 *Electrospinning setup a) setup for spinning random fibres, b) setup for spinning aligned fibres. Distance between steel rods = 8 cm, c) photograph of electrospinning setup.*

1) flow rate control pump, 2) syringe containing polymer solution, 3) needle connected to high voltage power supply, 4) high voltage power supply, 5) parallel iron bars to facilitate the production of aligned fibres, 6) microscope slide for the collection of electrospun fibres

3.4.2. Physical and Chemical Properties of Electrospun PVDF-TrFE Nanofibres

PVDF-TrFE nanofibres were electrospun in a static electric field set up between a needle and two earthed steel rods, using the parameters described in Section 3.4.1. The nanofibres were characterised to determine the molecular arrangement of polymer molecules within the fibres. The piezoelectric properties, mechanical properties, and macroscale alignment of the fibres were also investigated. Polarised FTIR measurements were performed by Viola and Chang. Piezoresponse force microscopy and surface modulus measurements were completed by Jomaa. I carried out the observations by SEM.

3.4.2.1. Determination of Molecular Alignment in PVDF-TrFE Electrospun Nanofibres

Samples of electrospun nanofibres for polarised FTIR were prepared on glass coverslips and imaged using a Jasco FTIR 4200 instrument, equipped with a Jasco PL-82 polariser. Spectra were recorded between 600- 1600 cm^{-1}.

Polarised FTIR was used to characterise the molecular alignment within the electrospun fibres and thus determine the poling direction of the C-F bonds. Scanning electron microscopy was used to determine the average fibre diameter.

Polarised FTIR measurements were made at 0° and 90°. The results for fibres made from 16%, 20% and 24% polymer solutions are shown in **Figure 3.15**. Polarised FTIR measurements for fibres made from 12% solution were inconclusive, likely due to the fibres being too sparse to obtain a precise reading.

Polarised FTIR measurements for PVDF-TrFE electrospun fibres show characteristic absorption bands of the copolymer, as shown in **Table *3.9***. The bands at 1284 cm^{-1} and 1245 cm^{-1} in particular, are exclusive to the β and γ phases, while bands only seen for the α phase are absent from the spectrum [183]. The absence of α phase bands (for instance at 975 cm^{-1} and 1209 cm^{-1}) allows the presence of the α phase in the fibres to be ruled out with a certain degree of confidence. The remaining peaks in the spectrum are observed for all phases of PVDF-TrFE. It is seen that rotating the polariser through 90° causes the intensity of some peaks to become diminished or enhanced, most notably the peaks at 1398 cm^{-1}, 1284 cm^{-1} and 1076 cm^{-1}, confirming that there is some molecular alignment within the fibres. Some differences are also observed for the peak

at 1428 cm^{-1}, although this is likely due to the peak being absorbed into a more intense
peak at 1398 cm^{-1}.
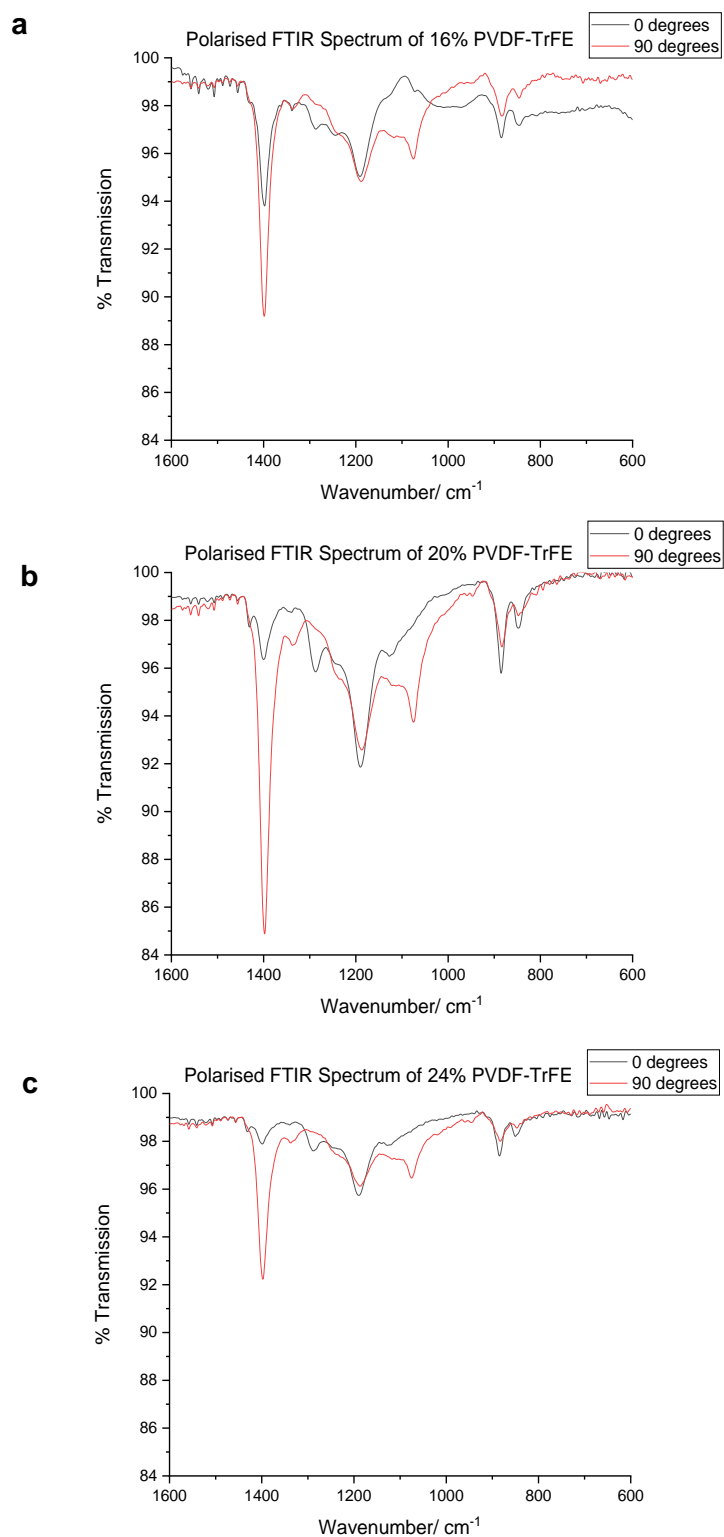
Figure 3.15 *Polarised Fourier transform infrared spectra of different concentrations
of PVDF-TrFE electrospun fibres taken at polarisation angles of 0° (black line) and
90° (red line). a) 16%, b) 20%, c) 24%*

Table 3.9 Key vibrational modes, positions and intensity ratios of polarised FTIR absorption bands for 16%, 20% and 24% PVDF-TrFE electrospun nanofibres. Ratios below 1 represent absorption peaks which are more intense at 0° than 90° and ratios above 1 represent absorption peaks which are more intense at 90° than 0°.

		0°: 90° intensity ratio		
Vibrational Mode	Wavenumber/ cm^{-1}	16%	20%	24%
F-C-F symmetric stretching	845	0.99	0.99	1.00
F-C-F asymmetric stretching	882	0.99	0.99	0.99
F-C-F wagging	1076	1.03	1.04	1.02
F-C-F asymmetric stretching	1185	1.00	0.99	1.00
F-C-F asymmetric stretching	1245	1.00	1.00	1.00
F-C-F symmetric stretching	1284	0.97	0.96	0.98
C-H wagging	1398	1.05	1.14	1.06
C-H wagging	1428	1.00	0.98	0.98

3.4.2.2. Morphology of PVDF-TrFE Electrospun Nanofibres

PVDF-TrFE nanofibres were electrospun onto 12 mm diameter glass coverslips. The coverslips were fixed to SEM stubs using carbon tape and samples were sputtered with gold (20 mA, 120 s) prior to imaging.

Samples were imaged in a Zeiss Evo SEM at a voltage of 9 kV. Multiple (>3) micrographs of different locations in the sample were captured for each sample at a magnification range of 500x – 24,000x. The displayed micrographs in **Figure 3.16** are representative of the samples imaged.

The diameters of the electrospun fibres were measured from SEM images, using FIJI image processing software. The micrographs show that there was some variation in fibre diameter between concentrations, with fibre diameters falling within the range of ~300 – 700 nm.
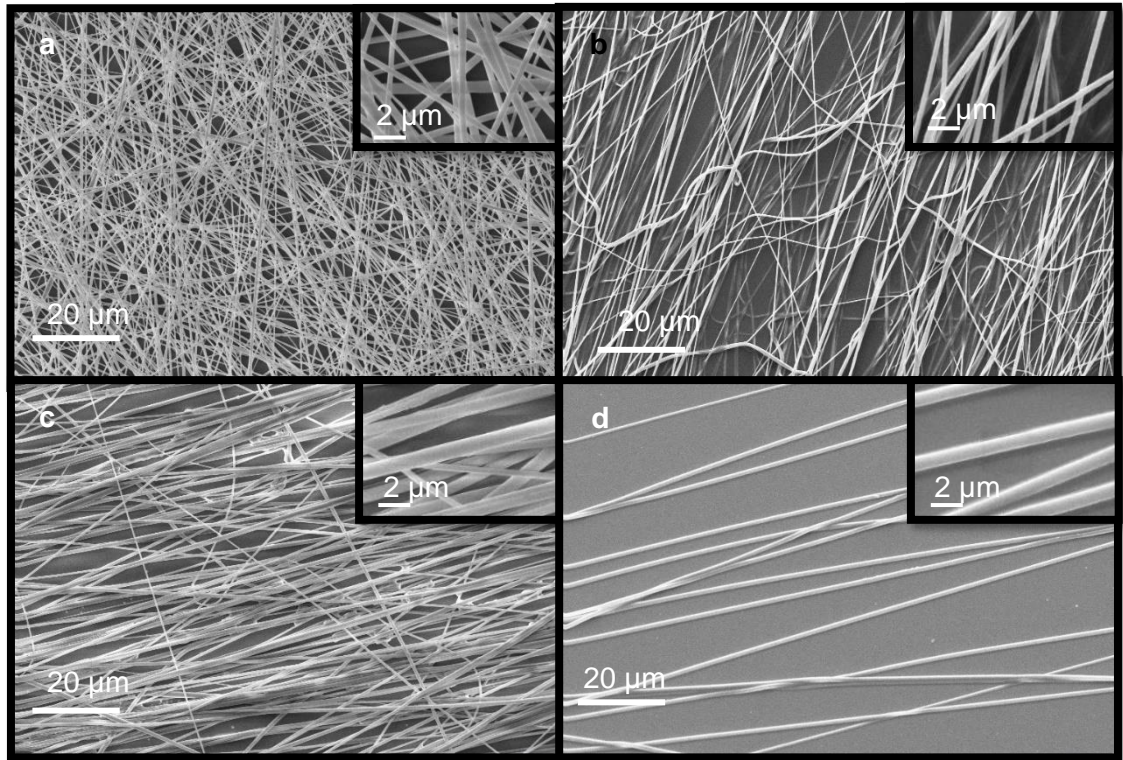
Figure 3.16 *Scanning electron micrographs of nanofibres electrospun from different concentration solutions of PVDF-TrFE. a) 12%, b) 16%, c) 20%, d) 24%. The insert shows a higher magnification, highlighting slight variations in the fibre diameters.*

3.4.2.3. Nano-piezoelectric Properties of PVDF-TrFE Electrospun Nanofibres

Piezoresponse force microscopy was used to provide insight into the nanoscale piezoelectric properties of PVDF-TrFE nanofibres. Measurements were made by M. Jomaa according to the procedure described in Section 2.2.11.

The piezoelectric coefficients d_{33} of PVDF-TrFE nanofibres electrospun from solutions containing different ratios of PVDF-TrFE (personal communication, Jomaa, M., December 2019) are shown in **Figure 3.17**. There is a trend for the d_{33} of PVDF-TrFE electrospun fibres to decrease as the fibre diameter increases due to decreased molecular alignment and crystallinity in fibres with larger diameters. A literature value for the d_{33} of electrospun PVDF-TrFE nanofibres is shown for comparison.
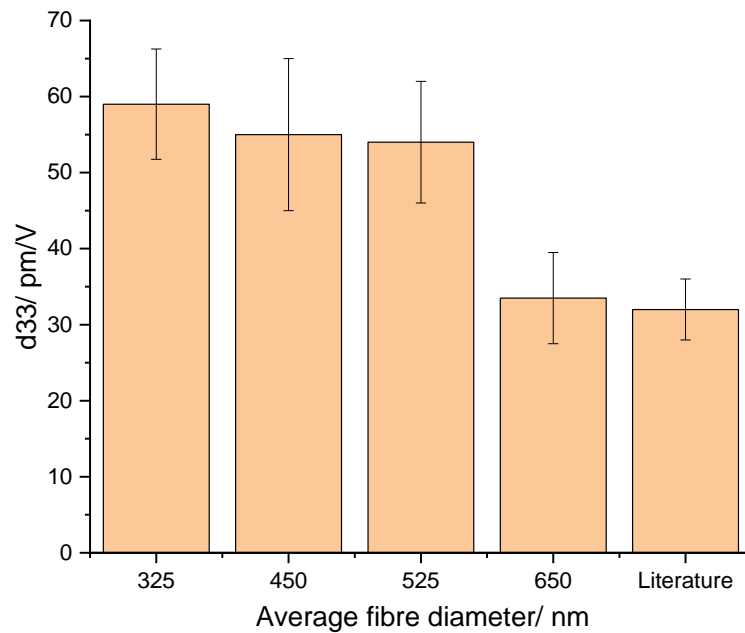
Figure 3.17 *Relationship between PVDF-TrFE fibre diameter and the piezoelectric coefficient d_{33} of electrospun nanofibres. Literature value is of a PVDF-TrFE electrospun nanofibre with diameter 375 nm [184].*

3.4.2.4. Nanoscale Mechanical Properties of PVDF-TrFE Electrospun Nanofibres

The surface modulus of PVDF-TrFE nanofibres was measured by Jomaa using an atomic force microscope in force spectroscopy mode, as described in Section 2.2.11.

The surface modulus of PVDF-TrFE nanofibres electrospun from solutions containing different amounts of PVDF-TrFE are shown in **Figure 3.18**. There is a trend for the surface modulus to decrease as the polymer fibre diameter increases. A literature value is included for comparison and shows a surface modulus approximately double that recorded for fibres of similar diameter produced in this work. The PVDF-TrFE powder from which the literature sample fibres were produced contained 30% TrFE compared to the PVDF-TrFE powder used here, which contained 25% TrFE. It is likely that the difference in copolymer composition, combined with differences between the electrospinning setups in both cases, contributed to the significant difference in Young's modulus.
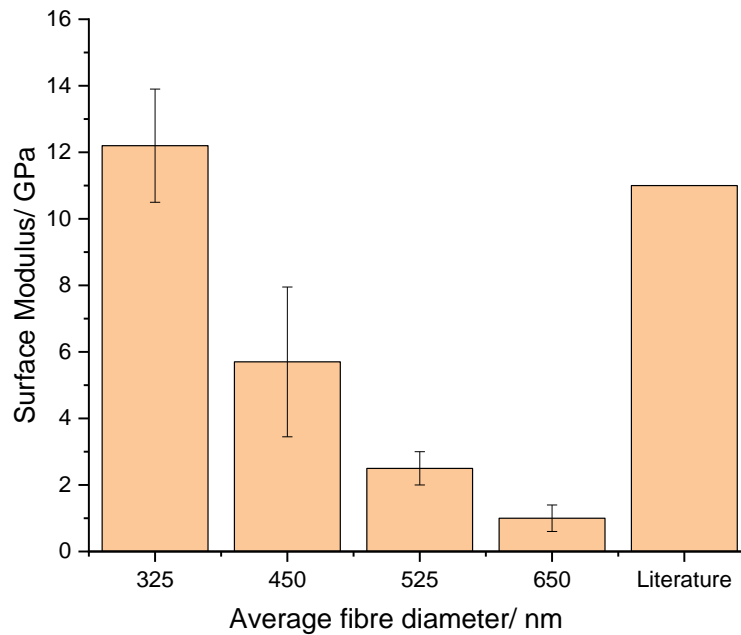
Figure 3.18 *Relationship between PVDF-TrFE fibre diameter and Young's modulus
of electrospun nanofibres. Literature value is of a PVDF-TrFE electrospun nanofibre
with diameter 375 nm* [184]*.*

3.5. Human Cell Response to the Piezoelectric Materials Investigated

3.5.1. Effect of Diphenylalanine Microtubes on Human Dermal Fibroblasts and Human Schwann Cells *in Vitro*

To investigate the toxicity of the diphenylalanine materials, Human Dermal Fibroblasts
and Human Schwann cells were cultured on L-, D- and Fmoc-diphenylalanine in 24-
well plates. For these experiments, toxicity is defined as extensive cell death (<50% of
cells surviving at day 7 (HDF) or day 5 (HSC) relative to day 1), or severely hindered
cell proliferation (>60% decrease in cell metabolic activity on day 7 (HDF) or day 5
(HSC) relative to positive control). Cells were grown on clean glass coverslips as a
positive control and wells containing medium but no cells were used as a negative
control. Cells were seeded on day 0 and cell metabolic activity was recorded on days
1, 3 and 7 or days 1, 3 and 5 for HDFs and HSCs respectively.

Human Dermal Fibroblasts were cultured to passage 10 and Human Schwann cells
were cultured to passage 3 or 4, using the methods described in Sections 2.4 and 2.5.

L- and D-diphenylalanine solutions were prepared with a concentration of 100 mg ml^{-1} in HFIP. Suspensions of diphenylalanine microtubes were also prepared as described in Section 3.3. The solutions and suspensions were then drop coated onto clean 12 mm glass coverslips. The coverslips were dried in a biosafety cabinet (BSC) for 30 mins before being covered and moved to a vacuum oven. The vacuum oven was cleaned by wiping down with 70% IMS before being used to further dry the coated coverslips. The coverslips were dried at 60 °C for 18 h at 80 mbar.

A Fmoc-diphenylalanine solution was prepared with a concentration of 100 mg ml^{-1} in DSMO. A Fmoc-diphenylalanine hydrogel was also formed using the procedure described in Section 3.3.7. The solutions were drop coated onto clean 12 mm glass coverslips and a stainless steel microspatula was used to transfer a small amount of the hydrogel to clean 12 mm glass coverslips. The coverslips were dried as described above.

For experiments using HDF cells, the dried materials were inserted into 24-well plates. 500 µl supplemented DMEM was added to each well and incubated at 37 °C for 18 h overnight.

After overnight incubation, the medium was aspirated from the plates and HDF suspension was prepared at a density of 50 000 cells/ ml. 500 µl cell suspension was seeded into each well excluding negative controls.

For HSC culture, the dried materials were inserted into 24-well plates, coated with poly-L-lysine (PLL) and incubated at 37 °C for 1 h. The PLL was removed by tilting the plates and removing the liquid slowly from the edges of the wells, using a 1000 µl Gilson pipette. The wells were then washed with distilled water before adding 500 µl complete HSC medium and incubating the plates at 37 °C for 18 h overnight.

After incubating with medium, 500 µl of cell suspension with density 80 000 cells/ ml was seeded on top of incubating medium. Incubating medium was not removed beforehand, due to diphenylalanine dissolving in the medium.

Cell response to diphenylalanine was investigated by growing Human Dermal Fibroblasts on diphenylalanine casts, microtubes and Fmoc-diphenylalanine hydrogels over a period of seven days to provide an indication of the general toxicity of the materials. Human Schwann Cells were also seeded on diphenylalanine coated cover slips separately over five days to investigate the effect of the materials on a neural cell environment.

The viability of cells grown on diphenylalanine was determined by the Presto Blue assay for metabolic activity [136]. Metabolic activity was measured on days 1, 3 and 7 (HDF) or days 1, 3 and 5 (HSC) to observe the cell behaviour over time. The results for HDFs and HSCs are shown in **Figure 3.19**. The metabolic activities of cells grown on diphenylalanine were compared to a positive control of cells grown on glass coverslips, the value of which was normalised to 100% viability at day 7 or day 5 for HDFs and HSCs respectively.
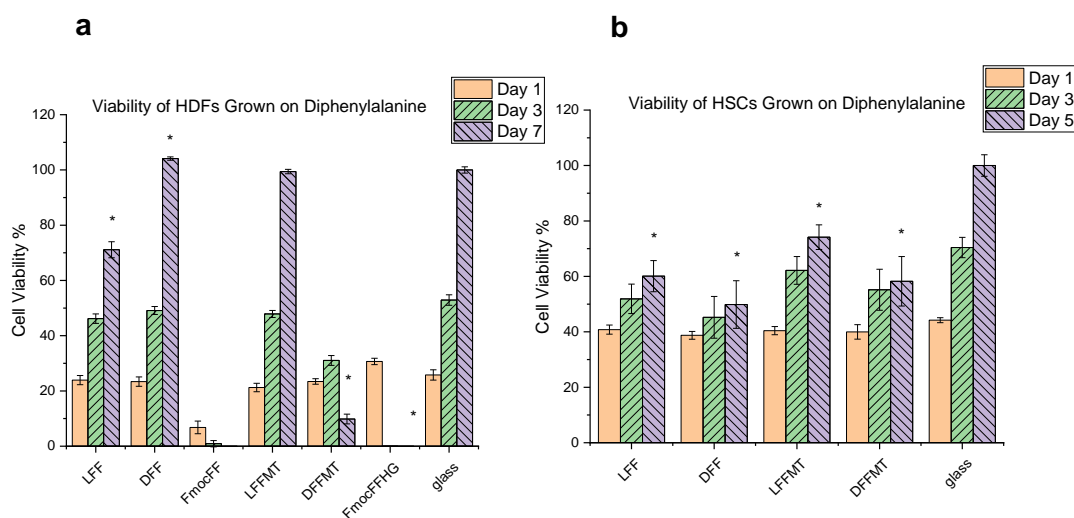
Figure 3.19 *Metabolic activity of cells grown on diphenylalanine coated glass and glass coverslips a) Human Dermal Fibroblasts, n=3 (3 biological replicates were prepared per sample, experiment was conducted once to obtain preliminary results), b) Human Schwann cells, n=12 (4 biological replicates were prepared per sample, experiment was repeated 3 times). An * indicates a significance level of p< 0.05 at day 5*

Figure 3.19a shows the preliminary cell toxicity data for HDFs grown on diphenylalanine. While the results for L- and D-diphenylalanine show inconclusive results, both Fmoc materials show high toxicity levels and extensive cell death over the seven-day experiment.

Figure 3.19b shows the toxicity data for HSCs grown on diphenylalanine. The Fmoc-diphenylalanine materials were excluded from further study based on the preliminary HDF results. Student's t-test statistics with p< 0.05 revealed that diphenylalanine casts and microtubes reduce cell viability significantly by day five. If the results for L-diphenylalanine and D-diphenylalanine are compared, there is a small, but statistically insignificant difference in cell viability between the two.

3.5.2. Effect of Poly[Vinylidene Fluoride-co-Trifluoroethylene] Nanofibres on Human Schwann Cells *in Vitro*

The cell response to electrospun PVDF-TrFE nanofibres was investigated by growing HSCs on the nanofibres. This work I carried out myself. Cells were grown on clean glass coverslips as a positive control and wells containing medium. Wells containing medium with no cells were used as a negative control. Cells were seeded on day 0 and cell metabolic activity was recorded on days 1, 3 and 5.

The edges of electrospun PVDF-TRFE fibres were sealed onto 12 mm coverslips using medical grade silicone adhesive. The sealed fibres were sprayed lightly with 70% IMS and then immersed in PBS for 2 h to reduce the hydrophobicity of the fibres and prevent the coverslips from floating.

The coverslips were then inserted into 24-well plates, coated with PLL and incubated at 37 °C for 1 h. The PLL was removed and the wells washed with distilled water. Complete HSC medium was then added to the wells and the plates were incubated for 18 h overnight.

After overnight incubation, medium was removed and 1 ml cell suspension with density 40 000 cells/ ml was added to each well except negative controls.

Since there already exist reports in the literature confirming the ability of PVDF materials to support cell growth [60], HDF cells were not first grown on PVDF-TrFE. Cell response to PVDF-TrFE nanofibres was investigated by growing Human Schwann Cells on the PVDF-TrFE nanofibres over five days to investigate the effect of the materials on a neural cell environment.

The viability of cells grown on PVDF-TrFE nanofibres was determined by the Presto Blue assay for metabolic activity and the cell proliferation was determined using the total DNA assay. The results for HSCs are shown in **Figure 3.20**. The metabolic activities and proliferation of cells grown on PVDF-TrFE nanofibres were compared to a positive control of cells grown on glass coverslips, the value of which was normalised to 100% viability at day 5.

It can be seen from **Figure 3.20** that HSC response is similar regardless of fibre diameter. Student's t-test statistics with $p < 0.05$ showed that both cell viability and cell proliferation are significantly reduced by day five, compared to the positive control but are not significantly different from each other.
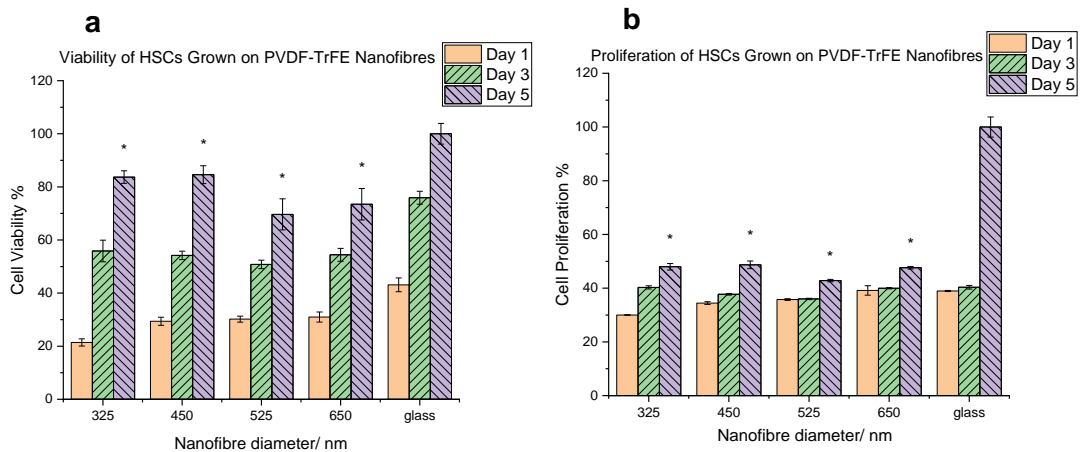
Figure 3.20 *Cell response of Human Schwann cells grown on PVDF-TrFE electrospun nanofibres a) Metabolic activity, b) Proliferation, determined by total DNA, n=8 (4 biological replicates were prepared per sample, experiment was repeated twice). An * indicates a significance level of p< 0.05 at day 5*

The fluorescence microscopy images in **Figure 3.21** show HSCs grown on 500 nm diameter fibres compared to HSCs grown on glass coverslips. The fibres have a clear directing effect on the direction of cell growth and the cells are seen to proliferate on the fibres over the five-day period.
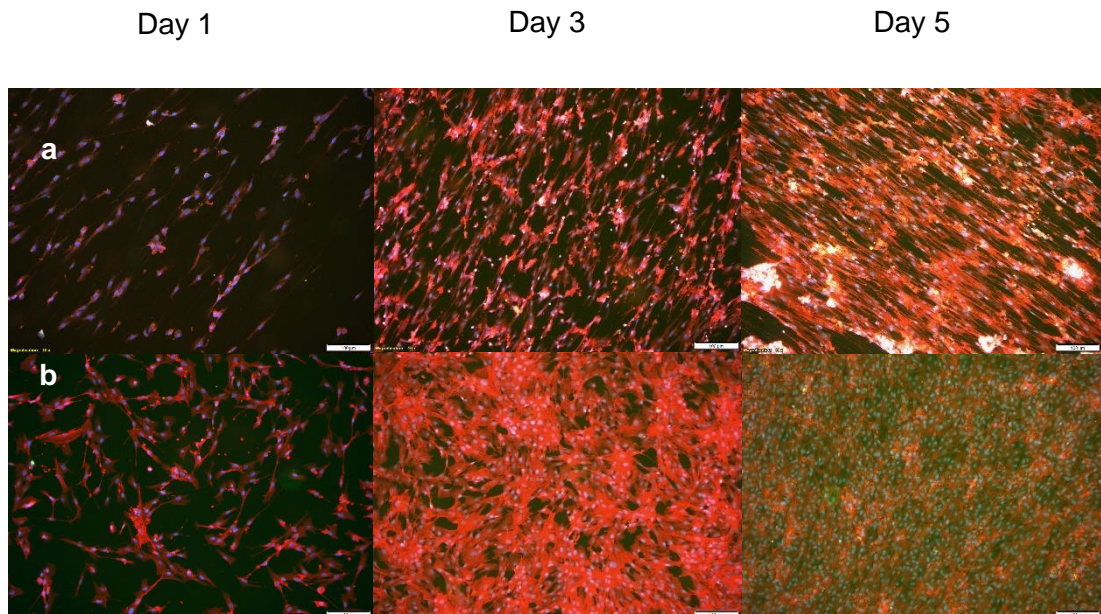
Figure 3.21 *Fluorescence microscope images of HSCs stained with phalloidin (red, actin marker) and DAPI (blue, nucleus marker), scale bar 100 μm a) HSCs on 500 nm PVDF-TrFE electrospun nanofibres, b) positive control*

Figure 3.22 is a comparison of fluorescent microscopy images showing cell alignment and proliferation on different diameter fibres. All sizes of electrospun nanofibres appear to direct cell growth but there is no clear relationship between fibre diameter and cell proliferation. Hoop et al. [29] have stated that fibre modulus would not be expected to affect cell proliferation/ differentiation since the fibres have moduli in the GPa range, which is far greater than the range within which cells can sense gradients of stiffness (kPa - MPa range). This is in an agreement with the experimental results obtained.
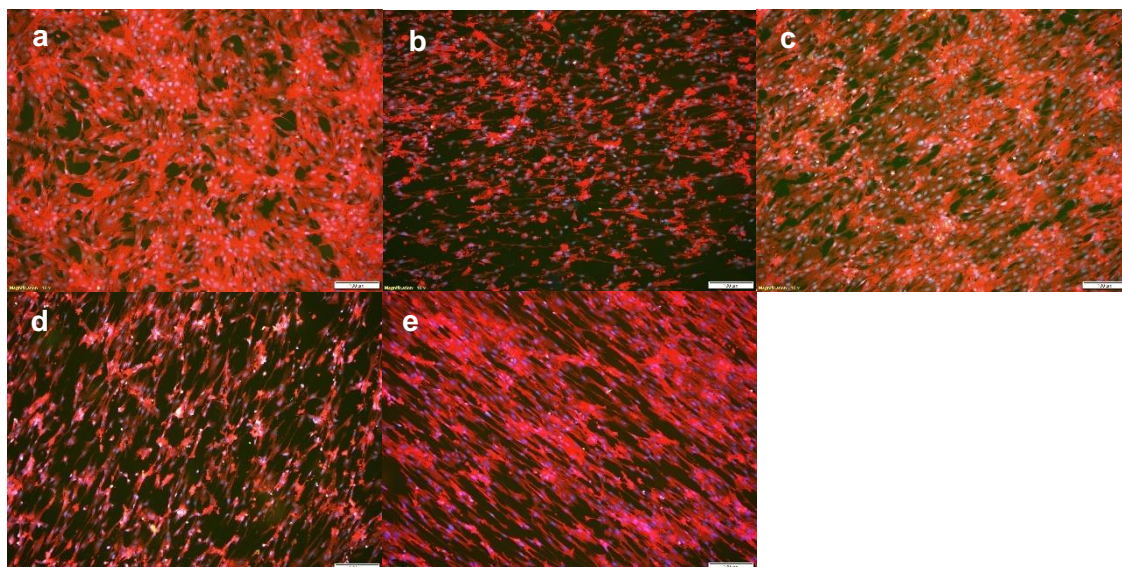
Figure 3.22 *Fluorescence microscope images of day 3 HSCs grown on glass and PVDF-TrFE electrospun nanofibres. Cells are stained with phalloidin (red, actin marker) and DAPI (blue, nucleus marker), scale bar 100 μm a) positive control, b) 12% c) 16%, d) 20%, e) 24%*

3.6. Discussion

3.6.1. Diphenylalanine

Self-Assembly of Separate Enantiomers of Diphenylalanine

Diphenylalanine dissolves fully in the low polarity, protic solvent hexafluoroisopropanol (HFIP). When dissolved at a concentration between 85-120 mg ml^{-1}, diphenylalanine self-assembles into hexagonal habit microtubes upon the addition of water. It is postulated that this self-assembly is driven by extensive hydrogen bonding, aromatic interactions, hydrophobic/ hydrophilic interactions and electrostatic interactions.

153

The concentration of the diphenylalanine solution is key to determining the morphology of the crystals formed. It has been reported that diphenylalanine solutions at different concentrations can self-assemble into microtubes, nanotubes, nanoribbons, micelles and laminar sheets [181, 185]. This observation has also been confirmed by molecular dynamics simulations [174]. At high concentrations, diphenylalanine molecules are closer together and have a greater number of interactions in solution. As a result, they undergo a greater amount of intermolecular hydrogen bonding, leading to the formation of structures such as microtubes and laminar sheets. In lower concentration solutions, there are fewer opportunities for interactions between diphenylalanine molecules, leading to the formation of less tightly packed assemblies such as micelles. **Figure 3.23** shows a schematic representation of the self-assembly of diphenylalanine into different microstructures at different concentrations. The molecule is represented in a form in which the hydrophilic and hydrophobic regions of the molecule have already been aligned through intramolecular hydrogen bonding.

Interest in the diphenylalanine hexagonal microtube structure is due to it being well characterised [16] and possessing a very high piezoelectric coefficient. For microstructures of the same molecule with different habits, they are of no interest unless they have a higher piezoelectric coefficient, and a cursory search of the literature has revealed no candidate.

In this work, modifications to the conditions under which diphenylalanine was self-assembled, were found to induce changes in microtube formation. This has been attributed to changes in hydrogen bonding, aromatic π-π interactions and kinetics, all of which are key factors in the self-assembly of diphenylalanine microtubes. The chemical and physical properties of diphenylalanine microtubes were probed using a range of microscopic and spectroscopic techniques and these properties were evaluated with regard their suitability for application in a piezoelectric device. Two methods for aligning diphenylalanine self-assembled structures were explored and vertically aligned forests of diphenylalanine nanorods and nanotubes were obtained.

Diphenylalanine hydrophilic region (NH$_2$ and COOH groups)

Diphenylalanine hydrophobic region (phenyl groups)

Concentration/ mg ml^{-1}	Molecular Arrangement	Microstructure
50 - 85		
85 - 120		
120 - 155		
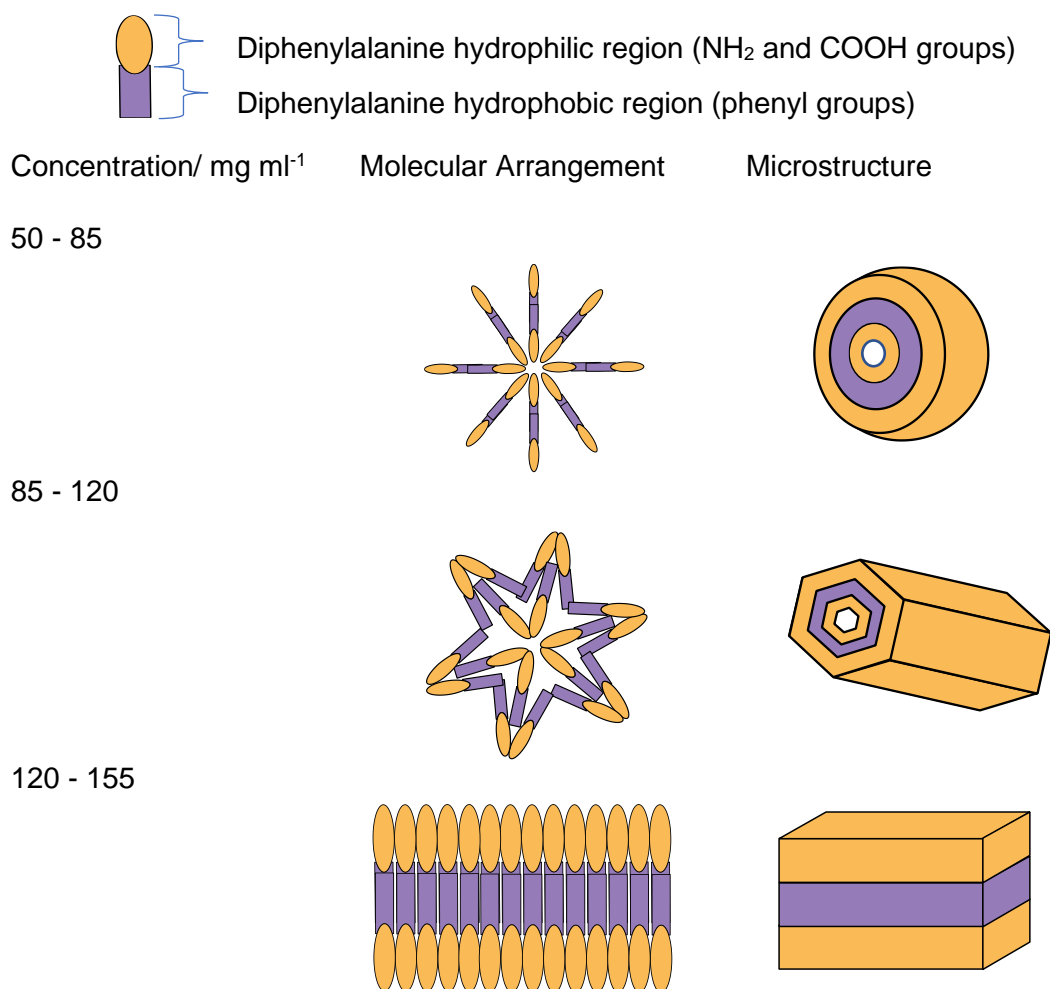
Figure 3.23 *Schematic diagrams of the self-assembly of diphenylalanine—molecular arrangements and microstructures of diphenylalanine molecules dissolved in hexafluoroisopropanol at different concentrations and self-assembled upon the addition of water. Concentration ranges taken from Guo, C., et al.* [174]

Molecular Packing of Diphenylalanine

The FTIR spectra for L- and D-diphenylalanine differ slightly in band intensity and position, from that of Fmoc-diphenylalanine. Many of the band assignments are discussed in Section 3.3.4.3, therefore only the additional FTIR features arising from resonance structures in Fmoc-diphenylalanine will be discussed here.

The FTIR spectrum of Fmoc-diphenylalanine in **Figure 3.4c** shows distinct bands for aliphatic and aromatic C—H bonds. The reason for this band separation stems from the difference between intramolecular bond strengths for aliphatic and aromatic systems. In a resonance structure, the bond strengths lie between those of single and double bonds. The positions of bands in an FTIR spectrum depend on the polarity and strength of each bond, with stronger and more polar bonds displaying peaks at higher wavenumber. It therefore follows that a difference between the band wavenumbers of bonds between identical atoms likely arises from a difference in bond strength. This

155

can be confirmed by comparing the different hydrogen environments in Fmoc-diphenylalanine.

In the aliphatic hydrogen environments, the C—H bonds are weakened by electron density withdrawing atoms in the vicinity; there is also an aromatic hydrogen environment, in which the C—H bond is strengthened by the sp^2 hybridisation of the bonding carbon atoms. The increased bond strength resulting from the adjacent resonance structure causes the aromatic C—H bonds to appear at higher wavenumber than their aliphatic counterparts. It is also observed that the FTIR bands for aromatic (C—C and C—H) bond stretching appear as multiplets. This is due to movement of delocalised electrons in the resonance structure.

Broadening of the aromatic band at 1400 cm^{-1} to 1600 cm^{-1} is also visible in the Fmoc-diphenylalanine spectrum. The presence of fluorene, in particular, broadens the FTIR aromatic bands because of the energy differences between fluorene and benzene. This aromatic effect is also seen in the Fmoc-diphenylalanine Raman spectra as a peak with greatly enhanced intensity at 1600 cm^{-1}, the wavenumber characteristic of C—C ring stretching. The Fmoc-diphenylalanine Raman spectrum also showed peak wavenumbers being red or blue shifted by up to 10 cm^{-1} compared to L- and D-diphenylalanine spectra.

Inspection of the Raman spectra inserts in **Figure 3.5** reveal peak splitting of what appears, at first glance, to be a singlet peak. The splitting of the C—H ring bending peak at 1032 cm^{-1} into a doublet has been associated in the literature [179] with water adsorbed on the outside of diphenylalanine microtubes or inside the hydrophilic channels. At elevated temperatures the separation between the doublet peaks reduces until the peak becomes a singlet at temperatures above 110 °C.

It was suggested by Wu *et al.* in their 2012 paper [186] that the position of the lower wavenumber peak of the doublet at ~1032 cm^{-1} could be directly correlated to the number of water molecules in contact with diphenylalanine inside the microtube channel. Other water molecules may contribute to the total number of water molecules contained within the channel, but those not in contact with the microtube walls cannot be detected using this method. According to the data obtained by Wu *et al.*, it was estimated that per molecule of diphenylalanine, eight water molecules encapsulated inside the LFFMT and DFFMT hydrophilic channels are directly in contact with the diphenylalanine walls. Since DFFMT has a larger diameter than LFFMT, it is expected that DFFMT will have a larger total number of water molecules inside its hydrophilic channel.

A larger diphenylalanine microtube Young's modulus is correlated with a greater number of water molecules inside the hydrophilic channel. This supports the prediction that the DFFMT channel contains a greater total number of water molecules than LFFMT, since mechanical measurements show that the Young's modulus of DFFMT is larger than that of LFFMT.

Crystal Structure of Diphenylalanine

The XRD peak positions for diphenylalanine prepared here were determined and compared to computer generated peak positions (2θ) calculated from published structure using crystallographic software (Mercury, Cambridge Crystallographic Data Centre). There was general agreement between experimental values in this work and computer-generated peak positions in the X-ray diffractograms for L-, D- and Fmoc-diphenylalanine. The obtained peak patterns were also concurrent with the crystal structures and space groups reported in the literature [187].

The space group of a molecule provides information about its symmetry; it is an alphanumeric code that incorporates the Bravais lattice, crystal system and translational information of a molecule. Enantiomers of the same molecule generally belong to different space groups, called enantiomorphic space groups. This is true of diphenylalanine for which L-diphenylalanine and its microtubes belong to the enantiomorphic space group $P6_1$, and D-diphenylalanine and its microtubes belong to the corresponding enantiomorphic space group, $P6_5$ [187]. The P6 represents a hexagonal, primitive unit cell with lattice points only on the cell corners. The subscript number gives information about the screw axis, a combination of a rotation and a translation in a defined direction. In this case, the numbers are 1 and 5 because the rotational symmetry is different for enantiomers rotating in opposite directions in space.

When obtaining peptides from commercial sources, the term Fmoc-diphenylalanine is generally used to refer to Fmoc-*L*-diphenylalanine. This form of diphenylalanine belongs to the enantiomorphic orthorhombic space group $P2_12_12_1$ [188].

In addition to providing information about the space group of a sample, XRD can also give information about the spacing between crystal planes within a sample. The crystal planes, defined by their Miller indices (h,k,l), can be used in combination with Bragg's Law to calculate the d spacing between parallel crystal planes. Bragg's Law, introduced in Section 2.2.3, Equation 2.1, states that

$$n\lambda = 2d\sin\theta \qquad\qquad (2.1)$$

In this work, the source of X-rays was Cu Kα, with a wavelength of 0.154 nm and n has a value of 1 for all observed reflections.

157

The hexagonal unit cell of diphenylalanine, as described by C. H. Görbitz [189] is shown in **Figure 3.24**. The axes, shown in the same figure govern the direction of the unit cell dimensions '*a, b* and *c*'. For a regular hexagonal prism, the dimensions a and b are equal and the unit cell can be defined by a and c alone.
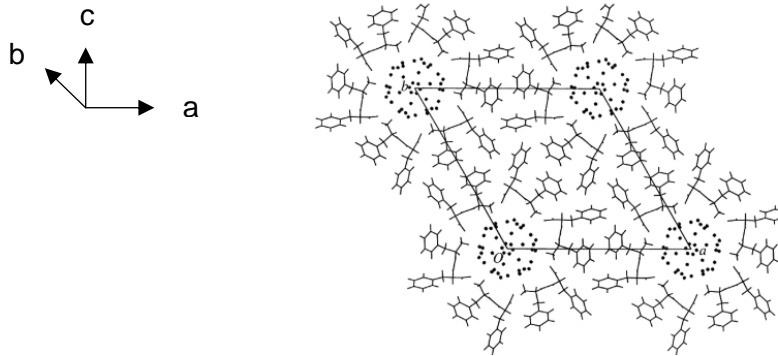
Figure 3.24 *The unit cell and molecular packing of L,L-diphenylalanine, viewed along the c axis. Water molecules are shown as small spheres. Reprinted with permission from* [189]

The unit cell dimensions can be related to the d spacing between crystal planes using Equation 3.1:

$$\frac{1}{d_{hkl}^2} = \frac{4}{3}\left(\frac{h^2 + k^2 + hk}{a^2}\right) + \frac{l^2}{c^2}$$

(3.1)

where:

d_{hkl} = d spacing for a crystal plane with Miller index (hkl)

a = unit cell dimension in the 'a' direction

c = unit cell dimension in the 'c' direction.

Applying Equation *3.1* to the (200) plane, with d spacing 1.02 nm, yields:

$$\frac{1}{1.02^2} = \frac{4}{3}\left(\frac{4}{a^2}\right) = \frac{16}{3a^2}$$

$$3a^2 = 1.04 \; x \; 16$$

$$a = 2.4 \; nm$$

The value of c can then be calculated using the d spacing of the (101) plane and the above calculated value of a (2.4 nm). Performing this calculation gives a value of 0.55 nm for unit cell dimension *c*.

The volume of the unit cell can then be calculated using Equation 3.2, for a hexagonal crystal:

$$V = a^2 c \, sin(60°) \qquad\qquad (\,3.2\,)$$

yielding a unit cell volume of 2.7 nm^3.

The density of diphenylalanine can then be estimated from the unit cell volume and mass, using Equation 3.3 and parameters below:

$$\rho = \frac{Z M_r}{N_A V} \qquad\qquad (\,3.3\,)$$

where:

Z = number of molecules per hexagonal unit cell (6)

M_r = molar mass of hydrated diphenylalanine (356.87 [189])

N_A = Avogadro's number (6.02 x10^{23})

V = diphenylalanine unit cell volume 2.7 nm^3.

This gives a value of 1.3 g cm^{-3} for the density of diphenylalanine.

The XRD peak patterns of diphenylalanine powders were recorded alongside that of their respective microtubes. Analysis and comparison of their peak shapes and intensities can offer insight into crystallite size and atomic positions within the crystal.

Diphenylalanine microtubes show similar or larger integrated peak intensities than their equivalent powder samples for most values of 2θ. Notable exceptions to this are seen at low values of 2θ, particularly 7.36° and 8.31°, where the integrated peak intensity is lower for microtubes than it is for powder samples. This can be explained by examining the self-assembly process and final shape/ orientation of the self-assembled microtubes.

When prepared for XRD measurements, the microtubes are flattened in a way that aligns most crystals in a horizontal direction, whereas the powder sample are not constrained with regard to orientation direction. The horizontal orientation of the microtubes combined with the alignment of individual diphenylalanine molecules perpendicular to the crystal length, contributes to intensity differences between powder and microtube samples and is responsible for the reduced integrated peak intensity at

7.36° and 8.31°. A similar effect is observed for the Fmoc-diphenylalanine hydrogel, which has lower integrated peak intensities than the powder sample.

The broadening of lines in an XRD pattern can be used to calculate the size of nanoscale crystallites within a powder. To achieve this, the Scherrer equation [190], Equation 3.4, is applied.

$$\tau = \frac{K\lambda}{\beta cos\theta}$$
(3.4)

where:

τ = grain size

K = a dimensionless shape factor with value ~1.1 for octahedral crystallites [190]

λ = X-ray wavelength (0.154 nm for a Cu Kα source)

β = full width at half maximum (FWHM) broadening in radians

θ = Bragg angle in radians.

For example, the (5-10) plane for L-diphenylalanine powder corresponds to a reflection at 2θ = 19.33 with a FWHM of 0.265. Converting these values to radians and applying Equation 3.4 yields:

$$\tau = \frac{1.1 \text{ x } 0.154}{0.0046 \ cos \ (0.17)} = \ 37 \ nm$$

Repeating this calculation for different angles gives a mean crystallite size of 37 nm for L-diphenylalanine compared to D-diphenylalanine powder which has a mean crystallite size of 48 nm. The microtube forms of both L- and D-diphenylalanine have larger FWHM values than their powder forms, indicating a larger crystal size. This increased size contributes to the greater XRD reflection intensity at high angles. A quantitative value for the crystal size of L- and D-diphenylalanine microtubes cannot be obtained using the Scherrer equation, since the equation is only applicable to nano-scale crystallites.

Electronic Transitions and Secondary Structure of Diphenylalanine

It has been widely reported that diphenylalanine forms a β-sheet structure during dimer formation [176], however a few molecular modelling studies have reported that diphenylalanine folds into a helical structure early in the self-assembly process [187]. The circular dichroism (CD) spectra of L- and D-diphenylalanine show three maxima/ minima at 189 nm, 198 nm and 218 nm. This matches the characteristic CD spectrum of β-turns, with maxima/ minima at ~190 nm, ~200 nm and ~220 nm, and supports the initial helical structure hypothesis. The subsequent arrangement of diphenylalanine molecules into antiparallel β-sheets during dimer formation is confirmed by the presence of the amide I peak in the FTIR spectrum at 1686 cm^{-1}. This is in agreement with previous reports from literature [48].

The CD spectra of L- and D-diphenylalanine display the Cotton effect [191], in which is a strong change in the direction of circular dichroism of a substance, results in a maximum and a minimum both being observed as the wavelength of radiation is varied near an absorption band. This effect is often observed for chiral molecules and exciton couplets, as is the case here. Diphenylalanine shows strong variation in optical rotation between 190 nm and 200 nm which is associated with an exciton couplet. An exciton is a bound energy state formed by an excited electron and its associated electron hole. The excited electron occupies the lowest unoccupied molecular orbital (LUMO) while the hole occupies the highest occupied molecular orbital (HOMO).

In a diphenylalanine molecule, the two phenyl groups act as separate chiral chromophores (**Figure 3.25a**) each with a separate π-π* transition. This leads to the formation of two excitons which produce CD maxima/ minima with opposite signs but similar wavelengths, as shown in **Figure 3.25b**. The wavelength overlap between the excitons causes them to become coupled and appear in the CD spectrum as an exciton couplet with minima/ maxima at 189 nm and 198 nm. The maximum in the diphenylalanine spectrum at 218 nm is due to the n-π* transition of electrons in the nitrogen lone pair [192].

a

b

Chromophore 2
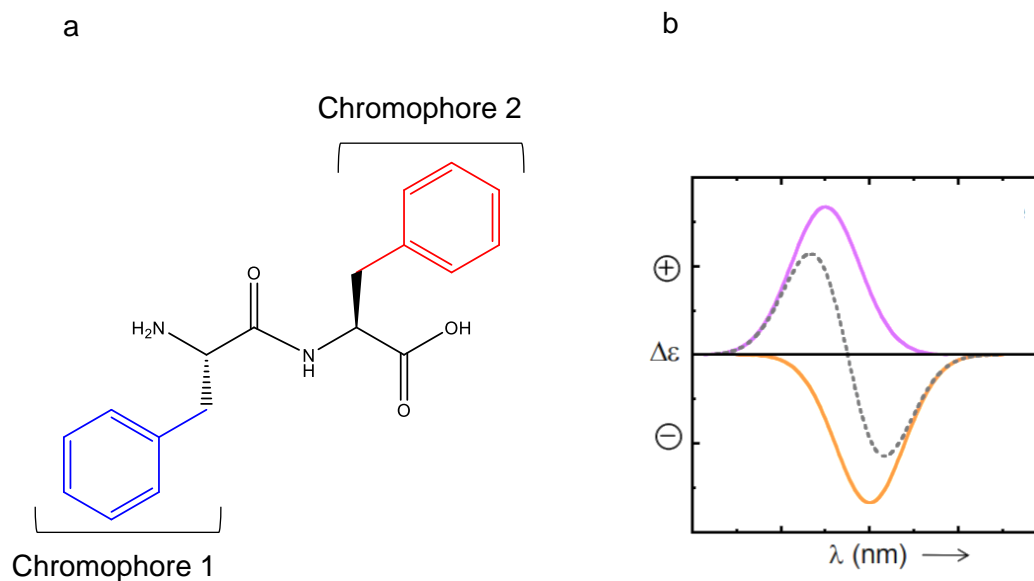
Chromophore 1

Figure 3.25 *a) Skeletal formula of diphenylalanine with chromophores 1 and 2 highlighted in blue and red, b) Exciton peaks arising from chromophores 1 and 2 (purple and yellow lines). Coupling of the exciton maximum/ minimum leads to the production of an exciton couplet (dashed line). Exciton couplet diagram reprinted from G. Pescitelli, Exciton-coupled CD spectroscopy in the study of supramolecular systems: functional polymers, organogels, retinylidene proteins.*

Effect of Diphenylalanine Chirality on Self-assembled Microtube Size

The dimensions of self-assembled diphenylalanine microtubes were investigated by scanning electron microscopy. Scanning electron micrographs of L- and D-diphenylalanine were obtained at magnifications between 197x and 32kx. The average length and diameter of L-diphenylalanine microtubes were measured to be ~300 µm and ~2 µm respectively. Light microscope images obtained during investigations into the effect of temperature on self-assembly showed L-diphenylalanine microtubes with a wider range of lengths (132-1200 µm) and diameters (3–23 µm) at 20 °C. It is of note that the discrepancy between the measurements may be due to differences in the resolution of the two microscopes. The type of pipette used to deposit the microtubes for SEM and light microscopy might also influence the measurement due to the size of the microtubes. A modified pipette with a wide (~5 mm) opening was used to deposit microtubes for light microscopy whereas a standard P200 pipette tip with a diameter of ~1 mm, was used to deposit microtubes for SEM. The smaller tip diameter prevented larger microtubes from being deposited on SEM pins.

The dimensions measured by SEM for L-diphenylalanine microtubes contrast with those measured for D-diphenylalanine microtubes, which had average length ~100 µm

and average diameter ~4 μm. The differences in the microtube dimensions were unexpected since the two materials are chemically identical and differ only in stereochemistry.

The average size of L-diphenylalanine microtubes has been reported by a number of studies and is consisted with the measurements reported here, however D-diphenylalanine is not often discussed in the literature. At the time this observation was made in this work, a search of the literature did not locate any previously published comment regarding a difference in size between the L- and D- enantiomers of diphenylalanine. However, Zelenovskiy *et al.* reported in 2019 to have observed this and confirmed the observation as real [193]. Another recent paper from the same group [187] compared the properties of L- and D-diphenylalanine using semi-empirical computational methods and also reported that there is a phenomenological difference in size between the L- and D- diphenylalanine enantiomers. The researchers studied the crystallisation energy of both enantiomers, the energy released by molecules during crystallisation, and postulated that D-diphenylalanine has a higher crystallisation energy in the direction perpendicular to the microtube length [187] which causes D-diphenylalanine to grow more in the vertical direction than the lateral direction, leading to thicker, shorter microtubes compared to L-diphenylalanine. The computational predictions are supported by the results in this work. The computational models reveal that the difference in crystallisation energy likely arises from differences between the electrostatic dipole interactions of the two enantiomers.

Feasibility of Diphenylalanine Microtubes as Piezoelectric Resonators in Cochlear Implants

The surface modulus measurements yield values of 6.5-7 GPa for L- and D-diphenylalanine. This is slightly lower than results in the literature which report moduli of 9-24 GPa [47]. However, it has been established that the degree of water filling inside the diphenylalanine channel can have a significant effect on the modulus values recorded. Values of 8 GPa have been reported for dry diphenylalanine microtubes with no water inside the channel. This is consistent with computational models [194] and close to the results reported here. It is possible that several water molecules inside the diphenylalanine microtube hydrophilic channel evaporated before surface modulus measurements were taken. This could be related to the preparation method, since the microtubes were fixed to TempFix at elevated temperature prior to measurement. The low surface modulus could also arise from differences between the sample preparation technique used in this work and in the literature.

The resonant frequency of the microtubes offers crucial insight into the feasibility of applying diphenylalanine microtubes as the piezoelectric component of an implantable device. The modulus values obtained by AFM and dimensions captured by SEM/ light microscopy facilitate the calculation of the resonant frequency of the microtubes. Assume that a diphenylalanine microtube inside a device would be fixed at one end. The microtube can then be considered as a cantilever and the formula for calculating the natural frequency of a cantilever can be applied [195], Equation 3.5:

$$f = \frac{\beta^2}{2\pi l^2} \sqrt{\frac{EI}{\rho A}}$$ (3.5)

where:

f = cantilever natural frequency

β = smallest positive solution of the equation $cos(x)\, cosh(x) = -1$

l = length

E = Young's modulus

I = area moment of inertia (moment of inertia with regard to the cantilever cross section)

ρ = density

A = cross-sectional area.

For a hexagonal prism-shaped cantilever, the area moment of inertia (I) and the cross-sectional area (A) can be calculated using Equation 3.6 and Equation 3.7:

$$I = \frac{5\sqrt{3}a^4}{16}$$ (3.6)

$$A = \frac{3\sqrt{3}a^2}{2}$$ (3.7)

where a = length of one edge of the hexagon.

Substituting these and β = 1.875 [196] into Equation 3.5 yields

$$f = \frac{1.875^2}{2\pi} \frac{a}{l^2} \sqrt{\frac{5E}{24\rho}}$$

For an average L-diphenylalanine microtube, the equation parameters would be:

a = 1 μm (by measurement of a diphenylalanine SEM image)

l = 300 μm (by measurement of a diphenylalanine SEM image)

E = 6.59 GPa

ρ = 1.3 g cm^{-3} (from unit cell volume and density calculations).

When input into Equation 3.5 above, the calculation yields a resonant frequency of ~6.4 kHz for an average L-diphenylalanine microtube. For an average D-diphenylalanine microtube with a = 3 μm, l = 100 μm, E = 6.8 GPa, the resonant frequency is calculated as ~175 kHz.

Stimulation of the cantilever by an external driving force at the cantilever natural frequency produces resonance. At this resonant frequency, the vibrational motion of a crystal is at its largest and consequently the greatest piezoelectric response would also be expected at this frequency. To maximise the efficacy of a cochlear implant, the resonant frequencies of the piezoelectric components would need to be within the frequency range of human hearing (30-20 000 Hz). In theory, an L-diphenylalanine microtube of average size would have resonant frequency within this range and it might be possible to modify the precipitation conditions to obtain diphenylalanine microtubes with different dimensions, that resonate at different frequencies. It should be noted however, that controlling the dimensions of the self-assembled microtubes can be difficult and it is likely that frequency selectivity would be low. The resonant frequency for an average size D-diphenylalanine microtube is well outside the frequency range for human hearing and it would seem therefore is unsuitable for application in a cochlear implant.

Kinetics of Diphenylalanine Self-assembly

Changes in self-assembly temperature were found to have the greatest effect on diphenylalanine self-assembly in this work. A range of lengths were measured for diphenylalanine microtubes grown at each temperature, producing skewed distributions, although these are not greatly different from a normal Gaussian distribution. Larger crystals were observed at high temperatures and smaller crystals observed at low temperatures. The effect of temperature on the size of crystals can be explained by examining the kinetics of the crystallisation process. The change in Gibb's free energy (ΔG) of a system is defined in terms of the change in enthalpy (ΔH), temperature (T) and change in entropy (ΔS) as Equation 3.8:

$$\Delta G = \Delta H - T\Delta S \qquad\qquad (3.8)$$

Crystallisation occurs spontaneously if ΔG is negative. It is accompanied by a release of energy, known as the lattice formation enthalpy or crystallisation energy.

The rate of crystal growth should also be considered in crystallisation studies. Crystallisation as a thermally initiated process often occurs in two major steps: The first step is nucleation, and the second step is crystal growth; the latter is also dependent upon the temperature of the system. When the crystallisation temperature is low, the intra- and inter-molecular interactions are reduced and the molecules are moving more slowly. Nucleation is faster and more nuclei form since the molecules are closer together but the entropy is decreased (unfavourable) since the system is becoming more ordered. Crystal growth is also fast at low temperature since crystallisation is an exothermic process (enthalpy is favourable), so many small crystals grow from the nuclei. The converse is true at high temperature. There are fewer nucleation sites and the crystals are larger but grow more slowly.

Diphenylalanine contains both hydrophilic and hydrophobic groups in the form of amine/ carboxyl groups and phenyl rings, respectively. Its amphiphilic structure also contributes to the crystallisation process, particularly when water is first introduced into the system. The hydrophobic effect causes the movement of hydrophobic portions of a molecule away from the solvent and toward the centre of a protein (known in protein chemistry as 'burial of hydrophobic residues') [197]. This is an entropically favourable process because it results in the breakage of hydrogen bonds between the peptide and solvent.

Effect of pH and Physical Constraints on Diphenylalanine Crystallisation

The self-assembly of diphenylalanine relies heavily on hydrogen bonding. If the hydrogen bonding process is disrupted at any stage, self-assembly becomes less likely and in some cases, highly improbable. Between pH 3.5 and 7.5, diphenylalanine molecules form zwitterions in solution which increases the number of intermolecular interactions between diphenylalanine molecules. Changing the position of equilibrium by altering the pH, causes the molecule to lose this zwitterionic behaviour and thus influences the crystal habit upon crystallisation.

A pH of 5.4 represents the isoelectric point of diphenylalanine [198], the pH at which the molecule carries no net electric charge on average. Decreasing the pH of a diphenylalanine solution in HFIP, by increasing the concentration of H^+ ions in the solution, causes the NH_2 group of diphenylalanine to become protonated **Figure 3.26a**. The protonation disrupts the formation of β-sheets and dimers, making the molecules

unable to form microtubes. In a similar way, increasing the pH of the solution by increasing the concentration of OH⁻ ions, causes the H⁺ ions to be removed from the carboxylic acid group, **Figure 3.26b**. This also disrupts hydrogen bonding, β-sheet and dimer formation as above, preventing microtube formation.
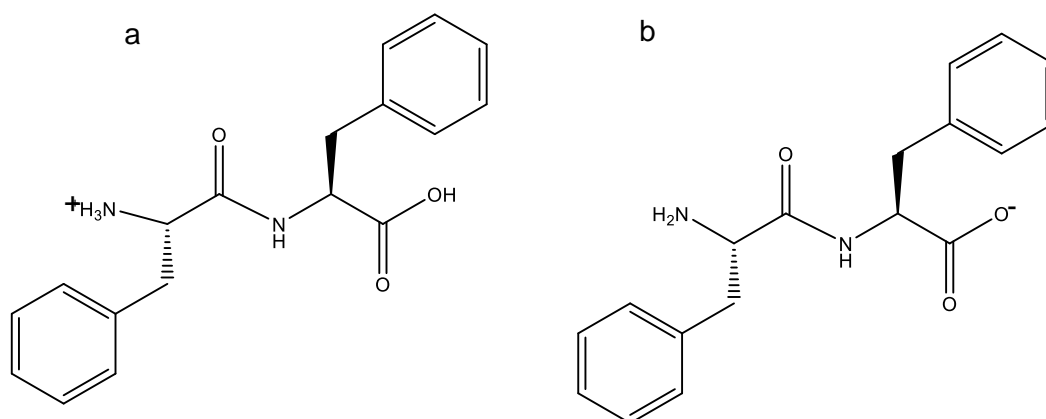
Figure 3.26 *Skeletal formulae of a) protonated and b) deprotonated diphenylalanine molecules*

Diphenylalanine powder dissolved directly into water does not form microtubes since the diphenylalanine molecules are unable to pre-assemble into β sheets and dimers. Instead, the hydrophobic groups of diphenylalanine clump together while the hydrophilic groups form hydrogen bonds with water.

The work presented here differs in part from published literature. A study investigating the effect of changing the pH on diphenylalanine self-assembly [182] added solutions of 0.1 M HCl or 0.1 M NaOH to solutions of diphenylalanine in HFIP. The researchers added acid or alkali until the solution reached pH 3 or pH 10 and then observed the diphenylalanine self-assembly. They concluded from their results that increasing the pH inhibits hydrogen bonding and disrupts self-assembly. This effect was also observed in this work. However, the researchers also concluded that decreasing pH does not affect the hydrogen bonding, which contrasts with the results presented in this work. Their results show that microtubes formed at pH 3, although the structures were approximately 200 nm in diameter. This is 10x smaller than the average diameter of microtubes formed under standard self-assembly conditions- pH 5, 20 °C, and suggests that lowering the pH does affect the hydrogen bonding process and causes significant changes to microtube formation. This is in line with the results and conclusions drawn here. It is also possible that peptide nanotubes may have formed in

the solutions described in this work, although they are not visible to the naked eye or light microscopy.

The effect of forming self-assembled structures from mixed chirality solutions of L- and D-diphenylalanine was also investigated. A racemic mixture of L- and D-diphenylalanine was found to crystallise into multiple structures, in contrast to the hexagonal habit crystals consistently observed for pure enantiomer diphenylalanine solutions.

One noticeable difference between microtubes formed from single enantiomers and microtubes formed from a racemic mixture is that the latter can form curved structures. This is a feature of the steric clashes between the L and D enantiomers. As the molecules interact with each other in solution, steric restrictions may cause helical structures to be more energetically favourable than the β-sheets formed by single chirality solutions. The formation of microscale helical structures may be the cause of the curved microstructures formed upon the addition of water.

Another unusual microstructure observed for the LFF-DFF hybrid was a flattened 'ribbon' structure. The self-assembly of L-diphenylalanine into microribbons has previously been described in the literature for diphenylalanine crystallisation in the presence of ethylene glycol [42]. The researchers attributed the formation of this alternative structure to the hydrogen bond donor ability of ethylene glycol, which is able to donate twice as many hydrogen bonds as water. The researchers described the microribbons as orthorhombic in structure, with a rectangular cross section, similar to the microribbons observed for the racemic mixture self-assemblies in this work. It was determined that the structure belonged to the crystal class mm2 and that the microribbons exhibited a piezoelectric response slightly lower than that seen for their hexagonal microtube counterparts [42].

Templated Growth of Diphenylalanine Nanostructures

Diphenylalanine microtubes freely self-assembled in liquid have no defined orientation. Each microtube in suspension will display a lateral piezoelectric response with respect to its axial direction, thus diminishing the net piezoelectric response in any single direction. Controlling the alignment of diphenylalanine microtubes would offer significant opportunities for application as the piezoelectric component in a device, in which the maximum piezoelectric response is desirable. Recent studies have described the use of an epitaxial seed layer to obtain aligned arrays of diphenylalanine microstructures [46]. Growth from an epitaxial seed layer was attempted in this work, as

168

well as growth of diphenylalanine within the confines of an external anodised aluminium oxide (AAO) template. Aligned arrays with dissimilar nanostructures were obtained using the different methods. Formation of arrays using the epitaxial growth method produced peptide nanorods with localised alignment confined within micro-domains, similar to the diphenylalanine nanorods obtained by Ryu and Park [199]. Growth within an AAO template produced diphenylalanine nanotubes with general vertical alignment.

It is hypothesised that the nanorods produced in this work likely precipitated from self-assembled nanostructures formed at the interface between the suspended diphenylalanine solution and surrounding water vapour. The assembly is driven by the combination of HFIP evaporation from the diphenylalanine solution and the presence of water vapour in the system. When water vapour comes into contact with the diphenylalanine molecules on the surface of the solution, these molecules arrange into a structure that minimises the contact between the hydrophobic aromatic regions and water. This local arrangement influences the molecular assembly of other solvated diphenylalanine molecules in the vicinity. Continued HFIP evaporation leads to the formation of extended diphenylalanine structures, such as the nanorods observed in this work.

Peptide nanotubes were formed by Reches and Gazit using a similar epitaxial growth layer but excluding water from the self-assembly process and rapidly evaporating the HFIP solvent [44]. The nanotubes had a similar hollow structure to diphenylalanine microtubes formed in solution although the hexagonal structure of the microtubes was somewhat disrupted.

Disruption of the hexagonal structure of diphenylalanine nanotubes was also observed in this work for nanotube arrays formed using an anodised aluminium oxide (AAO) template. The constraints applied by the AAO template appeared to affect the self-assembly process by restricting hydrogen bonding and molecular arrangements. This led to the formation of nanotubes with partially deformed hexagonal structures. Diphenylalanine nanotubes constrained within AAO templates grew to heights ranging from 1–10 µm above the surface of the AAO template (depth = 60 µm). The template had a pore size of 200 µm but the aligned nanotubes appear to have a range of diameters, from 200 nm –1 µm. Scanning electron microscopy provides evidence that the larger diameter structures may not have the same hollow interior channel as their freely self-assembled counterparts, but may instead consist of smaller, 200 nm, nanotubes that have coalesced into larger micron-sized rods. Other significantly larger microtubes with no alignment were also observed, signifying that excess

diphenylalanine solution is able to crystallise into freely self-assembled diphenylalanine microtubes despite the presence of a template.

3.6.2. **Interactions Within Self-assembled Diphenylalanine Microtubes**

A range of interactions occur within a solution of diphenylalanine during microtube self-assembly. The formation of these interactions is driven by the presence of hydrophobic and hydrophilic groups within diphenylalanine, as well as the use of high polarity solvents.

Hexafluoroisopropanol, $CF_3CHOHCF_3$, is a polar solvent which plays a key role in the self-assembly of diphenylalanine. Its ability to form hydrogen bonds with other moieties stems from the presence of a hydroxyl group.

Further consider the hydroxyl group; because there is a difference in electronegativity between oxygen (3.0) and hydrogen (2.1), there is a tendency for electrons within the bond to be polarised toward the oxygen creating a polarised $O^{\delta-}$—$H^{\delta+}$ bond. This $H^{\delta+}$ atom is labile; that is, it can be easily solvated to become an acidic proton, H^+, a proton surrounded by displaceable water molecules (usually represented by H_3O^+) that move aside when it encounters a molecule it can form a bond with. Solvents with H atoms bonded to electronegative atoms are described as being 'protic' because their labile hydrogen can contribute towards the formation of hydrogen bonds. In hexafluoroisopropanol, the carbon atom attached to the oxygen is also attached to two carbon atoms each bearing three fluorine atoms (electronegativity 4) that draw electron density from the C–O bond. This makes the hydrogen on the opposite side of the oxygen yet more labile.

The polar and protic properties of some solvents used in this work can be seen in **Table 3.10**.

Table 3.10 Examples of solvents with various polarities and protic properties

Solvent	Chemical Formula	Polarity	Proticity	pKa	Density/ kgm^{-3}
Water	HOH	High	Protic	14	1000
Dimethylformamide (DMF)	$(CH_3)_2NC(O)H$	High	Aprotic	-0.3	944
Hexafluoroisoproanol (HFIP)	$CF_3CHOHCF_3$	High	Protic	9.3	1600

Electrostatic interactions

Polar regions in molecules undergo electrostatic interactions, such as hydrogen bonding and dipole-dipole interactions, due to attraction between their electron rich and electron deficient atoms. This is the case with diphenylalanine. Within the molecule, hydrogen atoms which are attached to electronegative atoms, including oxygen, nitrogen or fluorine, become slightly positively charged, represented by the Greek letter δ. This causes them to be attracted to areas of high electron density such as lone pairs of electrons. The interaction between a $H^{\delta+}$ and a lone pair is defined as a hydrogen bond. This type of bonding is unique to hydrogen because hydrogen is the only non-metal Hydrogen bonding can occur within and between diphenylalanine molecules, as well as between diphenylalanine and neighbouring solvent molecules (**Figure 3.27**).

Dipole-dipole interactions are electrostatic interactions in which the slightly positively charged part of a molecule is attracted to the slightly negatively charged part of another molecule. At long distances (> 0.35 nm), diphenylalanine-diphenylalanine and diphenylalanine-solvent hydrogen bonds become purely electrostatic, acting in much the same way as dipole-dipole interactions. At shorter distances (0.2-0.3 nm) [200], repulsion between the lone pair of electrons and electrons associated with the donor hydrogen (Pauli repulsion) [187], and delocalisation of the lone pair electron density, play much larger roles. This accounts for the increased strength of intramolecular hydrogen bonds and intermolecular hydrogen bonds between neighbouring diphenylalanine molecules.

The average strength of a hydrogen bond is between that of dipole-dipole interactions and covalent/ ionic bonds. This accounts for why hydrogen bonds are stronger than other dipole-dipole interactions but are disrupted by the interference of covalent or ionic bonds.

The presence of localised polar regions within HFIP encourage the folding of diphenylalanine molecules into hydrophobic and hydrophilic regions via intramolecular hydrogen bonding. Diphenylalanine molecules individually fold into what are known as β-turn structures, aligning the phenyl rings and NH_2/ COOH groups separately. During the formation of diphenylalanine microtubes, these folded diphenylalanine molecules undergo intermolecular H-bonding between the NH_2/ COOH groups of different molecules. Aromatic stacking and the alignment of the molecules into anti-parallel β-sheets leads to the formation of diphenylalanine dimers.

171
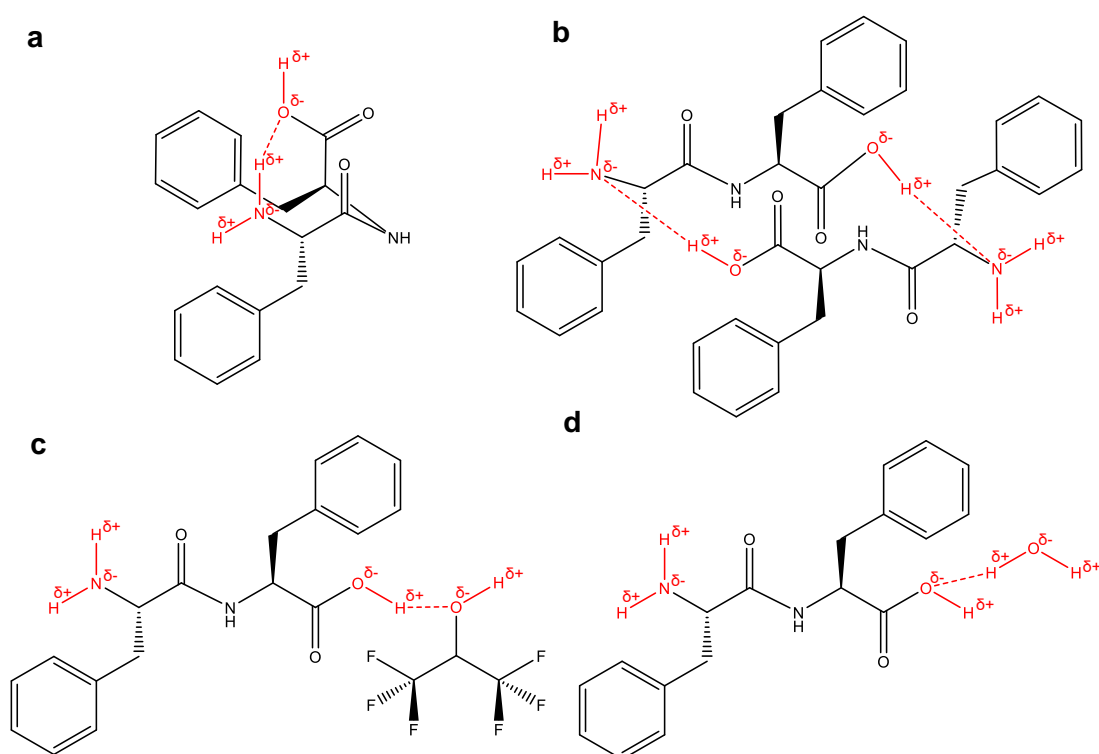
Figure 3.27 *Examples of a) intramolecular hydrogen bonding within diphenylalanine molecules, b) intermolecular hydrogen bonding between diphenylalanine molecules and c,d) intermolecular hydrogen bonding between diphenylalanine and solvent molecules.*

Aromatic interactions

Aromatic rings contain delocalised π-electrons which can interact non-covalently with other aromatic rings through π-π stacking. The stacking of aromatic rings is an attractive interaction which acts over distances up to 0.44 nm [200] and increases the stability of the system. The presence of two terminal phenyl groups on diphenylalanine allow π-π stacking to occur during the self-assembly process.

Upon the addition of water, the phenyl rings of folded diphenylalanine molecules stack together, forming hydrophobic and hydrophilic regions (**Figure 3.28**).
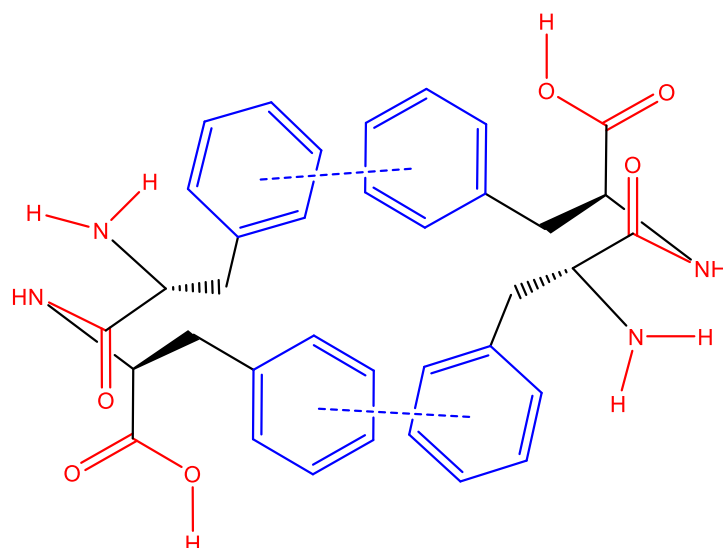
Figure 3.28 *Representation of aromatic stacking between diphenylalanine molecules. The π-π interaction is represented by the blue dashed line. The resulting hydrophobic and hydrophilic regions are highlighted in blue and red respectively.*

The diphenylalanine molecules orientate to allow the hydrophilic regions to surround as many water molecules as possible thus creating the most energetically favourable configuration. In order to fully encapsulate the water molecules, diphenylalanine dimers join together to form hexagonal based prisms with an inner hydrophilic channel.

3.6.3. Poly[Vinylidene Fluoride-co-Trifluoroethylene]

In the electrospinning of PVDF-TrFE nanofibres, a clear relationship between higher polymer concentration and larger fibre diameter was observed. This is probably because higher concentration polymer solutions have higher viscosity and in turn experience a larger frictional force as the droplet travels through the needle and leaves the nozzle, compared to lower viscosity solutions. The most effective way to control the properties of electrospun fibres is to vary the concentration of the initial polymer solution, however, changing the electrospinning parameters can also have a significant effect on the fibre properties.

Preliminary results showed that increasing the spinning height led to fibres with smaller diameters. It was also observed that increasing the flow rate while keeping the electrospinning voltage the same caused the Taylor cone, the conical droplet which forms at the end of the nozzle, to become unstable. This led to polymer blebs forming along with the fibres and a decreased uniformity between the fibres because the Taylor

173

cone was not sufficiently stretched by the electric field before the polymer reached the plate.

Molecular Alignment Within PVDF-TrFE Nanofibres

The β-phase of PVDF-TrFE represents a conformation in which all the carbon – fluorine bonds are aligned perpendicular to the carbon chain [201]. This alignment means that the C—F bonds will only fully absorb one direction of radiation. This feature allows the molecular alignment in PVDF-TrFE electrospun fibres to be probed by polarised Fourier Transform Infrared Spectroscopy (FTIR).

A comparison of the polarised FTIR spectra for PVDF-TrFE nanofibres at 0° and 90° shows that the absorption band at 1284 cm^{-1} (C-F symmetric stretching) is stronger at 0° compared to 90° whereas the absorption bands at 1076 cm^{-1} (C-F wagging) and 1398 cm^{-1} (C-H wagging) are stronger at 90° than at 0°. This suggests that the C–F bonds are aligned perpendicular to the fibre length, as depicted in **Figure 3.29**.
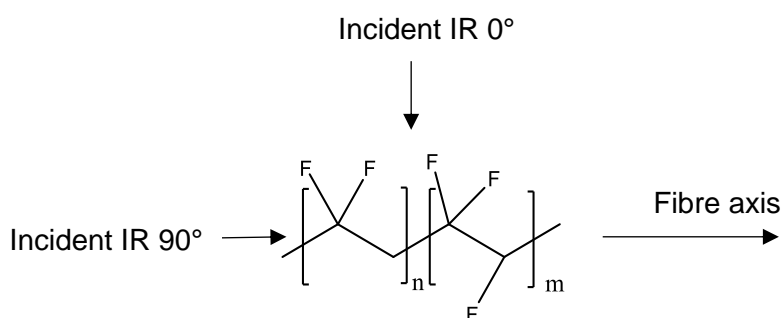
Figure 3.29 *Skeletal formula of PVDF-TrFE with axis along fibre length and direction of incident radiation labelled.*

Relationship Between PVDF-TrFE Fibre Nanostructure and Piezoelectric/ Mechanical Properties

Variations in piezoelectric response were recorded at different positions along the electrospun PVDF-TrFE nanofibres. This is likely due to the semi-crystalline structure of the PVDF-TrFE copolymer. Some areas of the fibre are highly crystalline and display a high piezoelectric response while other areas are amorphous and have no piezoelectric response; piezoresponse force microscopy (PFM) is able to provide information on the localised piezoelectric properties of polymer nanofibres rather than the bulk polymer properties.

The magnitude of the piezoelectric coefficient, d_{33}, of a PVDF-TrFE nanofibre is largely dependent on its β phase content since the net dipole of the β phase is greater than the net dipoles of α and γ phases. Increased molecular alignment and crystallinity in nanofibres with smaller diameters have been attributed for the trend of increased d_{33} and enhanced mechanical properties observed with decreasing diameter [184].

The piezoelectric response of diphenylalanine proved difficult to measure by PFM since individual diphenylalanine microtubes required immobilisation to allow measurements to be taken. Piezoresponse force microscopy is a contact technique, in which the tip is in constant contact with the material surface. Diphenylalanine microtubes immobilised with vertical orientation would have facilitated the measurement of the d_{33} while horizontal clamping of the microtubes would have facilitated measurement of the d_{15}. Neither vertical immobilisation by growth within an anodised aluminium oxide template, or horizontal immobilisation by sealing with conductive glue or partial embedding in epoxy were successful in this work. All PFM attempts for diphenylalanine were hindered by microtubes moving during measurement. The same issues were not encountered during the measurement of PVDF-TrFE nanofibres by PFM. Although the nanofibre diameters are smaller than that of diphenylalanine microtubes, the entangled electrospun fibres form a soft membrane which is stable and able to support the PFM measurements.

3.6.4. Human Cell Response to the Piezoelectric Materials Investigated

Investigation of the general cell toxicity of L-diphenylalanine, D-diphenylalanine, Fmoc-diphenylalanine and their respective self-assembled microstructures *in vitro* revealed that L- and D-diphenylalanine casts were able to support human dermal fibroblast growth, while Fmoc-diphenylalanine casts and hydrogel caused widespread necrosis by day 3. Truong *et al.* previously reported a cytotoxic effect caused by Fmoc-diphenylalanine leeching into the cell culture medium [202]. However, there are contradictory reports in the literature regarding the cytotoxicity of Fmoc-diphenylalanine materials, with some concluding that Fmoc-diphenylalanine supports cell growth *in vitro* [203], while others claim that Fmoc-diphenylalanine is highly toxic *in vitro* [202]. It is likely that studies recording a non-toxic effect of Fmoc-diphenylalanine *in vitro* are using very low concentrations of the material. Other studies have reported non-toxicity of self-assembled peptide hydrogels [204] and it was suggested by Truong *et al.* that metabolic processes inside a living organism would be capable of clearing solubilised peptide before it was able to reach toxic concentrations. The concentration of Fmoc-

diphenylalanine used for the experiments described here is clearly above the cytotoxicity threshold and the material was not studied further at this concentration.

Both L- and D-diphenylalanine changed morphology after extended contact (>24 h) with cell culture medium. The medium caused some microtube formation on the surface of the diphenylalanine cast materials and caused dissolution of a large proportion of the diphenylalanine microtubes. Enough medium was added to each well to last for the whole experiment, so the diphenylalanine materials were not removed during the experiments despite dissolution. The L- and D-diphenylalanine materials showed similar cell viability to the cells grown on glass coverslips with the exception of D-diphenylalanine microtubes, which showed an unusual delayed toxicity effect. Later experiments revealed that Fmoc-diphenylalanine not only kills cells in direct contact but also has a detrimental effect on cells in neighbouring wells. In the preliminary experiment, D-diphenylalanine microtube samples were positioned next to the Fmoc-diphenylalanine materials and may have been affected by their toxicity. A delayed toxicity effect for D-diphenylalanine materials was not observed in any later experiments.

Further investigations studied the effect of diphenylalanine casts and microtubes on human Schwann cells. The results showed that all the diphenylalanine materials supported cell growth to a similar degree but caused cells to grow slower than on glass coverslips. It is possible that dissolved diphenylalanine does not have a detrimental effect on cells in culture but cells less readily attach to diphenylalanine materials than glass.

Measurement of the metabolic activity and cell proliferation of human Schwann cells grown on PVDF-TrFE nanofibres revealed that cell viability is reduced by approximately 20- 30% in the presence of the nanofibres. Cell proliferation is largely the same for all fibre diameters across all timepoints but a large decrease in cell proliferation is observed by day 5 when compared to the positive control. Fibre diameter also had little effect on the cell viability, with all day 5 results showing cell viabilities within the range of 70-80%.

Fluorescence microscopy revealed that PVDF-TrFE nanofibres directed the growth of the Schwann cells, with cells aligning along the fibre length. Alignment of neural type cells along the length of piezoelectric fibres has been described in previous studies with Schwann cells and dorsal ganglion neurons [60, 61], with researchers reporting that electrospun nanofibres coated with proteins showed improve cell attachment and enhanced cell growth along the fibres.

A study by Wu *et al.* discussed the attachment of Schwann cells directly to PVDF-TrFE nanofibres or to Matrigel, a gelatinous mouse protein mixture [60], and reported that cells had a much higher affinity for attaching to Matrigel coated PVDF-TrFE fibres than uncoated PVDF-TrFE nanofibres. The HSCs used in this work were coated with poly-L-lysine prior to seeding to encourage attachment but later studies could apply Matrigel instead to further enhance cell attachment and proliferation.

3.7. **Summary**

The work described in this chapter on the controlled assembly of piezoelectric materials, focused on an investigation of the formation and properties of diphenylalanine microtubes and PVDF-TrFE nanofibres.

The average crystallite sizes of L- and D-diphenylalanine powders were calculated as 37 nm and 48 nm respectively, using the Scherrer equation. A difference in L- and D-diphenylalanine microtube size was also observed by SEM, with L-diphenylalanine microtubes having average length 300 μm and diameter 2 μm, and D-diphenylalanine microtubes having average length 100 μm and diameter 4 μm. The size difference was attributed to D-diphenylalanine having a large crystallisation energy in the direction perpendicular to the microtube length, causing it to self-assemble into thicker, shorter microtubes compared to L-diphenylalanine.

L- and D-diphenylalanine microtubes were considered as hexagonal prism-shaped cantilevers and their average resonant frequencies were calculated as ~6.4 kHz and ~175 kHz respectively. The average resonant frequency of a L-diphenylalanine microtube falls within the frequency range of human hearing whereas that for a D-diphenylalanine microtube of average dimensions is ~ 7.5x greater than the highest frequency perceivable by the human ear.

For at least some applications, diphenylalanine microtubes need to be arranged in an aligned array to maximise the piezoelectric output. Growth within an AAO template produced diphenylalanine nanotubes with general vertical alignment. The constraints applied by the AAO template appeared to affect the self-assembly process by restricting hydrogen bonding and molecular arrangements. Investigations into the piezoelectric properties of nanotubes grown within AAO templates would be required before any applications could be considered.

Polarised FTIR of PVDF-TrFE nanofibres suggested that C–F bonds are aligned perpendicular to the fibre length. This was supported by an enhanced absorption band

at 1284 cm^{-1} (F-C-F symmetric stretching) and diminished absorption bands at 1076 cm^{-1} (F-C-F wagging) and 1398 cm^{-1} (C-H wagging) in the spectrum recorded at 0°.

Variations in piezoelectric response of PVDF-TrFE were recorded at different positions along the electrospun nanofibres due to the semi-crystalline structure of the PVDF-TrFE copolymer. The d_{33} recorded for PVDF-TrFE electrospun nanofibres increased from 32 pmV^{-1} to 59 pmV^{-1} as the nanofibre diameter decreased from 650 – 325 nm. A similar trend was observed for mechanical properties, with the Young's modulus increasing from 0.8 GPa to 12.1 GPa over the same diameter range. The trends have been attributed to structural changes within the fibre, such increased crystallinity and a higher degree of order in the microstructure of the polymer chains.

The piezoelectric response of diphenylalanine proved difficult to measure by piezoresponse force microscopy (PFM) since individual diphenylalanine microtubes required immobilisation to allow measurements to be taken. All PFM attempts for diphenylalanine were hindered by microtubes moving during measurements.

Human Schwann cells grown on diphenylalanine and PVDF-TrFE materials showed reduced viability compared to cells grown on glass coverslips. PVDF-TrFE nanofibres were found to direct cell growth along the length of the fibres. This could prove useful for applications in regenerative medicine where directed cell growth around an implanted device may be desirable.

Diphenylalanine has been identified as a promising candidate piezoelectric material. It has been characterised and compared to PVDF-TrFE nanofibres, which have been explored by other members of the same research group. The next stage in the programme is to combine these materials with carbon nanotubes to provide the means of transferring charge, which is the work of the next chapter.

Chapter 4   **Covalent Assemblies of Carbon Nanotubes and Diphenylalanine**

The previous chapter explored piezoelectric materials as the source for an electric potential difference. It is then necessary to consider how the charge can be accumulated and transported between a device and a neuron. On a nanoscale, a candidate material is the carbon nanotube. Contact between the two is likely to be best achieved by the formation of a complex.

4.1.   **Carbon Nanotube-Diphenylalanine Assemblies**

Carbon nanotubes and diphenylalanine can be combined to form complexes and composites. The properties of synthesised materials and assemblies can comprise aspects of both carbon nanotubes and diphenylalanine; properties can be tailored towards the desired application by adjusting the quantities of each component or using an alternative synthesis method.

A few reports in the literature explore the combination of carbon nanotubes with diphenylalanine and its derivatives. A covalently bonded carbon nanotube-diphenylalanine complex has been formed by employing an organic compound linker to join the two moieties. It was suggested that the synthesised complex could be developed into a hydrogel for biomedical applications [121]. Physically assembled carbon nanotube-diphenylalanine composites have also been demonstrated and have been explored as electrode coatings for biosensors [205].

In both the above examples, the carbon nanotubes were functionalised by oxidative acid treatment, which is known to greatly disrupt their sp^2 hybridised graphitic structure [206]. This disruption diminishes the carbon nanotube conductivity and limits the applications of assembled materials, particularly in cases where the material is required to facilitate charge transfer. The studies cited here have investigated specific properties relevant to their desired applications; however, full characterisation of a carbon nanotube-diphenylalanine complex with a range of spectroscopic and microscopic techniques is yet to be reported.

It is desirable that the synthesised complex should have a high electrical conductivity; this work therefore explores the covalent linkage of plasma functionalised carbon nanotubes with multiple derivatives of diphenylalanine. A carbon nanotube-diphenylalanine complex comprising plasma functionalised carbon nanotubes has the

179

potential to exhibit higher conductivity than complexes containing acid treated carbon nanotubes. This is because the graphitic carbon nanotube structure sustains less damage during plasma treatment [116] compared to the damage caused by treatment with strong acids. The use of multiple diphenylalanine derivatives allows exploration into the effect of amine terminus-protected diphenylalanine on the properties of a complex compared to free carboxyl terminus and free amine terminus diphenylalanine derivatives.

4.2. **Aims**

Diphenylalanine is a candidate material for the piezoelectric component of an implantable device. The work described in this chapter on covalent assemblies investigates the feasibility of directly linking diphenylalanine with carbon nanotubes. The materials are being combined towards the aim of forming an electrode material capable of harvesting the piezoelectric energy generated by diphenylalanine microtubes in response to sound. This involves the synthesis of a carbon nanotube-diphenylalanine complex through the formation of amide linkages between the two materials and subsequent characterisation of the synthesised complex. The objectives of this work were to:

- synthesise carbon nanotube-diphenylalanine covalently bonded complexes employing three diphenylalanine derivatives;
- characterise the carbon nanotube-diphenylalanine complex;
- explore the self-assembly of aligned diphenylalanine microtubes around the synthesised carbon nanotube-diphenylalanine complex;
- evaluate the effect of the synthesised complex on Human Schwann cells in culture

4.3. **Carbon Nanotube-Diphenylalanine Complex Synthesis**

Carboxylic acid functionalised multiwall carbon nanotubes were covalently linked to L-diphenylalanine or D-diphenylalanine to create a complex, as illustrated in **Figure 4.1**. Similarly, amine functionalised multiwall carbon nanotubes were covalently linked to Fmoc-diphenylalanine to create a complex, as shown in **Figure 4.2**.
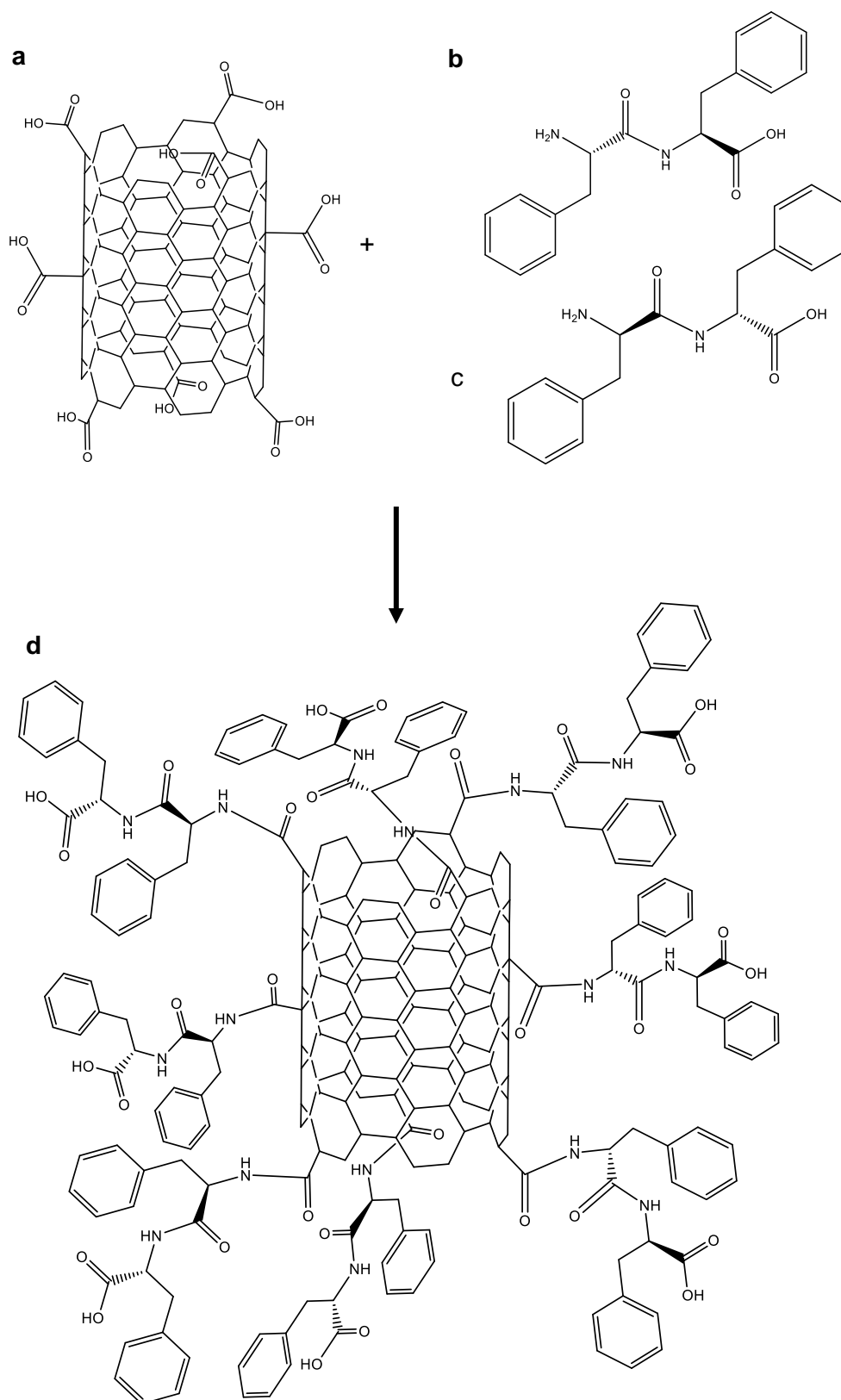
Figure 4.1 *Schematic of diphenylalanine addition to carboxylated carbon nanotubes.
a) MWCNT-COOH, b) L-diphenylalanine, c) D-diphenylalanine, d) Multiwall carbon
nanotube-diphenylalanine complex*
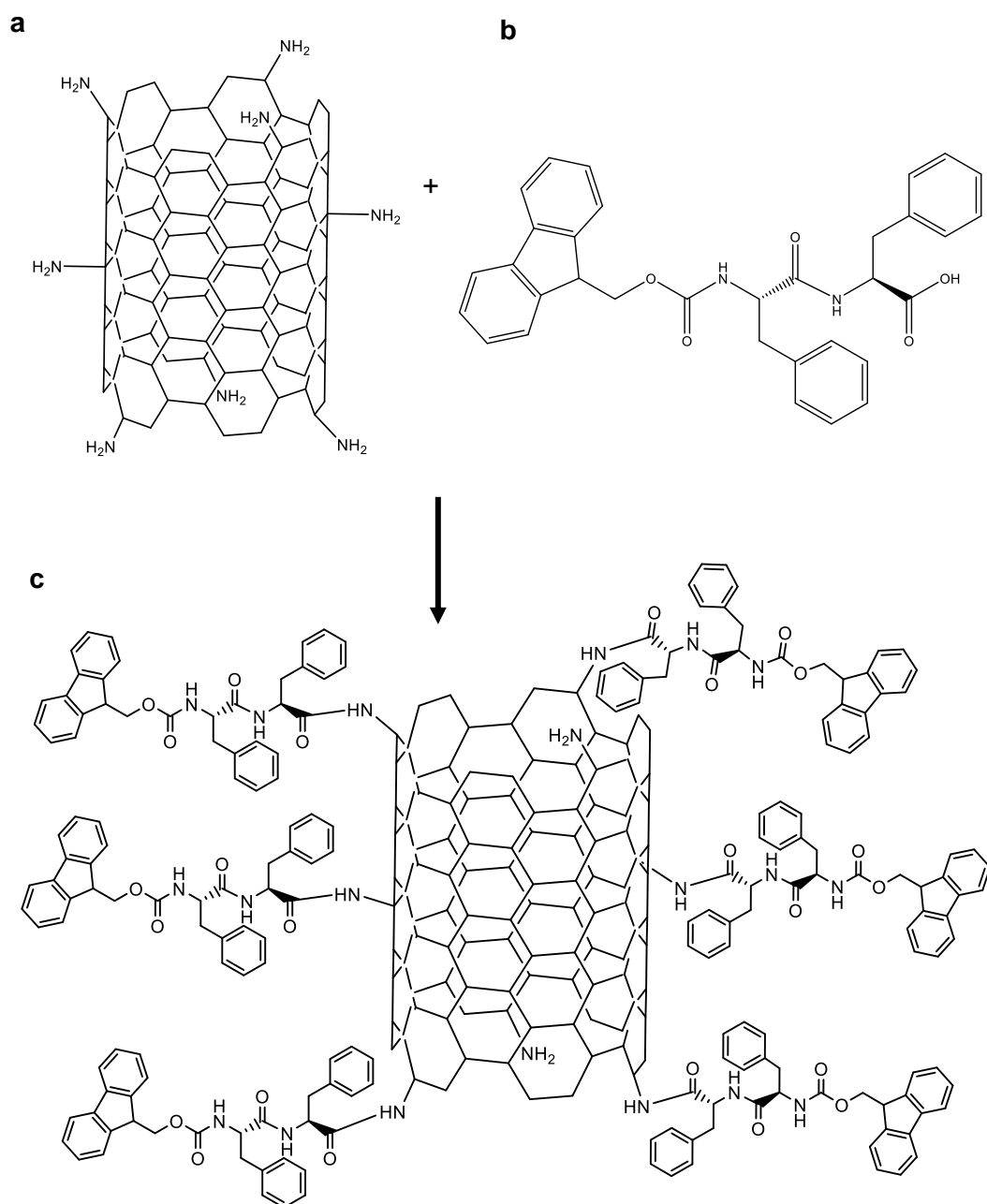
Figure 4.2 *Schematic of Fmoc-diphenylalanine addition to amine functionalised carbon nanotubes. a) MWCNT-NH$_2$, b) Fmoc-diphenylalanine, c) Multiwall carbon nanotube-Fmoc-diphenylalanine complex*

The covalent complex was prepared by activating either the carboxylic acid terminus of carboxylated carbon nanotubes or the carboxyl terminus of Fmoc-diphenylalanine. The process for preparing complexes with L- and D- diphenylalanine differed from that for Fmoc-diphenylalanine and they will be described separately.

4.3.1. Estimation of Molar Amounts of COOH and NH₂ Groups Present on Functionalised Carbon Nanotubes

The amount of diphenylalanine to be added for each reaction was calculated based on an estimate of the molar amount of COOH and NH_2 groups on the plasma functionalised carbon nanotubes.

Based on data from a commercial supplier of functionalised carbon nanotubes [207], an estimated 10% of the surface of a carboxylic acid functionalised single wall carbon nanotube (SWCNT-COOH) (Haydale) is made up of COOH groups.

For 1 mg SWNT, there are 0.1 mg of COOH. The relative molecular mass (RMM) for a COOH group is 45 g, therefore, using the equation *moles = mass/ RMM,* it can be estimated that COOH functionalised SWNTs contain 2.2×10^{-6} moles of COOH per mg. If less than half of the mass of a MWCNT is due to the mass of surface atoms, it can be estimated that ~ 1×10^{-6} moles of COOH are present per mg of COOH functionalised MWCNT.

For amine functionalised multiwall carbon nanotubes, it is estimated that 0.6% of the surface of MWCNT is NH_2. Following the argument from above, less than half of the MWCNT mass is due to surface atoms. Therefore, for 1 mg MWCNT, it can be estimated that 0.17×10^{-6} moles of NH_2 are present.

4.3.2. Synthesis of Multiwall Carbon Nanotube- L-Diphenylalanine and Multiwall Carbon Nanotube-D-Diphenylalanine Complex

The protocol for the formation of a covalent carbon nanotube-diphenylalanine complex was developed according to a general carboxylic acid-HBTU-amine protocol which was verbally communicated by Dr. Bala Ramesh (Academic Laboratory Lead, Department of Surgical Biotechnology, UCL).

Carboxyl functionalised multiwall carbon nanotubes (MWCNT-COOH), 9.9 mg, and HBTU, 3.79 mg, were added to a 250 ml round bottom flask. The molar ratio of MWCNT-COOH to HBTU was 1:1 based on the estimated number of moles of COOH groups per milligram of MWCNT-COOH, as described in Section 4.3.1. 50 ml of a mixed solvent of 0.6 M N-methylmorpholine (NMM) in dimethylformamide (DMF), was added to the round bottom flask and the mixture was exposed to ultrasonic agitation for 5 mins. A magnetic stirring bar was added to the flask and the mixture was stirred for ten mins at 20 °C.

The black suspension was transferred to centrifuge tubes and centrifuged at 4000 rpm for 30 mins. Following centrifugation, the supernatant, which was still darkly coloured, was discarded to remove unreacted coupling agent. The sediment was resuspended in DMF/NMM mixed solvent and centrifuged and this process was repeated until the supernatant was almost clear. The remaining sediment was returned to the round bottom flask and suspended in 50 ml DMF/NMM mixed solvent.

One molar equivalent of L-diphenylalanine or D-diphenylalanine, which was calculate as 3.12 mg, was added to the flask and the mixture was stirred for 1 h. To monitor the progress of the reaction, one microspatula of 3,4 dihydro-3-hydroxy-4-oxo-1,2,3,benzotriazine, an indicator for the presence of primary amines, was added. The indicator, which was initially yellow in colour, became colourless as the reaction proceeded and primary amine became depleted. After 1 h, the yellow colour of the indicator had disappeared and the reaction was considered complete. The suspension was transferred to centrifuge tubes and centrifuged at 4000 rpm for 30 mins. The supernatant was then discarded and the sediment was returned to the round bottom flask and suspended in 50 ml DMF/NMM mixed solvent.

A second molar equivalent, 3.12 mg of L-diphenylalanine or D-diphenylalanine was added to the flask and stirred for 1 h. This step was included to maximise the final product yield in case of any unwanted side-reactions during the first reaction period. The process of centrifugation and decanting of the supernatant was repeated as previously described. The sediment was removed from the centrifuge tube and spread in a thin layer on a glass evaporating dish. The product, multiwall carbon nanotube- L-diphenylalanine (MWLFF) or multiwall carbon nanotube-D-diphenylalanine (MWDFF), was dried in a vacuum oven at 60 °C for 18 h.

The dried product was transferred to a pre-weighed glass vial and sealed with parafilm. The mass of the product was 8.2 mg in both cases, giving a yield of 63%. A mass of 0.2 mg of the product was transferred to a fresh glass vial with 1 ml DMF/NMM mixed solvent. The mixture was exposed to ultrasonic agitation for 10 mins. The resulting suspension was left undisturbed for one month to test the stability of the complex. Parallel to this, two samples of 0.2 mg of the product were transferred to glass vials and dispersed in industrial methylated spirit (IMS) and water respectively. The samples were exposed to ultrasonic agitation and left undisturbed also for one month to test their stability.

4.3.3. Synthesis of Multiwall Carbon Nanotube- Fmoc-Diphenylalanine Complex

Molar equivalents of Fmoc(-L)-diphenylalanine, 5.35 mg, and HBTU, 3.79 mg, were added to a 100 ml round bottom flask along with 25 ml DMF/NMM mixed solvent and stirred for 20 mins. Parallel to this, amine functionalised multiwall carbon nanotubes (MWCNT-NH$_2$), 52.6 mg, were suspended in 50 ml DMF/NMM mixed solvent in a 250 ml round bottom flask and exposed to ultrasonic agitation for 10 mins. The molar ratio of MWCNT-NH$_2$ to HBTU was 1:1 based on the number of moles of NH$_2$ groups per milligram of MWCNT-NH$_2$ estimated in Section 4.3.1. The solution of Fmoc-diphenylalanine was added to the round bottom flask containing the suspended MWCNT-NH$_2$. The mixture was stirred for 1 h at 20 °C.

The suspension was transferred to centrifuge tubes and centrifuged at 4000 rpm for 30 mins. The supernatant was discarded and the sediment was resuspended in DMF/NMM mixed solvent and centrifuged at 4000 rpm for 15 mins. The supernatant was discarded and the sediment was resuspended in DMF/NMM mixed solvent. The centrifugation process was repeated to remove any unreacted coupling agent from the suspension.

The sediment was removed from the centrifuge tube and spread in a thin layer on a glass evaporating dish. The product, multiwall carbon nanotube- Fmoc-diphenylalanine (MWFmocFF) was dried in a vacuum oven at 60 °C for 18 h.

The dried product was transferred to a pre-weighed glass vial and sealed with parafilm. The mass of the product was 54.7 mg, giving a yield of 94%. A mass of 0.2 mg of the product was transferred to a fresh glass vial with 1 ml DMF/NMM mixed solvent. The mixture was exposed to ultrasonic agitation for 10 mins. The resulting suspension was left undisturbed for 1 month to test the stability of the complex. Parallel to this, two samples of 0.2 mg of the product were transferred to glass vials and dispersed in IMS and water respectively. The samples were exposed to ultrasonic agitation and left undisturbed for one month to test their stability.

4.4. Characterisation of Physical and Chemical Properties of Carbon Nanotube-Diphenylalanine Complexes

The relationship between the structures of carbon nanotube-diphenylalanine complexes and their properties were investigated using a range of characterisation

techniques. The macro, micro and nanoscale behaviour of the complexes was
compared to those of functionalised carbon nanotubes to determine the effect of the
covalently bonded diphenylalanine component within the complexes.

4.4.1. Stability of Carbon Nanotube Complexes Suspended in Solvents

Prepared complex suspensions were tested for their physical stability; that is, their
ability to remain suspended and dispersed in the particular solvent over time, generally
on a timescale of months. Samples of MWLFF, MWDFF and MWFmocFF dispersed in
a mixture of DMF, a high polarity, aprotic solvent, and N-methylmorpholine, a low
polarity, aprotic solvent, showed the greatest stability, remaining well dispersed in the
solvent after more than a year, where samples dispersed in water, a high polarity,
protic solvent, showed low stability, with large agglomerates forming and sinking to the
bottom of the vial almost immediately. Samples dispersed in industrial methylated
spirit, another high polarity, protic solvent, remained stable for approximately one hour
before some of the complex began to settle to the bottom. The remaining complex
agglomerated and settled slowly over a 24-hour period.

To confirm that the stability of the complex arose from covalent functionalisation, a
mixture of carbon nanotubes and diphenylalanine was dispersed in a DMF/NMM mixed
solvent alongside the carbon nanotube complex dispersion (**Figure 4.3**). Both vials
were exposed to ultrasonic agitation for 5 minutes before being left to stand
undisturbed for 1 h. After an hour had passed, the complex remained well dispersed,
while the mixture showed suspended aggregates and a carbon nanotube sediment.

4.4.2. Effect of Complex Formation on the Graphitic Structure of Carbon Nanotubes

The purpose of employing Raman spectroscopy in this work was twofold: to determine
if the formation of a covalently bonded carbon nanotube-diphenylalanine complex
introduced additional defects into the carbon nanotube graphitic basal plane, and to
identify whether there was any interaction between diphenylalanine and the carbon
nanotube walls.

Powder samples of the starting carbon nanotube materials (MWCNT-COOH and
MWCNT-NH$_2$) and covalent complexes (MWLFF, MWDFF and MWFmocFF) were
placed on a glass microscope slide, flattened using a second microscope slide and

imaged in a Renishaw inVia Raman microscope. The settings of the Raman microscope are detailed in Section 2.2.2.

Figure 4.3 *Dispersions (in a DMF/ N-methylmorpholine mixed solvent) of MWLFF complex (left) and a mixture of MWCNT-COOH and L-diphenylalanine (right) after a one hour resting period post dispersion*

As discussed in Section 2.2.2, the Raman spectrum of a pristine multiwall carbon nanotube typically consists of three or four scattering peaks. These peaks appear at wavenumbers 1335 cm^{-1} (D band),1570 cm^{-1} (G band), 2670 cm^{-1} (2D resonance band) and 2910 cm^{-1} (G+D band) as shown in the Raman spectra in **Figure 4.4**. The D band arises as a result of defects in the carbon nanotube structure, which are often created during functionalisation. It is therefore expected that functionalised carbon nanotubes would exhibit a high intensity D band with a D:G band ratio >1. It is seen from **Table 4.1** that the D:G band ratios of the covalent complexes are similar in magnitude to those of the functionalised carbon nanotubes. This indicates that forming a complex between carbon nanotubes and diphenylalanine does not introduce further defects into the carbon nanotube graphitic structure. A decrease in the D:G ratio is observed for MWFmocFF compared to MWCNT-NH$_2$. This could indicate a physical association between MWFmocFF and the carbon nanotube walls.

A small peak at ~2300 cm^{-1} is visible in the spectrum of MWCNT-NH$_2$. This may be
caused by the C-N bonds between the carbon nanotubes and amine functional groups.
This has not however, been reported widely in the literature and could also arise due to
the presence of atmospheric nitrogen. The peak at 2435 cm^{-1} in the spectra of the
MWCNT-NH$_2$ and MWFmocFF samples is likely an overtone of the D and D' bands [208].
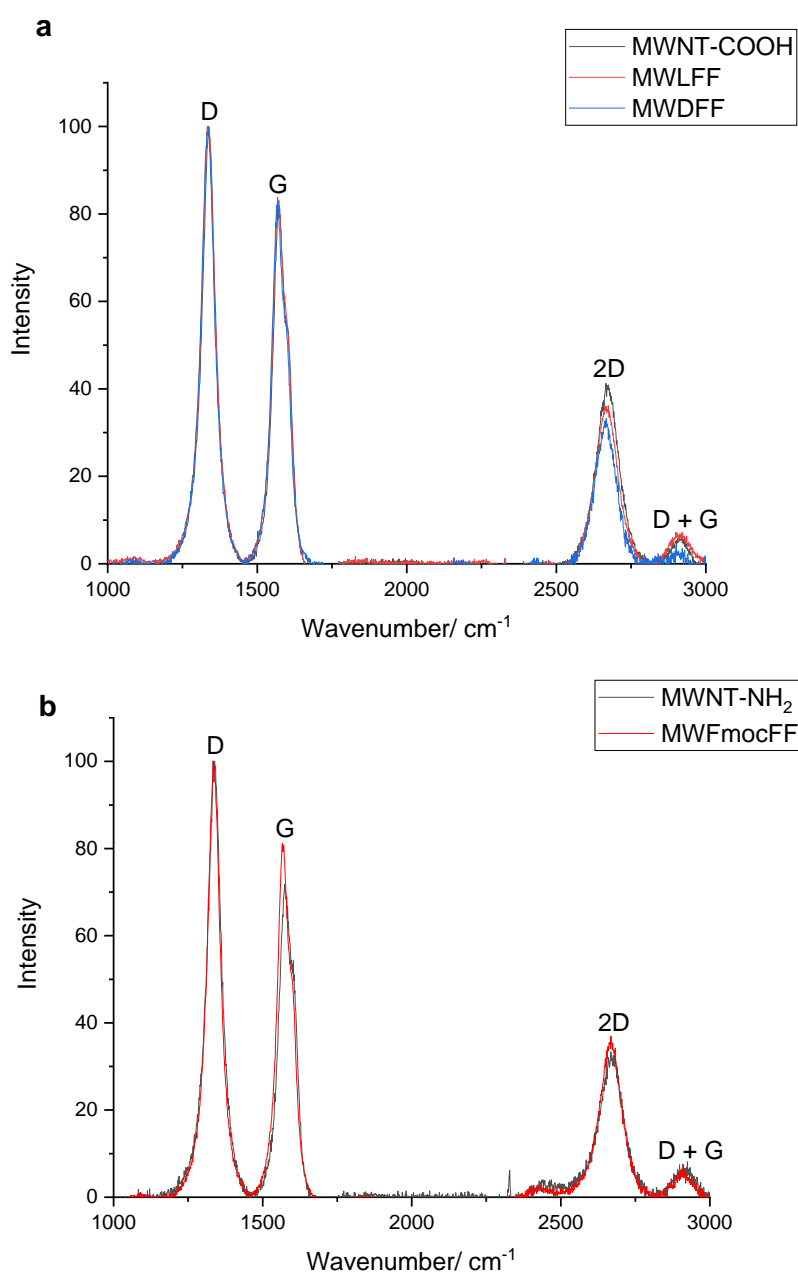
Figure 4.4 Raman spectra of functionalised carbon nanotubes and carbon nanotube
complexes. a) MWCNT-COOH, MWLFF, MWDFF, b) MWCNT-NH$_2$, MWFmocFF. All
graphs show the D band (1335 cm^{-1}), G band (1570 cm^{-1}) and 2D band (~2700 cm^{-1})
characteristic of carbon nanotubes.

Table 4.1 Comparison of D and G band positions and intensities for the Raman
spectra of functionalised carbon nanotubes and carbon nanotube complexes.
Literature values for MWCNT are included for reference

Sample	D band Position/ cm^{-1}	G band Position/ cm^{-1}	2D band Position/ cm^{-1}	D + G band Position/ cm^{-1}	D:G Intensity Ratio
MWLFF	1335	1569	2666	2912	1.14
MWDFF	1335	1569	2666	2912	1.17
MWFmocFF	1335	1566	2668	2907	1.19
MWCNT-COOH	1338	1573	2670	2915	1.18
MWCNT-NH$_2$	1339	1573	2671	2922	1.29
MWCNT [208]	1365	1598	2711	2966	0.383

4.4.3. Crystal Structure of Carbon Nanotube-Diphenylalanine Complexes

The crystal structures of the synthesised carbon nanotube-diphenylalanine complexes
were investigated using X-ray powder diffraction. Powder samples of the starting
carbon nanotube materials (MWCNT-COOH and MWCNT-NH$_2$) and covalent
complexes (MWLFF, MWDFF and MWFmocFF) were measured using the procedure
described in Section 2.2.3.

X-ray diffractograms of the functionalised carbon nanotubes and carbon nanotube-
diphenylalanine complexes (**Figure 4.5**) show two broad peaks at ~25.5° and ~43°,
corresponding to the graphite (002) and graphite (100) planes respectively. The
relationship between the crystal planes, XRD peak position and d-spacing of
functionalised carbon nanotubes and the carbon nanotube-diphenylalanine complexes
are shown in **Table 4.2**.

Table 4.2 The d-spacings calculated from XRD peak positions for functionalised
carbon nanotubes and carbon nanotube-diphenylalanine complexes. The d spacings
for graphite and corresponding Miller Indices for all samples are shown for reference.

	Miller Index	XRD Peak Position (2θ)/ °	d spacing/ nm	Crystallite Size/ nm
MWCNT-COOH	002	25.6	0.348	1.09
	100	43.2	0.209	
MWLFF	002	25.4	0.350	1.11
	100	43.3	0.209	
MWDFF	002	25.4	0.350	1.11
	100	43.4	0.208	
MWCNT-NH$_2$	002	25.7	0.346	1.47
	100	42.9	0.211	
MWFmocFF	002	25.7	0.346	2.23
	100	42.9	0.211	
Graphite	002 [209]		0.335	38
	100		0.246 [92]	
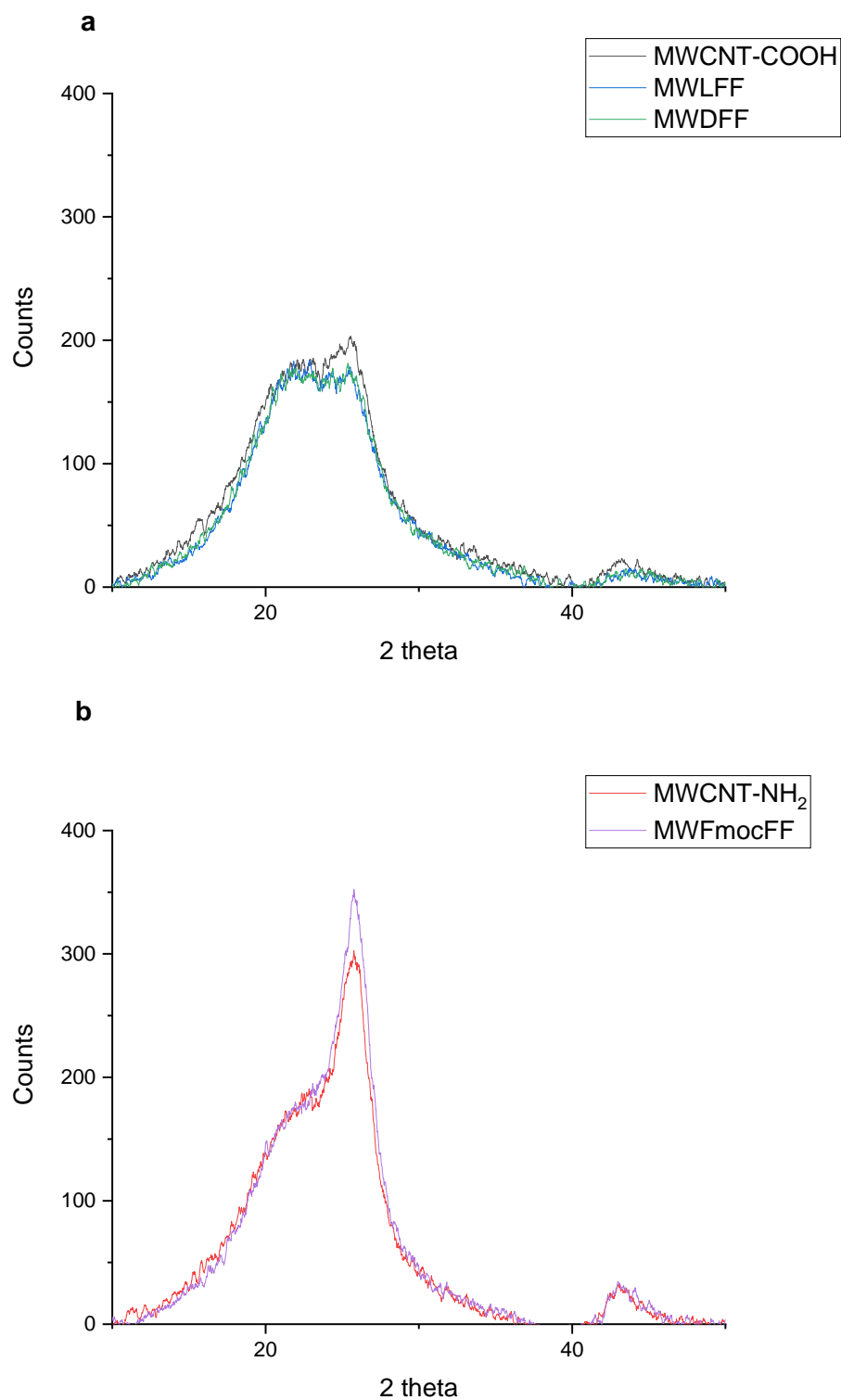
Figure 4.5 *X-ray diffractograms of functionalised carbon nanotubes and carbon nanotube complexes. a) MWCNT-COOH, MWLFF, MWDFF, b) MWCNT-NH₂, MWFmocFF.*

The sharper diffraction peaks observed for the MWCNT-NH$_2$ and MWFmocFF samples indicate greater crystallinity and a more ordered graphite structure than the MWCNT-COOH, MWLFF and MWDFF samples. A comparison of crystallite size also supports this, with MWCNT-COOH and MWCNT-NH$_2$ having crystallite sizes of 1.09 nm and 1.47 nm respectively. This could be expected since a greater percentage (~10%) of the MWCNT-COOH surface is functionalised compared to ~0.6% for MWCNT-NH$_2$. Functionalisation is known to introduce defects and reduce crystallinity [116].

4.4.4. Surface Morphology and Nanoscale Internal Structure of Carbon Nanotube-Diphenylalanine Complexes

The surface morphologies of carbon nanotube-diphenylalanine complex depositions were observed by scanning electron microscopy. Carbon nanotubes and covalent complexes were dispersed in IPA at a concentration of 0.2 mg ml^{-1} and subjected to ultrasonic agitation for 10 mins prior to depositing a 50 µl aliquot of each sample directly onto SEM stubs. The samples were dried at 20 °C for 18 h prior to imaging. Samples were imaged using a Zeiss scanning electron microscope, as detailed in Section 2.2.9.

The scanning electron micrographs reveal diphenylalanine modifying the surface of the carbon nanotubes. From the micrographs shown in **Figure 4.6**, it can be seen that addition of the peptide causes the carbon nanotubes to arrange into irregular macro assemblies. This could be due to encapsulation of peptide clumps, but the internal structure of the macro assemblies cannot be determined from these images.

The nanoscale arrangements and internal structures of carbon nanotube-diphenylalanine complexes were visualised by transmission electron microscopy. Dispersions of carbon nanotubes and covalent complexes in IPA, described above, were also used to prepare samples for TEM. Each 0.2 mg ml^{-1} suspension was exposed to ultrasonic agitation for 10 mins before transferring a 200 µl aliquot to a fresh glass vial and diluting with 2 ml IPA. The diluted suspension (0.02 mg ml^{-1}) was exposed to ultrasonic agitation for 5 mins and a 50 µl drop applied to holey carbon coated copper TEM grids. The samples were touched lightly onto filter paper to remove excess liquid and left to dry under an evaporating basin for 18 h. The samples were imaged using a JEOL JEM-2100 TEM as described in Section 2.2.10. Images were analysed using Digital Micrograph, Gatan Microscopy Suite 3 (GMS3) software.

Transmission electron micrographs showed the carbon nanotube-diphenylalanine complexes to be more scattered on the supporting grid than starting nanotubes (**Figure

4.7). Peptide layers surrounding the nanotubes were visible, but prolonged exposure to
the electron beam caused damage to the peptide, causing it to burn and reducing the
amount of peptide detail the instrument was able to capture. An example of such
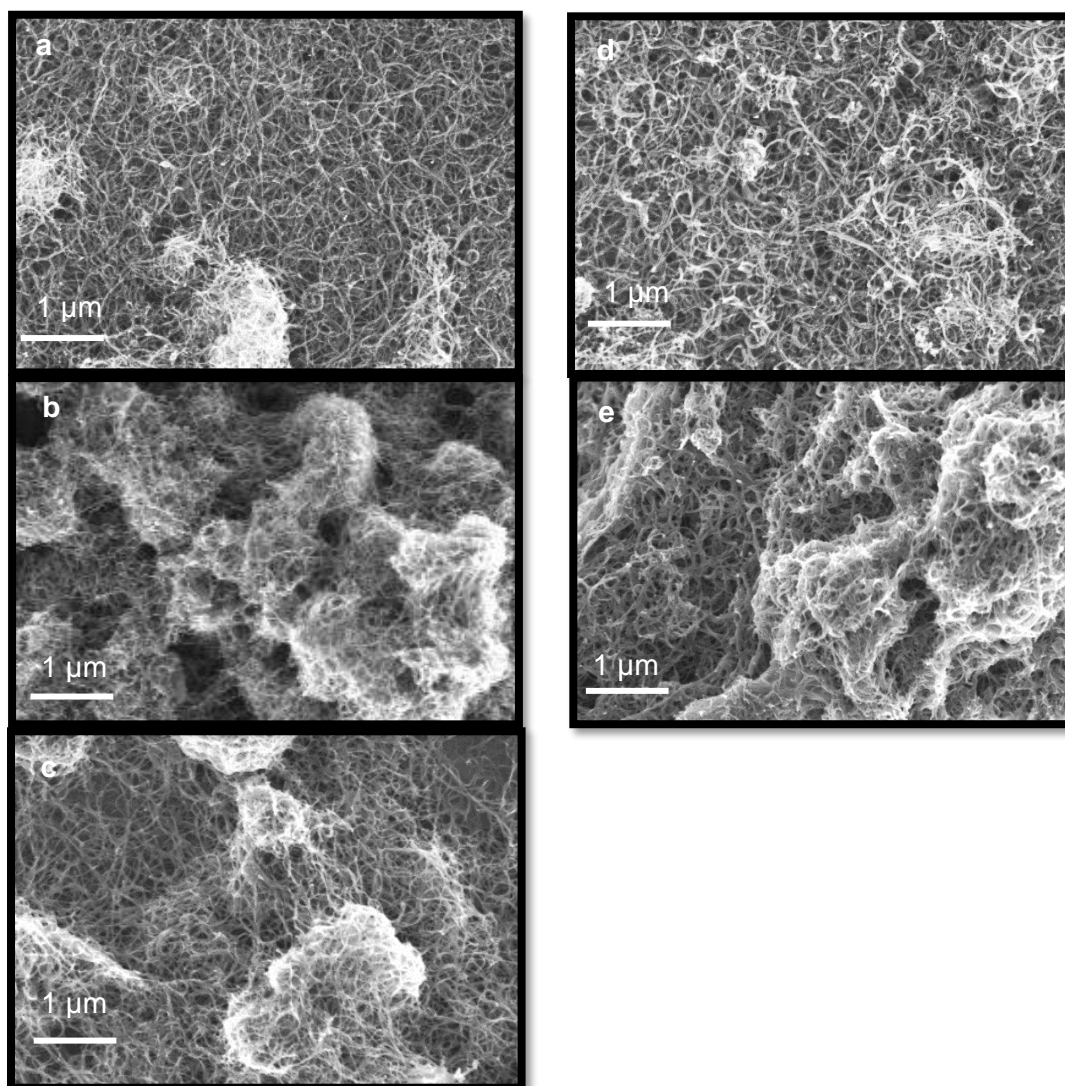
*Figure 4.6 Scanning electron micrographs of carbon nanotubes and complexes a)
MWCNT-COOH, b) MWLFF, c) MWDFF, d) MWCNT-NH₂ e) MWFmocFF. Image
contrast gives information about the degree of peptide functionalisation.*

damage can be seen in **Figure 4.8** and is also visible in the 1 µm micrograph of
MWFmocFF in **Figure 4.7**.

The cross-sectional profiles of arbitrarily selected samples of MWCNT-NH$_2$ and
MWFmocFF were obtained using the GMS3 software. Analysis of the profiles, shown in
Table 4.3, revealed that typically, MWFmocFF had larger diameters than MWCNT-
NH$_2$, although some overlap was observed. An example of the TEM images and profile
analysis used are seen in **Figure 4.7**.

Table 4.3 Diameter analysis of MWCNT-NH$_2$ and MWFmocFF (n= 30) obtained by
measuring the cross-sectional profiles of TEM images

Diameter	MWCNT-NH$_2$	MWFmocFF
Average	11.08	22.50
Standard deviation	5.27	6.83
Max	27.10	36.40
Min	5.68	13.74
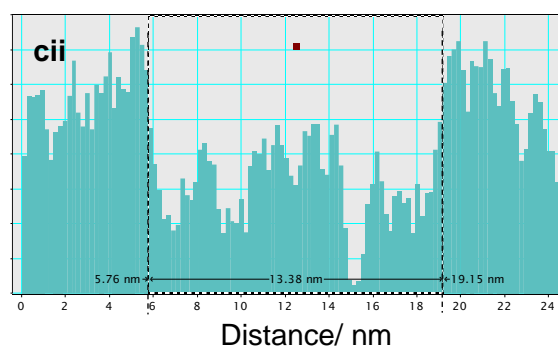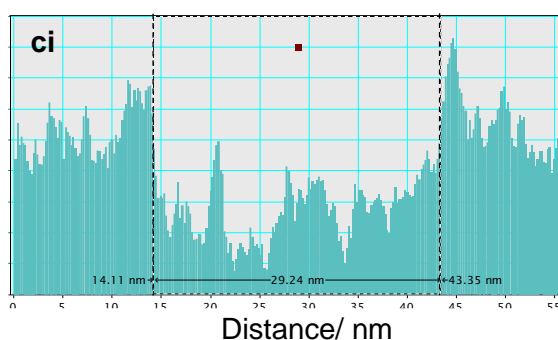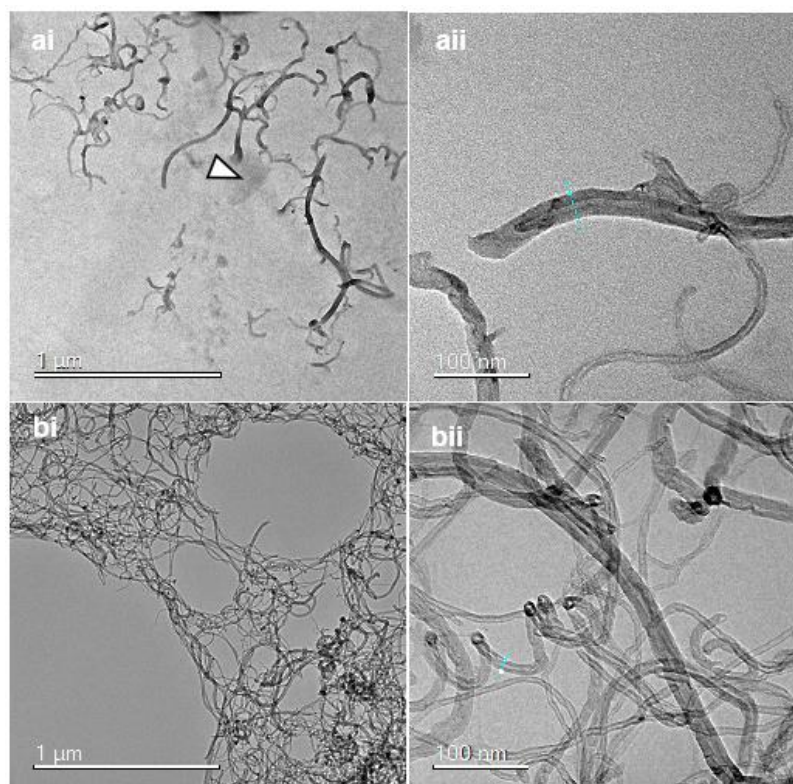
Figure 4.7 Transmission electron micrographs of a) MWFmocFF, b) MWCNT-NH$_2$,
c) Profiles of i) MWFmocFF and ii) MWCNT-NH$_2$ across the white line sections
indicated in a) and b). The distances between the dashed lines in ci and cii are 29.24
nm (MWFmocFF) and 13.38 nm (MWCNT-NH$_2$). Arrow in a) indicates burn damage
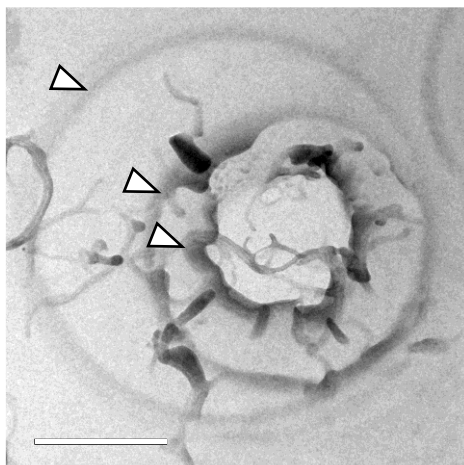
Figure 4.8 *Transmission electron micrograph of the MWFmocFF sample damaged by electron beam. Arrows indicate burn damage, scale bar 500 nm*

Magnification of individual carbon nanotubes by 1,700,000x, revealed the graphitic structure of the multiwall carbon nanotube walls. The transmission electron micrograph in **Figure 4.9** shows the spacing between each graphene plane and also the hollow cavity in the middle of the nanotube. The interlayer spacing measured from the image and taking the magnification indicated by the scale bar is 0.32 nm, which is roughly consistent with the d spacing calculated from the (002) XRD plane (0.348 nm) and falls within the range of values reported in the literature [209].
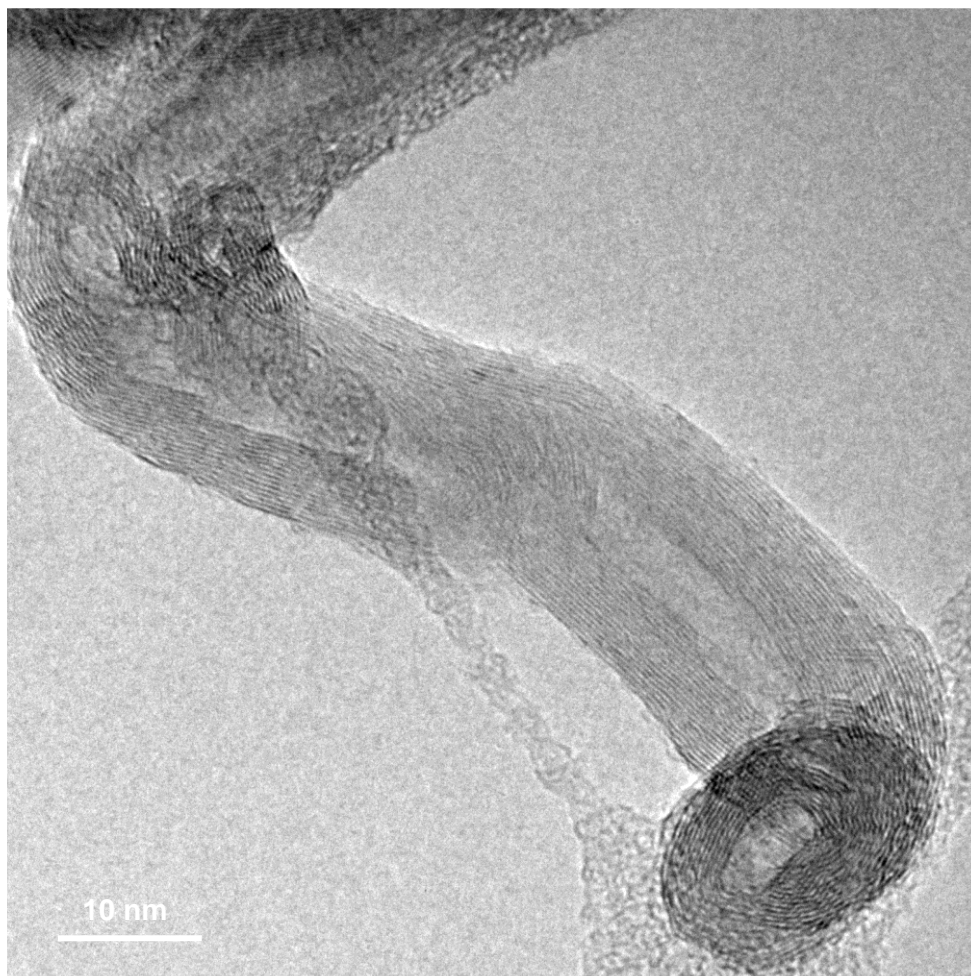
Figure 4.9 *Transmission electron micrograph of an individual MWCNT-NH$_2$. The
graphitic walls of the carbon nanotube can be seen on either side of the hollow
cavity.*

The formation of the carbon nanotube-L-diphenylalanine and carbon nanotube-D-
diphenylalanine complexes involved the activation of the carboxylic acid groups on
carboxylated carbon nanotubes and their subsequent linkage to primary amine groups
on the diphenylalanine molecules. For Fmoc-diphenylalanine, the NH$_2$ groups were
protected and unable to be involved in the reaction, therefore the carboxylic acid
groups on Fmoc-diphenylalanine were activated and linked to the amine groups on
amine functionalised carbon nanotubes. Unlike L- and D-diphenylalanine, Fmoc-
diphenylalanine could only undergo one reaction due to the protective Fmoc-group
present on the diphenylalanine molecule. This likely contributed to the comparatively
higher yield of MWFmocFF.

4.4.5. Electrical Conductivity of Carbon Nanotube-Diphenylalanine Complexes

The electrical conductivity of carbon nanotube-diphenylalanine complexes was determined by measuring the electrical resistance (DC measurement) and impedance (AC measurement) of the samples. Resistance and impedance measurements were set up using a multimeter and impedance spectroscopy, respectively. A detailed description of each setup can be found in Section 2.2.5. The dispersions of starting carbon nanotubes and covalent complexes in IPA, described in Section 4.4.4 were used to prepare samples for resistance and impedance measurements. The dispersions were exposed to ultrasonic agitation for 10 mins and subsequently applied to the central section of impedance analysis slides, described in Section 2.2.5. The dispersions were applied in 10 µl aliquots up to 50 layers and solvent removal was accelerated by applying a warm air flow from a distance of 30 cm from the sample for 2 mins between each layer, total preparation time two hours. Prior to the addition of each subsequent layer, the sample resistance was measured using a multimeter.

The sample impedance was measured after the addition of the 50th layer and revealed that carbon nanotube materials and complexes show behaviour characteristic of a resistor, with impedance being independent of AC frequency. Since no inductance or capacitance were measured for the materials, the reactance tends to zero and the numerical values for resistance and impedance are approximately equal.

The depth (h) of each slide was measured using a digital caliper before the deposition of the first layer of sample and after the application and drying of the 50th layer of sample, to obtain the sample thickness. 50 sample layers corresponded to a thickness of between 4 – 10 µm. A schematic diagram of a coated impedance analysis slide and the sample dimensions is shown in **Figure 4.10**.
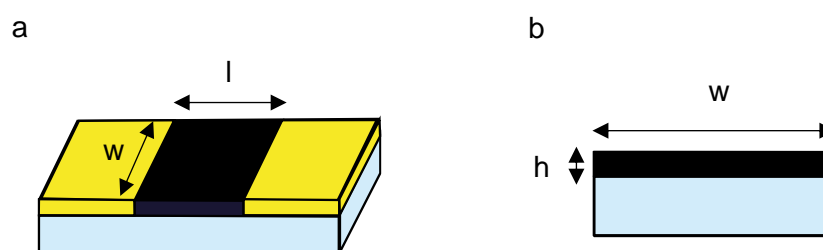
Figure 4.10 *Schematic diagram of a) coated impedance analysis slide with length and width labelled, b) cross section of coated impedance analysis slide with width and height labelled*

The sample dimensions and resistance measurements were used to calculate the
conductivity of each sample using Equation 4.1:

$$\sigma = \frac{1}{R} \times \frac{L}{A}$$ (4.1)

where:

σ = the conductivity

R = resistance

L = sample length

A = cross-sectional area (w x h).

The conductance of each sample was determined by taking the reciprocal of
resistance, then the sample dimensions were used to obtain a value for the sample
conductivity.

The conductivities of the starting carbon nanotube materials and carbon nanotube
complexes can be seen in **Figure 4.11**.
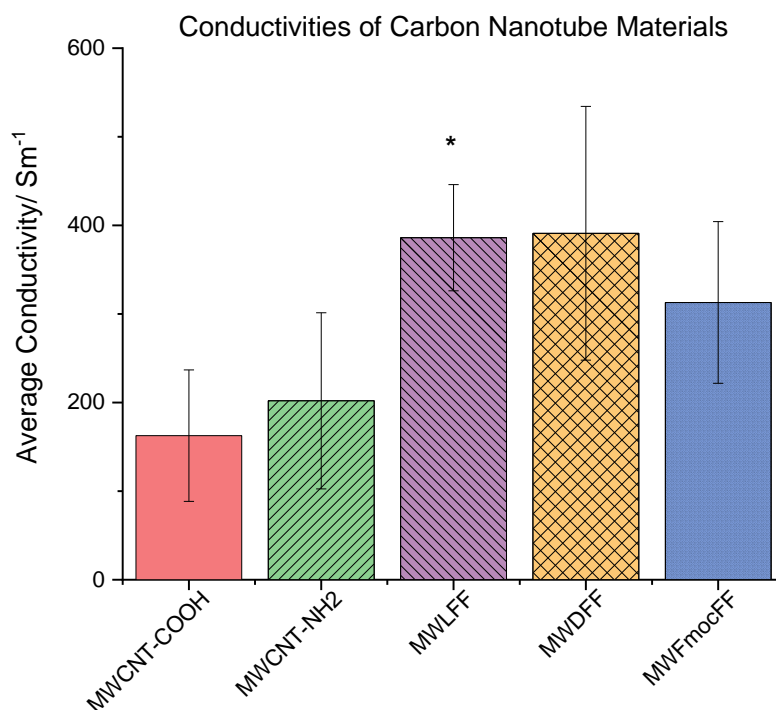
Figure 4.11 *Conductivity measurements of functionalised carbon nanotubes and
carbon nanotube complexes, n= 3 for each sample. An * indicates a significance
level of p< 0.05.*

4.5. Self-Assembly of Diphenylalanine in the Presence of a Carbon Nanotube-Diphenylalanine Complex

The carbon nanotube-diphenylalanine complex was evaluated for its ability to provide a nucleation site for the self-assembly of diphenylalanine microtubes. Within the MWLFF complex, the amine terminus of L-diphenylalanine is involved in the covalent linkage to carbon nanotubes but the carboxyl terminus and the phenyl rings are left unchanged, which is expected because within general organic chemistry these are known to be unreactive. It was therefore expected that if MWLFF is dispersed in a solution of L-diphenylalanine, hydrogen bonds and aromatic interactions should form between L-diphenylalanine confined within the complex and free L-diphenylalanine molecules in the surrounding environment. Use of a carbon nanotube-diphenylalanine complex as a nucleation site was expected to direct hydrogen bonding and aromatic interactions, encouraging the growth of uniform diphenylalanine microtubes.

A solution of L-diphenylalanine in HFIP was prepared with a concentration of 200 mg ml^{-1}. A suspension of MWLFF complex in HFIP was prepared in parallel with a concentration of 2 mg ml^{-1}. The carbon nanotube-diphenylalanine suspension was exposed to ultrasonic agitation for 20 mins before being added to the L-diphenylalanine solution. The mixture formed an unstable suspension in which small aggregates of the carbon nanotube complex were visible. A volume of 1 ml deionised water was then added to the mixture in 200 µl aliquots to induce precipitation.

A sample of the L-diphenylalanine and MWLFF hybrid was deposited directly onto an SEM stub. The sample was dried at 20 °C for 18 h before being gold coated (20 mA, 120 s). The sample was imaged using a Zeiss scanning electron microscope, as detailed in Section 2.2.9. Upon the addition of water to a mixture of L-diphenylalanine and MWLFF complex suspended in HFIP, two precipitates formed within the glass vial. First to appear was a grey-coloured precipitate of no particular visible description. The second was a white crystalline precipitate of the same form and crystal habit as L-diphenylalanine microtubes. Inspection of the grey precipitate by scanning electron microscopy revealed that it comprised aggregates of MWLFF complex surrounded by diphenylalanine nanowire dendrites extending outwards in all directions (

Figure 4.12). The diphenylalanine nanowires can be distinguished from the MWLFF complex due to their larger diameter and flat, elongated structures. The micrographs also confirmed that the white crystals were indeed self-assembled hexagonal diphenylalanine microtubes, similar to those observed in the self-assembly of diphenylalanine described in 3.3.

200
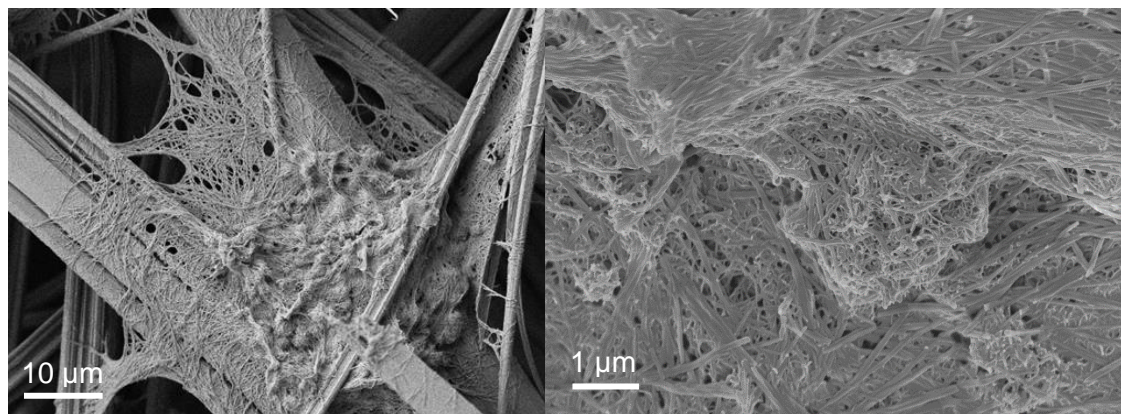
Figure 4.12 *SEM image of diphenylalanine structures precipitated from a suspended mixture of carbon nanotube-L-diphenylalanine complex and solvated diphenylalanine. a) Low magnification image of the complex seed, showing irregular carbon nanotube networks in the centre of the micrograph, with diphenylalanine nanowire dendrites extending from the seed. Larger diphenylalanine microtubes are also visible and show a clear phase separation from the MWLFF complex. b) Higher magnification image of the complex seed, showing small aggregates of MWLFF entangled with diphenylalanine nanowires*

4.6. Effect of Carbon Nanotube-Diphenylalanine Complexes on Human Schwann Cells *in vitro*

To investigate the toxicity of the carbon nanotube materials, Human Dermal Fibroblasts and Human Schwann cells were cultured on top of the carbon nanotube materials in 24-well plates. For these experiments, toxicity is defined as extensive cell death (<50% of cells surviving at day 7 (HDF) or day 5 (HSC) relative to day 1) or severely hindered cell proliferation (>60% decrease in cell metabolic activity on day 7 (HDF) or day 5 (HSC) relative to positive control). Cells were grown on top of clean glass coverslips as a positive control and wells containing medium but no cells were used as a negative control. Cells were seeded on day 0 and cell metabolic activity was recorded on days 1, 3 and 7 or days 1, 3 and 5 for HDFs and HSCs respectively.

Human Dermal Fibroblasts were cultured to passage 10 and Human Schwann cells were cultured to passage 3 or 4, using the methods described in Sections 2.4 and 2.5.

Carbon nanotube control materials (MWCNT-COOH and MWCNT-NH$_2$) and complexes (MWLFF, MWDFF and MWFmocFF) were prepared by suspending the carbon nanotube material in IPA at a concentration of 0.2 mg ml^{-1}. The suspensions were exposed to ultrasonic agitation for 5 mins until the suspension was black and no agglomerates were visible to the eye. 12 mm coverslips were sterilised by soaking in

IPA for a minimum of 2 hours. A volume of 50 µl of each suspension was then drop coated onto the clean 12 mm glass coverslips inside a microbiological safety cabinet. The coverslips were dried in air for 30 mins before being covered and moved to a vacuum oven. The vacuum oven was cleaned by wiping down with 70% IMS before being used to further dry the coated coverslips. The coverslips were dried at 60 °C for 18 h at 80 mbar.

For experiments using HDF cells, the dried materials were inserted into 24-well plates. 1 ml supplemented DMEM was added to each well and incubated for 18 h overnight.

After overnight incubation, medium was removed and HDF suspension was prepared at a density of 25 000 cells/ ml. 1 ml cell suspension was seeded into each well excluding negative controls.

The metabolic activity of the cells was measured using the method described in Section 2.6

For Human Schwann Cell (HSC) experiments, the dried materials were inserted into the 24-well plates, coated with poly-L-lysine (PLL) with a concentration of 2 µg/ cm^2 and incubated for 1 h. The PLL was removed and the wells washed with distilled water. Complete HSC medium was then added to the wells and the plates were incubated for 18 h overnight.

After overnight incubation, medium was removed and HSC suspension was prepared at a density of 40 000 cells/ ml. 1 ml cell suspension was seeded into each well except negative controls.

The metabolic activity of the cells was measured using the method described in Section 2.6.

Cell response to carbon nanotube-diphenylalanine complexes was investigated by growing Human Dermal Fibroblasts on the carbon nanotube materials over a period of seven days to test the general toxicity of the materials. This was followed by growing Human Schwann Cells on the carbon nanotube materials over five days to investigate the effect of the materials on a neural cell environment.

The viability of cells grown on the carbon nanotube materials was determined by the Presto Blue assay for metabolic activity. The results for HDFs and HSCs are shown in **Figure 4.13**. The metabolic activities of cells grown on carbon nanotube materials were

compared to a positive control of cells grown on glass coverslips, the value of which was normalised to 100% viability at day 7 or day 5 respectively.

Student's t-test statistics with p< 0.05 revealed that for HDFs, there is a significant decrease in cell viability after seven days of culture on carbon nanotube materials compared to glass. In all cases studied, the drop in cell viability occurs gradually over a seven-day period. A similar trend is seen for HSCs after five days of culture.

The decrease in cell viability and proliferation is also qualitatively observable by comparison of fluorescence microscopy images of HSCs grown on the carbon nanotube-Fmoc-diphenylalanine complex and HSCs grown on glass. It should be noted however, that the cells grown on MWFmocFF have similar morphology to the positive control cells (**Figure 4.14**). This is contrary to the cell necrosis observed when HSCs were grown on pure FmocFF described in Section 3.5.1.
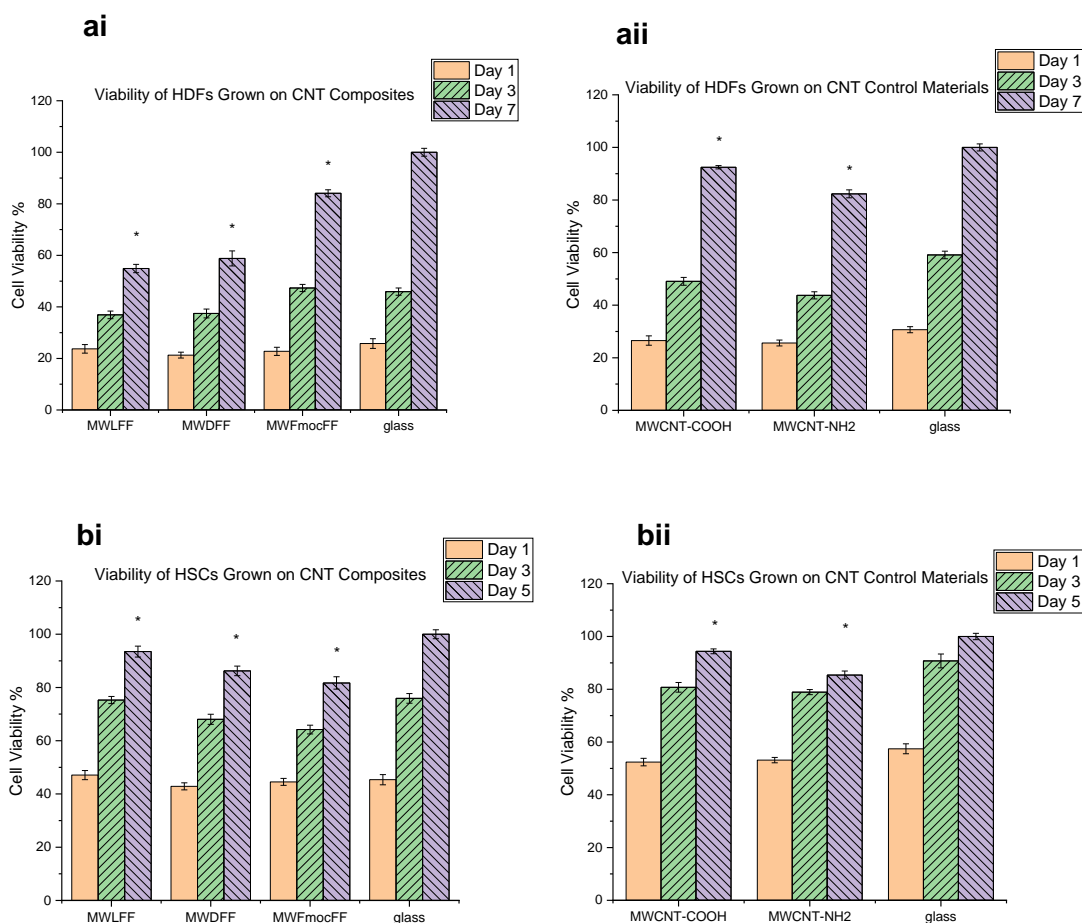
Figure 4.13 Metabolic activity of cells grown on carbon nanotube materials and glass coverslips a) Human Dermal Fibroblasts, n=5 (5 biological replicates were prepared per sample, experiment was conducted once to obtain preliminary results), b) Human Schwann Cells, n=15 (5 biological replicates were prepared per sample, experiment was repeated 3 times). An * indicates a significance level of p< 0.05 at day 5
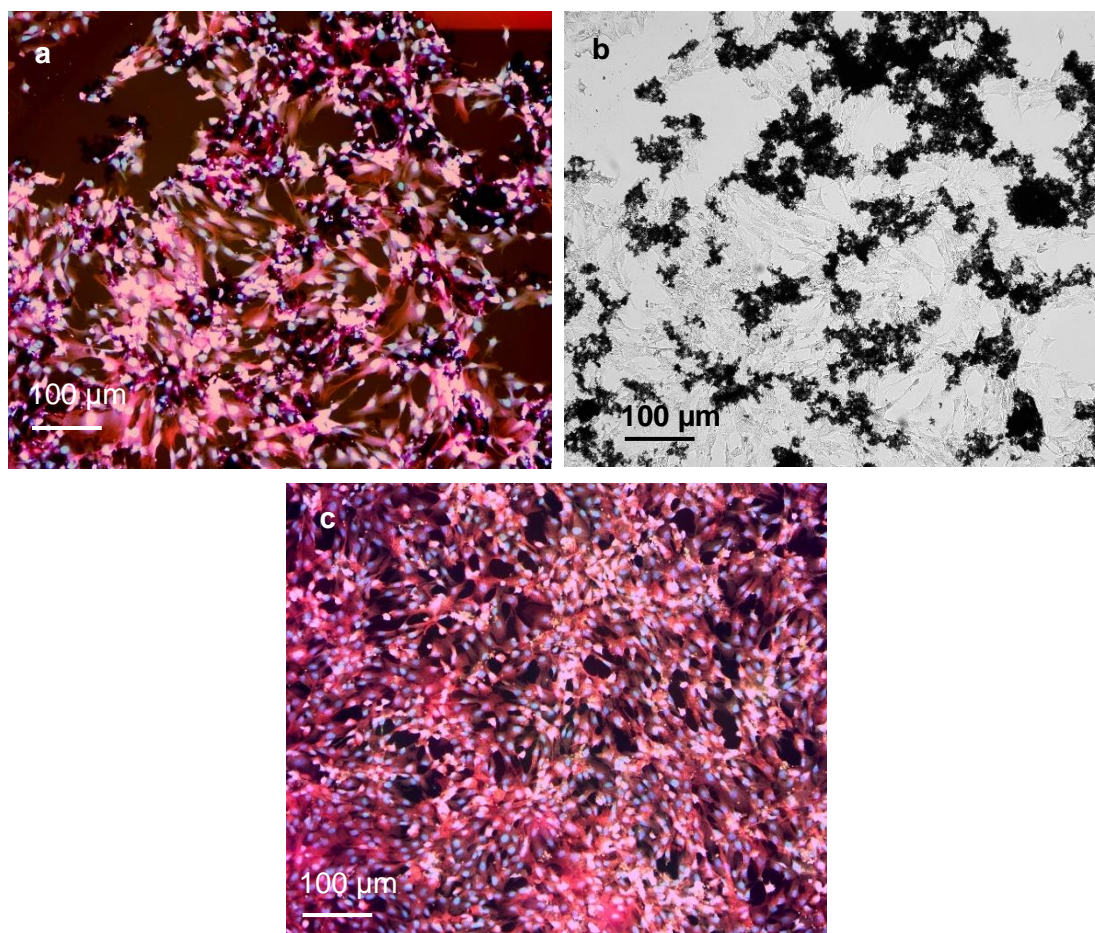
Figure 4.14 *Fluorescence microscopy and transmitted light microscopy images of Day 3 Human Schwann cells. a) Fluorescence microscope image of HSCs grown on carbon nanotube-Fmoc-diphenylalanine (MWFmocFF) *, b) transmitted light microscope image of HSCs grown on carbon nanotube-Fmoc-diphenylalanine, with black MWFmocFF islands visible *, c) Fluorescence microscope HSCs grown on glass (positive control). Cells are stained with phalloidin (red, actin marker) and DAPI (blue, nucleus marker).*

* a) and b) are images of the same area of the CNT-FmocFF sample

4.7.   **Discussion**

4.7.1. **Carbon Nanotube-Diphenylalanine Complex Synthesis**

Coupling Agent Selection

Complex synthesis involved the formation of amide linkages between carbon nanotubes and diphenylalanine molecules. The carboxylic acid and primary amine groups on these molecules are stable and do not react spontaneously. A coupling

agent must therefore be employed to first 'activate' the carboxylic acid group and make it susceptible to nucleophilic attack from the amine group.

Coupling agents, such as 1-[Bis(dimethylamino)methylene]-1H-1,2,3-triazolo[4,5-b]pyridinium 3-oxide hexafluorophosphate (Hexafluorophosphate Azabenzotriazole Tetramethyl Uronium, HATU) and 2-(1H-benzotriazol-1-yl)-1,1,3,3-tetramethyluronium hexafluorophosphate (Hexafluorophosphate Benzotriazole Tetramethyl Uronium, HBTU), are often used for peptide synthesis. The compounds were initially classified as uronium salts (O-isomer) but after intensive study were reclassified as guanidinium salts (N-isomer) [210]. Guanidinium salt coupling agents facilitate amide linkage formation in a similar way to carbodiimides; the carboxylic acid group is activated by conversion into a reactive intermediate, in this case, a hydroxybenzotriazole (HOBt) ester (**Figure 4.15**). The bulkiness of the ester intermediate causes the final stage of the reaction to proceed quickly upon addition of the primary amine. Guanidinium salts are stable in DMF, enable efficient carboxyl group activation under basic conditions and result in a high amide yield. HBTU mediated syntheses are often carried out in a DMF/methylmorpholine mixed solvent. Methylmorpholine is added to increase the basicity since this shifts the carboxylic acid equilibrium from COOH towards COO$^-$, increasing its reactivity and the reaction efficiency.

A different class of coupling agents – carbodiimides, such as 1-ethyl-3-(3-dimethylaminopropyl)carbodiimide (EDC) (often used as EDC/ N-hydroxysuccinimide (NHS)) and N,N-dicyclohexylcarbodiimide (DCC), can also be used as coupling agents for amide linkage formation. Carbodiimides react most efficiently at pH 6.5 and the unstable intermediate formed is prone to hydrolysis. A brief comparison of guanidinium salt and carbodiimide coupling agents is found in **Table 4.4**.

Table 4.4 Comparison of the efficiency and optimal reaction conditions for carbodiimide and guanidinium salt coupling agents.

	Carbodiimide	Guanidinium salt
Coupling efficiency (under optimal conditions)	80%	95%
Solvent	water	DMF/ methylmorpholine
Optimal pH	6.5	> 7

Previous studies have reported that DMF is a suitable solvent for the suspension of carbon nanotubes [104]. This information combined with the benefits of guanidinium salt coupling agents described above, informed the decision to select a guanidinium salt coupling agent for the formation of a carbon nanotube-diphenylalanine complex. HBTU was selected due to availability.
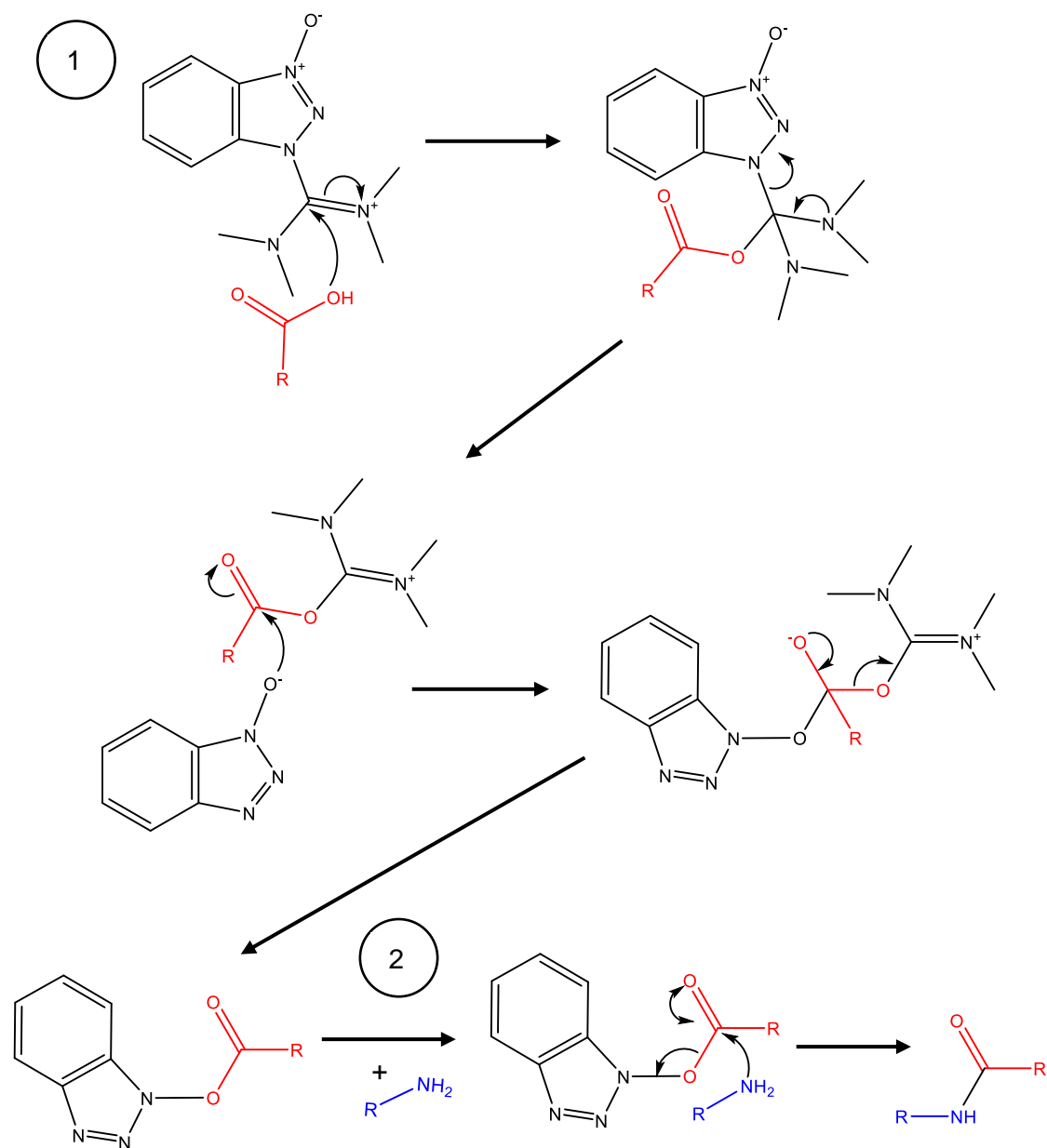
Figure 4.15 *Activation mechanism of HBTU.* **Step 1** *shows the reaction of HBTU with a carboxylic acid and subsequent rearrangement to form the HOBt ester.* **Step 2** *shows the reaction between the ester and a primary amine to produce the amide product. The carboxylic acid and amine groups are highlighted in red and blue respectively, for clarity.*

Diphenylalanine Complex Synthesis

Functionalised carbon nanotubes and diphenylalanine were combined to prepare a covalently bonded complex via the formation of amide linkages between the two moieties. To synthesise complexes with L- or D- diphenylalanine, carboxyl functionalised carbon nanotubes were employed. The carboxyl groups on the carbon nanotubes were 'activated' (substituted with a large, bulky leaving group) by initial reaction with the coupling agent, HBTU. Unreacted coupling agent was washed out of the reaction mixture prior to the addition of diphenylalanine, however, it is difficult to ensure that all the coupling agent is removed, leading to the possibility that the carboxyl termini on diphenylalanine molecules could also be activated. The activation of carboxyl groups on both carbon nanotubes and diphenylalanine may cause side reactions to occur, reducing the final product yield.

The formation of the Fmoc-diphenylalanine complex involved the activation of the carboxyl terminus of the Fmoc-diphenylalanine molecule by HBTU. The activated Fmoc-diphenylalanine was then reacted with the amine groups on amine functionalised carbon nanotubes. The amine group (N-terminus) on Fmoc-diphenylalanine was protected by a large aromatic group and was excluded from participating in any reactions. The only carboxyl group available for activation was the carboxyl group on diphenylalanine, and carbon nanotubes provided the only amine groups available for reaction. The lack of carbon nanotube carboxyl groups and free diphenylalanine amine groups allowed only the desired reaction between diphenylalanine carboxyl group and carbon nanotube amine groups to take place. This maximised the yield of the carbon nanotube- Fmoc diphenylalanine reaction and resulted in a significantly higher yield compared to the carbon nanotube- L- and D-diphenylalanine reactions. The yields of the carbon nanotube-L-diphenylalanine, carbon nanotube- D-diphenylalanine and carbon nanotube-Fmoc-diphenylalanine reactions were 63%, 63% and 94% respectively.

The formation of a carbon nanotube-diphenylalanine complex carried out by Dinesh *et al.* [121], used a similar approach by using Boc-diphenylalanine, which also has a protected N-terminus. The researchers attached a diaminotriethylene glycol linker to the carboxyl group on acid functionalised carbon nanotubes to facilitate the formation of an amide linkage. The linker was not removed upon reaction with diphenylalanine and instead formed part of the complex.

The extent of diphenylalanine addition is limited by number of functional groups on carbon nanotubes, therefore, a greater degree of initial carbon nanotube functionalisation will lead to the formation of a greater number of amide bonds. As discussed in Section 1.4.2, acid functionalisation adds functional groups mainly onto the ends of carbon nanotubes [114], whereas plasma functionalisation adds functional groups to the sidewalls of carbon nanotubes as well as the ends [118]. The plasma functionalised carbon nanotubes used in this work are therefore more likely to have formed complexes with a greater number of covalent bonds between carbon nanotubes and diphenylalanine than could be achieved using acid functionalised carbon nanotubes.

4.7.2. Characterisation of the Physical and Chemical Properties of Carbon Nanotube-Diphenylalanine Complexes

Carbon Nanotube-Diphenylalanine Complex Stability

The physical stability of the synthesised complexes suspended in a DMF/NMM mixed solvent is evidenced by their ability to remain in suspension for extended periods of time (> 1 year). This stability is derived from two main sources – the attachment of sterically bulky diphenylalanine groups to the functional groups on carbon nanotubes, and the presence of both high and low polarity solvents. Neither solvent contains a strong hydrogen bonding donor.

The attachment of diphenylalanine to carbon nanotubes, reduces the probability of nanotube agglomeration by reducing π-π interactions between carbon nanotube sidewalls. This, in turn, leads to better dispersion of nanotubes in solvents and is expected to result in greater uniformity upon deposition.

The choice of solvent also plays a key role when both non-polar, hydrophobic groups and polar, hydrophilic groups are present in the same molecule/ complex. A solvent which contains both polar and non-polar regions is able to support solvent-polar and solvent-non-polar interactions, leading to stable suspensions. In this work, a DMF/NMM mixed solvent was identified as the solvent best able to maintain a stable complex suspension. The mixed solvent was able to accommodate the non-polar, hydrophobic hexagonal carbon lattice, and also the polar, hydrophilic carboxylic acid, amine and amide groups on diphenylalanine. This solvent interaction, combined with the reduced propensity for carbon nanotube agglomeration, resulted in a physically stable suspension. The weak hydrogen bonding in the system also helped prevent complex

particle agglomeration since no strong hydrogen bonded networks were formed between the solvent molecules.

Attempts at obtaining a stable suspension were also made with IMS and water. Results showed that IMS was able to temporarily support a stable suspension (precipitation after ~ 1 hour) whereas water was unable to support a suspension for anything longer than minutes. The key difference that allowed IMS to sustain a suspension while water was unable to, despite them both being high polarity, protic solvents, is the presence of the ethyl group in ethanol. This non-polar carbon chain was able to interact with the hydrophobic nanotube regions and prevent them from agglomerating. Conversely, the sample dispersed in water separated into hydrophilic and hydrophobic regions because the protic solvent formed a large hydrogen-bonded network, excluding the carbon nanotube-diphenylalanine complex and causing the nanotube regions to clump together and sink.

Crystal Structure of Carbon Nanotube-Diphenylalanine Complexes

X-ray diffractograms of the functionalised carbon nanotubes and carbon nanotube-diphenylalanine complexes revealed two broad reflections at ~25.5° (002) and ~43° (100) which were used to calculate their d-spacing and crystallite size (**Table 4.2**). The d-spacings calculated from the (002) plane had values of 0.346 – 0.350 nm and
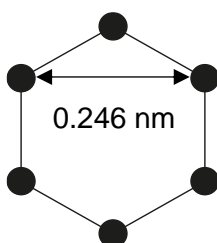
Figure 4.16 *Schematic diagram of the distance between carbon atoms within a graphite layer. The distance corresponds to the d-spacing for the (100) plane* [92].

correspond to the interlayer spacing of graphite (0.335 nm) The values are similar to those reported in the literature [209]. The d-spacings calculated from the (100) plane had values of 0.209 – 0.211 nm and correspond to the distance between parallel (non-adjacent) carbon atoms within a graphite layer, as illustrated in **Figure 4.16**.

The Raman spectra and X-ray diffractograms of MWLFF and MWDFF complexes showed little change from those of MWCNT-COOH. The crystallite sizes of all three materials were also similar, indicating that little surface modification of the starting carbon nanotubes had occurred by covalent functionalisation. Conversely, analysis of

209

the Raman spectrum of MWFmocFF (**Table 4.1**) showed a reduced D:G intensity ratio of 1.19 compared to a ratio of 1.29 for MWCNT-NH$_2$. The reduced ratio could be due to FmocFF modifying the surface of MWCNT-NH$_2$ and dampening the C – C bond vibrations. XRD peak analysis identified an increase in peak intensity at 25.7°, and an increase in crystallite size, from 1.47 nm (MWCNT-NH$_2$) to 2.23 nm (MWFmocFF), providing further evidence of the surface modification of MWCNT-NH$_2$.

Increased XRD peak intensity is often related to the position of the atoms in space. In this case, increased intensity at 25.7°, would suggest greater density in the (002) plane. This could result from an increased number of sp^2 hybridised carbon atoms aligned parallel to the plane of the CNT walls and at a distance equal to the graphitic interlayer distance. The aromatic Fmoc group in Fmoc-diphenylalanine could provide a source of planar sp^2 hybridised carbon atoms and has the potential to form a physical association with the carbon nanotube walls via the formation of π-π bonds. Increased XRD intensity is not observed for MWLFF and MWDFF complexes relative to the MWCNT-COOH intensity. L- and D-diphenylalanine lack the large planar, aromatic Fmoc group and are therefore less likely to produce same effect.

The diffractograms display none of the characteristic peaks of diphenylalanine, suggesting that hexagonal diphenylalanine structures do not form as part of the carbon nanotube-diphenylalanine complexes. As a result, the carbon nanotube-diphenylalanine complexes are unlikely to display piezoelectric properties.

Surface Morphology and Internal Structure of Carbon Nanotube-Diphenylalanine Complexes

The contrast in SEM images of carbon nanotubes and complexes was similar. However, since sample composition and topography can affect contrast, the amount of peptide in each complex cannot be deduced with any confidence using image contrast. When comparing the complexes to the control samples, the impression gained (no attempt has been made to quantify it) is that flatter structures are observed for control samples while more globular structures are seen for the complexes. Similar globular structures have been described by Lima *et al*. [211] in their study of carbon nanotube-polyurethane composites.

The diameter of the multiwall carbon nanotubes is reported by the supplier as being 10 nm, which is similar to the average diameter of ~ 11 nm, calculated from TEM line profiles in this work (**Table 4.3**). Line sections across peptide coated carbon nanotubes showed that they have an average diameter of ~ 23 nm. Assuming that the carbon nanotubes in both samples have a similar range of diameters, and that the thickness of

the peptide layer is constant, the thickness of the peptide layer surrounding the carbon nanotubes in the MWFmocFF sample can be calculated as ~ 6 nm. Transmission electron microscopy provides further evidence of aromatic interactions between the MWFmocFF complex and free Fmoc-diphenylalanine peptide. The TEM of a peptide coated carbon nanotube (**Figure 4.7aii**) shows a large peptide extension on the end of the carbon nanotube. The extension is ~50 nm in length, approximately 6x larger than the peptide extensions observed on the side walls of the nanotubes. This could be due to π-π interactions between individual FmocFF molecules and between FmocFF and carbon nanotubes, as was suggested above.

The quality of high resolution TEM analysis of diphenylalanine peptide is limited by damage caused to the sample by the electron beam, which can lead to potentially inaccurate measurements. These challenges could be overcome by cryo-TEM although this technique was unfortunately unavailable for these studies.

Conductivity of Carbon Nanotube-Diphenylalanine Complexes

Electrical resistances of the carbon nanotube starting materials and carbon nanotube-diphenylalanine complexes were measured using a two-electrode method. The measured resistances were later used to calculate the conductivity of the materials. The conductivities of the carbon nanotube materials varied over a range of not much more than a factor of two (400 – 170 Sm^{-1}) and followed the trend MWLFF/ MWDFF > MWFmocFF > MWCNT-NH_2 > MWCNT-COOH (**Figure 4.11**). If the carbon nanotube-diphenylalanine complexes are dispersed and then the dispersant medium removed, simply from considerations of morphology, the material will reaggregate different from functionalised carbon nanotubes alone. This will result in an arrangement of different pathways. In dealing with nanomaterials, we frequently find that properties can change by orders of magnitude, therefore, in nanoscale terms, a factor of two is not a significant difference.

The complexes, which contained approximately 76% carbon nanotube and 24% diphenylalanine, had conductivities falling within the range of those reported in the literature. In particular, the values fall between those from the studies conducted by Luo *et al.* [127] and Kim *et al.* [137], who reported a carbon nanotube/ PDMS composite with a conductivity of 75 Sm^{-1}, and a carbon nanotube/ PVP composite with a conductivity of 2450 Sm^{-1} respectively. Preparative methods and post deposition processes, such as pyrolysis and carbon nanotube alignment, affect the conductivity of composite materials, as was shown in **Table 1.4**. For the complexes prepared in this work, it can be predicted that alignment of the carbon nanotubes would lead to a significant increase in conductivity.

It is also interesting to note that the MWFmocFF sample yielded lower conductivity values than MWLFF and MWDFF despite the similar preparation methods. The lower-than-expected conductivity for MWFmocFF could be related to a higher proportion of Fmoc-diphenylalanine loading on carbon nanotube, compared to the reactions with L- and D-diphenylalanine, which could arise from the absence of side reactions during synthesis. The conductivity decrease could also be a result of aromatic interactions between free Fmoc-diphenylalanine and the complex. The additional aromatic systems in the Fmoc group of Fmoc-diphenylalanine are likely to assemble more insulating FmocFF structures than MWLFF or MWDFF.

The conductivity of an electrode is going to be a factor in deciding the overall energy consumption of a final device. It is therefore of interest to know what the conductivity is and the factors that determine it. At this stage of research, conductivity is a parameter of interest, but not one to be specified. Electrode conductivities within an order of magnitude of existing electrodes might constitute an acceptable target range and currently the conductivity of complexes is an order of magnitude lower than that reported for carbon nanotube-based materials which are being used as electrodes [137].

4.7.3. Self-Assembly of Diphenylalanine in the Presence of a Carbon Nanotube-Diphenylalanine Complex

A small amount of the synthesised MWLFF complex was added to a solution of L-diphenylalanine in HFIP and water added to facilitate microtube formation. This was an initial test to identify whether particles of the complex could behave as nucleation sites for the self-assembly of diphenylalanine microtubes. An acceptable final outcome was for diphenylalanine molecules that were covalently linked to carbon nanotubes to direct and support the self-assembly of uniform, aligned diphenylalanine microtubes, leading to an enhanced piezoelectric response. The obtained result from the initial test, however, showed a clear phase separation between an irregular dendritic structure of peptide nanowires and a central globular assembly of MWLFF complex (**Figure 4.12**).

A similar result was observed by Dinesh *et al.* [121] in their 2015 study. The researchers prepared a similar system of a covalently bound carbon nanotube-peptide complex in a peptide solution, and precipitated self-assembled structures using ethanol. Dinesh attributed the dendritic structure formation to hydrogen bonding between the unbonded functional group on the covalently bonded peptide and the functional groups on the free peptide in solution. This was confirmed by observing the disruption of the dendritic structures when the pH of the mixture was changed. Similar disruption to self-assembled structures as a result of a pH change has been observed in this work

(Section 3.3.7). It is likely that the dendrites are diphenylalanine molecules in a nanowire structure, similar to that described by Huang *et al.* [43] in 2014. The researchers found that diphenylalanine underwent a structural transition from solution at high temperature to nanowires at low temperature. The SEM images reported in their work show formation of both large nanofibers and small, thin nanowires, which has also been observed in this work (**Figure 4.12**). The crystal structure of the nanowires observed by Huang *et al.* was analysed by XRD and showed the same crystal structure, $P6_1$, as that previously reported for L-diphenylalanine microtubes.

Intermolecular forces, such as π-π interactions between the carbon nanotubes and the aromatic groups on diphenylalanine, also prevent diphenylalanine from being mobile to form microtubes. In addition to this, the carbon nanotube-diphenylalanine complex does not share the same crystal structure as diphenylalanine and therefore cannot be incorporated into the packing for hexagonal microtube formation. Instead, a random packing arrangement is obtained. This arrangement likely minimises the energy of the system, although computational modelling would be required to confirm this.

4.7.4. Effect of Carbon Nanotube-Diphenylalanine Complexes on Human Schwann Cells *in vitro*

Human Dermal Fibroblasts (HDFs) and Human Schwann Cells (HSCs) were grown on top of the carbon nanotube materials to evaluate the materials' suitability for use in a cell environment. Initial tests with HDF cells showed that the cells were able to survive contact with the materials over a seven-day period, thus the experiment was expanded to HSCs. Measurement of HSC metabolic activity showed that cell viability remained above 80% (compared to the viability recorded for positive controls for both complex and control CNT materials) (**Figure 4.13**).

The fact that the carbon nanotube and complex coatings did not cover entire glass coverslip surface, must be considered as one reason why cell viability is higher for the carbon nanotube materials than for diphenylalanine, discussed in Section 3.5.1. The concentration of diphenylalanine applied to the glass coverslips in Section 3.5.1 was also approximately 500x higher than the concentrations of carbon nanotube-diphenylalanine complex applied to glass coverslips in Section 4.6 (diphenylalanine concentration 100 mg ml^{-1} compared to carbon nanotube-diphenylalanine concentration 0.2 mg ml^{-1}). Different concentrations were used to maintain comparability within their groups. Diphenylalanine self-assembles at 100 mg ml^{-1} and so was deposited at this concentration, whereas the highest stable concentration achievable for the carbon nanotube complex in IPA was 0.2 mg ml^{-1} before significant

213

sedimentation occurred. Higher concentrations of carbon nanotubes would have led to different amounts of carbon nanotube being deposited over different repeats and lower diphenylalanine concentration would have caused different self-assembled morphologies to form, making the experiment incompatible with other investigations in this work.

Fluorescence microscopy images supported the quantitatively observed reduction in cell viability measured by the metabolic activity assay. Fewer cells are visible in the image of cells grown on MWFmocFF than on glass coverslips. However, comparison of cell morphology of HSCs grown on both carbon nanotube complex and glass substrates shows that cells grown on both substrates have a similar elongated shape, which is commonly seen for healthy Schwann cells. From the transmitted light microscopy image, the position of the carbon nanotube complex islands can be seen. The cells are seen to congregate on and around the carbon nanotube complex, with the complex islands influencing the direction of cell growth in some cases. A similar directing effect was also observed for cells grown on MWLFF and MWDFF samples.

4.8.   **Summary**

Three carbon nanotube-diphenylalanine complexes were synthesised by formation of amide linkages between diphenylalanine and plasma functionalised carbon nanotubes. Plasma functionalised carbon nanotubes were found to facilitate effective complex formation due to the greater number of functional groups grafted onto the carbon nanotube during the plasma functionalisation process (compared to wet functionalisation techniques). Yields of 63% were recorded for the carbon nanotube- L-/D-diphenylalanine complexes and a yield of 94% was recorded for the carbon nanotube-Fmoc-diphenylalanine complex. The synthesised complexes were successfully suspended in a DMF/NMM mixed solvent and remained stable for > 1 year without forming a sediment. This demonstrated a marked improvement in the dispersibility of carbon nanotubes.

Characterisation of functionalised carbon nanotubes and carbon nanotube-diphenylalanine complexes by XRD and Raman spectroscopy, gave an indication of the degree of covalent coupling between carbon nanotubes and diphenylalanine. Analysis of the Raman spectra for MWLFF, MWDFF and MWCNT-COOH showed that the three samples have similar D:G intensity ratios. A similar crystallite size was also calculated from XRD data, providing little evidence of extensive covalent linkage between MWCNT-COOH and diphenylalanine. In comparison, a drop in the D:G

intensity ratio and an increased crystallite size for MWFmocFF compared to MWCNT-NH$_2$ suggested that the surface of MWCNT-NH$_2$ had been modified by Fmoc-diphenylalanine. It is likely that the large aromatic structures that form part of FmocFF molecule formed interactions with the side walls of MWCNT-NH$_2$. Line profiles taken from TEM images provided further evidence for this, showing that the diameter of MWFmocFF was, on average, 12 nm larger than that of MWCNT-NH$_2$, indicating a peptide layer 6 nm thick around the carbon nanotube.

Conductivities of the synthesised carbon nanotube complexes were of similar magnitude and were greater than the conductivities of the functionalised carbon nanotube starting materials. The conductivities followed the trend MWLFF/ MWDFF > MWFmocFF > MWCNT-NH$_2$ > MWCNT-COOH. Impedance of the materials was entirely ohmic, as is characteristic of conductors. The sufficiently low resistance of carbon nanotube-diphenylalanine depositions suggest that they could feasibly form the conductive component of a device.

A conductive carbon nanotube-diphenylalanine complex was synthesised with the intention of applying it as a nucleation site for the self-assembly of diphenylalanine microtubes. This application was explored by self-assembling diphenylalanine in the presence of the complex. Observation of the hybrid material under SEM revealed that the complex was ineffective as a nucleation site. Non-uniform diphenylalanine crystals with a range of micro and nanostructures formed around aggregates of the carbon nanotube-diphenylalanine complex in a random arrangement.

Both Human Dermal Fibroblasts and Human Schwann Cells were able to grow on the carbon nanotube and carbon nanotube-diphenylalanine complexes. Measurement of HSC metabolic activity showed that cell viability remained above 80%, although non-continuous coating of carbon nanotube and complex depositions on the glass coverslips must be considered as one reason for the high cell viability. Viability of cells grown on continuous layers of carbon nanotube materials will be explored further in the next chapter.

Fluorescence microscopy images showed that HSCs appear to congregate on and around the carbon nanotube-diphenylalanine complexes, indicating that islands of the complex can influence the direction of cell growth. This could prove useful in the development of tissue engineering scaffolds for nerve regeneration.

This chapter has established the characteristics and properties of complexes. It is now necessary to consider how these materials can be fabricated into the macrostructures. In principal, the complexes are multiple constituent, pourable mixtures; that is, they are

not macroscopic objects to be sculptured into their final form but they need to be assembled and bound into a final form. Among the options for deposition are moulding and 3D printing.The approach explored next is nozzle printing as a formulated ink.

Chapter 5   **Carbon Nanotube-based Nanocomposite Inks and Electrodes**

The goal is to fabricate the carbon nanotube-diphenylalanine complex into a macroscopic object which is here-called an electrode. The electrode is essentially 2D; that is, a flat, thin shape. One way to achieve this is by printing a suspension through an appropriately wide nozzle, and with an appropriate infill pattern. A suspension which can be deposited onto a substrate in a defined geometry, is referred to as an ink.

5.1.   **Conductive Carbon Nanomaterial and Nanocomposite Inks**

Carbon nanocomposites are materials comprised of a carbon nanomaterial, such as graphene or carbon nanotubes, and one or more additional constituent material. They are often developed for one of two purposes: to enhance the mechanical properties of a polymer material, for example, to improve the compressive strength of cement [90] or to create a highly conductive suspension that can be deposited as a conductive pattern [128].

Studies in the literature describe the deposition of carbon nanotube or graphene-based composite inks as highly conductive (6700 Sm^{-1} [126]) patterns and electrode arrays [153]. For a carbon nanocomposite ink to produce high quality electrode patterns, it must be able to:

- maintain a stable suspension without forming a sediment
- be printed into a uniform arrangement
- dry into a continuous pattern.

Inks have been formulated in aqueous or organic solvents, and with a wide range of viscosities depending on their application. The selection of a suitable polymer for the nanocomposite ink is also based on the properties required for the application. Polymers which could be used to prepare nanocomposites for applications in electronics, may not always be suitable for biomedical applications due to their potential cytotoxicity, and an alternative polymer would need to be selected.

A suitable polymer for the formation of a biocompatible carbon nanocomposite ink must be non-toxic and able to maintain a stable suspension with the associated carbon

nanotubes. Nafion is a sulfonated fluoropolymer that has been shown to have interactions with carbon nanotubes [149] and has also been studied in a biological context [212]. The application of nafion as part of a carbon nanocomposite meets the above requirements for the development of a printable, conductive, biocompatible ink.

It is claimed that the versatility of carbon nanotube-based inks allows them to be applied as electrode coatings, as well as stand-alone stimulating and recording electrodes [152]. When considering the development of implantable electrodes, carbon nanotubes are attractive for several reasons, including their ability to promote and guide neuron growth and differentiation [136], their high bio-inertness and high charge injection capacity; that is, their ability to transfer charge without causing irreversible chemical reactions to occur between the electrode and surrounding tissue [213]. The potential toxicity of individual carbon nanotubes must also be acknowledged but could be minimised by encapsulating the carbon nanotubes within a polymer matrix.

The formulation of a low toxicity carbon nanocomposite ink, which is conductive and able to be printed into a custom pattern, can prove useful in the development of cell growth scaffolds and implantable electrodes. Electrodes made from these inks can also be softer and more flexible than commonly used metal electrodes, thus supporting neural cell growth more effectively [153] and reducing fibrosis.

5.2.   **Aims**

The work described in this final phase of the work on carbon nanotube-based inks and electrodes will describe the addition of stabilising/ adhesive agents to carbon nanotube materials with the intention of creating a printable ink. Deposition of the ink onto glass surfaces and cell response will then be described. The objectives of this work were to:

- formulate a printable ink from the carbon nanotube materials and suitable stabilising agents and/ or polymer matrices;
- characterise the physical properties of the ink;
- deposit the ink into stable, flat layers of particular geometries as the basis of an electrode;
- test the effect of the nanocomposite on cells cultured *in vitro.*

5.3. Selection of a Stabilising Agent/ Polymer Matrix for the Formation of a Carbon Nanotube Composite

The carbon nanotube-diphenylalanine complexes described here in Chapter 4 were shown to form stable suspensions in organic solvents. It was found that diphenylalanine acts as a stabiliser to prevent carbon nanotube agglomeration, while maintaining the conductivity of the carbon nanotubes. When the complex was deposited from DMF/ NMM suspension onto a glass surface, small agglomerates of carbon nanotubes were visible. When deposited from isopropanol (IPA), the complex formed larger agglomerates on the glass surface.

Seemingly regardless of the solvent used, these depositions were very fragile; the lightest touch, for example with tweezers, caused material to be removed, introducing scratches and discontinuities between gold electrodes during conductivity measurements.

This is interpreted as a sign that the surface affinity of the composite in suspension was lower for the glass than for itself. This made the composite alone unsuitable for use as a printable ink.

Four alternative stabilising agents and polymer matrices were trialled to obtain a stable suspension with a high carbon nanotube loading, which maintains its surface integrity when deposited onto a glass substrate – polydopamine, PVDF-TrFE, ionic liquids and Nafion.

Research into the adhesive proteins in mussels (*Mytilidae* family) led to the discovery [214] that dopamine can self-polymerise under basic conditions to forms layers of adhesive polydopamine. It was thought that the combination of polydopamine and carbon nanotubes may form a stable suspension and a scratch resistant coating upon deposition.

Polydopamine was synthesised in this work through an oxidative polymerisation reaction of dopamine hydrochloride. Dopamine hydrochloride was added to a pH 8 solution of TRIS buffer in a 250 ml round bottom flask and stirred at 20 °C in air for 20 h to facilitate oxidative polymerisation. A colour change from colourless to black was observed over this time period. The reaction mixture was transferred to centrifuge tubes and centrifuged at 3500 rpm for 10 mins. The supernatant was decanted and the product, a black viscous liquid, remained in the centrifuge tubes. The centrifuge tubes and contents were dried under vacuum at 20 °C for 48 h. The centrifuge tubes were then removed from the vacuum and the black solid was transferred to a glass vial.

To establish the suitability of polydopamine as an adhesive agent for a carbon nanotube ink, polydopamine was ground using a porcelain pestle and mortar with MWCNT-NH$_2$ and DMF/ NMM mixed solvent at 20 ° for 10 mins. The ink was spread onto a glass microscope slide and dried in air at 40 °C for 10 mins.

Poly[vinylidene fluoride-co-trifluoroethylene] can be electrospun into piezoelectric fibres, as described in Chapter 3. Mindful that future applications will look to combine PVDF-TrFE fibres with the carbon nanotube electrode to create a piezoelectric sensing device, it seemed reasonable to include PVDF-TrFE as an adhesive agent in the carbon nanotube complex, on the grounds that this would keep to a minimum the number of different materials being explored.

Carboxyl functionalised carbon nanotubes and PVDF-TrFE powder were added to a glass vial at a ratio of 3% : 5% MWCNT-COOH : PVDF-TrFE. Dimethylformamide/ N-methylmorpholine mixed solvent was added to the powder and the mixture was stirred with a magnetic stirrer for 1 h to obtain a homogeneous ink suspension. The ink was deposited onto a glass microscope slide by direct writing and dried in air at 40 °C for 10 mins.

Ionic liquids are salts in their liquid state. Salts with melting points of < 100 °C, are referred to as room temperature ionic liquids (RTIL) [215]. An example of a RTIL is 1-butyl -3-methyl-imidazolium chloride (BMIMCl), which was investigated here as a candidate adhesive material due to its high electrical conductivity and ability to support cell growth.

The ionic liquid, BMIMCl, was placed in an agate mortar at 70 °C and melted. An equal mass of MWCNT-COOH was added to the mortar and ground for 5 mins, resulting in a homogeneous, high viscosity ink. The ink was spread onto a glass microscope slide.

Nafion is a perfluoro-sulphonated polymer known for its ion exchange properties and proton conductivity [216]. It consists of a stable, hydrophobic polytetrafluoroethylene (PTFE) backbone with perfluorinated vinyl-polyether side chains containing sulfonic acid (–SO$_3$H) end groups. The structure of Nafion is shown in **Figure 5.1**.
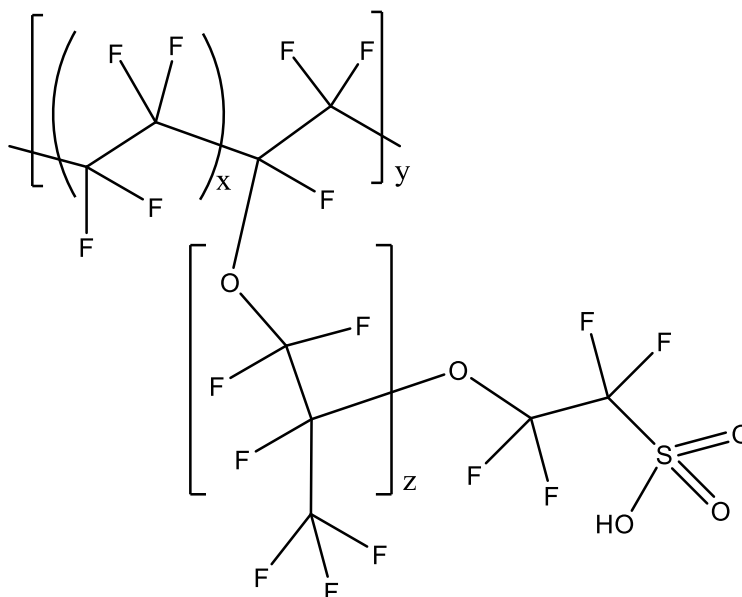
Figure 5.1 *Skeletal formula of one unit of Nafion*

The desired application of any developed electrode will be in a nerve environment;
therefore, it was considered that nerve impulses involve ion conduction as well as
electron conduction. The combination of Nafion with carbon nanotubes was expected
to provide the opportunity for the conduction of both electrons and protons/ ions.

Nafion D-520 solution, a solution containing 5% Nafion dissolved in aliphatic alcohols
and water, was added to the MWCNT-COOH or MWCNT-NH$_2$ at different w:w ratios
detailed in Section 5.4. The mixture was ground in an agate pestle and mortar heated
to 60 °C before adding DMF/ NMM mixed solvent to the mixture and grinding until the
mixture formed a glossy black ink.

Inks were transferred to syringes and degassed in a vacuum oven at 80 mbar, 20 °C
overnight to draw air bubbles out of the ink. The inks were then deposited onto glass
microscope slides and dried in air at 60 °C for 10 mins.

A summary of the conductivity and stability of the attempted combinations is shown in
Table *5.1*.

Table 5.1 Table showing materials trialled as adhesive agents for carbon nanotube ink. * Conductivity of 20 Sm^{-1} roughly corresponds to a resistance of 1 kΩ for samples of the average dimensions used for conductivity tests

Adhesive Agent	Conductivity > 20 Sm^{-1} *	Stability
Diphenylalanine	Yes	unstable
PVDF-TrFE	No	unstable
Polydopamine	No	stable
Ionic liquid	Yes	unstable
Nafion	Yes	Stable

While covalent functionalisation was used to join diphenylalanine to carbon nanotubes, forming a complex, the stabilising agents and polymer matrices physically interacted with and exfoliated carbon nanotubes bundles to form composite materials. This was facilitated through either grinding the materials together in a mortar or mixing the materials on a magnetic stirring plate.

The results obtained with each stabilising agent are described below.

- The carbon nanotube-PVDF-TrFE ink was highly viscous, with a paste-like consistency, but fluid enough to be direct written from a syringe with a 22-gauge needle. However, upon drying, the printed patterns shrunk, cracked and were not able to maintain a continuous structure and stable conductivity.

- The carbon nanotube- polydopamine ink was low viscosity and could be directly written with a 22-gauge or 25-gauge needle but the dried result too was non-conductive.

- The carbon nanotube- ionic liquid ink showed good conductivity but since the ionic liquid, BMIMCl, is a liquid at room temperature, it was not possible to dry the ink into a stable nanocomposite film.

- The carbon nanotube -Nafion ink was able to be direct written, dried to a stable cast and maintain a continuous structure and stable conductivity.

Nafion was therefore selected as a suitable adhesive agent for the formulation of a carbon nanotube-based ink.

5.4. **Formulation of Carbon Nanotube/ Nafion Nanocomposite for a Printable Ink**

The ratio of carbon nanotube:nafion required to obtain an optimally conductive, stable and printable ink was investigated by combining different volumes of Nafion with a fixed mass of carbon nanotubes.

The weight percentages of carbon nanotube and Nafion in each ink formulation and the weight: weight ratio of carbon nanotubes:nafion are found in **Table 5.2**.

Table 5.2 Weight % of CNT compared to total mass of each ink formulation (CNT + nafion + solvent), ratio of CNT:Nafion for each ink variation and weight % of CNT + Nafion in each ink variation. a) MWCNT-COOH, b) MWCNT-NH$_2$

a

MWCNT-COOH wt% in ink	CNT:Nafion w:w	MWCNT-COOH + Nafion wt%
2.38	1 : 3.5	10.7
2.35	1 : 4.0	11.7
2.33	1 : 4.4	12.6
2.27	1 : 5.6	14.9

b

MWCNT-NH$_2$ wt% in ink	CNT:Nafion w:w	MWCNT-NH$_2$ + Nafion wt%
5.60	1 : 2.8	21.2
5.39	1 : 3.5	24.2
5.25	1 : 4.0	26.0
4.95	1 : 5.1	30.3

Since different volumes of Nafion solution were used for each variation of the carbon nanotube/ Nafion ink formulation, the grinding time was adjusted in proportion to the Nafion solution volume (assuming a constant rate of alcohol evaporation over short time periods of 30 mins or less). Inks made with a larger volume of Nafion were ground for longer periods of time to allow a greater volume of Nafion solvent to evaporate before adding the ink solvent, DMF/NMM. This was done with the aim of keeping the final ink viscosities similar across all the samples and maintaining reproducibility.

The inks were then stored in syringes and sealed with parafilm until use. Ink stability was tested by transferring one syringe of ink to a glass vial, leaving the vial undisturbed for 8 weeks and inspection to evaluate any separation of the solid and liquid phases.

It was expected that a higher ratio of carbon nanotubes would produce inks with higher conductivity, however, using a carbon nanotube mass corresponding to a ratio greater than 1:4 for MWCNT-COOH and 1:3.5 for MWCNT-NH$_2$ produced printed patterns that cracked upon drying and flaked off the glass surface. A comparison of the conductivity and mechanical stability of viable inks revealed that inks containing more Nafion were less conductive but were able to withstand greater tensile stress before fracture (*Figure 5.2*).

The optimal weight percentages of carbon nanotube in the ink were found to 2.35% and 5.39% for MWCNT-COOH and MWCNT-NH$_2$ respectively, because of their high conductivity. Although these percentages of carbon nanotube also corresponded to the tensile strength values lower than the maximum measured values, it was deemed sufficient that the samples were devoid of cracks.

Once the optimal ratio of carbon nanotube:Nafion had been determined, parameters for the formulation of a stable, printable ink suspension were considered. The ink needed to be of a suitable viscosity and consistency for printing reproducible patterns with high resolution.

For this stage of the formulation of a carbon nanotube/ Nafion ink, the ratio of carbon nanotube:Nafion was held constant (1:4 for MWCNT-COOH and 1:3.5 for MWCNT-NH$_2$) and the concentration of carbon nanotube/ Nafion in a dimethylformamide/ methyl morpholine (DMF/NMM) mixed solvent was varied. This solvent system was selected since DMF/NMM had previously been found to produce stable dispersions of carbon nanotubes. The different ink formulations produced were deposited in line patterns, dried at 60 °C in air for 15 mins, and tested for stability, by lightly scratching the surface, and conductivity, using a multimeter.
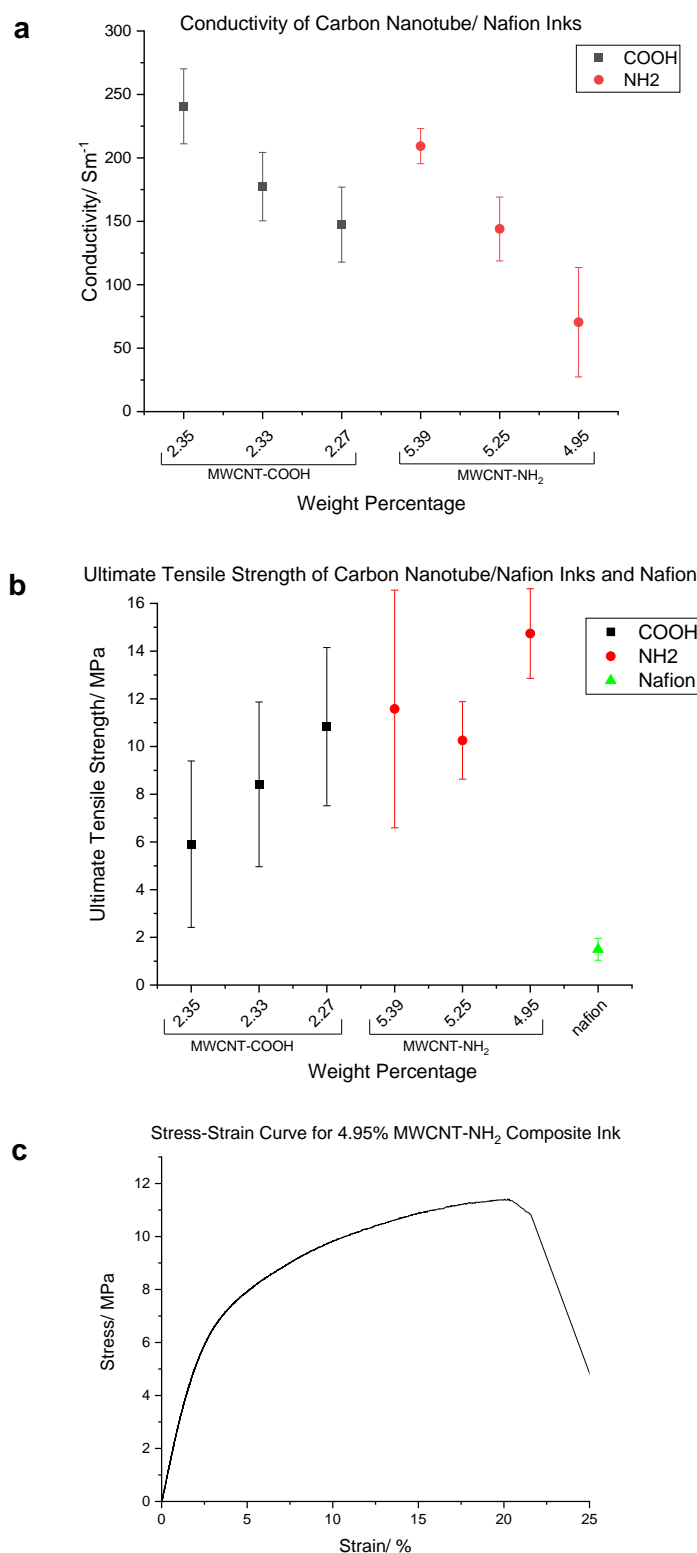
Figure 5.2 *Comparison of the a) Young's modulus (n = 5) and b) conductivity (n = 3) of carbon nanotube inks formulated with different weight percentages of carbon nanotube. c) A stress-strain curve of the 4.95% MWCNT-NH₂/ Nafion sample included as a representative example of the stress-strain curves for all samples.*

The concentration of carbon nanotube and Nafion in the inks was directly linked to the ink viscosity and was found to have a maximum functional range of 10.5 – 15.0% MWCNT-COOH/ Nafion and 21.5 – 27.7% MWNCNT-NH_2/ Nafion. Inks containing a low concentration of CNT/ Nafion had low viscosity, and often spread outside the printed area, lowering the printing resolution and making it more difficult to produce well defined patterns. On the other hand, if the concentration was too high, the ink became a thick paste and clogged the small diameter needle during extrusion. The introduction of a larger diameter needle to accommodate the high viscosity ink, led to a reduction in the printing resolution.

Carbon nanotubes and Nafion solution were ground together to break apart carbon nanotube bundles and allow a physical interaction to develop between the carbon nanotubes and Nafion. A minimum grinding time of 12 mins was required to produce a uniform carbon nanotube/ Nafion ink. Shorter grinding times produced non-uniform inks, the depositions of which contained both stable, continuous sections, and cracked, flaking sections. In some cases, shorter grinding times also caused a phase separation to occur between the carbon nanotubes and Nafion, with a Nafion residue being visible around the edges of the ink pattern.

It is prudent in any process where drying is involved to explore the limits of acceleration of the drying process by using an elevated temperature. Ink patterns deposited from the same formulation were dried at 60 °C and 160 °C. The patterns dried at the lower temperature showed good continuity without cracks. The solvent evaporated slowly and was removed from all sections of the pattern at a roughly even rate. However, the patterns dried at the higher temperature showed extensive cracks. This was because at high temperatures, the rate of evaporation was uneven across the sample, causing more solvent to be removed from some sections than others due to slight differences in the ink layer thickness in different areas. The areas from which more solvent had evaporated shrunk more and became detached from other sections from which less solvent had evaporated. A similar effect is observed when other porous materials, such as clay, are dried quickly. Since the higher temperature is also above the boiling temperature of the DMF/NMM solvent, this could also have introduced bubbles on the sample surface.

5.5. Characterisation of the Physical and Chemical Properties of a Carbon Nanotube/ Nafion Nanocomposite Ink

The inks remained stable over the 8-week period during which they were left undisturbed. They showed little to no separation of the carbon nanotube component from the solvent and were able to produce continuous line patterns when deposited onto a glass substrate.

5.5.1. Effect of Composite Formation on the Graphitic Structure of Carbon Nanotubes

Carbon nanotube/ Nafion nanocomposite films for Raman spectroscopy were prepared by depositing a pea-sized (ca. $\varnothing$ = 4 mm) aliquout of MWCNT-COOH/ Nafion or MWCNT-NH$_2$/ Nafion ink from a syringe onto 12 mm glass coverslips and spreading into a qualitatively even layer across the glass surface with a spatula. The coated coverslips were then dried on a hotplate at 60 °C. The nanocomposite films were imaged in a Renishaw inVia Raman microscope. The Raman microscope settings are detailed in Section 2.2.2.

The Raman spectra for carbon nanotube/ Nafion inks (**Figure 5.3**) exhibit the D, G, 2D and G+D bands characteristic of carbon nanotubes. A comparison of the nanocomposite Raman spectra with the spectra of functionalised carbon nanotube powders shows that there is a decrease in the D:G ratio for the MWCNT-NH$_2$/ Nafion nanocomposite film and an increase in D:G ratio for the MWCNT-COOH/ Nafion nanocomposite film. The Raman spectra of the starting functionalised carbon nanotubes are underlaid in **Figure 5.3** for reference. The band positions and D:G ratios for the carbon nanotube/ Nafion inks and unmodified carbon nanotube powders, shown in **Table 5.3**, were compared with the band positions and D:G ratios for the carbon nanotube-diphenylalanine complexes, shown in **Table 4.1**. The comparison revealed that more significant changes from the D:G ratio for MWCNT-COOH or MWCNT-NH$_2$ are observed for the carbon nanotube/ Nafion nanocomposite than for the carbon nanotube-diphenylalanine complex.
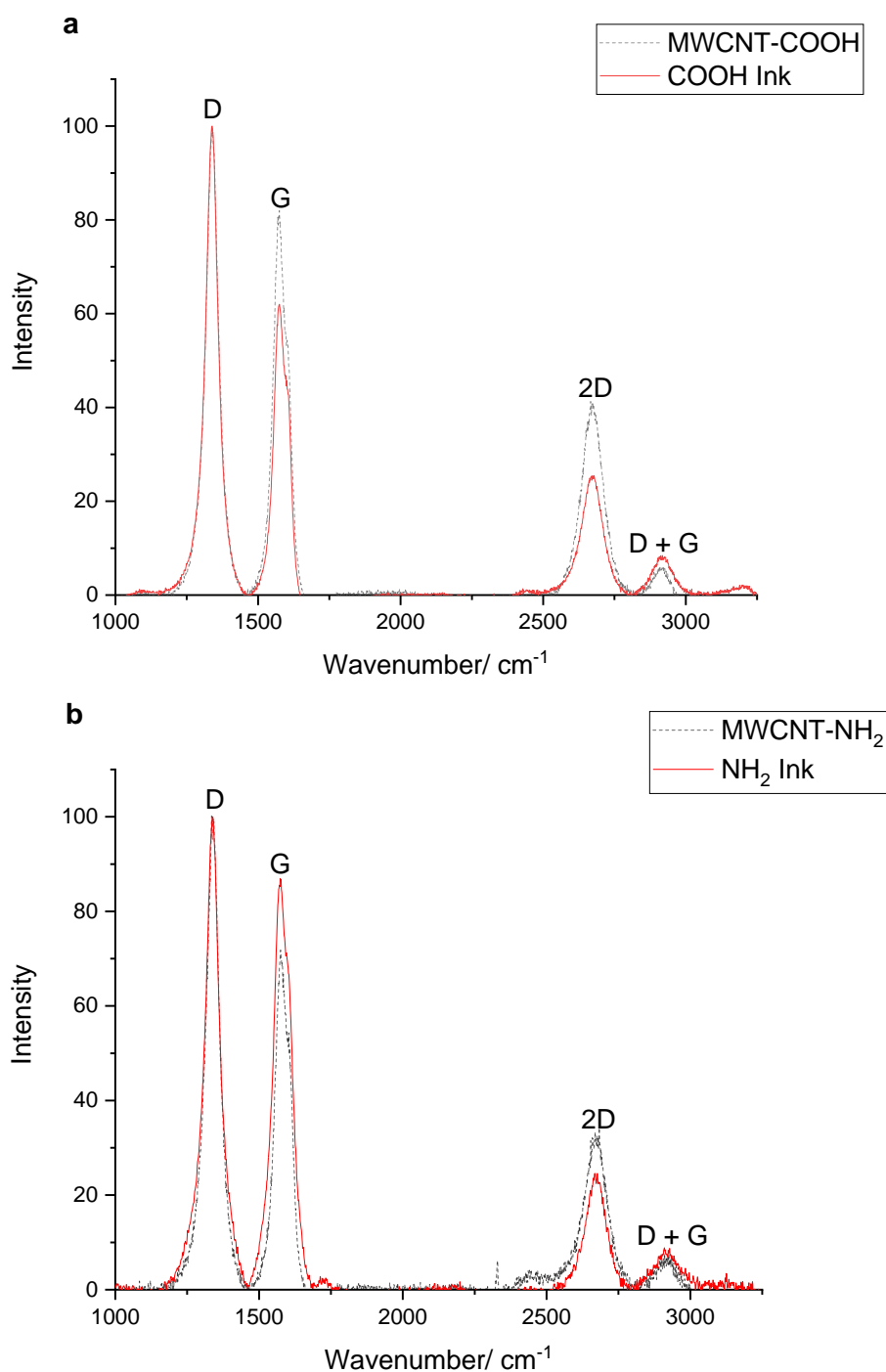
Figure 5.3 *Raman spectra of carbon nanotube-based inks showing the D band (~ 1300 cm^{-1}), G band (~ 1500 cm^{-1}) and 2D band (~ 2600 cm^{-1}). A smaller D+G band is also visible at ~ 2910 cm^{-1} in both spectra. a) MWCNT-COOH/ Nafion nanocomposite (red), MWCNT-COOH powder (underlaid in black) b) MWCNT-NH$_2$/ Nafion nanocomposite (red), MWCNT-NH$_2$ powder (underlaid in black).*

Table 5.3 Comparison of D and G band positions and intensities for the Raman spectra of functionalised carbon nanotubes and carbon nanotube/ Nafion nanocomposites.

Sample	D band Position/ cm^{-1}	G band Position/ cm^{-1}	2D band Position/ cm^{-1}	D + G band Position/ cm^{-1}	D:G Intensity Ratio
MWCNT-COOH/ Nafion	1338	1574	2672	2920	1.61
MWCNT-COOH	1338	1573	2670	2915	1.18
MWCNT-NH$_2$/ Nafion	1338	1574	2673	2918	1.15
MWCNT-NH$_2$	1339	1573	2671	2922	1.29

5.5.2. **Morphology of Carbon Nanotube/ Nafion Nanocomposites**

Nanocomposite films prepared for Raman spectroscopy were mounted onto SEM stubs and examined by SEM. The upper and under sides of the nanocomposite films were imaged to investigate the polymer distribution within the nanocomposites. The imaging process was followed as detailed in Section 2.2.9.

Scanning electron micrographs of the upper side of both MWCNT-COOH/ Nafion and MWCNT-NH$_2$/ Nafion nanocomposites are found in **Figure 5.4**. At high magnification, intertwining of carbon nanotubes with sections of Nafion polymer can be seen.

Scanning electron micrographs of the cross section of the MWCNT-NH$_2$/ Nafion nanocomposite are shown in **Figure 5.5**. They reveal that most of the carbon nanotubes are well dispersed in the Nafion matrix and that the material has a porous internal structure. The micrograph of the underside of MWCNT-NH$_2$/ Nafion, shown in **Figure 5.5d**, shows high contrast carbon nanotubes with areas of patchy low contrast, indicating some non-uniform distribution of carbon nanotube aggregates within the Nafion matrix.
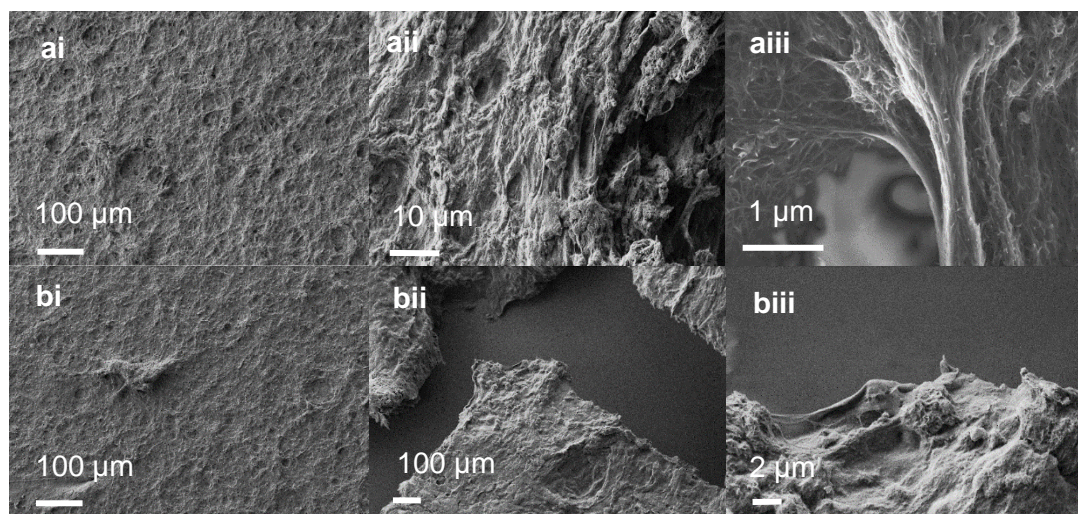
Figure 5.4 Scanning electron micrographs of the nanocomposite upper surface at low and high magnification. a) MWCNT-COOH/ Nafion, b) MWCNT-NH$_2$/ Nafion
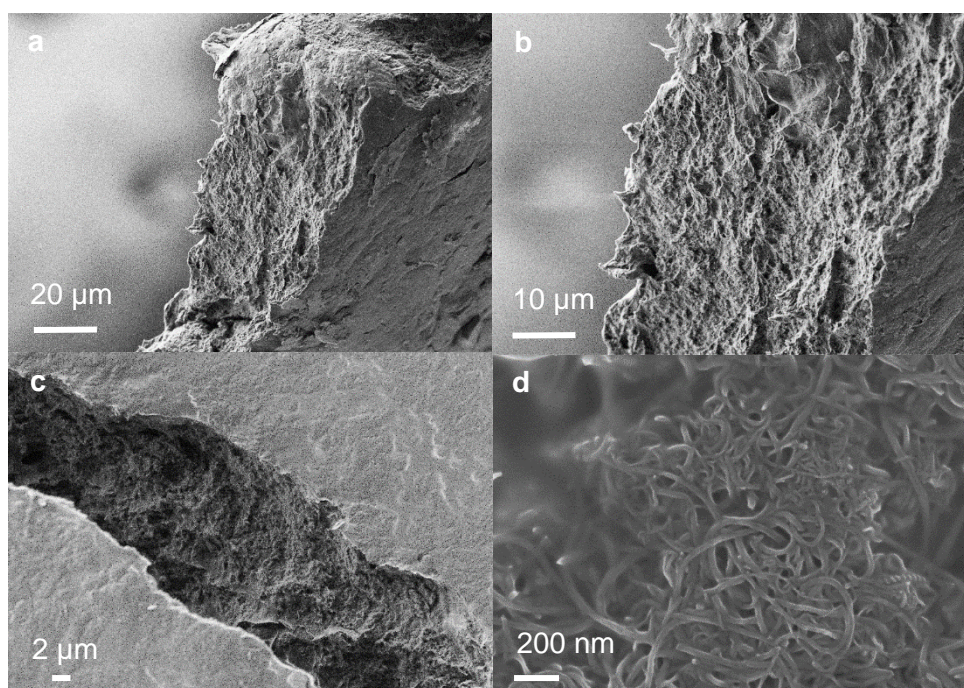
Figure 5.5 Scanning electron micrographs of MWCNT-NH$_2$/ Nafion. a-c) cross section of MWCNT-NH$_2$/ Nafion, showing microcracks and the porous structure of the nanocomposite, d) high magnification micrograph of the nanocomposite underside- captured with InLens SEM detector

5.5.3. **Carbon Nanotube/ Nafion Nanocomposite Ink Viscosity**

The viscosity of a carbon nanotube-based ink has considerable influence on the printability of the ink and the integrity of printed patterns. It was therefore important to ensure that the inks prepared in this work were of similar viscosity so that any observed differences between their printability and the quality of their printed patterns could be attributed to differences in ink components rather than differences in their viscosities. The viscosities of the carbon nanotube/ Nafion inks were determined using the method described in Section 2.2.7.

The graphs in *Figure 5.6* show the relationship between carbon nanotube ink viscosity and shear rate. The inks display a shear-thinning effect characteristic of non-Newtonian fluids. The shear-thinning of the MWCNT-COOH/ Nafion ink follows a linear regime whereas the shear-thinning of the MWCNT-NH$_2$/ Nafion ink diverges from a linear regime as the shear rate increases. At a shear rate of 100 s^{-1}, the MWCNT-COOH/ Nafion and MWCNT-NH$_2$/ Nafion inks have viscosities of 0.73 and 0.86 Pa s respectively. (This is similar to the consistency of a proprietary hand cream.)

The Power Law model (Ostwald-de Waele relationship) is a widely used model for describing the behaviour of Non-Newtonian fluids. It relates the viscosity (η) and shear rate (γ) to constants K and n (Equation 5.1) where K is the consistency index and n is the flow behaviour index.

$$\eta = K\gamma^{n-1} \qquad\qquad (5.1)$$

Applying Equation 5.1 to the data in *Figure 5.6* gives values of n = 0.174, K = 32.7 Pa s for the MWCNT-COOH/ Nafion ink, and n = 0.29, K = 22.7 Pa s for the MWCNT-NH$_2$/ Nafion ink.

Values of n < 1 confirm the pseudoplastic behaviour of the inks (n = 1 for a Newtonian fluid) and K gives an indication of the apparent viscosity of the inks in the absence of shear stress. It is interesting to note that the value of K for the MWCNT-COOH/ Nafion nanocomposite containing 2.35% CNT, is greater than that for the MWCNT-NH$_2$/ Nafion nanocomposite, containing 5.39% CNT.

a Relationship Between COOH Ink Viscosity and Shear Rate

b Relationship Between NH$_2$ Ink Viscosity and Shear Rate
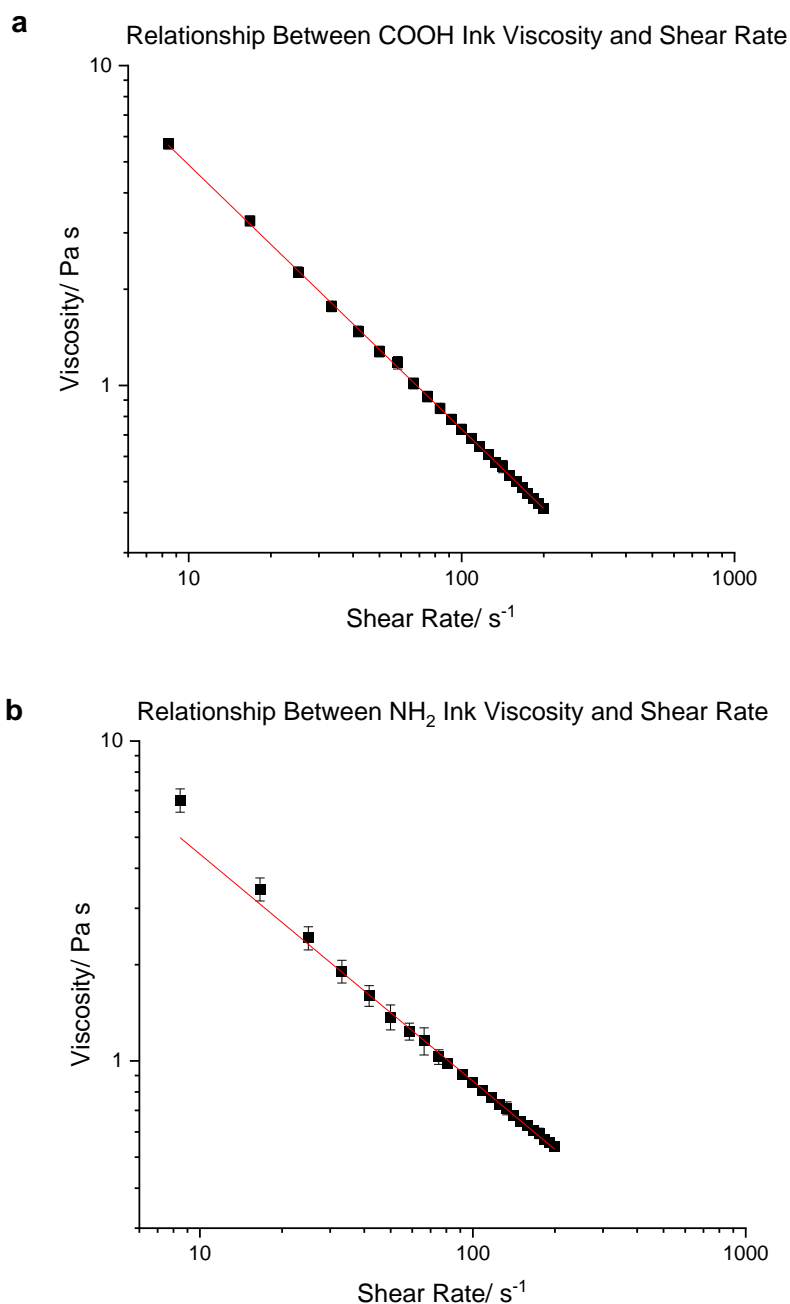
Figure 5.6 Viscosity of carbon nanotube-based inks against shear rate, n = 3 for both samples. A pre-shear rate of 400 s^{-1} was applied before the start of the measurement. a) MWCNT-COOH (2.35%)/ Nafion ink, b) MWCNT-NH$_2$ (5.39%)/ Nafion ink. The error bars for MWCNT-COOH/ Nafion ink are too small to be visible on the present scale.

5.5.4. Bulk and Nanoscale Mechanical Properties of Carbon Nanotube/ Nafion Nanocomposites

The mechanical properties of carbon nanotube/ Nafion ink depositions were investigated at bulk and nanoscale surface, using an ElectroForce Biodynamic® Test Instrument, as described in Section 2.2.8, and atomic force microscopy (AFM), as described in Section 2.2.11, respectively.

The stress-strain profiles for the composite materials (*Figure 5.7*) were analysed and used to calculate the ultimate tensile strengths of the MWCNT-COOH/ Nafion and MWCNT-NH$_2$/ Nafion nanocomposites, as shown in **Table 5.4**. The stress- strain profile of the MWCNT-COOH/ Nafion nanocomposite is comparable to that of a brittle material, with no distinguishable necking region before failure. This differs from the profiles observed for MWCNT-NH$_2$/ Nafion and Nafion casts, which both undergo necking once the ultimate tensile strength has been reached, before failure.

The ultimate tensile strengths of the MWCNT-COOH/ Nafion and MWCNT-NH$_2$/ Nafion nanocomposites are greater than that recorded for Nafion casts suggesting that much of the nanocomposite mechanical strength is derived from the carbon nanotube component.
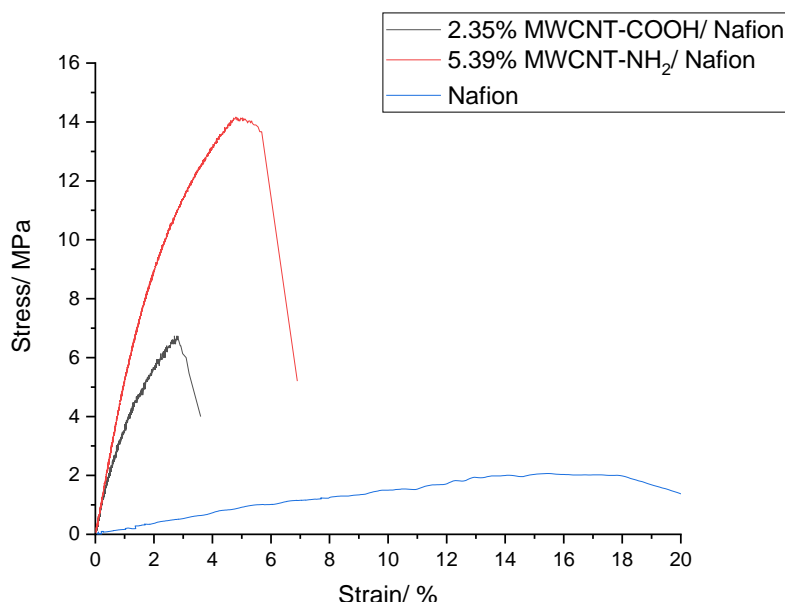
Figure 5.7 Representative stress-strain curves for casts of MWCNT-COOH/ Nafion, MWCNT-NH$_2$/ Nafion and Nafion

For AFM mechanical tests, dried nanocomposite films were transferred to the AFM chamber. Measurements were taken as described in Section 2.2.11.

The surface moduli of the MWCNT-COOH/ Nafion and MWCNT-NH$_2$/ Nafion nanocomposites (**Table 5.5**) are of the order of 10^9 Pa. This is one order of magnitude greater than the Young's modulus of the same materials, showing that while the carbon nanotubes themselves have high mechanical strength, the joints between carbon nanotubes introduce weak points into the nanocomposite film. The surface modulus recorded for Nafion is an order of magnitude smaller than the Young's modulus recorded for the same material.

Table 5.4 Ultimate tensile strength, Young's modulus and strain at break of carbon nanotube-based nanocomposites and Nafion films measured by Electroforce mechanical measurements. MWCNT-COOH/ Nafion n = 4, MWCNT-NH$_2$/ Nafion n = 4, Nafion n = 3

Sample	Mean Ultimate Tensile Strength/ MPa	SD (+/-) /MPa	Young's Modulus/ MPa	SD (+/-)/ MPa	Strain at break/ %
MWCNT-COOH/ Nafion Ink	5.9	3.5	410	160	2.8
MWCNT-NH$_2$/ Nafion Ink	11.6	5.0	518	95	5.6
Nafion	1.5	0.5	15	2	18.0

Table 5.5 Surface moduli of carbon nanotube nanocomposite films and Nafion casts measured at different scales by AFM with cantilever tip diameter = 20 nm. a) NH$_2$ ink, b) COOH ink, c) Nafion.

a

MWCNT-NH$_2$ Nafion Ink Scale	Surface Modulus/ GPa
8um	5 - 15
5um	2.5 - 10
1.4um	5 - 8.5
0.6um	5.5 - 7

b

MWCNT-COOH/ Nafion Ink Scale	Surface Modulus/ GPa
5um	0.5 - 1
1.4um	0.8 - 1
1.2um	1 - 1.15
0.6um	0.9 - 1.05

c

Nafion Scale	Surface Modulus/ MPa
8um	0.1 - 0.9
5um	0.1 - 0.3
1.4um	0.02 - 0.7
0.6um	2-5

5.5.5. **Wettability of Carbon Nanotube/ Nafion Nanocomposites**

The contact angle of a material gives an indication of its hydrophilicity and can offer insight into whether the material is likely to support cell growth. Materials with contact angles > 90° are considered hydrophobic, while materials with contact angles < 90° are considered hydrophilic [136]. Contact angle measurements were made to compare the hydrophilicity of carbon nanotube/ Nafion inks to their corresponding functionalised carbon nanotube starting material and glass. Nanocomposite films were prepared by depositing a pea-sized (ca. Ø = 4 mm) aliquot of ink onto 12 mm glass coverslips and spreading into a qualitatively even layer across the glass surface with a spatula. The coated coverslips were then dried on a hotplate at 60 °C and measurements were taken as described in Section 2.2.6.

Once dried, some of the nanocomposite films were used for further experiments, including cell culture. For those purposes, nanocomposite films were submerged in water to release them from the glass coverslips onto which they had been deposited. It was noticeable that while the upper side of the nanocomposite films had a matte finish, the underside of the nanocomposite films, which had previously been in contact with the glass surface, had a glossy appearance, similar to that of dried depositions of pure Nafion. It was suspected that a higher proportion of Nafion may be found on the underside of the nanocomposite films. This was tested by measuring the contact angle of the underside of an MWCNT-NH$_2$/ Nafion nanocomposite film and comparing this to the contact angles of the MWCNT-NH$_2$/ Nafion nanocomposite film upper side and pure Nafion.

The contact angles for functionalised carbon nanotubes and carbon nanotube/ Nafion nanocomposite samples are shown in **Table 5.6**. Nafion and the underside of the MWCNT-NH$_2$/ Nafion nanocomposites have the smallest contact angles, followed by glass. The contact angles of the nanocomposites are slightly above that of glass, with the functionalised carbon nanotubes having the largest contact angles of the studied materials. It is noteworthy that the contact angles of carbon nanotube inks are lower than the contact angles of functionalised carbon nanotubes as this indicates that the hydrophilicity of Nafion influences the wettability of carbon nanotubes within the carbon nanotube/ Nafion nanocomposite inks. The reduction in contact angle measured for the carbon nanotube/ Nafion inks suggests that the nanocomposites may be more suitable for supporting cell growth than carbon nanotubes alone.

Carbon Nanotube-based Nanocomposite Inks and Electrodes | Characterisation of
the Physical and Chemical Properties of a Carbon Nanotube/ Nafion Nanocomposite
Ink

Table 5.6 Contact angles of water deposited onto glass, functionalised carbon
nanotubes, carbon nanotube nanocomposite films and Nafion films

Sample	Contact Angle / °	SD (+/-) / °
Glass (control)	70.0	5.5
MWCNT-COOH	110.6	10.5
MWCNT-NH$_2$	105.5	9.6

Sample	Contact Angle / °	SD (+/-) / °
MWCNT-COOH/ Nafion	75.2	4.5
MWCNT-NH$_2$/ Nafion	80.9	4.3
Nafion	63.9	1.0
MWCNT-NH$_2$ underside	66.1	8.0

The photographs in **Figure 5.8** show the behaviour of water droplets deposited onto
the MWCNT-NH$_2$/ Nafion nanocomposite film, and Nafion film. The greater
hydrophilicity of Nafion is visible by the higher degree of water droplet spreading on the
Nafion surface. The nanocomposite films are shown to be less hydrophilic, with the ink
droplets remaining more rounded on the surfaces of the MWCNT-NH$_2$/ Nafion
nanocomposite.

a

$\theta= 80.9° ± 4.32°$

b

$\theta= 63.9° ± 1.00°$
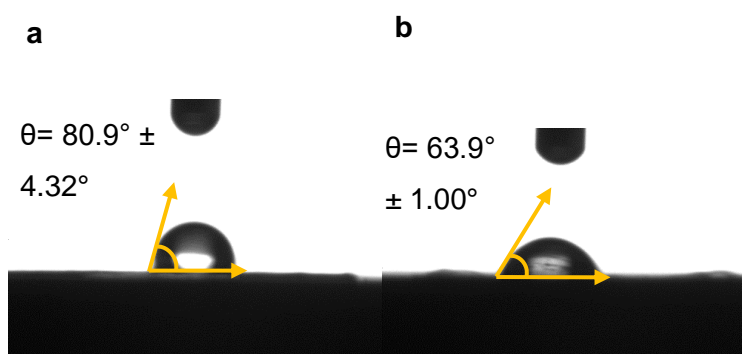
*Figure 5.8 Contact angle images of water droplets on a) MWCNT-NH$_2$ nano-
composite film, b) Nafion film. The angles marked on the images correspond to θ.*

5.5.6. Electrical Conductivity of a Carbon Nanotube/ Nafion Nanocomposite

The electrical properties of carbon nanotube/ Nafion ink depositions were evaluated by
resistance and impedance measurements. Impedance analysis slides, identical to
those described in Section 2.2.5 were used to prepare the samples. The conductivity of

the inks was evaluated by depositing 30 µl of ink between the two gold sputtered ends. The ink was extruded for 12 s using a flow rate control pump set to 9 ml/ hr and was spread in a qualitatively even layer on the glass using a spatula. Samples were dried for 15 mins on a hotplate in air at 60°C before measuring the resistance using a multimeter across the two gold electrodes. From the resistance measurements and sample dimensions, it was calculated that the conductivities of MWCNT-COOH/ Nafion and MWCNT-NH$_2$/ Nafion nanocomposites were 240 ± 30 Sm^{-1} and 209 ± 14 Sm^{-1} respectively.

Impedance measurements were conducted after the resistance measurements, using the same samples. Impedance measurements were taken to explore the AC conductivity of the nanocomposite materials and investigate whether frequency had any effect on their conductive behaviour. The impedance analysis slides were connected to a Zahner IM6 electrochemical workstation and Bode plots were recorded using the parameters described in Section 2.2.5.

The Bode plots for MWCNT-COOH/ Nafion and MWCNT-NH$_2$/ Nafion nanocomposites (**Figure 5.9**) show results characteristic of conductors whereas the Nafion Bode plot closely resembles that of a capacitor. The phase angle of Nafion approaches zero as the frequency increases, indicating an inverse relationship between capacitive effect and frequency. This behaviour changes above a frequency of 10^5 Hz, which is a point of inflection for the Nafion phase angle. Above this frequency, Nafion impedance shows an exponential increase. Within the human hearing range, 250 – 20 000 Hz, the impedance and phase of MWCNT-COOH/ Nafion nanocomposites and MWCNT-NH$_2$/ Nafion nanocomposites remain constant. In this same range, the impedance and phase of Nafion do not change drastically.
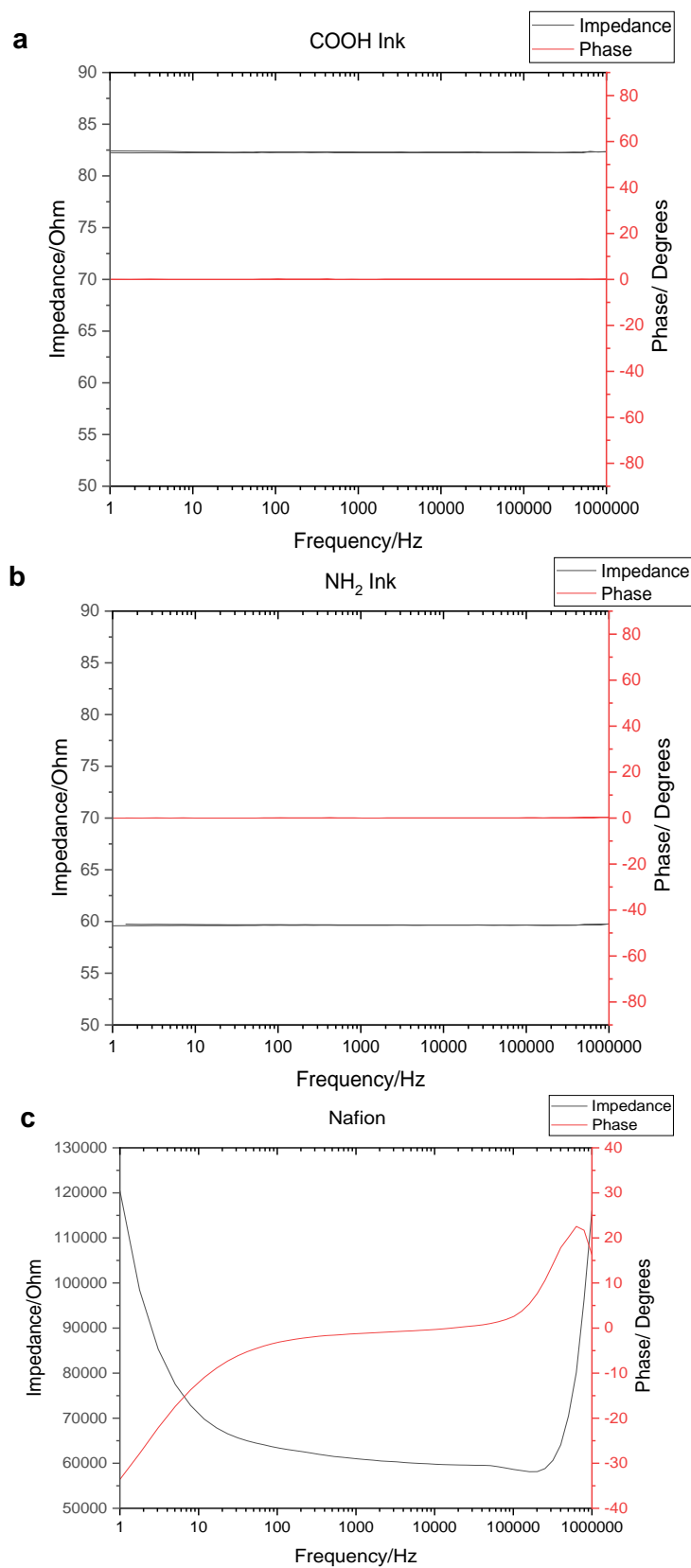
Figure 5.9 *Representative Bode plots of a) MWCNT-COOH/ Nafion nanocomposite, b) MWCNT-NH₂/ Nafion nanocomposite, c) Nafion*

5.5.7. **Electrochemistry of Carbon Nanotube/ Nafion Electrodes**

Electrochemistry facilitates the study of chemical reactions occurring on the surface of an electrode. It is often used to obtain qualitative and quantitative information about reactions in which one chemical species is oxidised and the other is reduced, known as redox reactions [157], and to investigate the ability of electrode materials/ coatings to collect and transfer electrons. In this work, electrochemistry was used to investigate the ability of the carbon nanotube/ Nafion nanocomposites to store and transfer charge, and to determine the mode of charge transfer – capacitive or Faradaic. Capacitive charge transfer is preferred for implantable electrodes since this type of charge transfer does not involve any permanent chemical changes.

The technique used in this work is cyclic voltammetry – in which the voltage inside an electrochemical cell is cycled between a predefined start and end potential, using a potentiostat. The electrochemical cell can consist of two-electrodes (working and counter electrodes), three-electrodes (working, counter and reference electrodes) or, less frequently, four-electrodes (working, working sense, counter and reference electrodes).

The working electrode is either the test material involved in the reaction or an inert material which can transfer current without suffering degradation. A test material can be applied to the polished surface of an inert working electrode. The counter electrode is the electrode that the current is transferred to/ from. The working-counter electrode pair creates a closed circuit within the system. The purpose of the reference electrode is then to provide an experimental reference point based on the electrode potential of a known couple, for example, a silver wire in a solution of silver chloride. Systems employing a fourth 'sense' electrode, measure the effect on the electrolyte solution, of the reaction between the working and counter electrodes, rather than the reaction itself.

The electrolyte is a conductive solution containing ions that can be oxidised or reduced at the working or counter electrodes. When studying reversible reactions, an appropriate electrolyte is ferrocyanide since it undergoes reversible oxidation to ferricyanide, as demonstrated in Equation 5.2 below. The Fe^{2+} ion in ferrocyanide is oxidised to Fe^{3+} in ferricyanide.

$$[Fe(CN)_6]^{4-} \rightleftharpoons [Fe(CN)_6]^{3-} + e^- \qquad E° = -0.36 \text{ V [217]} \qquad\qquad (5.2)$$
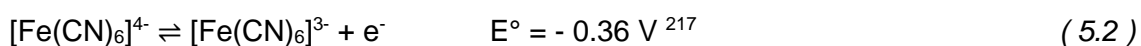
The electron transfer properties of carbon nanotube/ Nafion composites and Nafion were investigated using a three-electrode system with a ferrocyanide $[Fe(CN_6)]^{4-}$ electrolyte. Potassium ferrocyanide $(K_4[Fe(CN)_6] \cdot 3H_2O)$ was used to make up the 0.001 M ferrocyanide $[Fe(CN)_6]^{4-}$ solution and 0.01 M potassium chloride (KCl) solution was used as a background electrolyte. Fresh electrolyte solution was prepared as required determined by the extent of oxidation to ferricyanide assessed visually – solutions were generally discarded after three days.

The electrochemical cell was a custom-made borosilicate (pyrex) glass three-electrode cell with equidistant openings to accommodate each electrode. The working electrode (WE) was a glassy carbon electrode (GCE) with a working area of approximately 3mm diameter in the centre of the end of the electrode body, diameter 6.4mm. The counter electrode (CE) was 0.5mm diameter platinum wire. The reference electrode (RE) was a silver/ silver chloride reference electrode. A diagram of the three-electrode electrochemical system is shown in **Figure 5.10**.

The voltage was supplied by and current measurements made with a Zahner IM6 electrochemical workstation and the associated Thales software was used to make and record all electrochemical measurements. Cyclic voltammetry was measured between 0 – 700 mV at a scan rate of 20 mVs^{-1} and three cycles were completed per scan. Samples were prepared by drop coating 10 μl of ink or Nafion onto a clean glassy carbon electrode. Inks were then spread over the whole electrode area and dried by applying a warm air flow from a distance of 10 cm for 3 mins. For Nafion samples, the drying distance was increased to 30 cm to avoid disturbing the liquid droplet.

Between samples and repeats, the working electrode was cleaned with 0.05 μm alumina abrasive powder and deionised water on a microfibre polishing pad (CH Instruments, CHI120).

Carbon Nanotube-based Nanocomposite Inks and Electrodes | Characterisation of
the Physical and Chemical Properties of a Carbon Nanotube/ Nafion Nanocomposite
Ink
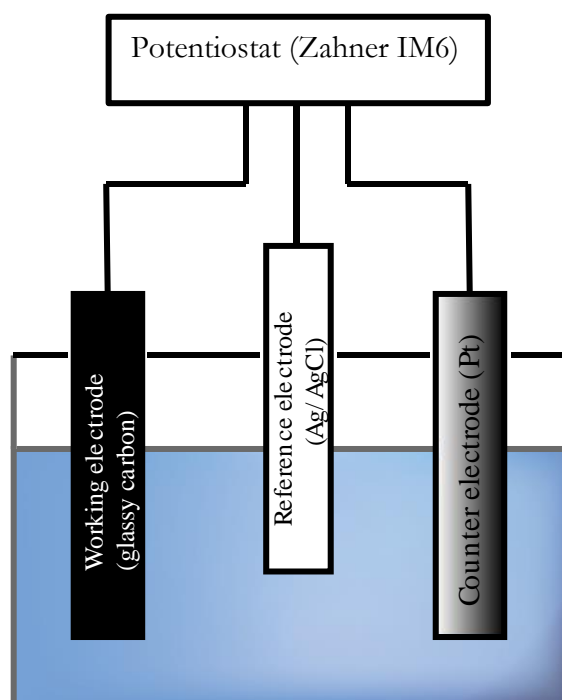
Figure 5.10 *Diagram of three-electrode electrochemical system*

Cyclic voltammetry measurements over a voltage range of 0 – 0.7 V revealed oxidation
and reduction peaks in current for the clean electrode but no clear peaks for the inks or
Nafion. The cyclic voltammograms displayed in **Figure 5.11** show that the current
response of the inks dried on top of the electrode is two orders of magnitude greater
than the current response of the clean electrode. The Nafion coated electrode behaved
as an insulator, giving rise to a current response that was an order of magnitude lower
than that seen for the clean electrode. This suggests that the Nafion makes no
contribution to the high electron transport seen for the inks. The MWCNT-NH$_2$/ Nafion
ink consistently yielded a current response approximately twice the response seen for
MWCNT-COOH/ Nafion ink. This is consistent with the MWCNT-NH$_2$/ Nafion ink
containing almost twice the mass of carbon nanotube per unit volume, compared to the
MWCNT-COOH/ Nafion ink (**Table 5.2**).

Carbon Nanotube-based Nanocomposite Inks and Electrodes | Characterisation of
the Physical and Chemical Properties of a Carbon Nanotube/ Nafion Nanocomposite
Ink

a

b

c

d
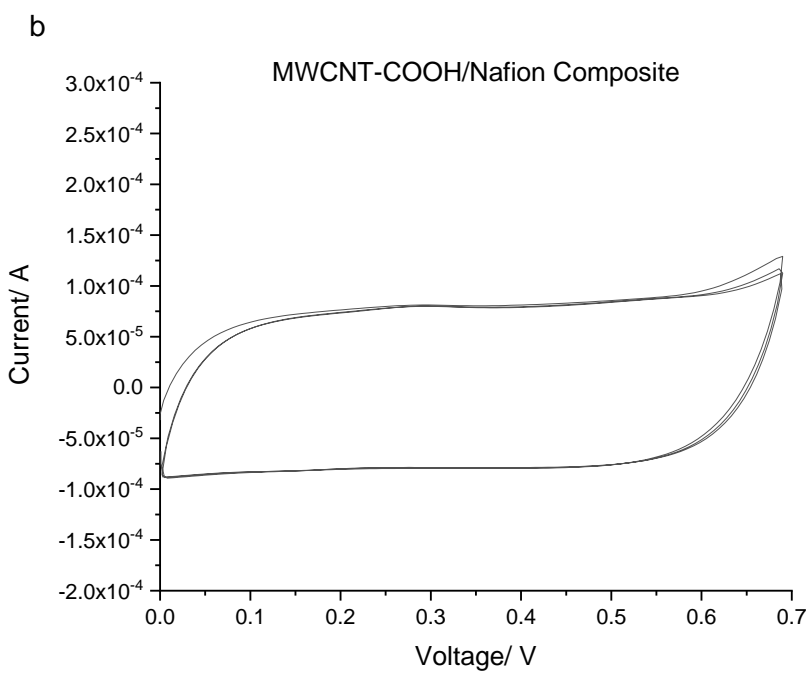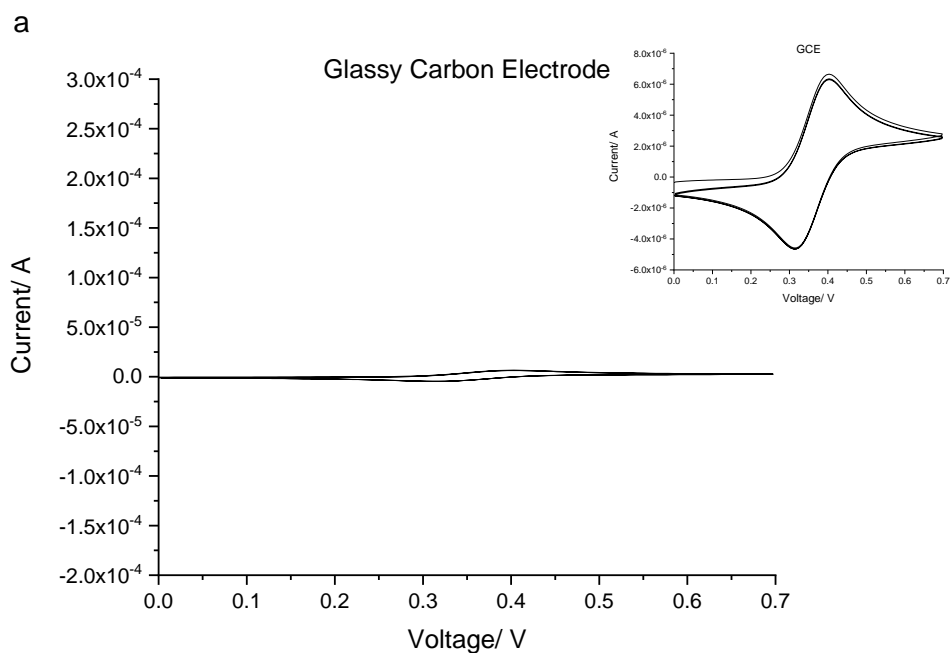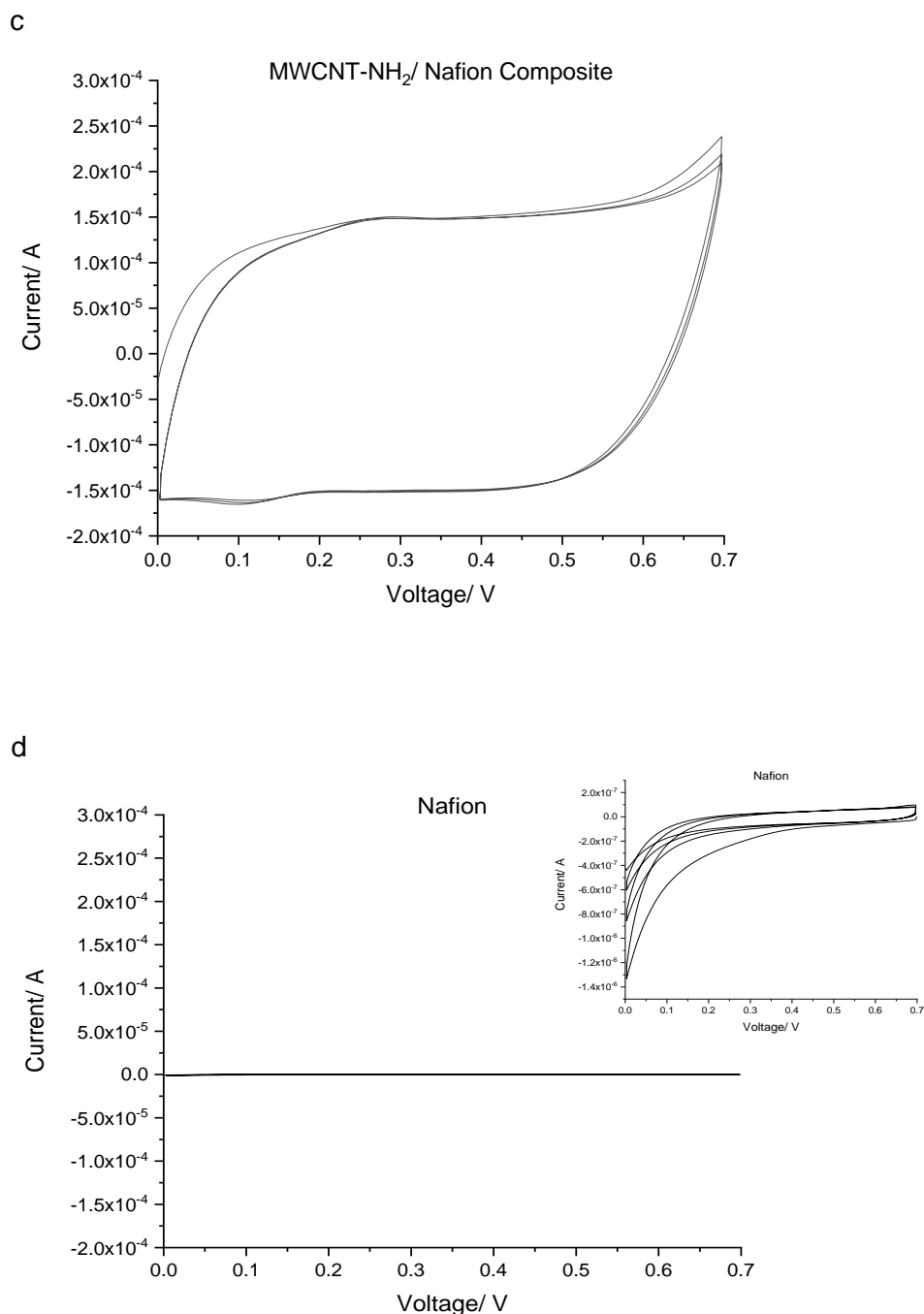
Figure 5.11 *Cyclic voltammograms of a glassy carbon electrode (GCE) in a [Fe(CN)$_6$]$^{4-}$ electrolyte. a) clean GCE, the y-axis scale of the insert ranges from -6 x10^{-6} – 8 x10^{-6} A, b) GCE coated with COOH ink, c) GCE coated with NH$_2$ ink, d) GCE coated with Nafion, the y-axis scale of the insert ranges from -1.4 x10^{-6} – 2 x10^{-7} A. The cyclic voltammograms show three cycles during which the currents of the clean GCE and CNT ink coated GCE systems stabilise after the first cycle. The Nafion system is unstable and the current continues to drift throughout the reading.*

The electrochemical properties of the electrode materials studied can be found in **Table** *5.7*. Of interest were the electroactive area and the charge storage capacity. Since the ferrocyanide-ferricyanide redox couple is a reversible system, the electroactive surface area can be calculated using the simplified Randles-Sevcik equation [218], Equation 5.3:

$$i_p = 268600 n^{\frac{3}{2}} A D^{\frac{1}{2}} C v^{\frac{1}{2}}$$

(5.3)

where:

i_p (A) = peak current

n = number of electrons transferred in the redox reaction (n = 1 in this case)

A (cm^2) = electroactive surface area

D (cm^2 s^{-1}) = diffusion coefficient (6 x10^{-6} for [Fe(CN)$_6$]$^{4-}$)

C (mol cm^{-3}) = concentration of the reactive species in the electrolyte

v (V s^{-1}) = scan rate

Table 5.7 Electrochemical properties of electrode materials. The geometric area for GCE was the working area of the electrode (area = 0.0707 cm^2), geometric area of carbon nanotube/ Nafion and Nafion coatings was equal to the area of the end of the electrode body (area = 0.322 cm^2). The cyclic voltammograms for Nafion showed significant drift for each cycle, which precluded calculation of the charge storage capacity

Electrode	Maximum Current/ A	Electroactive Surface Area/ cm^2 (3 s.f.)	% of Electrode Geometric Area	Charge Storage Capacity/ mC cm^{-2} (3 s.f)
GCE	6.35 x10^{-6}	0.0682	96.5	1.96
MWCNT-COOH/ Nafion	8.21 x10^{-5}	0.882	274	22.9
MWCNT-NH$_2$/ Nafion	1.51 x10^{-4}	1.62	504	41.3
Nafion	6.93 x10^{-8}	0.000745	0.231	-

The charge storage capacity was calculated by first finding the current density, then calculating the area inside the graph of current density vs voltage and dividing this number by the scan rate. This value was divided by 2 to obtain the charge density for either the cathodic or anodic phase.

5.6. Deposition of Carbon Nanotube/ Nafion Ink Using a 3D Bioprinter

After optimisation and characterisation of both MWCNT-NH$_2$/ Nafion and MWCNT-COOH/ Nafion inks, the MWCNT-NH$_2$/ Nafion ink was selected for the subsequent deposition stage as its casts had high conductivity and was more flexible and easier to manipulate than the MWCNT-COOH/ Nafion nanocomposites.

For the purpose of improving reproducibility, 3D printer was employed. Due to availability, the printer used in this work was an Incise Dental Scanner (Renishaw, UK), which had been modified to perform as a 3D printer. It had the capability to deposit cells and materials simultaneously, although only the materials printing capability was used here.

Electrode patterns were designed in Tinkercad (Computer Aided Design software, Autocad). Two electrode designs were prepared, a T-shaped electrode and a parallel bar electrode. The electrode designs are shown in **Figure 5.12**.
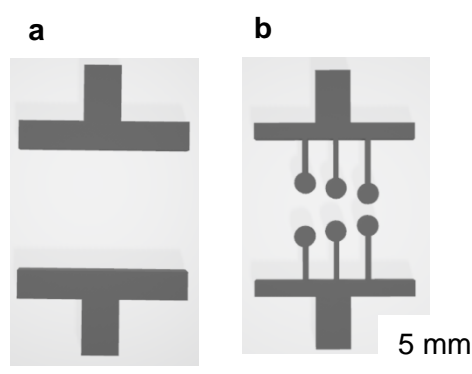
Figure 5.12 *Computer aided design drawings of electrode patterns. a) T-shaped electrode. Vertical distance between electrodes is 7 mm. b) parallel bars electrode. Vertical distance between bars is 3 mm, 2 mm, 1 mm from left to right*

The electrode designs were then manually translated into G-code to be read by the commercial bioprinter. The designs were printed onto glass microscope slides using the 3D bioprinter. The printer used hydraulic pressure to control the volume of ink deposited onto the surface (**Figure 5.13**), depositing ink in 20 nl steps, when using high resolution mode.
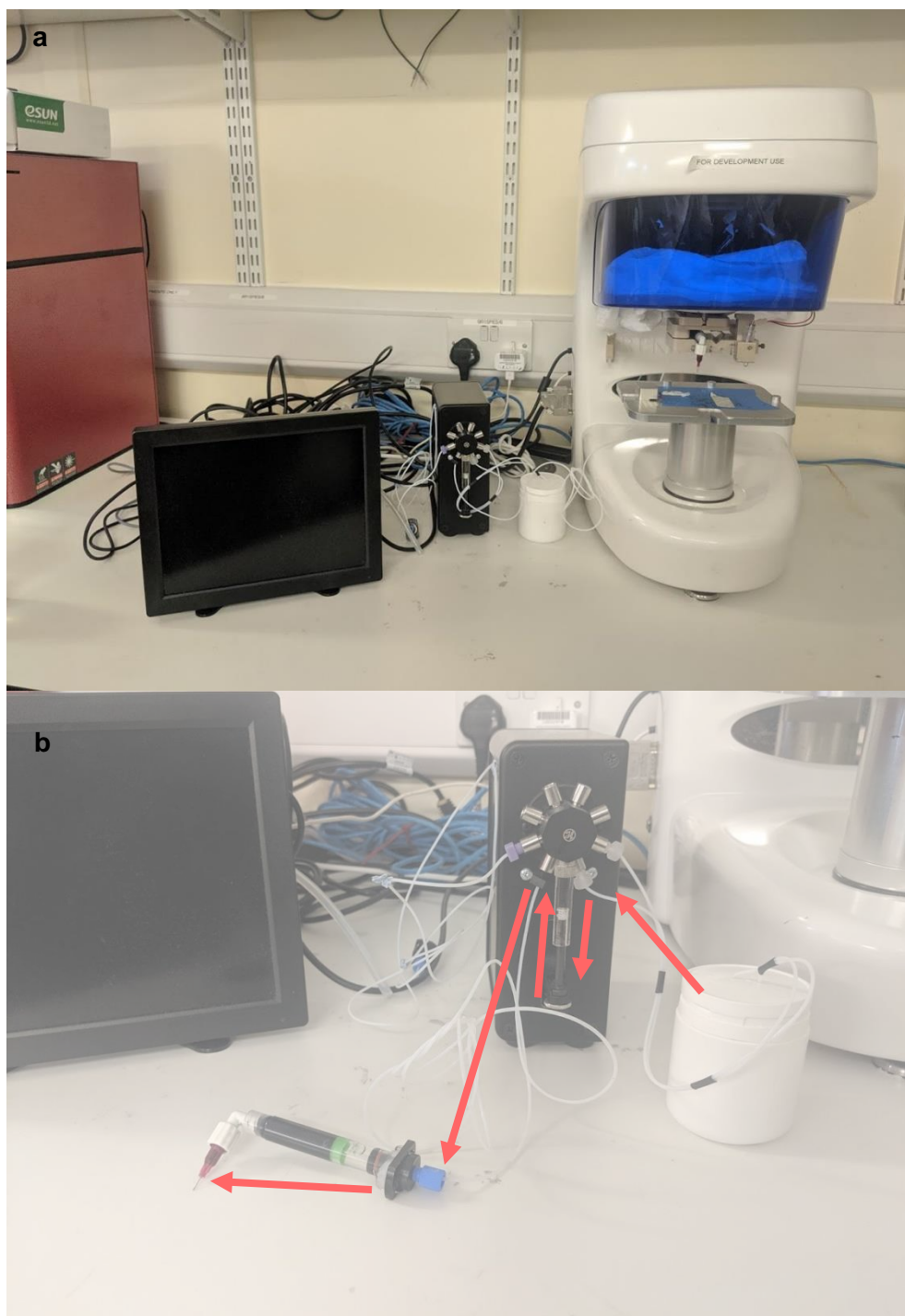
Figure 5.13 *Diagram of Renishaw dental scanner/ 3D bioprinter showing a) computer, hydraulic control pump and printing stage, b) annotated hydraulic control pump showing water flow from source (rightmost arrow) to carbon nanotube/ Nafion ink deposition (leftmost arrow)*

The printing parameters were determined by trial and error using an alginate hydrogel before fine-tuning with the carbon nanotube ink. Printing speeds of 1 mm s^{-1} and 5 mm s^{-1} were attempted and ink volume step size was varied based on line length. The printer setup and printing parameters were communicated to the bioprinter using a G-code programme. **Figure 5.14** and **Figure 5.15** show annotated excerpts of bioprinter G-code, defining some of the printing parameters.


```
# Test T shape
# use 250um Nozzle to give 250um thick print
# using Nozzle 1 with hardware trigger

# Nozzle 1 = N1h24007S8A24000k0K0
# Nozzle 2 = S14h24001D300
# Nozzle 3 = S27h24001H1D264M1000S14P500
# Nozzle 4 = S27h24001H1D400M1000S14P500
# Nozzle 5 = S27h24001H1D468M1000S14P800
# Nozzle 6 = S27h24001H1D200M1000S14P400
# Nozzle 7 = S27h24001H1D1200M1000S14P1000
# Nozzle 100 = T

# execute set-up of Nozzle
Nozzle 1
SLEEP 2000

# set print acceleration to 1000mm/s^2
a1000

# set Nozzle ready to print and rapid to offset position
Nozzle 2
SLEEP 2500
v50
X12.82 Y0 Z0
V5
```

Nozzle 1- prepares syringe 1 for printing. Fills water bank and sets instrument to 24000 steps (high resolution)

Nozzle 2- Pushes a small volume of ink to the tip of the needle to wet the printing surface and improve adhesion

Nozzle 3—7 Instructs the instrument to extrude the volume of ink required to draw each line

SLEEP 2500- Instructs instrument to wait for 2500 ms before executing next command

Nozzle 100- Terminates the program

v5- Sets platform movement speed to 5 mm s^{-1}

Figure 5.14 *Annotated excerpt of G-code for T-shaped electrode showing details of printer setup and printing parameters*

Instructs printer to wait for 1000 ms after printing a feature

Instructs printer to pause until a trigger command is given

Sets printer to 100 motor steps per second

Withdraws 500 steps of ink

```
# Nozzle 3 = S27h24001H1D264M1000S14P500
```

Instructs printer to use position 1 on the syringe pump

Extrudes 264 steps of ink

Sets printer to 800 motor steps per second
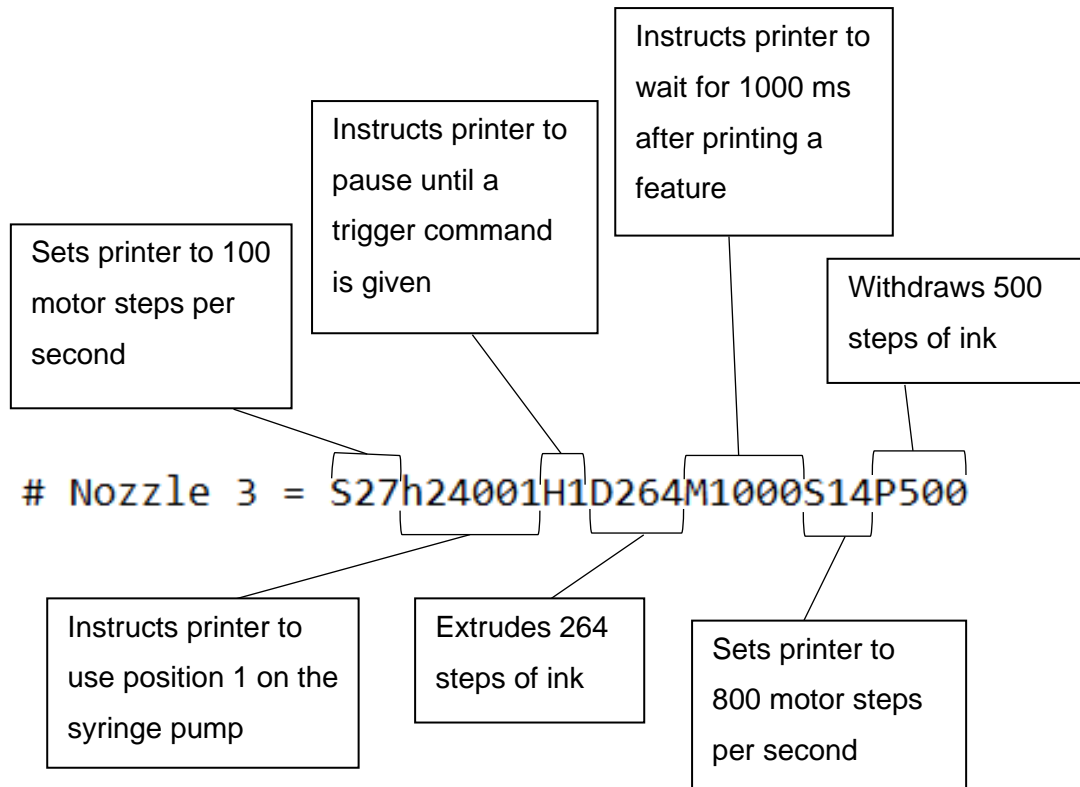
Figure 5.15 *Excerpt of annotated G-code defining the printing parameters in detail.*

This is a new technique, so there is a variation in terminology. The terms 'platform speed' and the 'ink syringe speed' are used interchangeably.

A needle with a luer lock connection was added to the syringe to facilitate printing. Printing was attempted using a 22-gauge and a 25-gauge needle since the needle diameter had a profound impact on printing resolution and integrity of final deposited pattern.

A larger, 22-gauge needle was attempted first and resulted in a low resolution deposition. A smaller 25-gauge needle was attempted and resulted in a higher resolution deposition. It was observed that when using the 25-gauge needle, the needle became clogged after waiting periods of greater than 30 mins between printing and also when using slower printing speeds. For this reason, the effect of printing pressure was investigated.

A study by B. Luo *et al.* [127] found that the integrity and resolution of 3D printed MWCNT/ PDMS ink patterns was dependent on the printing pressure. At pressures below a determined threshold, the ink separated and produced low resolution patterns.

Above a certain pressure, the needle became clogged and was unable to dispense the carbon nanotube ink. At an intermediate pressure of 390 kPa, the ink was able to be deposited in defined patterns.

The pressure (p) of the ink as it leaves the needle can be calculated from the Hagen-Poiseuille equation which gives the pressure drop of a Newtonian fluid between two ends of a pipe. The ink developed in this work exhibits non-Newtonian behaviour, as evidenced by the shear thinning observed during rheology measurements. As such, the Rabinowitsch correction [219] was applied to the Hagen-Poiseuille equation to correct for non-Newtonian fluids.

The Hagen-Poiseuille equation, Equation 5.4, is:

$$\Delta p = \frac{8\mu L Q}{\pi R^4} \qquad (5.4)$$

where:

μ = viscosity

L = pipe length

Q = flow rate

R = pipe radius.

Rearranging the equation to:

$$\frac{4Q}{\pi R^3} = \frac{1}{\mu}\frac{\Delta p R}{2L}$$

relates the shear rate at the tube wall for Newtonian fluids (left hand side) to the fluid viscosity and shear stress at the tube wall for all fluids (right hand side).

The Rabinowitsch correction, Equation 5.5 can be applied to the left hand side [220] to correct the shear rate for non-Newtonian fluids, γ, as follows:

$$\gamma = \frac{Q}{\pi R^3}\frac{3n+1}{n} \qquad (5.5)$$

where n is the slope of a graph of ln(shear rate) against ln(shear stress).

Substituting the corrected shear rate back into Equation 5.4 gives:

$$\frac{Q}{\pi R^3}\frac{3n+1}{n} = \frac{1}{\mu}\frac{\Delta p R}{2L}$$

Finally, rearranging for Δp gives the modified Hagen-Poiseuille equation, Equation 5.6:

249

$$\Delta p = \frac{2\mu L Q}{\pi R^4} \frac{3n+1}{n} \qquad\qquad (5.6)$$

For the MWCNT-NH$_2$/ Nafion ink, a plot of ln(shear rate) against ln(shear stress) over shear rates from 0.1 – 200 s^{-1} yielded a non-linear graph (**Figure 5.16**). A shear rate of 100 s^{-1} is often within the range of shear rates reported in the literature. For this reason, the slope of a linear region between shear rates 75 – 117 s^{-1} was measured and n calculated as 3.44. The apparent viscosity at an apparent shear rate of 100 s^{-1} is 0.85 Pa s.
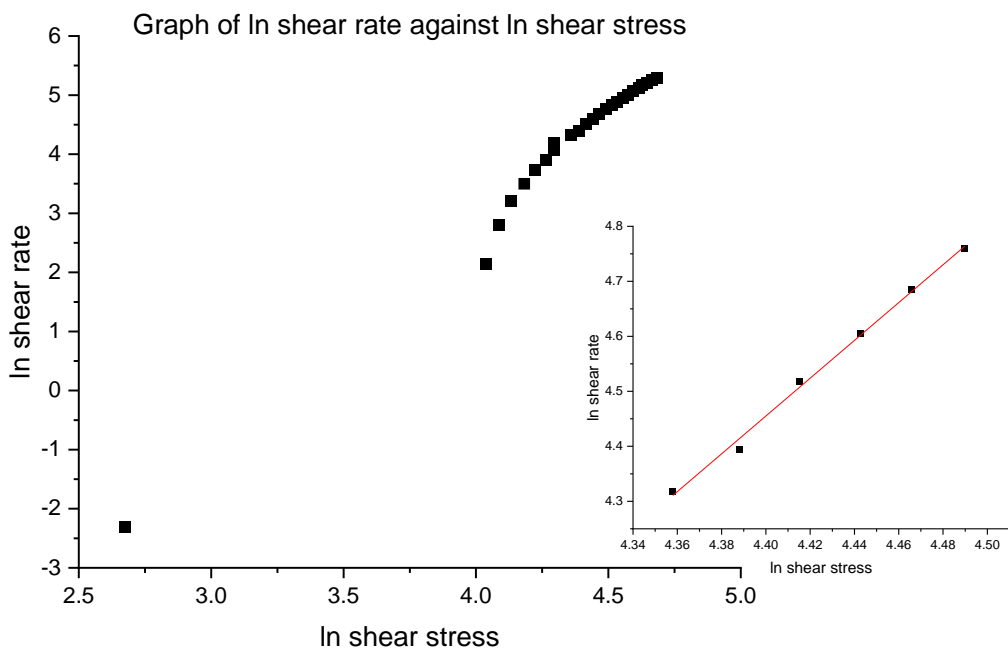
Figure 5.16 *Graph of ln shear rate against ln shear stress over a shear rate range of 0.1– 200 s^{-1}. Insert shows the linear region between shear rates 75 – 117 s^{-1} which was used for the calculation of n.*

The length of the needle = 6.35 mm and the diameter of the needle is 0.25 mm (25-gauge) and 0.41 mm (22-gauge) needles respectively. The flow rate is directly related to the syringe pump speed code, which instructs the printer of the number of motor steps to move per second. Speed code S27 correlates to 100 motor steps per second. For high resolution printing, the maximum number of steps is 2400. The source syringe has a volume of 500 µl, making the volume of liquid released 20 nl/ step. Therefore, for speed code S27, the flow rate is 2 µls^{-1}.

Inserting these parameters into Equation 5.6 gives the pressure drop (Δp) between the top of the needle and the needle exit. Since the ink is at atmospheric pressure (101 kPa) as soon as it leaves the needle, the pressure at the top of the needle can be calculated in kPa as 101 + Δp. A summary of the printing pressures and other parameter combinations is shown in **Table 5.8**

Table 5.8 Trial printing parameters used for printing MWCNT-NH$_2$/ Nafion ink. The parameters in the table will be referred to by their parameter set number in the subsequent text.

Parameter set	Needle internal diameter/ mm (gauge)	Flow rate/ ul/ s	Needle pressure/ kPa	Printing speed mm/s
1	0.41 (22)	1	107	1
2	0.41 (22)	2	114	1
3	0.25 (25)	1	148	1
4	0.25 (25)	2	195	5

The initial printing parameters, corresponding to parameter sets 1 and 3 were used to print the electrode patterns shown in **Figure 5.17**. Although the ink formulation is the same for both sets of electrodes, it can be seen from the photographs that the electrodes printed with the 25-gauge needle have visibly fewer cracks than those printed with the 22-gauge needle. Since all other variables were kept constant, this shows a direct correlation between printing pressure and pattern integrity.
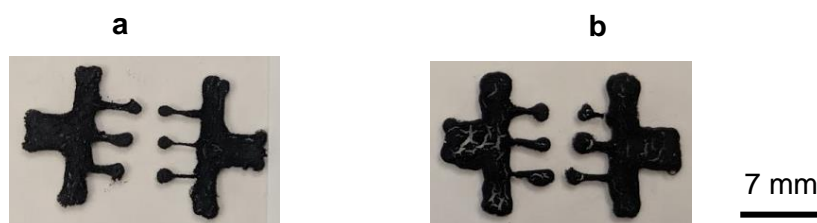
Figure 5.17 *Photographs of electrode patterns printed using a) a 25-gauge needle, b) a 22-gauge needle. All patterns were printed at a speed of 1 mm s^{-1}. Printing quality was later improved by printing at a higher pressure and speed.*

The 25-gauge needle was selected for later experiments as early results revealed that smaller needle diameter and higher printing pressure produced higher resolution patterns with greater structural integrity. Printed patterns obtained using parameter set 4 showed improved integrity over patterns obtained with parameter set 3. At the higher printing pressure, the printing speed had to be increased to 5 mm s^{-1} to maintain the pattern resolution.

Once the printed electrodes were dried, they were immersed in deionised water for 15 mins until they became detached from the glass surface. The free-standing electrodes were dried lightly on paper towels and stored in plastic petri dishes.

5.7. Effect of Carbon Nanotube/ Nafion Nanocomposites on Human Schwann Cells *in vitro*

Cell response to carbon nanotube/ Nafion nanocomposites was investigated by growing Human Schwann Cells on nanocomposite films over five days to investigate the toxicity of the materials in a neural cell environment. For these experiments, toxicity is defined as extensive cell death (<50% of cells surviving at day 5 relative to day 1) or severely hindered cell proliferation (>60% decrease in cell metabolic activity on day 5 relative to positive control).

Carbon nanotube/ Nafion nanocomposite films for cell work were prepared by depositing a pea-sized (ca. Ø = 4 mm) aliquot of ink onto clean 12 mm glass coverslips and spreading into a qualitatively even layer across the glass surface with a spatula. The coated coverslips were dried on a hotplate in air at 60 °C, then enclosed in pieces of aluminium foil for dry sterilisation. The coated coverslips were sterilised in an oven at 160 °C for 2 h. The foil packages containing the coated coverslips were then transferred to a biosafety cabinet (BSC) before being opened and the coverslips placed in 24-well plates.

It was observed that the nanocomposite films lift from the surface of the glass when they are exposed to water or media; therefore 3D printed hollow cylinders made of polyethylene terephthalate glycol (PETG), were inserted on top of the films to prevent them from floating. The cylinders were printed in PETG because the material is hard and discourages cell attachment. Poly-L-lysine (PLL) was then added to the well plates, incubated for 1h and removed. The wells were washed with distilled water before adding complete HSC medium and incubating for 18 h overnight.

After overnight incubation, medium was removed using a 1000 µl Gilson pipette and 1 ml cell suspension with density 30 000 cells/ ml was added to each well except negative controls.

The viability of cells grown on carbon nanotube/ Nafion inks was determined by the Presto Blue assay for metabolic activity using the method described in Section 2.6.
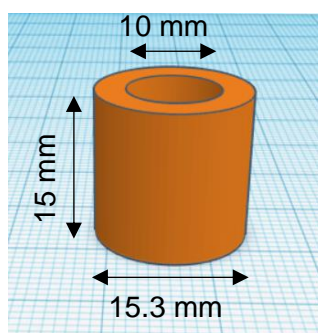
Figure 5.18 *Computer aided design of PETG 3D printed hollow cylinders for nanocomposite film cell culture experiments. Height = 15 mm, outer diameter = 15.3 mm, inner diameter = 10 mm, wall thickness = 2.65 mm.*

The metabolic activities of cells grown on carbon nanotube/ Nafion inks were compared to a positive control of cells grown on glass coverslips, the value of which was normalised to 100% viability at day 5 for HSCs (**Figure 5.19**).
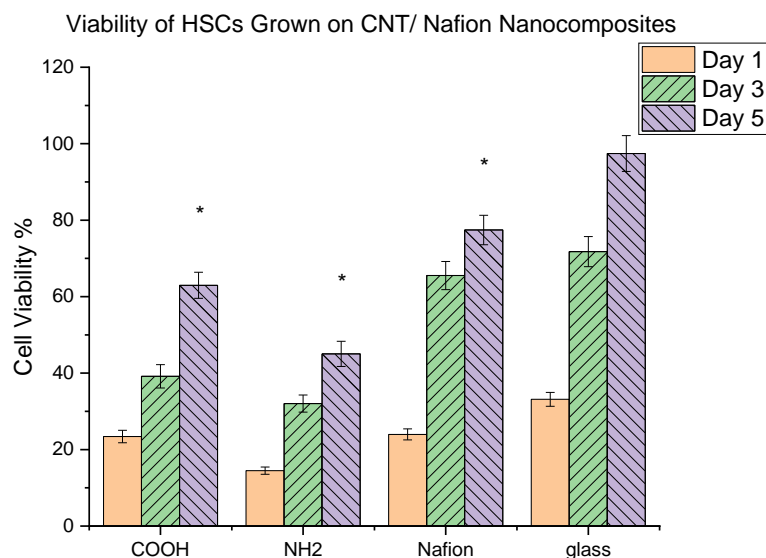
Figure 5.19 *Metabolic activity of Human Schwann cells grown on top of carbon nanotube-based nanocomposites, Nafion and glass, n=9 (3 biological replicates were prepared per sample, experiment was repeated 3 times). A * indicates a significance level of p< 0.05 at day 5*

Student's t-test statistics (n = 9) with p< 0.05 revealed that carbon nanotube/ Nafion inks reduce cell viability significantly by day five. However, fluorescence microscopy (**Figure 5.20**) reveals that the cells are able to grow on top of the nanocomposite films and do not appear to undergo necrosis, which is often seen for cells in a toxic environment.
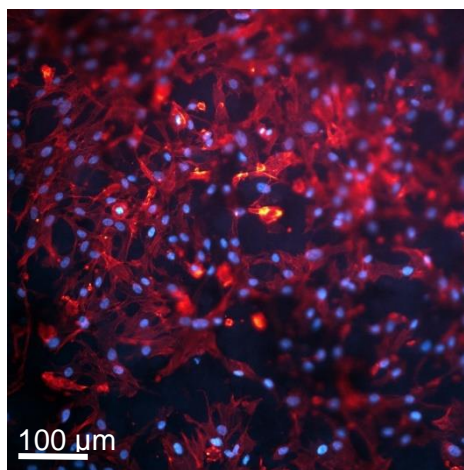
Figure 5.20 *Confocal fluorescence microscopy image of Day 3 Human Schwann cells grown on* MWCNT-NH$_2$/ Nafion nanocomposite. *Cells are stained with phalloidin (red, actin marker) and DAPI (blue, nucleus marker). Image was obtained as a stack of ten images recorded at different z planes*

5.8. **Discussion**

5.8.1. **Carbon Nanotube/ Nafion Ink Formulation and Optimisation**

Carbon nanotubes were combined with different adhesive agents with the intention of developing a printable, conductive ink. Nafion was found to be a suitable adhesive agent in a carbon nanotube-based ink which was both electronically conductive and physically stable upon deposition.

The process of grinding carbon nanotubes with Nafion forms a physical association between the hydrophobic carbon backbone and the carbon nanotube walls [149]. Interactions can also occur between the functional groups on the carbon nanotubes and the polar groups on Nafion.

Variation of the carbon nanotube/ Nafion ink components and formulation parameters directly influenced the ink viscosity. Low viscosity inks, containing a concentration of lower than 10.5% MWCNT-COOH/ Nafion or 21.5% MWNCNT-NH$_2$/ Nafion produced patterns that were not continuous in their geometry and contained patches of agglomerated carbon nanotubes. Conversely, high viscosity inks, containing a concentration higher than 15.0% MWCNT-COOH/ Nafion and 27.7% MWNCNT-NH$_2$/ Nafion, clogged the syringe needle and printing was not possible. A similar relationship between printed pattern quality and ink viscosity was observed for the carbon nanotube-PDMS ink described by B. Luo *et al.* [127]. The researchers found that increasing the proportion of carbon nanotubes in the ink led to an increase in viscosity, which in turn affected the quality of the printed patterns and the limit of pattern complexity that could be achieved. At a printing pressure of 0.5 MPa, the printability of carbon nanotube-PDMS inks containing different weight percentages of carbon nanotubes followed the pattern shown in **Figure 5.21**. The distinction between simple and complex patterns refers to the ability of the printed pattern to maintain a porous 3D structure without collapsing or merging into a non-porous structure. Inks that produced simple patterns were too low viscosity to produce a free-standing, porous 3D structure and instead were better suited to the deposition of 2D patterns or non-porous 3D structures.

Spreading		Simple patterns	Complex patterns	Nozzle clogging

CNT%   0   5   7   9   13
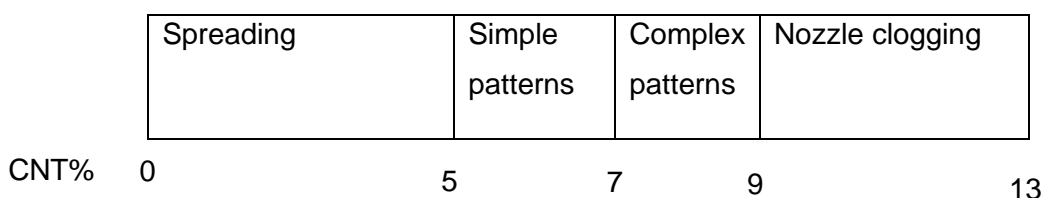
Figure 5.21 Printing outcomes for CNT-PDMS inks containing different concentrations of CNT, prepared by Luo et al. *Ink spreading (0-5% CNT), simple patterns (5-7%), complex patterns (7-9%) → nozzle clogging (9-13%).*

Inks made from carboxyl functionalised carbon nanotubes required proportionally more Nafion (~ 1% w:w) than amine functionalised carbon nanotubes to produce patterns which remained dimensionally stable upon drying. It was also observed that inks containing different concentrations of carboxyl and amine functionalised carbon nanotubes produced inks with similar viscosities at a shear rate of 100 s^{-1} – 0.73 Pa s for MWCNT-COOH/ Nafion ink containing 2.35% MWCNT-COOH and 0.86 Pa s for MWCNT-NH$_2$/ Nafion ink containing 5.39% MWCNT-NH$_2$.

Several factors likely contribute to these differences, including the degree of functionalisation of the carbon nanotubes (10% for MWCNT-COOH and 0.6% for MWCNT-NH$_2$) and hydrogen bonding between COOH or NH$_2$ groups on the CNTs and C–F or SO$_3$H groups on Nafion. The large difference between the degree of surface functionalisation of MWCNT-NH$_2$ and MWCNT-COOH, would lead to the expectation that Nafion would form significantly more hydrogen bonds with MWCNT-COOH than would be possible with MWCNT-NH$_2$. The increased number of intermolecular interactions between MWCNT-COOH and Nafion contributes to the MWCNT-COOH/ Nafion ink having a higher viscosity than would be expected based solely on its carbon nanotube content.

Other properties of the carbon nanotube/ Nafion inks, such as mechanical strength, are largely controlled by the proportion of carbon nanotube in the mixture and both MWCNT-COOH and MWCNT-NH$_2$ nanocomposites followed the same trend; as the carbon nanotube quantity was decreased, the conductivity and ultimate tensile strength of the nanocomposites decreased.

The percolation threshold for conductive polymer composites containing carbon nanotubes has often been reported as being below 1% CNT [221]. The MWCNT-COOH/ Nafion and MWCNT-NH$_2$/ Nafion inks formulated in this work contain 2.35% and 5.39% carbon nanotubes respectively. The inks were formulated and optimised for good printability and maximum conductivity by controlling the CNT concentration and thus formation of the carbon nanotube network.

256

A comparison of the conductivity data for the optimised MWCNT-COOH/ Nafion and MWCNT-NH$_2$/ Nafion nanocomposites showed that the electrical conductivity of the MWCNT-COOH/ Nafion nanocomposite was higher than that of the MWCNT-NH$_2$/ Nafion nanocomposite. This can be attributed to MWCNT-COOH forming a uniform dispersion in the Nafion matrix at a relatively low concentration and establishing a conductive network.

Nanocomposite films which contained the largest ratio of Nafion to carbon nanotube (a ratio of 5.6:1 for MWCNT-COOH/ Nafion and 5:1 for MWCNT-NH$_2$/ Nafion) displayed greatest flexibility compared to formulations with smaller ratios of Nafion to carbon nanotube. Increased flexibility was also observed for ink casts produced from MWCNT-NH$_2$/ Nafion ink containing 5.39% CNT compared to ink casts produced from MWCNT-COOH/ Nafion ink containing 2.35% CNT. The MWCNT-COOH/ Nafion inks dried into brittle nanocomposite films despite containing a higher ratio of Nafion than MWCNT-NH$_2$/ Nafion ink, which dried into nanocomposite films that could easily be manipulated. Since the printed patterns need to be stable enough to be manipulated for *in vitro* study and potential implantation, maximum tensile strength is not necessarily the goal, since a high ultimate tensile strength likely corresponds to a brittle material. A compromise between strength and flexibility needs to be found.

A summary of the properties of different ink formations is found in **Table 5.9**.

Table 5.9 Summarised properties of inks formulated with different types and wt% of carbon nanotubes and Nafion. Stars have been used to denote the optimised ink formulation for both nanotube types.

CNT Type	CNT Type and wt%	CNT:Nafion ratio w:w	Conductivity/ S m^{-1}	Ultimate Tensile Strength/ MPa	Viscosity/ Pa s (at a shear rate of 100 s^{-1})
COOH *	2.35	1 : 4.0	240	5.9	0.73
COOH	2.33	1 : 4.4	177	8.4	-
COOH	2.27	1 : 5.6	147	10.8	-
NH$_2$ *	5.39	1 : 3.5	209	11.6	0.86
NH$_2$	5.25	1 : 4.0	144	10.3	-
NH$_2$	4.95	1 : 5.1	71	14.7	-

The optimised MWCNT-COOH/ Nafion and MWCNT-NH$_2$/ Nafion inks were deposited onto glass slides and dried on a hotplate in air at 60 °C to remove the solvent and obtain nanocomposite films. The temperature at which the ink was dried into a film

could not exceed 80 °C since rapid solvent evaporation caused the nanocomposite films to crack. Once dried, however, some nanocomposite films would be heated to temperatures up to 160 °C for sterilisation purposes. Exposure to high temperatures after the drying stage did not induce any obvious deformation of the nanocomposite film samples.

5.8.2. Characterisation of the Physical and Chemical Properties of a Carbon Nanotube/ Nafion Composite Ink

Effect of Composite Formation on the Graphitic Structure of Carbon Nanotubes

When studying carbon nanotubes, Raman spectra can offer insight into the quality of their graphitic structure through analysis of their D and G bands. Comparison of a carbon nanotube D:G band ratio with that of a carbon nanotube-based nanocomposite can highlight changes to the surface of the carbon nanotube that may occur as a result of physical or chemical interactions between carbon nanotubes and other components.

Comparison of the D:G band ratios for carbon nanotubes and carbon nanotube/ Nafion inks (**Table 5.3**) showed that the D:G ratio for the MWCNT-NH$_2$/ Nafion nanocomposite decreased relative to the amine functionalised carbon nanotubes while the D:G ratio for the MWCNT-COOH/ Nafion nanocomposite increased relative to the carboxylic acid functionalised carbon nanotubes. By examining the hydrogen bonding interactions between amine/ carboxyl functionalised carbon nanotubes and Nafion, a partial explanation for the changes in D:G ratio can be found. Hydrogen atoms in the NH$_2$ groups of amine functionalised CNTs form strong interactions with the oxygen atoms in the SO$_3$H group in Nafion, likely forming an ordered hydrogen bonded network. Similarly, the hydroxyl component of the COOH groups in carboxyl functionalised CNTs can also form hydrogen bonds with the oxygens in the SO$_3$H group in Nafion. Due to the greater degree of functionalisation for MWCNT-COOH compared to MWCNT-NH$_2$, more hydrogen bonding is likely to take place between the functional groups on MWCNT-COOH and Nafion than MWCNT-NH$_2$ and Nafion. Since interactions between functional groups do not necessarily occur parallel to the carbon nanotube surface, these could appear as an increase in D:G ratio, indicating an increase in the disorder of the structure. Conversely, more interactions are likely to take place between the MWCNT-NH$_2$ sidewalls and the PTFE backbone of Nafion due to a lower degree of carbon nanotube functionalisation. These interactions, which occur parallel to the carbon nanotube surface could appear as a decrease in D:G ratio, indicating a decrease in disorder.

Morphology

Scanning electron micrographs of the carbon nanotube/ Nafion nanocomposite films show flat, uniform profiles at low magnification with sections of Nafion polymer becoming visible at higher magnifications. Carbon nanotubes enclosed in sections of Nafion are also visible, supporting the suggestion that Nafion exfoliates the carbon nanotubes by adhering to the carbon nanotube side walls. While the hydrophobic backbone of Nafion adheres to the carbon nanotube side walls, the hydrophilic parts of the Nafion polymer provide the adhesive properties which allow the ink to be deposited onto a physically stable material.

When observing non-gold-coated SEM samples, the conductivity of the sample is indicated by the amount of contrast between the material and the background. High contrast indicates high conductivity whereas low contrast suggests low conductivity. Since carbon nanotubes have high conductivity and Nafion has low conductivity, the contrast between the sample and background gives a good indication as to whether a carbon nanotube rich or Nafion rich area is being imaged. Micrographs of the underside of the $MWCNT-NH_2$/ Nafion nanocomposite films support the suggestion that large quantities of the Nafion polymer can be found on the underneath of the nanocomposite films since the contrast is lower than for other areas. This is potentially related to similarities between the contact angles for Nafion and glass.

The cross section of the $MWCNT-NH_2$/ Nafion nanocomposite revealed a porous internal structure, which differed from the smoother external surface. The irregular porosity arose from the random entangled between carbon nanotubes within the structure [222].

Viscous Properties

The viscosity of an ink is pivotal to the printing process and the properties of the final nanocomposite film. Rheology, the study of how fluids flow and deform under shear stress, is often used to probe the viscoelastic properties of materials. Fluids for which viscosity is independent of shear rate and shear stress, are described as being Newtonian fluids. Liquids that become more viscous as the shear rate increases, known as shear thickening, or less viscous as the shear rate increases (shear thinning) are non-Newtonian. Shear thinning, also known as pseudoplastic behaviour, is observed for the carbon nanotube/ Nafion inks developed in this work (*Figure 5.6*) and similar behaviour has been described for the carbon nanotube-PDMS inks developed by B. Luo *et al.* [127] in their 2018 study. Shear thinning of a carbon nanotube-based ink was also observed by Kim *et al.* [137], who suggested that the shear thinning could be

attributed to rearrangement of the carbon nanotubes under shear stress. Rearrangement of carbon nanotubes in inks indicates that shear thinning is a property of carbon nanotube-based inks, an idea that has been put forward in several studies in the literature [137, 140]. In this work, the rearrangement of both carbon nanotubes and Nafion polymer chains likely contribute to the observed shear thinning behaviour.

Pseudoplasticity makes carbon nanotube-based inks favourable for printing applications since shear thinning allows the ink to leave the nozzle under pressure but retain a specified shape upon deposition. Comparison of the rheology graphs and flow behaviour indices for MWCNT-COOH/ Nafion and MWCNT-NH$_2$/ Nafion inks reveals that MWCNT-NH$_2$/ Nafion ink exhibits slower shear thinning than the MWCNT-COOH/ Nafion ink. This could be because the MWCNT-COOH/ Nafion ink contains a lower percentage of carbon nanotube per unit volume than MWCNT-NH$_2$/ Nafion ink causing the carbon nanotubes and Nafion polymer chains in MWCNT-COOH/ Nafion to rearrange more readily than those in MWCNT-NH$_2$/ Nafion.

Bulk and Nanoscale Mechanical Properties

The elasticity of the carbon nanotube/ Nafion nanocomposites is non-linear from the first application of stress, while Nafion casts follow a roughly linear regime until maximum stress is reached (*Figure 5.7*). The stress-strain profile of MWCNT-COOH/ Nafion is consistent with that of a brittle material, whereas MWCNT-NH$_2$/ Nafion and Nafion both display more ductile behaviour and have a necking region prior to failure. The brittle behaviour of MWCNT-COOH/ Nafion was unexpected since the sample contains a lower proportion of carbon nanotubes (2.35%) than MWCNT-NH$_2$/ Nafion (5.39%) and would therefore be expected to be more ductile. The strong hydrogen bonds formed between MWCNT-COOH and Nafion may have caused the brittle behaviour observed.

Nanocomposite films prepared from the carbon nanotube- PDMS ink formulated by B. Luo *et al.* also displayed brittle behaviour in their stress/ strain profiles. This behaviour followed the expected trend, since PDMS has a brittle stress-strain profile and the inks also contained a high proportion (7%) carbon nanotube. Nanocomposite films prepared by B. Luo *et al.* had an average ultimate tensile strength of ~ 1.1 MPa; this is lower, but of the same order of magnitude as the ultimate tensile strength recorded for the carbon nanotube/ Nafion nanocomposites in this work.

Wettability

The contact angles of the carbon nanotube/ Nafion ink depositions were measured and compared to the contact angles of glass and carbon nanotubes deposited from an IPA suspension. The results (**Table 5.6**) showed that, while the starting carbon nanomaterials were hydrophobic, the addition of Nafion facilitated a transition from hydrophobic to hydrophilic, according to the numerical thresholds. The MWCNT-COOH starting material was found to be more hydrophobic than the MWCNT-NH$_2$, which is in line with results reported by Hsieh *et al.* [119], showing that carboxylic acid functionalised carbon nanotubes are more hydrophobic than amine functionalised carbon nanotubes. In comparison, Wang *et al.* [223] reported that pristine MWCNTs have a contact angle of 163°, making them superhydrophobic. The introduction of polar chemical groups onto the side walls of carbon nanotubes has a significant impact on the nanotube's ability to adsorb water onto its surface.

Nafion films can display hydrophilic or hydrophobic properties depending on the environment [212]. This dual behaviour stems from the presence of both hydrophilic sulfonic acid groups and a hydrophobic PTFE backbone. When in combination with carbon nanotubes, the Nafion hydrophobic backbone is in contact with the carbon nanotube walls, causing the hydrophilic side chains to dominate the surface behaviour. Nafion had the lowest contact angle measured in this work and was regarded to be the most hydrophilic.

Upon observation, the upper and under-sides of the nanocomposite films had different textures, with the upper side having a matte finish and the underside having a glossy finish. To investigate this, the contact angle of the nanocomposite films underside was measured in addition to the upper side. The contact angle of the nanocomposite film underside was significantly lower than that of the nanocomposite film upper side, which could be attributed to differences in their surface morphology. The upper side is significantly rougher than the underside and therefore has a smaller contact surface with the water droplet, indicating that it is more hydrophobic.

Contact angles between 40° and 80° are suggested to be suitable for promoting cell adhesion [224]. The carbon nanotube/ Nafion inks and Nafion all have contact angles within this range, which should be sufficient to support cell adhesion. However, cell adhesion and proliferation can be improved if proteins are adsorbed onto the material surface prior to cell seeding. The carbon nanotube/ Nafion nanocomposite films were coated with poly-L-lysine and preconditioned with cell culture medium to adsorb proteins onto the material surface.

Electrical Properties

Both MWCNT-COOH/ Nafion and MWCNT-NH$_2$/ Nafion inks have conductivities above 200 Sm^{-1}, which is slightly higher than the value of 174 Sm^{-1} reported by B. Luo *et al.* [127] but an order of magnitude lower than the value of 2540 Sm^{-1} reported by Kim *et al.* [137]. In the study by B. Luo and in this work, the polymer component remained in the ink and the final product, thus reducing the conductive capability of the material. Conversely, in the Kim *et al.* study, the printed structures were heated to 450 °C to induce polymer degradation, leaving only the conductive carbon nanotube component in the final structure and allowing a higher conductivity to be achieved. The conductivities achieved by Kim *et al.* set a benchmark for developers of electrode materials, as something manifestly achievable.

The Bode plots of the MWCNT-NH$_2$/ Nafion and MWCNT-COOH/ Nafion inks (**Figure 5.9**) show that their electrical behaviour is frequency independent. The carbon nanotube/ Nafion inks act as conductors in the circuit, with the Ohmic conduction pathway dominating the electrical properties. The carbon nanotube/ Nafion inks do not exhibit capacitive or inductive behaviour at any of the measured frequencies.

In contrast, the Bode plot of Nafion alone shows distinct frequency-dependent behaviour (**Figure 5.9**). The phase angle changes by 50° over the course of the measurement, in a manner which is more closely related to that of a capacitor than a resistor. Since Nafion is a non-electron-conductive material which was deposited between two gold electrodes, the system can be considered as a capacitor with gold plates and Nafion as the dielectric material.

The Bode plot of a Nafion membrane electrode assembly is shown in a study by Mollá *et al.* [225] and follows a similar trend to the results obtained in this work. The flat portion of the graph at high frequencies has been attributed to the intrinsic resistance of the material. In this case, the intrinsic resistance of Nafion alone in this configuration was ~ 6 x10^4 Ω.

Bode plots for Nafion and Nafion-based materials appear to follow the expected trend for a capacitor, with impedance decreasing with increasing frequency. In this work, the phase angle reduces exponentially at frequencies below 50 Hz, toward an inflection at 0°. Over the span of the inflection, between 50 – 10^5 Hz, the impedance approximately levels with a slight downward trend. Above a frequency of 10^5 Hz, the behaviour of Nafion changes and is no longer in line with the trend expected for a capacitor.

A closer look at the movement of Nafion dipoles in response to the changing electric field can suggest an explanation for the behaviour [226]. At low frequencies, the Nafion

262

dipoles can fully align with the electric field between the gold electrodes, resulting in a total polarisation parallel to the electric field. As the frequency increases, it becomes more difficult for the dipoles to reorient themselves with the changing electric field, and the polarisation parallel to the electric field decreases. At very high frequencies, the Nafion dipoles can no longer align with the electric field and polarisation parallel to the electric field tends to zero.

Surface Chemistry

When discussing cyclic voltammograms, the shape of the voltammogram trace gives information about the presence of capacitive charge transfer, which is identified by a flat profile, and Faradaic charges, which are identified as features in the trace. Cyclic voltammetry of the carbon nanotube/ Nafion electrodes produced rectangular cyclic voltammograms, with no clear maxima or minima. This is characteristic of electrode materials for which charge transfer is mainly capacitive.

An electrode immersed in a fluid develops an electrical double layer on its surface. The electrical double layer consists of ions which adsorb directly onto the electrode surface due to positive or negative charges on the electrode surface. When the voltage is swept towards zero during the cathodic phase of cyclic voltammetry, the delocalised electrons in carbon nanotubes move toward the electrode surface, giving it a net negative charge. Electrolyte ions coming into contact with the surface of a carbon nanotube-based electrode are more likely to adsorb onto the surface during this phase if they carry a net positive charge. In a potassium ferrocyanide electrolyte, it is the movement of positively charged potassium ions towards the carbon nanotube/ Nafion electrode that forms the electrical double layer and contributes to the build-up of additional negative charge on the surface of the electrode. This is known as capacitive charging of the electrolyte double layer and allows charges to move without any chemical reactions occurring (Faradaic current). This relates directly to implantable devices through the charge injection limit and charge storage capacity.

The charge injection limit of a material is defined as the amount of charge that the material can transfer to its surroundings and *vice versa* without inducing an irreversible chemical reaction. The charge storage capacity (CSC) is the total amount of reversible charge that can be stored by an electrode [227]. The charge storage capacity has been used to predict the value of the charge injection limit, although it has been found to overestimate the amount of charge that can be injected during neural stimulation [228]. The reasons for this are mostly linked to differences between controlled experimental conditions, and biological conditions during neural stimulation. An example of this is that under laboratory conditions, the CSC is calculated at near equilibrium conditions

whereas, during neural stimulation, short pulse durations (on the scale of hundreds of microseconds) mean that the system has not yet reached equilibrium when the charge is applied.

A large charge storage capacity and charge injection limit are desirable since this allows the electrode to transfer a greater amount of charge to the surrounding tissue without causing damage, thus acting as a more efficient electrode. A range of values for the charge storage capacities of carbon nanocomposites can be found in the literature, with one group reporting a CSC of 2.2 mC cm^{-2} for a MWCNT-PEGDA nanocomposite [136] and another reporting a CSC of 70 mC cm^{-2} for a CNT/ PEDOT electrode coating [157]. In this work, the charge storage capacities of MWCNT-COOH/ Nafion and MWCNT-NH$_2$/ Nafion were calculated as being 22.85 mC cm^{-2} and 41.25 mC cm^{-2} respectively. The difference between these values is likely linked to their electroactive surface areas.

The electroactive areas of MWCNT-COOH/ Nafion and MWCNT-NH$_2$/ Nafion were calculated as 0.882 cm^2 and 1.62 cm^2 respectively. It was expected that the electroactive area of MWCNT-COOH/ Nafion would be smaller than that of MWCNT-NH$_2$/ Nafion since the former has a significantly lower (~ 50% less) carbon nanotube content and Nafion is barely involved in electron transport (electroactive surface area = 7.45 x10^{-4} cm^{-2}). Both carbon nanotube/ Nafion nanocomposites had a calculated electroactive surface area larger than the geometric surface area of the glassy carbon electrode onto which they were coated. This can be attributed to the roughness of the nanocomposite materials, which provide a larger surface area for electrochemical reactions to take place.

The rectangular shape of the carbon nanotube/ Nafion nanocomposite cyclic voltammogram is desirable when considering applications in implantable devices since it indicates a greater charge injection limit than some commonly used materials such as platinum [156]. A study by Vitale *et al.* [152] reported that carbon nanotube fibre electrodes had a charge injection limit of 6.52 mCcm^{-2}, almost 50x greater than that of a platinum electrode with 10x larger surface area. The charge transfer pathway of most metals is Faradaic [153]. Platinum is no exception, transferring charges through a redox reaction at its electrode surface. A widely studied material with a larger charge injection limit than carbon nanotubes is the conductive polymer, poly(3,4-ethylenedioxythiophene) (PEDOT). While PEDOT has a charge injection limit of 15 mC cm^{-2} [156], its method of charge transfer is mainly Faradaic and the material has been shown to lose stability and degrade when exposed to repeated voltage cycles over long time-periods (days). In contrast, carbon nanotube fibre electrodes studied by Vitale *et al.* remained stable

after 9 days of continuous cycling. Another study reported that the stability of PEDOT electrodes was improved by combining the polymer with carbon nanotubes [229], again highlighting the beneficial effect of carbon nanotubes on the electrode properties. The electrode developed here is also a combination of polymer with carbon nanotubes but while evidence exits that the carbon nanotubes have a favourable effect on the electrochemical properties, at this stage, there is no data to indicate how the material would behave when exposed to repeated voltage cycles.

Although it was not measured in this work, Vitale *et al.* [152] reported that carbon nanotube fibre electrodes have a wide water window; that is, a wide voltage range over which water is not electrolysed. Another recent study [213] also reported a similarly wide water window for graphene, indicating that carbon nanomaterials may be good candidates for use as electrodes in implantable device since they remain inert over a wide range of voltages.

Another electrode property that is important when selecting materials for implantable devices is the impedance of the material over a range of frequencies. Measurement of the carbon nanotube/ Nafion nanocomposite impedance by electrochemical impedance spectroscopy (EIS) shows that the nanocomposite impedance has no frequency dependence and is constant over a wide range of frequencies. This suggests that the material is stable and unlikely to exhibit unexpected electrical behaviour at any frequency within the measured range, thus reducing the risk of tissue damage. A study by Bareket-Keren *et al.* [153] supports these finding and also shows that the impedance of carbon nanotube electrodes has little dependency on frequency. The study also reported that the impedance of carbon nanotube electrodes is lower than that of metal electrodes with the same surface area.

5.8.3. Deposition of Carbon Nanotube/ Nafion Ink Using a 3D Bioprinter

3D bioprinting is an emergent technique which facilitates the simultaneous deposition of materials and cells. The materials and cells to be printed are prepared in syringes, in a similar way as the direct writing and 3D printing techniques, and the deposition is controlled by hydraulic or pneumatic pressure, causing small droplets of sample to be deposited onto the substrate. The 3D bioprinter used in this work employed a system controlled by hydraulic pressure, which was able to deposit the samples at higher resolution than a system controlled by pneumatic pressure, due to the incompressibility of water. Although the 3D bioprinter is capable of printing cells, this feature was not used for the work described here.

The MWCNT-NH$_2$/ Nafion carbon nanotube/ Nafion ink was deposited into defined 2D patterns, similar to the simple patterns printed by B. Luo *et al.* [127] in their 2018 study. The researchers described that inks containing between 5-7% carbon nanotubes were able to print 2D patterns whereas inks containing between 7-9% carbon nanotubes were able to print 3D structures. The formulated inks had viscosities in the region of 1000 Pa s at a shear rate of 100 s^{-1}, with the higher carbon nanotube percentage inks having higher viscosities than the lower carbon nanotube percentage inks. In comparison, the MWCNT-NH$_2$/ Nafion ink contains ~5.4% carbon nanotube and has a viscosity of 0.86 Pa s. The carbon nanotube content corresponds to the lower range (5-7%) from Luo *et al.'s* study and similar printed results were obtained.

The MWCNT-NH$_2$/ Nafion ink was unable to support 3D structures likely due to its low viscosity. However, the idea that low viscosity inks cannot result in 3D structures is challenged by Kim *et al.* [137], who printed 3D structures using a carbon nanotube-PVP ink, with a viscosity of 0.1 Pa s, slightly higher than the viscosity of inkjet printer ink. The researchers achieved this by depositing the ink and rapidly evaporating off the solvent, to leave a rigid structure. It is feasible that the rapid solvent evaporation technique could be applied to the carbon nanotube/ Nafion ink during deposition to obtain 3D structures. To obtain patterns which maintained a crack-free, continuous geometry upon drying, the printing parameters were optimised. This included the syringe needle diameter, printing pressure and printing speed, which were also identified by B. Luo *et al.* [127] as key parameters for obtaining high quality printed patterns.

The printing pressure was calculated using the modified Hagen-Poiseuille equation, Equation 5.6, which contained a modification to account for the non-Newtonian behaviour of the carbon nanotube/ Nafion ink:

$$\Delta p = \frac{2\mu L Q}{\pi R^4} \frac{3n + 1}{n}$$

(5.6)

Equation 5.6 was used to calculate the pressure at the top of the syringe needle, immediately preceding deposition. The results showed a printing pressure of 107 kPa for a 22-gauge needle (diameter = 0.41 mm) at a flow rate of 1 µl s^{-1} and a printing pressure of 148 kPa for a 25-gauge needle (diameter = 0.25 mm) at a flow rate of 1 µl s^{-1}. For patterns printed at 1 mm s^{-1} (**Figure 5.17**), the pattern printed at the 107kPa show larger and more numerous cracks than the pattern printed at 148 kPa, although small cracks are still visible for the sample printed at higher pressure. Higher printing quality was achieved using a printing pressure of 195 kPa through a 25-gauge needle.

The print resolution required ultimately will be determined by the fidelity of sound it is intended to achieve. Current cochlear implants have 24 electrodes, cover an audible range of approximately 4½ octaves and deliver a quite poor quality of sound. The impossible dream would be an artificial cochlea that would have the range of a piano and distinguish semitones; that is, it would cover eight octaves containing 104 semitones. An octave, in sound, covers a range of frequencies of a factor of two and therefore wavelengths of a factor of two. In Fig 5.17, the difference in separation between the top and bottom digits is a factor of two. To distinguish a semitone, as a rough calculation, would require an ability to distinguish 13 increments of separation, which in an electrode of this size would be 0.1 mm. The print resolution therefore would be required to be ~ 20 µm. The resolution achieved here is approximately 500 µm so far falls very far short of such a specification.

5.8.4. Effect of Carbon Nanotube/ Nafion Nanocomposites on Human Schwann Cells in vitro

Growth of Human Schwann cells on carbon nanotube/ Nafion nanocomposite films caused an average reduction of 50% of the cell viability after day 5. This is a larger reduction in cell viability than that observed for HSCs grown on Nafion, although cells grown on Nafion still show a significant drop in cell viability compared to the cells grown on glass coverslips.

Confocal microscopy of Human Schwann cells (**Figure 5.20**) shows that cells can attach to the carbon nanotube/ Nafion nanocomposite films and spread on the surface. A study by Baraket-Keren [153] discussed the preference for neural cells to attach to rough surfaces, and the suitability of carbon nanotubes to act as a substrate for neural cell adhesion. It is possible that the observed reduction in metabolic activity of cells grown on carbon nanotube/ Nafion nanocomposite films is partially due to carbon nanotube fluorescence quenching, which has been reported in the literature [93]. The fluorescence quenching effect of carbon nanotubes was not noticeable for the carbon nanotube-diphenylalanine composite described in Chapter 4, since only a small quantity of carbon nanotubes was present in each well. However, the nanocomposites contain significantly more carbon nanotubes per well than the carbon nanotube-diphenylalanine composite, causing the quenching effect to be more noticeable.

5.9.   **Summary**

Carbon nanotube/ Nafion nanocomposites have been developed and formulated into inks. The inks were both electronically conductive and physically stable upon deposition due to the conductive properties of carbon nanotubes and the stability provided by hydrogen bonding and hydrophobic interactions between Nafion and the carbon nanotubes. The properties of the inks were optimised in a way that allowed them to be deposited onto a glass surface both manually and using a commercial 3D bioprinter.

Two nanocomposites were developed: a MWCNT-COOH/ Nafion nanocomposite containing 2.35% MWCNT-COOH and a MWCNT-NH$_2$/ Nafion nanocomposite containing 5.39% MWCNT-NH$_2$. Both formulations contained carbon nanotube proportions that were expected to be above the percolation threshold for this system and the conductivities of both nanocomposites were above 200 Sm^{-1}. The charge transfer pathway for the carbon nanotube/ Nafion nanocomposites was found to be capacitive, caused by charging of the electrical double layer. The nanocomposites had high charge storage capacities of 22.85 mC cm^{-2} (MWCNT-COOH/ Nafion) and 41.25 mC cm^{-2} (MWCNT-NH$_2$/ Nafion). This could make them favourable for use in implantable devices as they may be less likely to cause tissue damage through Faradaic charge transfer.

The carbon nanotube/ Nafion inks had non-Newtonian viscosities of 0.73 Pa s (MWCNT-COOH/ Nafion) and 0.86 Pa s (MWCNT-NH$_2$/ Nafion) at a shear rate of 100 s^{-1}. Their shear thinning behaviour has been attributed to the rearrangement of carbon nanotubes and Nafion polymer chains under increasing shear stress. The MWCNT-NH$_2$/ Nafion ink was deposited into free-standing, electrically conductive patterns using a 3D bioprinter. Printing pressure was found to have a significant effect on the integrity of the printed shapes and a pressure of 195 kPa, through a 25-gauge needle selected as being suitable to obtain printed patterns with no visible cracks.

Fluorescence microscopy of Human Schwann cells grown on carbon nanotube/ Nafion nanocomposite films showed that HSCs were able to successfully attach to the nanocomposite film surface.

The hydrophilic behaviour of the carbon nanotube/ Nafion ink combined with its conductive properties and printability, suggest that the ink may make a suitable candidate for neuron stimulation devices; the ink could be employed either as a standalone electrode or as a coating for an electrode fabricated from other materials.

Chapter 6   **Conclusions and Future Directions**

6.1.   **Conclusions**

The objective in this work was to explore aspects of carbon nanotubes and candidate piezoelectric and polymer materials for use in bionic applications with particular reference to cochlear implants. The study was conducted in parallel with a formal project with defined objectives but this project was a free-ranging programme outside that project to explore areas of relevant and associated interest.

The work explored the preparation and properties of a covalently bonded carbon nanotube-diphenylalanine complex, and the self-assembly and properties of two piezoelectric materials, namely diphenylalanine and poly[vinylidene- co-trifluoroethylene] (PVDF-TrFE). The study has also included the development of a physically linked carbon nanotube/ Nafion composite, capable of being formulated into an ink that can be deposited by 3D printer to form the geometry required of an electrode for an implantable device.

The study revealed that the properties and self-assembly process of diphenylalanine can be tailored towards defined specifications. Self-assembling the peptide on templates supported the formation of microtubes with a range of sizes that resonate at distinct frequencies. Diphenylalanine exists in both a naturally occurring 'L' form, which can be degraded by enzymes, and an artificial 'D' form which is resistant to enzymatic degradation. This allows the material to be further tailored for applications requiring degradable or non-degradable components. The resonant frequencies of L- and D-diphenylalanine microtubes with average dimensions were calculated as ~6.4 kHz and ~175 kHz respectively. The resonant frequency of a L-diphenylalanine microtube of average dimensions falls within the frequency range of human hearing whereas the resonant frequency of D-diphenylalanine is well outside this range.

The self-assembly conditions can be tailored and controlled to obtain diphenylalanine microtubes with higher or lower resonant frequencies than those reported here, however, compared to PVDF-TrFE, diphenylalanine falls short in terms of ease of manipulation. To control the physical dimensions and alignment of diphenylalanine microtubes, photolithography, use of an anodised aluminium oxide (AAO) template or another guidance method is required to arrange the microtubes into an aligned array. Otherwise, PVDF-TrFE, aligned fibres can be obtained by electrospinning onto a rotating drum or between parallel steel bars thus making the manufacture of PVDF-

269

TrFE fibres with defined geometry and alignment easier than the construction of aligned arrays of diphenylalanine microtubes.

Carbon nanotubes can be formulated into physically bonded and covalently bonded complexes. This allows formation of a covalent complex with diphenylalanine, which prevents carbon nanotube agglomeration and allows well-dispersed suspensions to be obtained.

The carbon nanotube complexes synthesised in this work have comparable conductivity (300 - 400 Sm^{-1}) to carbon nanotube complexes described in the literature and while the conductivity is not yet at the level of copper or platinum, the materials show promise for future applications.

The formation of a covalent complex in the formation of an ink turned out to be an unnecessary extra step. The covalently bonded carbon nanotube-diphenylalanine complex was unable to function as an ink since the suspension split into beads when applied to glass and did not provide the coherent layer required of an electrode. Changing the proportion of solvent and solids did not resolve the problem. Therefore, diphenylalanine was excluded from the ink and replaced with a polymer component, Nafion. The carbon nanotube/ Nafion inks were found to have a conductivity of 200 – 250 Sm^{-1}, which is of the same order of magnitude as similar formulations described in the literature.

Deposition of carbon nanotube/ Nafion ink has been demonstrated by direct writing and inkjet printing (in a 3D printer, although the additive manufacturing, 3D, capability of the printer was not used). Parameter optimisation proved key to obtaining defined, coherent patterns. Viscosity is readily changed by modifying the proportions of carbon nanotube or solvent in the ink formulation. Use of the additive manufacturing facility in a 3D printer, that was not used in this work, opens up the possibility that different printing techniques could be used for inks with the same components in different proportions, allowing different structures to be explored.

In the investigation of biocompatibility, the cell response to the materials- piezoelectric, covalent complex and ink- showed that the materials significantly reduced cell viability but did not have an immediate toxic effect on the cells. Carbon nanotube/ Nafion nanocomposite films were able to support Human Schwann cell growth, although measurement of cell metabolic activity suggested that the carbon nanotube/ Nafion nanocomposite films were reducing cell viability. Human Schwann cells were also successfully grown on and around diphenylalanine and PVDF-TrFE materials, demonstrating the biocompatibility of the materials on a scale of days. The alignment of

the fibre lengths influences the alignment of cells grown on PVDF-TrFE electrospun fibres.

The work described here has shown that carbon nanocomposites are able to support neural cell adhesion and growth. The wettability of carbon nanotube-based systems increased with the addition of Nafion, which likely contributed to the ability of the nanocomposite films to support cell growth. The wettability and high electrical conductivity of the carbon nanocomposites developed in this work, show promise for use in conjunction with favourable properties from other components, such as cell alignment along the lengths of electrospun PVDF-TrFE fibres.

The viability of a device that uses the combined properties of these components remains a possibility and therefore justifies further exploration of combinations of carbon nanotube nanocomposites and piezoelectric materials for implantable devices.

Extensive work on carbon nanotubes has been carried out over the past few decades, with many researchers reporting the development of carbon nanotube complexes and composites with varied components. Diphenylalanine nano/microtubes were first reported in 2003 [48], with several additional diphenylalanine nano- and microstructures being reported since. Research into diphenylalanine nano- and microstructures has revealed a range of potential applications. The novelty in this work is in the consideration and investigation of self-assembled diphenylalanine nano/ microtubes as a component for piezoelectric cochlear implants. This is an application which has not been explored in diphenylalanine-related reports found in the literature, and for which diphenylalanine provides an alternative to other materials currently being studied.

6.2. **Future Directions**

The work described here was carried out in parallel with a defined programme to develop a cochlear implant based on the piezoelectric properties of PVDF-TrFE. That work came to an end in May 2019 and the team has dispersed.

This work has focused on what potential might be offered by carbon nanotubes and diphenylalanine and composites based on these. It has explored the properties and possible limitations of carbon nanotube nanocomposites and their combination with peptides and polymers. The study has only covered a small part of the field, many areas of interest are yet to be investigated.

Future work might include further development of a carbon nanotube-piezoelectric component device and characterisation of the acoustic wave transfer through the

device by laser vibrometry. This would give an indication of the suitability of the device to be applied to more specific applications, such as cochlear implants. Characterisation of the cell response to the device components *in vitro* should provide useful information regarding whether the device would be suitable for continuation into *in vivo* tests. Investigations might be carried out to measure how cells respond when the device is subjected to acoustic and electrical stimulation. A custom cell-stimulating setup could be developed to apply a pulsed electrical current to the cells via the carbon nanotube electrodes, although the parameters- duty cycle, pulse shape, pulse duration, voltage and stimulation length would need to be optimised for the custom setup.

If work were to be continued on diphenylalanine microtubes, a first step would be the characterisation of the physical and piezoelectric properties of aligned arrays of diphenylalanine microtubes produced by self-assembly. Since diphenylalanine microtubes with various lengths and diameters may be required for different applications, the formation of guidance channels by photolithography could provide an alternative template for the self-assembly of diphenylalanine microtubes with specified dimensions.

The results described here and in the literature suggest that carbon nanotube nanocomposites hold promise for application in the area of implantable devices. Their favourable properties and ability to be combined with other novel materials make them attractive candidates. However, there are still many areas to be explored and concerns to be overcome before widespread use of the materials in implantable devices is likely to be observed.

References

1.	Chen, Y., Y.-S. Kim, B.W. Tillman, W.-H. Yeo, and Y. Chun, *Advances in Materials for Recent Low-Profile Implantable Bioelectronics.* Materials (Basel, Switzerland), 2018. **11**(4): p. 522.

2.	Graz, H., V.K. D'Souza, D.E.C. Alderson, and M. Graz, *Diabetes-related amputations create considerable public health burden in the UK.* Diabetes Research and Clinical Practice, 2018. **135**: p. 158-165.

3.	Steckler, F., *Development of Acoustic Biosensors based on Electrospun PVDF-TrFE-ZnO Piezoelectric Nanofiber Composites*, in *Department of Nanotechnology and Regenerative Medicine.* 2018, University College London.

4.	Accoto, D., M. Calvano, D. Campolo, F. Salvinelli, and E. Guglielmelli, *Energetic Analysis for Self-Powered Cochlear Implants*, in *2009 Annual International Conference of the Ieee Engineering in Medicine and Biology Society, Vols 1-20.* 2009, Ieee: New York. p. 4860-+.

5.	Dhanasingh, A. and C. Jolly, *An overview of cochlear implant electrode array designs.* Hearing Research, 2017. **356**: p. 93-103.

6.	Feher, J., *4.7 - Hearing*, in *Quantitative Human Physiology*, J. Feher, Editor. 2012, Academic Press: Boston. p. 370-385.

7.	Mills, S.R. and M. Fletcher. *Here's what music sounds like through an auditory implant.* 2019 11/06/2020]; Available from: https://theconversation.com/heres-what-music-sounds-like-through-an-auditory-implant-112457.

8.	*A Dictionary of Physics.* 2009: Oxford University Press.

9.	Ortiz-Catalan, M., R. Brånemark, B. Håkansson, and J. Delbeke, *On the viability of implantable electrodes for the natural control of artificial limbs: review and discussion.* Biomedical engineering online, 2012. **11**: p. 33-33.

10.	Geddes, L.A. and R. Roeder, *Criteria for the Selection of Materials for Implanted Electrodes.* Annals of Biomedical Engineering, 2003. **31**(7): p. 879-890.

11.	İlik, B., A. Koyuncuoğlu, Ö. Şardan-Sukas, and H. Külah, *Thin film piezoelectric acoustic transducer for fully implantable cochlear implants.* Sensors and Actuators A: Physical, 2018. **280**: p. 38-46.

12.	Park, S., X. Guan, Y. Kim, F.X. Creighton, E. Wei, I. Kymissis, H.H. Nakajima, and E.S. Olson, *PVDF-Based Piezoelectric Microphone for Sound Detection Inside the Cochlea: Toward Totally Implantable Cochlear Implants.* Trends in Hearing, 2018. **22**: p. 2331216518774450.

13.	Zhao, C., K.E. Knisely, D.J. Colesa, B.E. Pfingst, Y. Raphael, and K. Grosh, *Voltage readout from a piezoelectric intracochlear acoustic transducer implanted in a living guinea pig.* Scientific Reports, 2019. **9**(1): p. 3711.

14.	Rajabi, A.H., M. Jaffe, and T.L. Arinzeh, *Piezoelectric materials for tissue regeneration: A review.* Acta Biomaterialia, 2015. **24**: p. 12-23.

15.	Khanbareh, H., *Expanding the Functionality of Piezo-Particulate Composites.* 2016.

16.	Vasilev, S., P. Zelenovskiy, D. Vasileva, A. Nuraeva, V.Y. Shur, and A.L. Kholkin, *Piezoelectric properties of diphenylalanine microtubes prepared*

from the solution. Journal of Physics and Chemistry of Solids, 2016. **93**: p. 68-72.

17. Sharma, P., Z. Ounaies, V. Varadan, and V. Varadan, *Dielectric and Piezoelectric Properties of Microwave Sintered PZT.* Smart Materials and Structures, 2001. **10**: p. 878.

18. Chorsi, M.T., E.J. Curry, H.T. Chorsi, R. Das, J. Baroody, P.K. Purohit, H. Ilies, and T.D. Nguyen, *Piezoelectric Biomaterials for Sensors and Actuators.* Advanced Materials, 2019. **31**(1): p. 1802084.

19. Nguyen, M.D., E.P. Houwman, and G. Rijnders, *Large piezoelectric strain with ultra-low strain hysteresis in highly c-axis oriented Pb(Zr0.52Ti0.48)O3 films with columnar growth on amorphous glass substrates.* Scientific Reports, 2017. **7**(1): p. 12915.

20. Ruan, L., X. Yao, Y. Chang, L. Zhou, G. Qin, and X. Zhang, *Properties and Applications of the β Phase Poly(vinylidene fluoride).* Polymers, 2018. **10**(3): p. 228.

21. Clower, W., V. Kaajakari, and C.G. Wilson, *Laser-Assisted Wet Etching of Quartz Crystal Resonators.* Journal of Microelectromechanical Systems, 2018. **27**(1): p. 22-24.

22. Haertling, G.H., *Ferroelectric Ceramics: History and Technology.* Journal of the American Ceramic Society, 1999. **82**(4): p. 797-818.

23. Ramadan, K.S., D. Sameoto, and S. Evoy, *A review of piezoelectric polymers as functional materials for electromechanical transducers.* Smart Materials and Structures, 2014. **23**(3): p. 033001.

24. Hattori, T., Y. Takahashi, M. Iijima, and E. Fukada, *Piezoelectric and ferroelectric properties of polyurea-5 thin films prepared by vapor deposition polymerization.* Journal of Applied Physics, 1996. **79**(3): p. 1713-1721.

25. Newman, B.A., P. Chen, K.D. Pae, and J.I. Scheinbeim, *Piezoelectricity in nylon 11.* Journal of Applied Physics, 1980. **51**(10): p. 5161-5164.

26. Harrison, J.S., *Piezoelectric Polymers*, in *Encyclopedia of Polymer Science and Technology*. 2001.

27. Ameduri, B., *From Vinylidene Fluoride (VDF) to the Applications of VDF-Containing Polymers and Copolymers: Recent Developments and Future Trends.* Chemical Reviews, 2009. **109**(12): p. 6632-6686.

28. Marino, A., G.G. Genchi, V. Mattoli, and G. Ciofani, *Piezoelectric nanotransducers: The future of neural stimulation.* Nano Today, 2017. **14**: p. 9-12.

29. Hoop, M., X.-Z. Chen, A. Ferrari, F. Mushtaq, G. Ghazaryan, T. Tervoort, D. Poulikakos, B. Nelson, and S. Pané, *Ultrasound-mediated piezoelectric differentiation of neuron-like PC12 cells on PVDF membranes.* Scientific Reports, 2017. **7**(1): p. 4028.

30. Laiarinandrasana, L., J. Besson, M. Lafarge, and G. Hochstetter, *Temperature dependent mechanical behaviour of PVDF: Experiments and numerical modelling.* International Journal of Plasticity, 2009. **25**(7): p. 1301-1324.

31. Martin, A.J.P., *Tribo-electricity in wool and hair.* Proceedings of the Physical Society, 1941. **53**(2): p. 186-189.

32. Ando, Y. and E. Fukada, *Piezoelectric properties of oriented deoxyribonucleate films.* Journal of Polymer Science: Polymer Physics Edition, 1976. **14**(1): p. 63-79.

33.   Yuan, H., P. Han, K. Tao, S. Liu, E. Gazit, and R. Yang, *Piezoelectric Peptide and Metabolite Materials.* Research, 2019. **2019**: p. 13.

34.   Adler-Abramovich, L., L. Vaks, O. Carny, D. Trudler, A. Magno, A. Caflisch, D. Frenkel, and E. Gazit, *Phenylalanine assembly into toxic fibrils suggests amyloid etiology in phenylketonuria.* Nature Chemical Biology, 2012. **8**: p. 701.

35.   Bonser, R. and P. Purslow, *The Young's modulus of feather keratin.* The Journal of experimental biology, 1995. **198**: p. 1029-33.

36.   Rossi, D.D., C. Domenici, and P. Pastacaldi, *Piezoelectric Properties of Dry Human Skin.* IEEE Transactions on Electrical Insulation, 1986. **EI-21**(3): p. 511-517.

37.   Bloom, K.S., *Beyond the code: the mechanical properties of DNA as they relate to mitosis.* Chromosoma, 2008. **117**(2): p. 103-110.

38.   Fukada, E. and Y. Ando, *Piezoelectricity in oriented DNA films.* Journal of Polymer Science Part A-2: Polymer Physics, 1972. **10**(3): p. 565-567.

39.   Martin, R.I. and P.W. Brown, *Mechanical properties of hydroxyapatite formed at physiological temperature.* Journal of Materials Science: Materials in Medicine, 1995. **6**(3): p. 138-143.

40.   Rodriguez, R., D. Rangel, G. Fonseca, M. Gonzalez, and S. Vargas, *Piezoelectric properties of synthetic hydroxyapatite-based organic-inorganic hydrated materials.* Results in Physics, 2016. **6**: p. 925-932.

41.   Huang, R., W. Qi, R. Su, J. Zhao, and Z. He, *Solvent and surface controlled self-assembly of diphenylalanine peptide: from microtubes to nanofibers.* Soft Matter, 2011. **7**(14): p. 6418-6421.

42.   Safaryan, S., V. Slabov, S. Kopyl, K. Romanyuk, I. Bdikin, S. Vasilev, P. Zelenovskiy, V.Y. Shur, E.A. Uslamin, E.A. Pidko, A.V. Vinogradov, and A.L. Kholkin, *Diphenylalanine-Based Microribbons for Piezoelectric Applications via Inkjet Printing.* ACS Applied Materials & Interfaces, 2018. **10**(12): p. 10543-10551.

43.   Huang, R., Y. Wang, W. Qi, R. Su, and Z. He, *Temperature-induced reversible self-assembly of diphenylalanine peptide and the structural transition from organogel to crystalline nanowires.* Nanoscale research letters, 2014. **9**(1): p. 653-653.

44.   Reches, M. and E. Gazit, *Controlled patterning of aligned self-assembled peptide nanotubes.* Nature Nanotechnology, 2006. **1**: p. 195.

45.   Marchesan, S., A.V. Vargiu, and K.E. Styan, *The Phe-Phe Motif for Peptide Self-Assembly in Nanomedicine.* Molecules, 2015. **20**(11): p. 19775-88.

46.   Nguyen, V., R. Zhu, K. Jenkins, and R. Yang, *Self-assembly of diphenylalanine peptide with controlled polarization for power generation.* Nature Communications, 2016. **7**: p. 13566.

47.   Zelenovskiy, P.S., T.A. Koryukova, V.V. Yuzhakov, S.G. Vasilev, A.S. Nuraeva, E.V. Gunina, D.S. Chezganov, A.L. Kholkin, and V.Y. Shur, *Piezoelectric properties and Young's moduli of diphenylalanine microtubes—oxide nanoparticles composites.* Ferroelectrics, 2018. **525**(1): p. 146-155.

48.   Reches, M. and E. Gazit, *Casting metal nanowires within discrete self-assembled peptide nanotubes.* Science, 2003. **300**(5619): p. 625-7.

49.   Petrossian, G., C.J. Hohimer, and A. Ameli, *Highly-Loaded Thermoplastic Polyurethane/Lead Zirconate Titanate Composite Foams*

with Low Permittivity Fabricated using Expandable Microspheres. Polymers, 2019. **11**(2): p. 280.

50. Stuber, V.L., D.B. Deutz, J. Bennett, D. Cannel, D.M. de Leeuw, S. van der Zwaag, and P. Groen, *Flexible Lead-Free Piezoelectric Composite Materials for Energy Harvesting Applications.* Energy Technology, 2019. **7**(1): p. 177-185.

51. Kahoul, F., L. Hamzioui, Z. Necira, and A. Boutarfaia, *Effect of Sintering Temperature on the Electromechanical Properties of (1-x)Pb(ZryTi1-y)O3-xSm(Fe3+0.5, Nb5+0.5)O3 Ceramics.* Energy Procedia, 2013. **36**: p. 1050-1059.

52. Cholleti, E.R., *A Review on 3D printing of piezoelectric materials.* IOP Conference Series: Materials Science and Engineering, 2018. **455**: p. 012046.

53. Cui, H., R. Hensleigh, D. Yao, D. Maurya, P. Kumar, M.G. Kang, S. Priya, and X. Zheng, *Three-dimensional printing of piezoelectric materials with designed anisotropy and directional response.* Nature Materials, 2019. **18**(3): p. 234-241.

54. Li, M., I. Katsouras, C. Piliego, G. Glasser, I. Lieberwirth, P.W.M. Blom, and D.M. de Leeuw, *Controlling the microstructure of poly(vinylidene-fluoride) (PVDF) thin films for microelectronics.* Journal of Materials Chemistry C, 2013. **1**(46): p. 7695-7702.

55. He, X. and K. Yao, *Crystallization mechanism and piezoelectric properties of solution-derived ferroelectric poly(vinylidene fluoride) thin films.* Applied Physics Letters, 2006. **89**(11): p. 112909.

56. Turnbull, G., J. Clarke, F. Picard, P. Riches, L. Jia, F. Han, B. Li, and W. Shu, *3D bioactive composite scaffolds for bone tissue engineering.* Bioactive Materials, 2018. **3**(3): p. 278-314.

57. Azuma, K., R. Izumi, T. Osaki, S. Ifuku, M. Morimoto, H. Saimoto, S. Minami, and Y. Okamoto, *Chitin, chitosan, and its derivatives for wound healing: old and new materials.* J Funct Biomater, 2015. **6**(1): p. 104-42.

58. Wiesmann, H.-P., M. Hartig, U. Stratmann, U. Meyer, and U. Joos, *Electrical stimulation influences mineral formation of osteoblast-like cells in vitro.* Biochimica et Biophysica Acta (BBA) - Molecular Cell Research, 2001. **1538**(1): p. 28-37.

59. Nguyen, H.T., C. Wei, J.K. Chow, L. Nguy, H.K. Nguyen, and C.E. Schmidt, *Electric field stimulation through a substrate influences Schwann cell and extracellular matrix structure.* Journal of Neural Engineering, 2013. **10**(4): p. 046011.

60. Wu, S., M.-S. Chen, P. Maurel, Y.-s. Lee, M.B. Bunge, and T.L. Arinzeh, *Aligned fibrous PVDF-TrFE scaffolds with Schwann cells support neurite extension and myelination in vitro.* Journal of Neural Engineering, 2018. **15**(5): p. 056010.

61. Lee, Y.-S., G. Collins, and T. Livingston Arinzeh, *Neurite extension of primary neurons on electrospun piezoelectric scaffolds.* Acta Biomaterialia, 2011. **7**(11): p. 3877-3886.

62. Chen, X.-Z., J.-H. Liu, M. Dong, L. Müller, G. Chatzipirpiridis, C. Hu, A. Terzopoulou, H. Torlakcik, X. Wang, F. Mushtaq, J. Puigmartí-Luis, Q.-D. Shen, B.J. Nelson, and S. Pané, *Magnetically driven piezoelectric soft microswimmers for neuron-like cell delivery and neuronal differentiation.* Materials Horizons, 2019. **6**(7): p. 1512-1516.

63. Tsentalovich, D.E., R.J. Headrick, F. Mirri, J. Hao, N. Behabtu, C.C. Young, and M. Pasquali, *Influence of Carbon Nanotube Characteristics on Macroscopic Fiber Properties.* ACS Applied Materials & Interfaces, 2017. **9**(41): p. 36189-36198.

64. Wyckoff, R.W.G., *Crystal structures.* 2 ed. Vol. 1. 1963, Malabar, Fla.: R.E. Krieger Pub. Co.

65. Pierson, H.O., *Handbook of Carbon, Graphite, Diamonds and Fullerenes: Processing, Properties and Applications.* 2012.

66. Stark, J.G. and H.G. Wallace, *Chemistry Data Book.* 1982: Murray.

67. Morgan, P., *Carbon Fibers and Their Composites.* 2005: CRC Press.

68. Frank, E., D. Ingildeev, and M. Buchmeiser, *High-performance PAN-based carbon fibers and their performance requirements.* 2017. p. 7-30.

69. Jeevanandam, J., A. Barhoum, Y.S. Chan, A. Dufresne, and M.K. Danquah, *Review on nanoparticles and nanostructured materials: history, sources, toxicity and regulations.* Beilstein journal of nanotechnology, 2018. **9**: p. 1050-1074.

70. Boverhof, D.R., C.M. Bramante, J.H. Butala, S.F. Clancy, M. Lafranconi, J. West, and S.C. Gordon, *Comparative assessment of nanomaterial definitions and safety evaluation considerations.* Regulatory Toxicology and Pharmacology, 2015. **73**(1): p. 137-150.

71. Binnig, G., H. Rohrer, C. Gerber, and E. Weibel, *Tunneling through a controllable vacuum gap.* Applied Physics Letters, 1982. **40**(2): p. 178-180.

72. Thrower, P.A., *Editorial.* Carbon, 1999. **37**(11): p. 1677-1678.

73. Osawa, E. and Z. Yoshida, *Aromaticity Chemical Monograph.* 1971: Kyoto: Kagaku-dojin.

74. Kroto, H.W., J.R. Heath, S.C. O'Brien, R.F. Curl, and R.E. Smalley, *C60: Buckminsterfullerene.* Nature, 1985. **318**(6042): p. 162-163.

75. Novoselov, K.S., A.K. Geim, S.V. Morozov, D. Jiang, Y. Zhang, S.V. Dubonos, I.V. Grigorieva, and A.A. Firsov, *Electric Field Effect in Atomically Thin Carbon Films.* Science, 2004. **306**(5696): p. 666-669.

76. Hennig, G., *Electron Microscopy of Reactivity Changes Near Lattice Defects in Graphite.* Chemistry and Physics of Carbon, 1966. **2**: p. 1.

77. Harris, P.S., F.S. Feates, and B.G. Reuben, *Controlled atmosphere electron microscopy studies of graphite gasification—4. Catalysis of the graphite-O2 reaction by silver.* Carbon, 1974. **12**(2): p. 189-197.

78. Pandikumar, A., G.T. Soon How, T.P. See, F.S. Omar, S. Jayabal, K.Z. Kamali, N. Yusoff, A. Jamil, R. Ramaraj, S.A. John, H.N. Lim, and N.M. Huang, *Graphene and its nanocomposite material based electrochemical sensor platform for dopamine.* RSC Adv., 2014. **4**(108): p. 63296-63323.

79. Vamvakaki, V., K. Tsagaraki, and N. Chaniotakis, *Carbon nanofiber-based glucose biosensor.* Anal Chem, 2006. **78**(15): p. 5538-42.

80. Golnabi, H., *Carbon nanotube research developments in terms of published papers and patents, synthesis and production.* Scientia Iranica, 2012. **19**(6): p. 2012-2022.

81. Monthioux, M. and V. Kuznetsov, *Who should be given the credit for the discovery of carbon nanotubes?* Carbon, 2006. **44**: p. 1621-1623.

82. Iijima, S., *Helical microtubules of graphitic carbon.* Nature, 1991. **354**(6348): p. 56-58.

83. Baker, R.T.K. and P.S. Harris, *Controlled atmosphere electron microscopy.* J. Phys. E: Sci. Instrum., 1972 **5**: p. 793-797.

84. Baker, R.T.K., P.S. Harris, R.B. Thomas, and R.J. Waite, *Formation of filamentous carbon from iron, cobalt and chromium catalyzed decomposition of acetylene.* Journal of Catalysis, 1973. **30**(1): p. 86-95.

85. Baker, R.T.K., P.S. Harris, and S. Terry, *Unique form of filamentous carbon.* Nature, 1975. **253**(5486): p. 37-39.

86. Radushkevich, L.V. and V.M. Lukyanovich, *The Structure of Carbon Forming in Thermal Decomposition of Carbon Monoxide on an Iron Catalyst.* Russian Journal of Physical Chemistry, 1952. **26**: p. 88-95.

87. Iijima, S. and T. Ichihashi, *Single-shell carbon nanotubes of 1-nm diameter.* Nature, 1993. **363**(6430): p. 603-605.

88. Bethune, D.S., C.H. Kiang, M.S. de Vries, G. Gorman, R. Savoy, J. Vazquez, and R. Beyers, *Cobalt-catalysed growth of carbon nanotubes with single-atomic-layer walls.* Nature, 1993. **363**(6430): p. 605-607.

89. Oberlin, A., M. Endo, and T. Koyama, *Filamentous growth of carbon through benzene decomposition.* Journal of Crystal Growth, 1976. **32**(3): p. 335-349.

90. Alsharef, J., M. Taha, and T. Khan, *Physical dispersion of nanocarbons in composites – A review.* Jurnal Teknologi, 2017. **79**.

91. Zhou, W., M.F. Islam, H. Wang, D.L. Ho, A.G. Yodh, K.I. Winey, and J.E. Fischer, *Small angle neutron scattering from single-wall carbon nanotube suspensions: evidence for isolated rigid rods and rod networks.* Chemical Physics Letters, 2004. **384**(1-3): p. 185-189.

92. Laird, E.A., F. Kuemmeth, G.A. Steele, K. Grove-Rasmussen, J. Nygård, K. Flensberg, and L.P. Kouwenhoven, *Quantum transport in carbon nanotubes.* Reviews of Modern Physics, 2015. **87**(703).

93. Green, A.A. and M.C. Hersam, *Properties and Application of Double-Walled Carbon Nanotubes Sorted by Outer-Wall Electronic Type.* ACS Nano, 2011. **5**(2): p. 1459-1467.

94. Miao, M. and J.H. Xin, *Table 16.2. Specifications of Nanospheres, Nanotubes and Nanofibers*, in *Engineering of High-Performance Textiles*. 2018, Elsevier.

95. Bekyarova, E., M.E. Itkis, N. Cabrera, B. Zhao, A. Yu, J. Gao, and R.C. Haddon, *Electronic Properties of Single-Walled Carbon Nanotube Networks.* Journal of the American Chemical Society, 2005. **127**(16): p. 5990-5995.

96. Tang, X., A. El-Hami, K. El-Hami, M. Eid, and C. Si, *Elastic properties of single-walled carbon nanotube thin film by nanoindentation test.* Scientific Reports, 2017. **7**(1): p. 11438.

97. Wu, Z., Z. Chen, X. Du, J.M. Logan, J. Sippel, M. Nikolou, K. Kamaras, J.R. Reynolds, D.B. Tanner, A.F. Hebard, and A.G. Rinzler, *Transparent, Conductive Carbon Nanotube Films.* Science, 2004. **305**(5688): p. 1273-1276.

98. Ebbesen, T.W., H.J. Lezec, H. Hiura, J.W. Bennett, H.F. Ghaemi, and T. Thio, *Electrical conductivity of individual carbon nanotubes.* Nature, 1996. **382**(6586): p. 54-56.

99. He, X., W. Gao, L. Xie, B. Li, Q. Zhang, S. Lei, J.M. Robinson, E.H. Hároz, S.K. Doorn, W. Wang, R. Vajtai, P.M. Ajayan, W.W. Adams, R.H. Hauge, and J. Kono, *Wafer-scale monodomain films of spontaneously*

aligned single-walled carbon nanotubes. Nature Nanotechnology, 2016. **11**(7): p. 633-638.

100. Sui, C., Z. Pan, R.J. Headrick, Y. Yang, C. Wang, J. Yuan, X. He, M. Pasquali, and J. Lou, *Aligned-SWCNT film laminated nanocomposites: Role of the film on mechanical and electrical properties.* Carbon, 2018. **139**: p. 680-687.

101. Arguin, M., F. Sirois, and D. Therriault, *Electric field induced alignment of multiwalled carbon nanotubes in polymers and multiscale composites.* Advanced Manufacturing: Polymer & Composites Science, 2015. **1**(1): p. 16-25.

102. Tune, D.D., B.W. Stolz, M. Pfohl, and B.S. Flavel, *Dry shear aligning: a simple and versatile method to smooth and align the surfaces of carbon nanotube thin films.* Nanoscale, 2016. **8**(6): p. 3232-3236.

103. Yamada, T., Y. Hayamizu, Y. Yamamoto, Y. Yomogida, A. Izadi-Najafabadi, D.N. Futaba, and K. Hata, *A stretchable carbon nanotube strain sensor for human-motion detection.* Nature Nanotechnology, 2011. **6**(5): p. 296-301.

104. Ausman, K.D., R. Piner, O. Lourie, R.S. Ruoff, and M. Korobov, *Organic Solvent Dispersions of Single-Walled Carbon Nanotubes: Toward Solutions of Pristine Nanotubes.* Journal of Physical Chemistry B, 2000. **104**(38): p. 8911-8915.

105. Lee, K., H.J. Lim, S.J. Yang, Y.S. Kim, and C.R. Park, *Determination of solubility parameters of single-walled and double-walled carbon nanotubes using a finite-length model.* RSC Advances, 2013. **3**(14): p. 4814-4820.

106. Arrigo, R., R. Teresi, C. Gambarotti, F. Parisi, G. Lazzara, and N.T. Dintcheva, *Sonication-Induced Modification of Carbon Nanotubes: Effect on the Rheological and Thermo-Oxidative Behaviour of Polymer-Based Nanocomposites.* Materials (Basel, Switzerland), 2018. **11**(3): p. 383.

107. Parra-Vasquez, A.N.G., N. Behabtu, M.J. Green, C.L. Pint, C.C. Young, J. Schmidt, E. Kesselman, A. Goyal, P.M. Ajayan, Y. Cohen, Y. Talmon, R.H. Hauge, and M. Pasquali, *Spontaneous Dissolution of Ultralong Single- and Multiwalled Carbon Nanotubes.* ACS Nano, 2010. **4**(7): p. 3969-3978.

108. Dalton, A.B., S. Collins, E. Muñoz, J.M. Razal, V.H. Ebron, J.P. Ferraris, J.N. Coleman, B.G. Kim, and R.H. Baughman, *Super-tough carbon-nanotube fibres.* Nature, 2003. **423**(6941): p. 703-703.

109. Ju, L., W. Zhang, X. Wang, J. Hu, and Y. Zhang, *Aggregation kinetics of SDBS-dispersed carbon nanotubes in different aqueous suspensions.* Colloids and Surfaces A: Physicochemical and Engineering Aspects, 2012. **409**: p. 159-166.

110. Wang, X., Y. Liu, W. Qiu, and D. Zhu, *Immobilization of tetra-tert-butylphthalocyanines on carbon nanotubes: a first step towards the development of new nanomaterials.* Journal of Materials Chemistry, 2002. **12**(6): p. 1636-1639.

111. La Torre, A., G.A. Rance, J. El Harfi, J.N. Li, D.J. Irvine, P.D. Brown, and A.N. Khlobystov, *Transport and encapsulation of gold nanoparticles in carbon nanotubes.* Nanoscale, 2010. **2**(6): p. 1006-1010.

112. Grossmann, D., A. Dreier, C.W. Lehmann, and W. Grunert, *Encapsulation of copper and zinc oxide nanoparticles inside small*

diameter carbon nanotubes. Microporous and Mesoporous Materials, 2015. **202**: p. 189-197.

113. Moraes, F.C., M.F. Cabral, L.H. Mascaro, and S.A.S. Machado, *The electrochemical effect of acid functionalisation of carbon nanotubes to be used in sensors development.* Surface Science, 2011. **605**(3): p. 435-440.

114. Banks, C.E. and R.G. Compton, *New electrodes for old: from carbon nanotubes to edge plane pyrolytic graphite.* Analyst, 2006. **131**(1): p. 15-21.

115. Zhang, N., J. Xie, and V.K. Varadan, *Functionalization of carbon nanotubes by potassium permanganate assisted with phase transfer catalyst.* Smart Materials and Structures, 2002. **11**(6): p. 962-965.

116. Morales-Lara, F., M.J. Pérez-Mendoza, D. Altmajer-Vaz, M. García-Román, M. Melguizo, F.J. López-Garzón, and M. Domingo-García, *Functionalization of Multiwall Carbon Nanotubes by Ozone at Basic pH. Comparison with Oxygen Plasma and Ozone in Gas Phase.* The Journal of Physical Chemistry C, 2013. **117**(22): p. 11647-11655.

117. Felten, A., C. Bittencourt, J.J. Pireaux, G.V. Lier, and J.C. Charlier, *Radio-frequency plasma functionalization of carbon nanotubes surface O2, NH3, and CF4 treatments.* Journal of Applied Physics, 2005. **98**(7): p. 074308.

118. Merenda, A., E.d. Ligneris, K. Sears, T. Chaffraix, K. Magniez, D. Cornu, J.A. Schütz, and L.F. Dumée, *Assessing the temporal stability of surface functional groups introduced by plasma treatments on the outer shells of carbon nanotubes.* Scientific Reports, 2016. **6**(1): p. 31565.

119. Hsieh, C.-T., H. Teng, W.-Y. Chen, and Y.-S. Cheng, *Synthesis, characterization, and electrochemical capacitance of amino-functionalized carbon nanotube/carbon paper electrodes.* Carbon, 2010. **48**(15): p. 4219-4229.

120. Ballesteros, B., G. de la Torre, C. Ehli, G.M. Aminur Rahman, F. Agulló-Rueda, D.M. Guldi, and T. Torres, *Single-Wall Carbon Nanotubes Bearing Covalently Linked Phthalocyanines − Photoinduced Electron Transfer.* Journal of the American Chemical Society, 2007. **129**(16): p. 5061-5068.

121. Dinesh, B., M.A. Squillaci, C. Menard-Moyon, P. Samori, and A. Bianco, *Self-assembly of diphenylalanine backbone homologues and their combination with functionalized carbon nanotubes.* Nanoscale, 2015. **7**(38): p. 15873-9.

122. Matsumoto, K., C. Sato, Y. Naka, A. Kitazawa, R.L. Whitby, and N. Shimizu, *Neurite outgrowths of neurons with neurotrophin-coated carbon nanotubes.* J Biosci Bioeng, 2007. **103**(3): p. 216-20.

123. Shin, S.R., H. Bae, J.M. Cha, J.Y. Mun, Y.-C. Chen, H. Tekin, H. Shin, S. Farshchi, M.R. Dokmeci, S. Tang, and A. Khademhosseini, *Carbon Nanotube Reinforced Hybrid Microgels as Scaffold Materials for Cell Encapsulation.* ACS Nano, 2012.

124. Li, Y., H. Zhang, Y. Liu, H.S. Wang, Z.H. Huang, T. Peijs, and E. Bilotti, *Synergistic effects of spray-coated hybrid carbon nanoparticles for enhanced electrical and thermal surface conductivity of CFRP laminates.* Composites Part a-Applied Science and Manufacturing, 2018. **105**: p. 9-18.

125. Liu, Y., H. Zhang, H. Porwal, J.J.C. Busfield, T. Peijs, and E. Bilotti, *Pyroresistivity in conductive polymer composites: a perspective on recent advances and new applications.* Polymer International, 2019. **68**(3): p. 299-305.

126. Alshammari, A.S., M. Shkunov, and S.R.P. Silva, *Inkjet printed PEDOT:PSS/MWCNT nano-composites with aligned carbon nanotubes and enhanced conductivity.* physica status solidi (RRL) – Rapid Research Letters, 2014. **8**(2): p. 150-153.

127. Luo, B., Y. Wei, H. Chen, Z. Zhu, P. Fan, X. Xu, and B. Xie, *Printing Carbon Nanotube-Embedded Silicone Elastomers via Direct Writing.* ACS Applied Materials & Interfaces, 2018. **10**(51): p. 44796-44802.

128. Vuorinen, T., J. Niittynen, T. Kankkunen, T.M. Kraft, and M. Mäntysalo, *Inkjet-Printed Graphene/PEDOT:PSS Temperature Sensors on a Skin-Conformable Polyurethane Substrate.* Scientific Reports, 2016. **6**: p. 35289.

129. Kernin, A., K.N. Wan, Y. Liu, X.T. Shi, J. Kong, E. Bilotti, T. Peijs, and H. Zhang, *The effect of graphene network formation on the electrical, mechanical, and multifunctional properties of graphene/epoxy nanocomposites.* Composites Science and Technology, 2019. **169**: p. 224-231.

130. Li, J., P.C. Ma, W.S. Chow, C.K. To, B.Z. Tang, and J.-K. Kim, *Correlations between Percolation Threshold, Dispersion State, and Aspect Ratio of Carbon Nanotubes.* Advanced Functional Materials, 2007. **17**(16): p. 3207-3215.

131. Zhang, H., E. Bilotti, W. Tu, C.Y. Lew, and T. Peijs, *Static and dynamic percolation of phenoxy/carbon nanotube nanocomposites.* European Polymer Journal, 2015. **68**: p. 128-138.

132. Deng, H., T. Skipa, E. Bilotti, R. Zhang, D. Lellinger, L. Mezzo, Q. Fu, I. Alig, and T. Peijs, *Preparation of High-Performance Conductive Polymer Fibers through Morphological Control of Networks Formed by Nanofillers.* Advanced Functional Materials, 2010. **20**(9): p. 1424-1432.

133. Zhang, S.M., L. Lin, H. Deng, X. Gao, E. Bilotti, T. Peijs, Q. Zhang, and Q. Fu, *Dynamic percolation in highly oriented conductive networks formed with different carbon nanofillers.* Colloid and Polymer Science, 2012. **290**(14): p. 1393-1401.

134. Venkataraman, A., E.V. Amadi, Y. Chen, and C. Papadopoulos, *Carbon Nanotube Assembly and Integration for Applications.* Nanoscale Research Letters, 2019. **14**(1): p. 220.

135. Sun, H., J. Zhou, Z. Huang, L. Qu, N. Lin, C. Liang, R. Dai, L. Tang, and F. Tian, *Carbon nanotube-incorporated collagen hydrogels improve cell alignment and the performance of cardiac constructs.* International Journal of Nanomedicine, 2017. **12**: p. 3109-3120.

136. Se-Jun, L., Z. Wei, N. Margaret, L. Grace, H. Dong Nyoung, K. Junghoon, Y.Z. Yi, and Z. Lijie Grace, *3D printing nano conductive multi-walled carbon nanotube scaffolds for nerve regeneration.* Journal of Neural Engineering, 2018. **15**(1): p. 016018.

137. Kim, J.H., S. Lee, M. Wajahat, H. Jeong, W.S. Chang, H.J. Jeong, J.-R. Yang, J.T. Kim, and S.K. Seol, *Three-Dimensional Printing of Highly Conductive Carbon Nanotube Microarchitectures with Fluid Ink.* ACS Nano, 2016. **10**(9): p. 8879-8887.

138. Gbordzoe, S., P.K. Adusei, D. Chauhan, N.T. Alvarez, M.R. Haase, K. Mansari, S.N. Kanakaraj, Y.Y. Hsieh, and V. Shanov, *A Simple Two-Step Process for Producing Strong and Aligned Carbon Nanotube-Polymer Composites.* C-Journal of Carbon Research, 2019. **5**(3).

139. Ogihara, H., H. Kibayashi, and T. Saji, *Microcontact Printing for Patterning Carbon Nanotube/Polymer Composite Films with Electrical Conductivity.* ACS Applied Materials & Interfaces, 2012. **4**(9): p. 4891-4897.

140. Botelho, E.C., M.L. Costa, E.R. Edwards, T. Burkhart, and B. Lauke, *Effects of carbon nanotube fillers dispersion on mechanical behavior of phenolic/carbon nanotube nanocomposite.* Journal of Materials Research, 2012. **27**(18): p. 2342-2351.

141. Licari, J.J. and L.R. Enlow, *4.2.1 Fine-Line Thick-Film Processes*, in *Hybrid Microcircuit Technology Handbook (2nd Edition)*. William Andrew Publishing/Noyes. p. 127.

142. Xu, L.C. and C.A. Siedlecki, *4.18 Surface Texturing and Control of Bacterial Adhesion*, in *Comprehensive Biomaterials II*, P. Ducheyne, Editor. 2017, Elsevier: Oxford. p. 303-320.

143. Licari, J.J. and L.R. Enlow, *2.8 Enameled Metal Substrates*, in *Hybrid Microcircuit Technology Handbook (2nd Edition)*. William Andrew Publishing/Noyes. p. 58.

144. Metters, J.P., M. Gomez-Mingot, J. Iniesta, R.O. Kadara, and C.E. Banks, *The fabrication of novel screen printed single-walled carbon nanotube electrodes: Electroanalytical applications.* Sensors and Actuators B: Chemical, 2013. **177**: p. 1043-1052.

145. Tortorich, R. and J.-W. Choi, *Inkjet Printing of Carbon Nanotubes.* Nanomaterials, 2013. **3**(3): p. 453-468.

146. Licari, J.J. and L.R. Enlow, *4.1.1 Screen-Printing*, in *Hybrid Microcircuit Technology Handbook (2nd Edition)*. William Andrew Publishing/Noyes. p. 104-105.

147. He, X.-X., J. Zheng, G.-F. Yu, M.-H. You, M. Yu, X. Ning, and Y.-Z. Long, *Near-Field Electrospinning: Progress and Applications.* The Journal of Physical Chemistry C, 2017. **121**(16): p. 8663-8678.

148. Liu, Z.H., C.T. Pan, L.W. Lin, and H.W. Lai, *Piezoelectric properties of PVDF/MWCNT nanofiber using near-field electrospinning.* Sensors and Actuators A: Physical, 2013. **193**: p. 13-24.

149. Zhang, J., L. Gao, J. Sun, Y. Liu, Y. Wang, J. Wang, H. Kajiura, Y. Li, and K. Noda, *Dispersion of Single-Walled Carbon Nanotubes by Nafion in Water/Ethanol for Preparing Transparent Conducting Films.* The Journal of Physical Chemistry C, 2008. **112**(42): p. 16370-16376.

150. Gabay, T., M. Ben-David, I. Kalifa, R. Sorkin, Z.R. Abrams, E. Ben-Jacob, and Y. Hanein, *Electro-chemical and biological properties of carbon nanotube based multi-electrode arrays.* Nanotechnology, 2007. **18**(3): p. 035201.

151. Gillis, W.F., C.A. Lissandrello, J. Shen, B.W. Pearre, A. Mertiri, F. Deku, S. Cogan, B.J. Holinski, D.J. Chew, A.E. White, T.J. Gardner, and T.M. Otchy, *Carbon Fiber on Polyimide Ultra-Microelectrodes.* bioRxiv, 2017: p. 123281.

152. Vitale, F., S.R. Summerson, B. Aazhang, C. Kemere, and M. Pasquali, *Neural Stimulation and Recording with Bidirectional, Soft Carbon Nanotube Fiber Microelectrodes.* Acs Nano, 2015. **9**(4): p. 4465-4474.

153. Bareket-Keren, L. and Y. Hanein, *Carbon nanotube-based multi electrode arrays for neuronal interfacing: progress and prospects.* Frontiers in neural circuits, 2013. **6**: p. 122-122.

154. Xue, W. and T. Cui, *A thin-film transistor based acetylcholine sensor using self-assembled carbon nanotubes and SiO2 nanoparticles.* Sensors and Actuators B: Chemical, 2008. **134**(2): p. 981-987.

155. Kang, B.C., J.Y. Jeon, Y.T. Byun, and T.J. Ha, *Functionalized Carbon Nanotube Sensors for the Detection of Sub-ppm Nitric Oxide Gas.* J Nanosci Nanotechnol, 2018. **18**(9): p. 6562-6564.

156. Jalili, R., A. Kanneganti, M.I. Romero-Ortega, and G.G. Wallace, *Implantable electrodes.* Current Opinion in Electrochemistry, 2017. **3**(1): p. 68-74.

157. Luo, X., C.L. Weaver, D.D. Zhou, R. Greenberg, and X.T. Cui, *Highly stable carbon nanotube doped poly(3,4-ethylenedioxythiophene) for chronic neural stimulation.* Biomaterials, 2011. **32**(24): p. 5551-5557.

158. Abdalla, S., F. Al-Marzouki, A.A. Al-Ghamdi, and A. Abdel-Daiem, *Different Technical Applications of Carbon Nanotubes.* Nanoscale Research Letters, 2015. **10**(1): p. 358.

159. Boyles, M.S.P., L. Young, D.M. Brown, L. MacCalman, H. Cowie, A. Moisala, F. Smail, P.J.W. Smith, L. Proudfoot, A.H. Windle, and V. Stone, *Multi-walled carbon nanotube induced frustrated phagocytosis, cytotoxicity and pro-inflammatory conditions in macrophages are length dependent and greater than that of asbestos.* Toxicology in Vitro, 2015. **29**(7): p. 1513-1528.

160. Song, W., X. Liu, A. Vilches, J. Gale, S. Saeed, and T. Maltby, *Piezoelectric Nano-Fibre Based Acoustic Sensors for Artificial Cochlea*. 2015, EPSRC: University College London.

161. Griffiths, P.R. and J.A. de Haseth, *Attenuated Total Reflection*, in *Fourier Transform Infrared Spectrometry*. 2007, John Wiley & Sons: New York, USA. p. 321-348.

162. Gardiner, D.J. and P.R.G. (Eds.), *Practical Raman Spectroscopy.* 1990.

163. Atkins, P. and T. Overton, *Shriver and Atkins' Inorganic Chemistry*. 2010: OUP Oxford.

164. Berndt, K.D. *Circular Dichroism Spectroscopy*. 1996 29/02/20]; Available from: http://www.cryst.bbk.ac.uk/PPS2/course/section8/ss-960531_21.html.

165. Marie, E. and W. Torbjörn, *4 - Surface Analytical Techniques Applied to Cleaning Processes*, in *Handbook for Cleaning/Decontamination of Surfaces*, I. Johansson and P. Somasundaran, Editors. 2007, Elsevier Science B.V.: Amsterdam. p. 747-789.

166. Macosko, C.W. and R. Larson, *Rheology : principles, measurements, and applications*. 1994, New York: VCH.

167. Assembayev, D. and V. Myrseth, *Establishing an experimental pre-conditioning procedure for rheological characterization of oil based drilling fluids.* Annual Transactions of the Nordic Rheology Society, 2015. **23**: p. 1.

168. Saba, N., M. Jawaid, and M.T.H. Sultan, *1 - An overview of mechanical and physical testing of composite materials*, in *Mechanical and Physical Testing of Biocomposites, Fibre-Reinforced Composites and Hybrid Composites*, M. Jawaid, M. Thariq, and N. Saba, Editors. 2019, Woodhead Publishing. p. 1-12.

169. Facility, U.o.I.C.M.R. *Transmission Electron Microscopy*. 08/02/20]; Available from: https://cmrf.research.uiowa.edu/transmission-electron-microscopy.

170. *Transmission Electron Microscopy and Spectroscopy*, in *Handbook of Nanophase and Nanostructured Materials*, Z.L. Wang, Y. Liu, and Z. Zhang, Editors. 2002, Springer US: Boston, MA. p. 372-441.

171. Foster, A. and W. Hofer, *Scanning Probe Microscopy: Atomic Scale Engineering by Forces and Currents*. Atomic Scale Engineering by Forces and Currents. 2006, New York, NY: Springer New York, New York, NY.

172. Proksch, R. and S. Kainin, *Piezoresponse Force Microscopy with Asylum Research AFMs*. 2014.

173. Student, *The Probable Error of a Mean*. Biometrika, 1908. **6**(1): p. 1-25.

174. Guo, C., Y. Luo, R. Zhou, and G. Wei, *Probing the Self-Assembly Mechanism of Diphenylalanine-Based Peptide Nanovesicles and Nanotubes*. ACS Nano, 2012. **6**(5): p. 3907-3918.

175. Pandey, G., J. Saikia, S. Sasidharan, D.C. Joshi, S. Thota, H.B. Nemade, N. Chaudhary, and V. Ramakrishnan, *Modulation of Peptide Based Nano-Assemblies with Electric and Magnetic Fields*. Sci Rep, 2017. **7**(1): p. 2726.

176. Ryan, K., J. Beirne, G. Redmond, J.I. Kilpatrick, J. Guyonnet, N.V. Buchete, A.L. Kholkin, and B.J. Rodriguez, *Nanoscale Piezoelectric Properties of Self-Assembled Fmoc-FF Peptide Fibrous Networks*. ACS Appl Mater Interfaces, 2015. **7**(23): p. 12702-7.

177. Görbitz, C.H., *The structure of nanotubes formed by diphenylalanine, the core recognition motif of Alzheimer's β-amyloid polypeptide*. Chemical Communications, 2006(22): p. 2332-2334.

178. (CCDC), C.C.D.C., *Mercury User Guide and Tutorials*. 2017.

179. da Silva Filho, J.G., F.E.A. Melo, J.A. Lima, G.S. Pinheiro, and P.T.C. Freire, *High-temperature Raman spectroscopy of L,L-diphenylalanine single-crystal*. Vibrational Spectroscopy, 2018. **97**: p. 75-84.

180. Perczel, A. and G.D. Fasman, *Quantitative analysis of cyclic β-turn models*. Protein Science, 1992. **1**(3): p. 378-395.

181. Yan, X., P. Zhu, and J. Li, *Self-assembly and application of diphenylalanine-based nanostructures*. Chemical Society Reviews, 2010. **39**(6): p. 1877-1890.

182. Acuna, S.M., M.C. Veloso, and P.G. Toledo, *Self-Assembly of Diphenylalanine-Based Nanostructures in Water and Electrolyte Solutions*. Journal of Nanomaterials, 2018. **2018**: p. 7.

183. Viola, G., J. Chang, T. Maltby, F. Steckler, M. Jomaa, J. Sun, J. Edusei, D. Zhang, A. Vilches, S. Gao, X. Liu, S. Saeed, H. Zabalawi, J. Gale, and W. Song, *Bioinspired Multiresonant Acoustic Devices Based on Electrospun Piezoelectric Polymeric Nanofibers*. ACS Applied Materials & Interfaces, 2020. **12**(31): p. 34643-34657.

184. Ico, G., A. Showalter, W. Bosze, S.C. Gott, B.S. Kim, M.P. Rao, N.V. Myung, and J. Nam, *Size-dependent piezoelectric and mechanical properties of electrospun P(VDF-TrFE) nanofibers for enhanced energy harvesting.* Journal of Materials Chemistry A, 2016. **4**(6): p. 2293-2304.

185. Souza, M.I., T. Prieto, T. Rodrigues, F.F. Ferreira, F.B. Nascimento, A.O. Ribeiro, E.R. Silva, F. Giuntini, and W.A. Alves, *Conjugation with L,L-diphenylalanine Self-Assemblies Enhances In Vitro Antitumor Activity of Phthalocyanine Photosensitizer.* Scientific Reports, 2017. **7**(1): p. 13166.

186. Wu, X., S. Xiong, M. Wang, J. Shen, and P.K. Chu, *Water-Sensitive High-Frequency Molecular Vibrations in Self-Assembled Diphenylalanine Nanotubes.* The Journal of Physical Chemistry C, 2012. **116**(17): p. 9793-9799.

187. Bystrov, V.S., P.S. Zelenovskiy, A.S. Nuraeva, S. Kopyl, O.A. Zhulyabina, and V.A. Tverdislov, *Chiral Peculiar Properties of Self-Organization of Diphenylalanine Peptide Nanotubes: Modeling of Structure and Properties.* Mathematical Biology and Bioinformatics, 2019. **14**(1): p. 94-125.

188. Arnon, Z.A., D. Pinotsi, M. Schmidt, S. Gilead, T. Guterman, A. Sadhanala, S. Ahmad, A. Levin, P. Walther, C.F. Kaminski, M. Fändrich, G.S. Kaminski Schierle, L. Adler-Abramovich, L.J.W. Shimon, and E. Gazit, *Opal-like Multicolor Appearance of Self-Assembled Photonic Array.* ACS applied materials & interfaces, 2018. **10**(24): p. 20783-20789.

189. Görbitz, C.H., *Nanotube Formation by Hydrophobic Dipeptides.* Chemistry – A European Journal, 2001. **7**(23): p. 5153-5159.

190. Langford, J.I. and A.J.C. Wilson, *Scherrer after sixty years: A survey and some new results in the determination of crystallite size.* Journal of Applied Crystallography, 1978. **11**(2): p. 102-113.

191. *Optical Rotatory Dispersion and Circular Dichroism*, in *Physical Chemistry of Macromolecules*. 2004. p. 267-283.

192. Huang, R., R. Su, W. Qi, J. Zhao, and Z. He, *Hierarchical, interface-induced self-assembly of diphenylalanine: formation of peptide nanofibers and microvesicles.* Nanotechnology, 2011. **22**(24): p. 245609.

193. Zelenovskiy, P.S., A.S. Nuraeva, S. Kopyl, S.G. Arkhipov, S.G. Vasilev, V.S. Bystrov, D.A. Gruzdev, M. Waliczek, V. Svitlyk, V.Y. Shur, L. Mafra, and A.L. Kholkin, *Chirality-Dependent Growth of Self-Assembled Diphenylalanine Microtubes.* Crystal Growth & Design, 2019. **19**(11): p. 6414-6421.

194. Zelenovskiy, P., I. Kornev, S. Vasilev, and A. Kholkin, *On the origin of the great rigidity of self-assembled diphenylalanine nanotubes.* Phys Chem Chem Phys, 2016. **18**(43): p. 29681-29685.

195. Itoh, H., Y. Aoshima, and Y. Sakaguchi. *Model for a quartz-crystal tuning fork using plate spring approximated to torsion spring adopted at the joint of the arm and the base.* in *Proceedings of the 2002 IEEE International Frequency Control Symposium and PDA Exhibition (Cat. No.02CH37234).* 2002.

196. Nazeer, H., L. Abelmann, N. Tas, H. W, M. Siekman, and M. Elwenspoek, *Determination of young's modulus of PZT and Co80Ni20 thin films by means of micromachined cantilevers.* Journal of Statistical Planning and Inference - J STATIST PLAN INFER, 2009.

197. Malleshappa Gowder, S., J. Chatterjee, T. Chaudhuri, and K. Paul, *Prediction and Analysis of Surface Hydrophobic Residues in Tertiary Structure of Proteins.* The Scientific World Journal, 2014. **2014**: p. 971258.

198. Han, T.H., W.J. Lee, D.H. Lee, J.E. Kim, E.-Y. Choi, and S.O. Kim, *Peptide/Graphene Hybrid Assembly into Core/Shell Nanowires.* Advanced Materials, 2010. **22**(18): p. 2060-2064.

199. Ryu, J. and C.B. Park, *Solid-Phase Growth of Nanostructures from Amorphous Peptide Thin Film: Effect of Water Activity and Temperature.* Chemistry of Materials, 2008. **20**(13): p. 4284-4290.

200. Farahani, A.D., A.D. Martin, H. Iranmanesh, M.M. Bhadbhade, J.E. Beves, and P. Thordarson, *Gel- and Solid-State-Structure of Dialanine and Diphenylalanine Amphiphiles: Importance of C···H Interactions in Gelation.* ChemPhysChem, 2019. **20**(7): p. 972-983.

201. Persano, L., C. Dagdeviren, Y. Su, Y. Zhang, S. Girardo, D. Pisignano, Y. Huang, and J.A. Rogers, *High performance piezoelectric devices based on aligned arrays of nanofibers of poly(vinylidenefluoride-co-trifluoroethylene).* Nature Communications, 2013. **4**(1): p. 1633.

202. Truong, W.T., Y. Su, D. Gloria, F. Braet, and P. Thordarson, *Dissolution and degradation of Fmoc-diphenylalanine self-assembled gels results in necrosis at high concentrations in vitro.* Biomaterials Science, 2015. **3**(2): p. 298-307.

203. Mahler, A., M. Reches, M. Rechter, S. Cohen, and E. Gazit, *Rigid, Self-Assembled Hydrogel Composed of a Modified Aromatic Dipeptide.* Advanced Materials, 2006. **18**(11): p. 1365-1370.

204. Tysseling-Mattiace, V.M., V. Sahni, K.L. Niece, D. Birch, C. Czeisler, M.G. Fehlings, S.I. Stupp, and J.A. Kessler, *Self-Assembling Nanofibers Inhibit Glial Scar Formation and Promote Axon Elongation after Spinal Cord Injury.* The Journal of Neuroscience, 2008. **28**(14): p. 3814-3823.

205. Yuan, J., J. Chen, X. Wu, K. Fang, and L. Niu, *A NADH biosensor based on diphenylalanine peptide/carbon nanotube nanocomposite.* Journal of Electroanalytical Chemistry, 2011. **656**: p. 120-124.

206. Kruss, S., A.J. Hilmer, J. Zhang, N.F. Reuel, B. Mu, and M.S. Strano, *Carbon nanotubes as optical biomedical sensors.* Advanced Drug Delivery Reviews, 2013. **65**(15): p. 1933-1950.

207. Nanocyl, *Research grades NC3101 Technical Data Sheet.* 2016.

208. Shuaib, M., N. Mohammed, and Z. Burhanudin, *Optimization of the Production of Aligned CNTs Array as the Gas Sensing Element.* Materials Science Forum, 2013. **756**: p. 156-163.

209. Kharissova, O.V. and B.I. Kharisov, *Variations of interlayer spacing in carbon nanotubes.* RSC Advances, 2014. **4**(58): p. 30807-30815.

210. Valeur, E. and M. Bradley, *Amide bond formation: beyond the myth of coupling reagents.* Chemical Society Reviews, 2009. **38**(2): p. 606-631.

211. M. F. Lima, A., V. G. de Castro, R. Borges, and G. Silva, *Electrical Conductivity and Thermal Properties of Functionalized Carbon Nanotubes/Polyurethane Composites.* Polimeros, 2012. **22**: p. 117-124.

212. Kim, G., H. Kim, I.J. Kim, J.R. Kim, J.I. Lee, and M. Ree, *Bacterial adhesion, cell adhesion and biocompatibility of Nafion films.* J Biomater Sci Polym Ed, 2009. **20**(12): p. 1687-707.

213. Cisnal, A., F. R Ihmig, J.-C. Fraile, J. Pérez-Turiel, and V. Muñoz-Martinez, *Application of a Novel Measurement Setup for Characterization of Graphene Microelectrodes and a Comparative Study of Variables Influencing Charge Injection Limits of Implantable Microelectrodes.* Sensors (Basel, Switzerland), 2019. **19**(12): p. 2725.

214. Lee, H., S.M. Dellatore, W.M. Miller, and P.B. Messersmith, *Mussel-Inspired Surface Chemistry for Multifunctional Coatings.* Science, 2007. **318**(5849): p. 426-430.

215. Armstrong, J.P., C. Hurst, R.G. Jones, P. Licence, K.R.J. Lovelock, C.J. Satterley, and I.J. Villar-Garcia, *Vapourisation of ionic liquids.* Physical Chemistry Chemical Physics, 2007. **9**(8): p. 982-990.

216. DeLuca, N.W. and Y.A. Elabd, *Polymer electrolyte membranes for the direct methanol fuel cell: A review.* Journal of Polymer Science Part B: Polymer Physics, 2006. **44**(16): p. 2201-2225.

217. Atkins, P. and J. de Paula, *Atkins' Physical Chemistry*. 2010: OUP Oxford.

218. Zhu, P. and Y. Zhao, *Cyclic voltammetry measurements of electroactive surface area of porous nickel: Peak current and peak charge methods and diffusion layer effect.* Materials Chemistry and Physics, 2019. **233**: p. 60-67.

219. Whelan, A. and D. Dunning, *The Rabinowitsch Correction*, in *Developments in Plastics Technology—1: Extrusion.* 2012, Springer Netherlands. p. 234.

220. Morrison, F.A., *Weissenberg-Rabinowitsch Correction for Nonparabolic Velocity Profile*, in *Understanding Rheology*. 2001, Oxford University Press. p. 387-392.

221. Asare, E., A. Basir, W. Tu, H. Porwal, H. Zhang, Y. Liu, J. Evans, M. Newton, T. Peijs, and E. Bilotti, *Effect of mixed fillers on positive temperature coefficient of conductive polymer composites.* Nanocomposites, 2016. **2**(2): p. 58-64.

222. Schütt, F., S. Signetti, H. Krüger, S. Röder, D. Smazna, S. Kaps, S.N. Gorb, Y.K. Mishra, N.M. Pugno, and R. Adelung, *Hierarchical self-entangled carbon nanotube tube networks.* Nature Communications, 2017. **8**(1): p. 1215.

223. Wang, Z., L. Ci, L. Chen, S. Nayak, P.M. Ajayan, and N. Koratkar, *Polarity Dependent Electrochemically Controlled Transport of Water Through Carbon Nanotube Membranes.* Nano Letters, 2007. **7**(3): p. 697-702.

224. Singh, A., S. Asikainen, A.K. Teotia, P.A. Shiekh, E. Huotilainen, I. Qayoom, J. Partanen, J. Seppala, and A. Kumar, *Biomimetic Photocurable Three-Dimensional Printed Nerve Guidance Channels with Aligned Cryomatrix Lumen for Peripheral Nerve Regeneration.* ACS Applied Materials & Interfaces, 2018. **10**(50): p. 43327-43342.

225. Mollá, S. and V. Compañ, *Polyvinyl alcohol nanofiber reinforced Nafion membranes for fuel cell applications.* Journal of Membrane Science, 2011. **372**(1): p. 191-200.

226. Mahrous, S. and T.A. Hanfy, *Dielectric analysis of chlorinated polyvinyl chloride stabilized with di-n-octyltin maleate.* Journal of Applied Polymer Science, 2009. **113**(1): p. 316-320.

227. Cisnal, A., J.-C. Fraile, J. Pérez-Turiel, V. Muñoz-Martinez, C. Müller, and F. R Ihmig, *A Measurement Setup and Automated Calculation Method to Determine the Charge Injection Capacity of Implantable Microelectrodes.* Sensors (Basel, Switzerland), 2018. **18**(12): p. 4152.

228. Hudak, E.M., D.W. Kumsa, H.B. Martin, and J.T. Mortimer, *Electron transfer processes occurring on platinum neural stimulating electrodes: calculated charge-storage capacities are inaccessible during applied stimulation.* Journal of Neural Engineering, 2017. **14**(4): p. 046012.

229. Mandal, H.S., J.S. Kastee, D.G. McHail, J.F. Rubinson, J.J. Pancrazio, and T.C. Dumas, *Improved Poly(3,4-Ethylenedioxythiophene) (PEDOT) for Neural Stimulation.* Neuromodulation: Technology at the Neural Interface, 2015. **18**(8): p. 657-663.